Politecnico di Bari

Repository Istituzionale dei Prodotti della Ricerca del Politecnico di Bari

Search for dark matter signal features in the energy spectra of Galactic gamma rays measured by the Fermi Large Area Telescope

This is a PhD Thesis

Original Citation:
Search for dark matter signal features in the energy spectra of Galactic gamma rays measured by the Fermi Large Area Telescope / Giliberti, Mario. - ELETTRONICO. - (2026).

Availability:
This version is available at http://hdl.handle.net/11589/295480 since: 2026-01-13

Published version
DOI:

Publisher: Politecnico di Bari

Terms of use:

(Article begins on next page)

23 April 2026

Department of Mechanics, Mathematics and Management
Experimental Physics
Ph.D. program in Engineering and Aerospace Sciences (DRISA)
SSD: FIS/01

Final Dissertation

Search for dark matter signal features in the energy spectra of Galactic gamma rays measured by the Fermi Large Area Telescope

by

Giliberti Mario

Supervisors:

dott. Mario Nicola Mazziotta

Prof. Francesco Loparco

Coordinator of Ph.D. Program:

Prof. Ing. Caterina Ciminelli

Course n°38, 01/11/2022-31/10/2025

Politecnico di Bari

Department of Mechanics, Mathematics and Management
Experimental Physics
Ph.D. program in Engineering and Aerospace Sciences (DRISA)
SSD: PHYS-01/A

Final Dissertation

Search for dark matter signal features in the energy spectra of Galactic gamma rays measured by the Fermi Large Area Telescope

by

Giliberti Mario

Referees:

Prof.ssa Raffaella Bonino

Prof. Aldo Morselli

Supervisors:

dott. Mario Nicola Mazziotta

Prof. Francesco Loparco

Coordinator of Ph.D Program:

Prof. Ing. Caterina Ciminelli

Course n°38, 01/11/2022-31/10/2025

Contents

Introduction **v**

1 The Dark Matter Puzzle **1**

1.1 Gravitational evidence 1

1.1.1 Spiral galaxies rotation curves 1

1.1.2 Galaxy clusters: the Coma cluster 5

1.1.3 Bullet Cluster brightness-mass distribution disparity 9

1.1.4 Dense baryonic DM candidates: MACHOs 10

1.2 Cosmological evidence 11

1.2.1 Cosmic Microwave Background temperature anisotropies . . 11

1.2.2 Big Bang Nucleosynthesis (BBN) 16

1.3 Particle candidates for dark matter 16

1.3.1 "Sterile" neutrinos 18

1.3.2 Axions and axion-like particles (ALPs) 19

1.3.3 The "WIMP Miracle" 22

2 Indirect dark matter searches: an overview **26**

2.1 Possible probes for indirect dark matter search 26

2.1.1 Dark matter distribution inside galaxies 28
2.2 Gamma-ray signals from dark matter 33
2.2.1 Astrophysical backgrounds to tackle 33
2.2.2 Gamma-ray spectral excesses as DM signatures 36
2.2.3 WIMP searches in gamma rays 39
2.3 Main targets for DM searches in gamma rays 44
2.3.1 The Sun 44
2.3.2 The Galactic Center 46
2.3.3 The Milky Way Halo 49
2.3.4 Dwarf Spheroidal Galaxies 53
2.3.5 Galaxy clusters 55
2.4 Neutrino signals from WIMPs 56
2.4.1 Solar neutrinos 56
2.4.2 Neutrinos from the Galactic Center 57
2.4.3 Search for spectral lines in the Galactic neutrino spectra . . 59
2.4.4 Neutrinos from galaxy clusters and dwarf spheroidal galaxies 60
2.5 Searching dark matter in cosmic rays: The rising positron fraction . 61

3 Spaceborne gamma-ray telescopes and the *Fermi* Mission 65
3.1 A bit of history: Vela and EGRET 65
3.2 From GLAST to *Fermi* 68
3.2.1 The -Y SADA anomaly and related observation strategies . 72
3.3 The Gamma-ray Burst Monitor (GBM) instrument 74
3.4 The Large Area Telescope (LAT) 78
3.4.1 The pair conversion tracker system (TKR) 79
3.4.2 The hodoscopic electromagnetic calorimeter (CAL) 82
3.4.3 The Anticoincidence Detector (ACD) 83
3.4.4 The Data Acquisition System (DAQ) 84

3.5 Pass 8 event reconstruction and classification 88
3.5.1 Track reconstruction 90
3.5.2 Event classification 91
3.6 *Fermi*-LAT Instrument Response Functions 92
3.6.1 Effective area 93
3.6.2 Acceptance and field of view 94
3.6.3 Point Spread Functions 96
3.6.4 Energy dispersion 98
3.7 Current gamma-ray space missions 101
3.7.1 The AGILE mission 101
3.7.2 The DAMPE mission 102
3.8 Future gamma-ray space missions 105
3.8.1 e-ASTROGAM 106
3.8.2 AMEGO 107
3.9 The APT mission 110

4 Search for line-like and box-like features with the *Fermi*-LAT data 113

4.1 Data access and event selection 113
4.2 Regions of Interest (ROIs) 116
4.3 Livetime, exposure and expected counts 119
4.4 Fit procedure 123
4.4.1 Flux models and likelihood function 125
4.4.2 Local significance 129
4.4.3 Global significance 131
4.5 Results for the monochromatic line search 131
4.5.1 Sensitivity to the null hypothesis in the line search 137
4.6 Search for box features in galactic gamma-ray spectra 141

4.6.1 Analysis procedure 142
4.6.2 Results for box-shaped features search 142
4.6.3 Global significance 147
4.7 A cross-check study with an Earth Limb photons dataset 148
4.8 Summary 153

5 Perspectives of spectral line searches as signature of DM with the future APT detector 155
5.1 Simulated data sample 155
5.2 Sensitivity study with the pseudoexperiments 159
5.3 Fit procedure and results 160

Conclusions 162

A Galactic coordinates 165

Appendix A: Galactic coordinates **165**

List of Figures 185

List of Tables 186

Bibliography 186

Introduction

The fact that our universe is filled up with an unconventional form of matter, which is still undetected and unidentified, earned it the evocative name of *dark matter* (DM). The existence of DM is solidly supported by gravitational and cosmological arguments.

Firstly, galactic rotational velocities involving many galaxy cluster populations exhibit a remarkable independence of the distance from the center of the galaxy itself. This result induced the scientific community, unless we modify the current understanding of gravity, to accept that a vast part of matter is not *bright* (i.e. does not couple with electromagnetic radiation) and therefore is *dark*.

Secondly, studies of Cosmic Microwave Background anisotropies not only suggest the existence of DM, but also the fact that it should account, as *Cold Dark Matter (CDM)*, for approximately 25% of the matter-energy content of the universe, while standard baryonic matter contributes about 5%, and dark energy accounts for the remaining part. This stands as an amazing change of perception of our Universe, whose directly observable and identifiable parts are just a small fraction of it.

Much more difficulty is met when the puzzle of the identification of DM is addressed. Indeed, this work does not discuss in depth scenarios that try to avoid the existence of dark matter as much as possible but instead assumes its existence and investigates the complicated problem of identifying its nature.

Further observational evidence points out that the candidates for the DM

constituent particles should be electromagnetically neutral, non-relativistic, and their interaction with ordinary matter should preferably be weak, though in a broad sense: not only by means of weak interactions, but also by other kinds of couplings.

Possible candidates for DM particles should meet the characteristics specified above. Such candidates cannot be easily found among the particles in the Standard Model (SM), and can be searched for in theories beyond the SM. Among possible DM particle candidates, a strong interest has been raised towards WIMPs (*Weakly Interacting Massive Particles*), i.e. particle states which interact only weakly with standard matter, which are not light as neutrinos, whose existence is predicted by theories beyond the Standard Model, and find a solid justification as relics from the Big Bang, with densities quantitatively comparable to the predicted DM density (*WIMP miracle*).

A great number of experiments are currently aimed at looking for DM signatures with different approaches, in the perspective of finding evidence of physics beyond the Standard Model, a goal which high-energy physics is pursuing with great effort in many ways. These approaches can be divided into three categories: direct searches, indirect searches, and searches in production at colliders.

One of the indirect approaches to look for DM signatures focuses on the products of possible annihilation and decay of DM candidate particles. These final states are searched by looking at the cosmic radiation from regions where DM is expected to be more abundant.

High-energy photons are among the possible final states of the predicted top-down processes involving WIMPs. Unlike charged particles, which could be produced as well, gamma rays are not deflected by the galactic magnetic field and therefore bring important information about their sources that we are not able to retrieve from charged radiation. Gamma rays can thus be considered an excellent probe for DM indirect searches.

Supposing that WIMPs can self-annihilate or directly decay into gamma rays at rest, a signature for these kinds of processes could be represented by line-

like features as excesses in the gamma-ray spectrum towards the chosen target, since the gamma rays eventually produced should be essentially monochromatic. The line-like gamma-ray signal is expected to be very small because of the small couplings with which DM is predicted to interact, making this kind of searches as intriguing as challenging.

Another possible signature, which can be viewed as a slight complication of the monochromatic line, is the box-shaped feature. This spectral signature stems from the assumption that WIMPs can annihilate into low-mass metastable mediators that in turn decay into gamma rays.

Many studies involving simulations claim that our own Galaxy resides in a DM *halo*, which therefore is a possible target for DM searches. In this work, a search for DM line-like and box-like signatures is performed by analyzing more than 15 years of the energy spectra of galactic gamma rays measured by *Fermi*-LAT.

The *Fermi* mission is still producing remarkable scientific feats after 17 years in orbit (and many more counting also the design phases), providing reliable data of gamma rays from 500 MeV to 1 TeV. If we look at the sensitivity of other currently active gamma-ray telescopes, what stands out is that we are almost completely blind in an energy window that spans between 0.5 and a few MeV, the so-called *MeV gap*.

This is why a strong effort is being undertaken to build the next generation of gamma-ray telescopes capable of detecting in the MeV range, and several scientific motivations are given to justify it, including the possibility that DM signatures of massive particle candidates (i.e. WIMPs) could also produce spectral signatures in that energy window currently not observable with adequate sensitivity.

This is the main motivation for a review of some of the current projects for future detectors, with particular focus on the *Advanced Particle-astrophysics Telescope (APT)*, which aims to decuplicate the on-axis effective area of *Fermi*-LAT and, with its increased exposure, could give decisive results in dark matter searches in gamma rays.

The thesis consists of five chapters:

- **Chapter 1:** A summary of the evidence pointing towards DM existence and

a list of some possible DM candidates (with emphasis on WIMPs).

- **Chapter 2:** A review of the main results in dark matter indirect searches, focusing on gamma rays as probes.

- **Chapter 3:** A presentation of some airborne gamma-ray telescopes, in particular the *Fermi* mission and its main instrument, the LAT. The characteristics and performance of LAT are described, along with insights on future telescopes such as APT.

- **Chapter 4:** The data analysis aimed at identifying DM signatures (monochromatic spectral lines and box-shaped features) and setting upper limits on feature intensity and constraints on the annihilation cross-section and decay time of WIMPs.

- **Chapter 5:** A study of the sensitivity to DM line features in gamma rays on an APT-like detector, taking advantage of the methodology developed in Chapter 4.

Chapter 1

The Dark Matter Puzzle

This chapter collects the evidence in favor of dark matter (DM) existence, outlining the main problem concerning its identification. A review of the most credited hypotheses on DM candidates is then given, focusing on particle candidates and WIMPs in particular, which the data analysis work presented in Chapter 4 aims to find. Much information follows the extensive review of M. Cirelli et al. [1].

1.1 Gravitational evidence

The first evidence of DM dates back to the early years of the twentieth century. The existence of DM is by now well established and surprisingly simple to understand, even within an essentially Newtonian framework of gravitation. What remains "dark" is its identity. In this section, the gravitational evidence in favor of the existence of DM will be illustrated.

1.1.1 Spiral galaxies rotation curves

The earliest evidence for DM came from the observation that various bright objects (stars, gas clouds, globular clusters, and even galaxies) move faster than one would expect from the gravitational attraction by other visible objects [2], where with

"visible" we mean any source that emits any form of electromagnetic radiation in any way (either directly or diffusing radiation from other sources).

This feature is particularly striking in the measurement of rotation curves of spiral galaxies. The rotational velocity v of an object moving on a stable Keplerian orbit of radius r inside a galaxy scales as follows:

$$v(r) \propto \sqrt{\frac{M(r)}{r}} \tag{1.1}$$

where $M(r)$ is the mass inside the orbit.

This stems directly from the virial theorem in a Newtonian gravity framework. For a gravitationally bound system in equilibrium, the total energy is always half of the time-averaged potential energy:

$$E = \frac{1}{2}\langle U \rangle. \tag{1.2}$$

Since the total energy can be expressed as $E = K + U$ where U is the potential energy and K is the kinetic energy, the theorem can be reformulated as follows:

$$\langle U \rangle = -2\langle K \rangle. \tag{1.3}$$

In the case of a point-like body of mass m moving along a circular orbit inside a galaxy at a distance r from the center, assuming a uniform mass density ρ, the average kinetic and potential energies are given by:

$$\langle K \rangle = \frac{1}{2}mv^2 \tag{1.4}$$

$$\langle U \rangle = -\frac{GM(r)m}{r} = -\frac{Gm}{r}\rho\frac{4}{3}\pi r^3 = -\frac{4}{3}Gm\pi\rho r^2. \tag{1.5}$$

From the virial theorem 1.3 it follows that:

$$mv^2 = \frac{4}{3}Gm\pi\rho r^2 \iff v(r) = \sqrt{\frac{4G\pi\rho}{3}}r \tag{1.6}$$

and therefore $v \propto r$.

If the orbit lies outside the mass distribution, the potential energy is given by:

$$\langle U \rangle = -\frac{GMm}{r} \tag{1.7}$$

In this case, from eq. 1.3 it follows that:

$$mv^2 = \frac{GMm}{r} \Longrightarrow v(r) = \sqrt{\frac{GM}{r}} \tag{1.8}$$

and therefore $v \propto r^{-1/2}$.

These two simple cases represent the two limiting scenarios for the rotational velocities of stars in a galaxy. The velocity $v(r)$ is expected to increase linearly with the radial distance r in the inner galaxy and to drop as $r^{-1/2}$ as the distance increases.

However, in most galaxies, one finds that v approaches a plateau as r increases. This behavior can be observed in Fig. 1.1, where rotation curves of a few spiral galaxies are shown. As an example, in our own galaxy, $v \simeq 220 km/s$ at the location of the Sun, with little change to the largest observable radial distances, as understood from the measurement of HI emission [3].[1]

A possible interpretation of this anomaly can be provided in terms of DM. Indeed, assuming that DM is distributed with a mass density $\rho_{DM} \propto r^{-2}$, the rotational velocity approaches a constant limiting value at large radial distances. Therefore, alongside the constant density attributed to the visible mass in the Galactic Plane, it is necessary to consider an additional component of non-visible mass distributed in a spherical halo around the Galactic Plane, characterized by a density profile that scales as r^{-2}.

Fig. 1.2 shows the rotational curve of the galaxy NGC3196. The curve is well reproduced assuming an exponential mass distribution within the disk and a mass density profile in the halo given by:

[1] HI emission consists in a characteristic spectral line at 21 cm wavelength due to excited electrons of hydrogen atoms undergoing a spin-flip transition. This line serves as a probe for measuring angular velocities thanks to Doppler effect, which shifts the line depending on the relative velocity of the source.

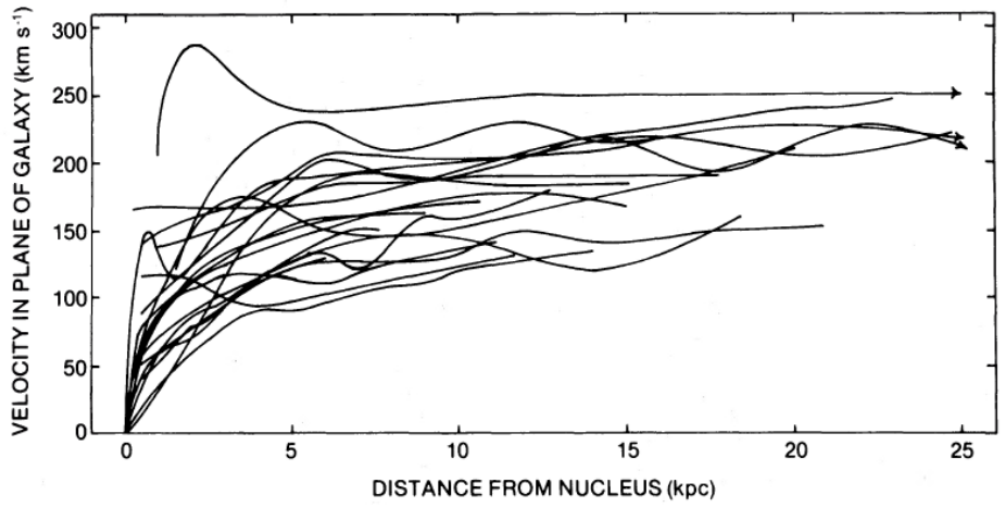

Figure 1.1: Rotation curves of 21 spiral galaxies studied in ref. [4].

$$\rho_{halo}(r) \propto \left[\left(\frac{a}{R_0}\right)^{\gamma} + \left(\frac{r}{R_0}\right)^{\gamma}\right]^{-1} \tag{1.9}$$

where $a = 8.5\,\mathrm{kpc}$, $\gamma = 2.1$ and $R_0 = 8\,\mathrm{kpc}$.

These results indicate the presence of mass that is not associated to visible objects in the galaxy, such as stars and nebulae, and is responsible for explaining the observed rotation curves. This unseen mass is in this sense "dark". However, this evidence does not reveal the fundamental nature of this undetected kind of matter.

An alternative way to solve the problem of rotational curves would imply a change in the theory of gravitation without introducing DM, or at least limiting its content at most possible. This is the attempt of the so-called modified Newtonian dynamics (MOND), which allow the reproduction of many galactic rotational curves and other galactic-scale parameters, without introducing DM [6]. However, MOND is a purely non–relativistic theory. Attempts to embed it into a relativistic field theory require the existence of additional fields (e.g. a vector field or a second metric), and introduce considerable arbitrariness without strong verifiable evidence yet. Moreover, as reported in Sec.1.2.1, cosmological arguments involving CMB anisotropies give strong evidence about the fact that most of the matter content

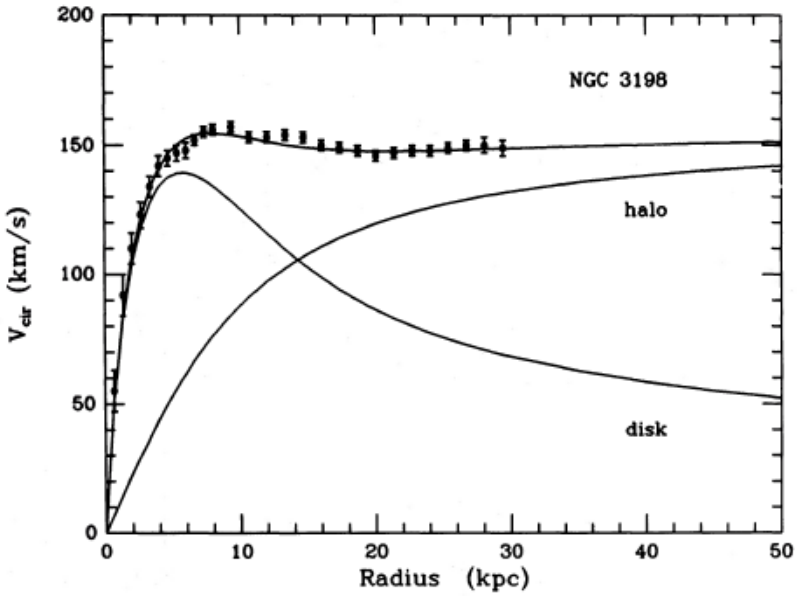

Figure 1.2: Rotation curve of the galaxy NGC3196 [5]. The data have been fitted assuming an exponential mass distribution in the disk and a dark matter density profile in the halo described by eq. 1.9.

of the universe doesn't couple with any radiation, yet does exist.

1.1.2 Galaxy clusters: the Coma cluster

Further evidence supporting the existence of a form of matter that does not trace the luminosity distribution of galaxies comes from the study of galaxy clusters — such as the Coma Cluster, investigated by F. Zwicky in his 1937 work. [7].

Galaxy clusters are gravitationally bound systems composed of numerous galaxies; for example, the previously mentioned Coma Cluster includes approximately 1000 galaxies, with an average separation of about 1 Mpc between each pair of galaxies. A simple calculation of the mass of a galaxy cluster can be performed applying the virial theorem (eq. 1.3).

The average kinetic energy of the cluster is given by:

$$\langle K \rangle = \sum_i \frac{1}{2} m_i \langle {v_i}^2 \rangle \tag{1.10}$$

where $\langle v_i^2 \rangle$ is the mean squared velocity of the i-th galaxy in the summation and m_i is its mass. Assuming that all galaxies have the same average velocity, i.e. $\langle v_i \rangle = \langle v \rangle$, the previous equation can be rewritten in the following form:

$$\langle K \rangle = \frac{1}{2} M \langle v^2 \rangle \tag{1.11}$$

where $M = \sum_i m_i$ is the mass of the cluster.

If galaxies are uniformly distributed inside a sphere of radius R, we can evaluate the density:

$$\rho = \frac{3M}{4\pi R^3} \tag{1.12}$$

The average potential energy can be evaluated assuming that the sphere consists of infinitesimal shells with different radii r, in the range from 0 to R. The potential energy associated to each individual shell is the energy needed to bring the shell from its position to infinity and is given by:

$$dU = -\frac{G m_{int} dm_{shell}}{r} = -\frac{G}{r} \rho \frac{4}{3} \pi r^3 \cdot \rho 4\pi r^2 dr = -\frac{16}{3} G \rho^2 \pi^2 r^4 dr \tag{1.13}$$

where $dm_{shell} = 4\pi\rho r^2 dr$ is the mass of the infinitesimal shell and $m_{int} = 4\pi\rho r^3/3$ is the mass of the inner sphere. The total potential energy is therefore given by:

$$U = \int_0^R dU = -\frac{16}{15} G \rho^2 \pi^2 R^5 = -\frac{3}{5} \frac{GM^2}{R} \tag{1.14}$$

Plugging now eqs. 1.11 and 1.14 in eq. 1.3, we can evaluate the total mass of the cluster:

$$2\langle K \rangle = -\langle U \rangle \Longrightarrow M \langle v^2 \rangle = \frac{3GM^2}{5R} \Longrightarrow M = \frac{5R\langle v^2 \rangle}{3G} \tag{1.15}$$

From eq. 1.15, using the data of the Coma cluster, in ref. [7], Zwicky estimated the mass of the cluster as $M = 3.5 \cdot 10^{14} M_\odot$.[2] In the same work, using a more

[2]The symbol $M_\odot$ indicates the solar mass $M_\odot \approx 2 \cdot 10^{30}$ kg.

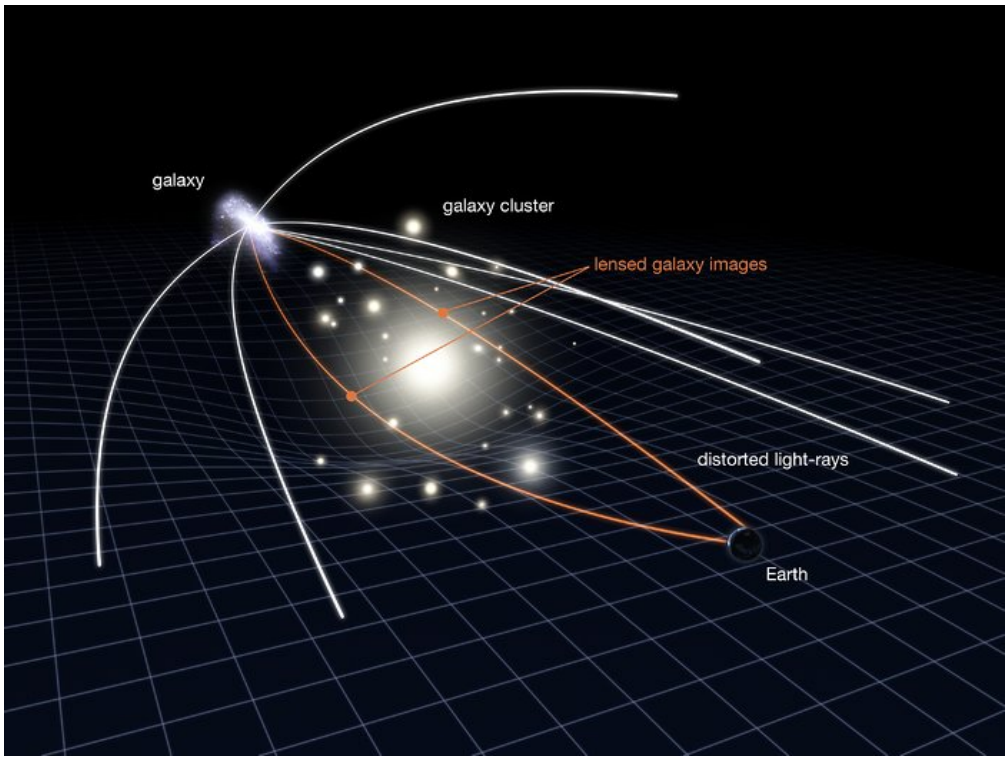

Figure 1.3: Gravitational lensing: galaxy clusters can bend light rays passing in their vicinity, in similar fashion to actual lenses, albeit for different reasons. Credit: NASA, ESA and L. Calçad

accurate approach than eq. 1.15, Zwicky obtained a better estimate of the Coma cluster mass $M = 4.5 \cdot 10^{13} M_{\odot}$.

However, the estimated mass of the Coma Cluster based on visible matter is $8.5 \cdot 10^{7} M_{\odot}$, which is almost six orders of magnitude lower than the mass derived using the virial theorem. This significant discrepancy offers additional support for the DM hypothesis. Indeed, if the virial theorem holds, the disparity between the mass inferred from visible stars and that calculated via the theorem must be ascribed to a substantial amount of unseen mass.

A better estimation comes from *mass mapping* measurements employing the *gravitational lensing* effect. One of the most recognizable results of general relativity is the fact that space-time is curved, and it is shaped by the presence of masses. The curvature of space-time depends on the distribution of the masses. The gravitational lensing effect is illustrated in Fig. 1.3. As the curvature of space-

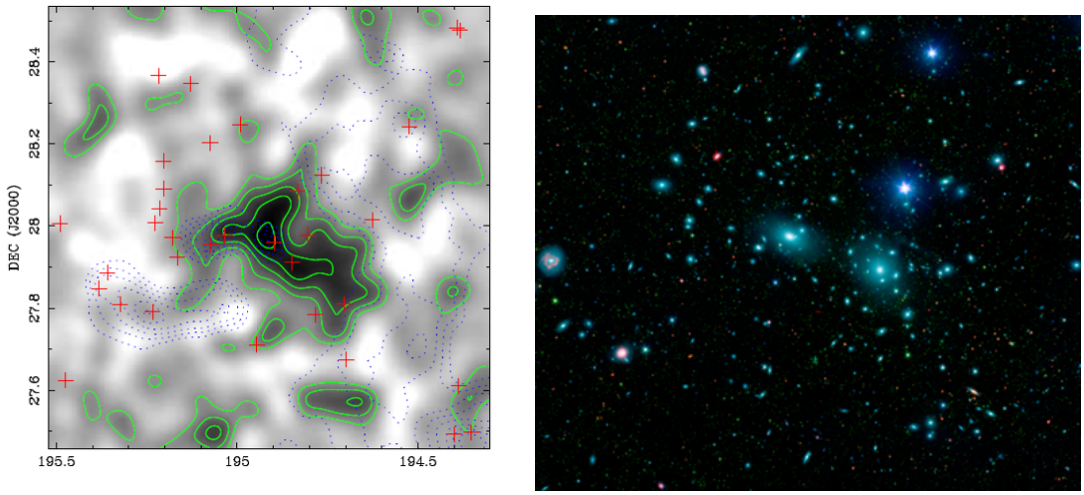

Figure 1.4: Left panel: Mass mapping of the Coma Cluster. Red crosses represent the visible matter (brightest galaxies in the cluster). The contours indicate the matter responsible for the gravitational potential. More matter is needed with respect to the observed matter to explain the gravitational potential [8]. Right panel: False-color mosaic of Coma Cluster combining images from the Sloan Digital Sky Survey (optical, shown in blue) with long- and short-wavelength infrared images (shown in red and green, respectively) from NASAs Spitzer Space Telescope. Image credit: NASA / JPL-Caltech / L. Jenkins (GSFC), taken from Ref. [9].

time increases near massive objects, they can bend light rays that pass close to them. A gravitational lens refers to a mass distribution — such as a galaxy cluster — located between a distant light source and an observer, which bends the light from the source as it travels toward the observer. This bending effect resembles that of an optical lens, though it arises from gravity rather than refraction. When the source, the lens, and the observer are perfectly aligned, the light from the source can produce a ring-shaped image, known as an Einstein ring

Lensing is strictly related to the mass of the lens, which can be evaluated by studying the distortion of the image (*"mass mapping"*), and is independent from the distribution of light sources, thus providing a proper method to trace mass distributions.

Fig. 1.4 shows the distribution of the masses in the Coma cluster derived from gravitational lensing measurements. The mass evaluated from these measurements is consistent with the virial mass and exhibits a mismatch with respect to the mass

inferred from visible matter.

1.1.3 Bullet Cluster brightness-mass distribution disparity

Fig. 1.5, which is taken from ref. [10] illustrates the matter distribution, obtained via mass mapping techniques involving gravitational lensing, in the Bullet Cluster 1E 0657-558, which formed as a result of the collision between two galaxy clusters. The hot gas, observable in X-rays because of the excited state due to the collision, constitutes the majority of the ordinary (baryonic) matter. Due to electromagnetic interactions, this gas is slowed down during the collision. In contrast, the DM component — detected indirectly through gravitational lensing of background objects — interacts only via gravity, and thus passes through the collision region with minimal resistance. This leads to an asymmetric distribution: the hot gas remains concentrated near the center, while the DM is found primarily in the outer regions.

This remarkable spatial separation puts a severe constraint on alternative models where DM is replaced by a modification of gravity. Such modifications cannot spatially separate from normal matter, unless they also introduce a component that effectively behaves like DM, so any anomalous lensing signal would be expected to trace the distribution of visible matter.

As outlined in Ref. [1], the observation that DM halos did not experience significant deceleration, following collisionless trajectories, sets an upper limit on the self-interaction probability $\mathcal{P} \sim \sigma n r_{cl} \lesssim 1$, where σ is the DM self-interaction cross section, n the DM number density, and r_{cl} the characteristic scale radius of the cluster.

In the specific case of the Bullet Cluster, the data suggest a cluster scale radius of approximately $r_{\mathrm{cl}} \sim 150\,\mathrm{kpc}$ and a DM density of about $\rho \sim 0.5\,\mathrm{GeV/cm^3}$. Since $\rho = Mn$, where M denotes the mass of a DM particle, an upper limit can be placed on the ratio σ/M:

$$\sigma n r_{cl} \lesssim 1 \implies \sigma \lesssim \frac{1}{n r_{cl}} = \frac{M}{\rho r_{cl}} \implies \frac{\sigma}{M} \lesssim 2 \frac{\mathrm{cm}^2}{\mathrm{g}} \tag{1.16}$$

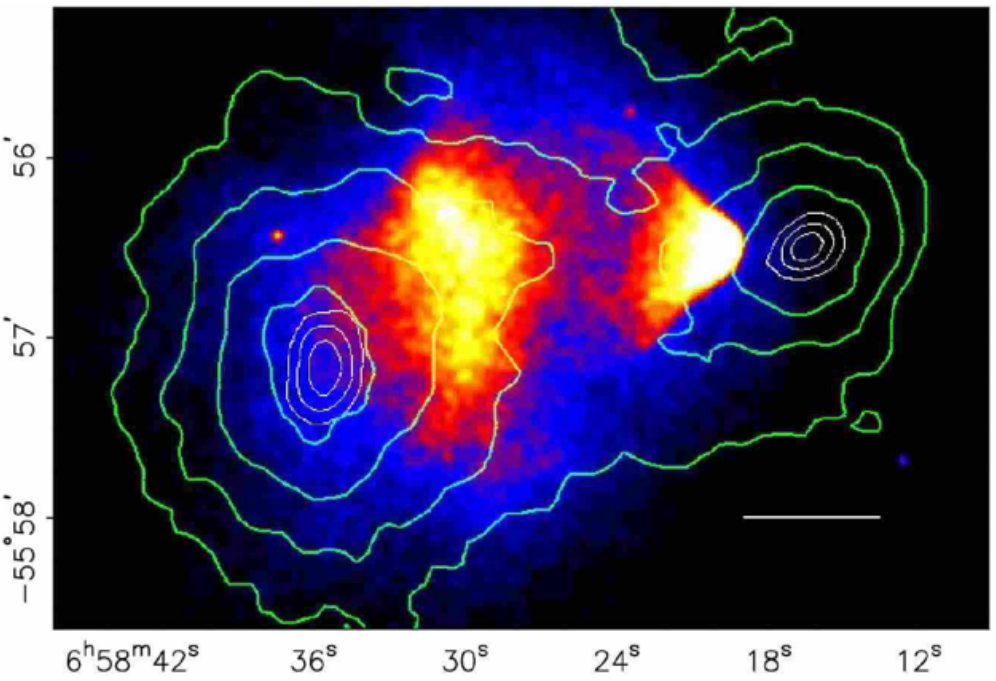

Figure 1.5: Color image of the merging Bullet Cluster 1E 0657-558 from the Chandra X-ray telescope and weak lensing gravitational potential. The two distributions appear separated: the peaks of the gravitational potential (green contour lines) are different from the peaks of X-ray emission (color scale) [10].

To get an idea, typical QCD cross sections are of about 50 mb, as in the case of the pp scattering. The bound in eq. 1.16 is thus satisfied if DM is made of particles heavier than protons and/or less strongly interacting than protons. The DM/matter cross section is similarly bound by astrophysics and cosmology to be roughly smaller than the QCD cross sections at $M \sim 1$ GeV. These properties are indeed satisfied by one of the most promising DM particle candidates which are investigated in this work: WIMPs, that will be introduced in Sec.1.3.

1.1.4 Dense baryonic DM candidates: MACHOs

Gravitational lensing observations are also exploited to search for the so-called MAssive Compact Halo Objects (MACHOs). This term encompasses a variety of

objects, including brown dwarfs, planets, primordial black holes, and other cold, non-luminous bodies that do not emit radiation at any wavelength. Because of their invisibility in electromagnetic observations and their mass, MACHOs have been considered potential candidates to account for the evidence supporting the DM hypothesis.

However, MACHOs have been extensively searched for with microlensing experiments and found too few in number to account for DM. In addition, there is evidence towards the fact that DM cannot be baryonic like ordinary matter, because that would be in conflict with the observed yield of light nuclei in the Big-Bang Nucleosynthesis (BBN) and with the results of a Cosmic Microwave Background (CMB) fluctuation analysis (see secs. 1.2.1 and 1.2.2).

A further remark should be made about primordial black holes (PBHs)[3]: the mass range allowed for them to be DM candidates is also quite restricted to the interval between $10^{17} M_\odot$ and $10^{25} M_\odot$, and such *behemoths* would be very unlikely to exist. All this makes it very likely that DM consists of a new type of particles (see ref. [11] for a detailed overview).

1.2 Cosmological evidence

1.2.1 Cosmic Microwave Background temperature anisotropies

The Cosmic Microwave Background (CMB) is the relic electromagnetic radiation from the earlier stages of the Universe. It is observed still today and exhibits an almost isotropic thermal blackbody spectrum peaked in the microwave region, at a temperature of 2.7 K.

In the framework of the Big Bang model, the expanding Universe undergoes a gradual cooling, passing through successive stages characterized by decreasing energy density (or temperature) and the formation of increasingly complex structures. Radiation gives rise to pairs of particles and antiparticles, which

[3]PBHs are hypothetical black holes that formed soon after the Big Bang consisting in extremely dense pockets of subatomic matter that collapsed

subsequently lead to the formation of all known structures in the Universe, including nuclei, atoms, stars, planets, and galaxies.

Within this context, the cosmic microwave background (CMB) is the remnant electromagnetic radiation from the epoch when free electrons and protons combined to form neutral hydrogen atoms (*recombination phase*). After this stage, the absence of charged matter results in a significant drop in photon-matter interactions, allowing photons to decouple from matter and propagate freely through the expanding Universe, in a process known as *photon decoupling*.

Under a simplified but physically reasonable approximation (neglecting the presence of heavier elements such as helium), recombination can be described as the balance between hydrogen atom formation and its photodisintegration:

$$\begin{aligned} p + e^- &\rightarrow \mathrm{H} + \gamma \\ \mathrm{H} + \gamma &\rightarrow p + e^- \end{aligned} \tag{1.17}$$

After the decoupling, assuming a flat expanding Universe, the wavelength of photons stretches proportionally to the scale factor $(1+z)$, where z is the redshift. As a consequence, the whole CMB spectrum has been redshifted by this factor since its emission. From this relation it can be estimated that the recombination epoch occurred at a redshift $z_{\mathrm{rec}} \sim 1300 - 1400$, corresponding to an epoch of $\sim 380000\,\mathrm{yrs}$ after the Big Bang [12].

The CMB is expected to be isotropic, and it is mostly the case. In the years after its existence was established by A. Penzias and R. Wilson in 1965 [14], many experiments (e.g. COBE [15], WMAP [16] and Planck [17]) measured anisotropies in the distribution of the temperatures of the CMB, due to fluctuations of the matter density in the early Universe, which gave rise to the large structures observed today. Fig. 1.6 shows a map of the CMB temperature anisotropies observed by Planck. CMB anisotropies result from simple linear processing of the primordial fluctuations through gravitational and particle interactions, which themselves may have their origin in a period of very rapid expansion which carried quantum mechanical fluctuations to cosmological scales. Alternatively, a phase transition in the early Universe may have left topological defects analogous to

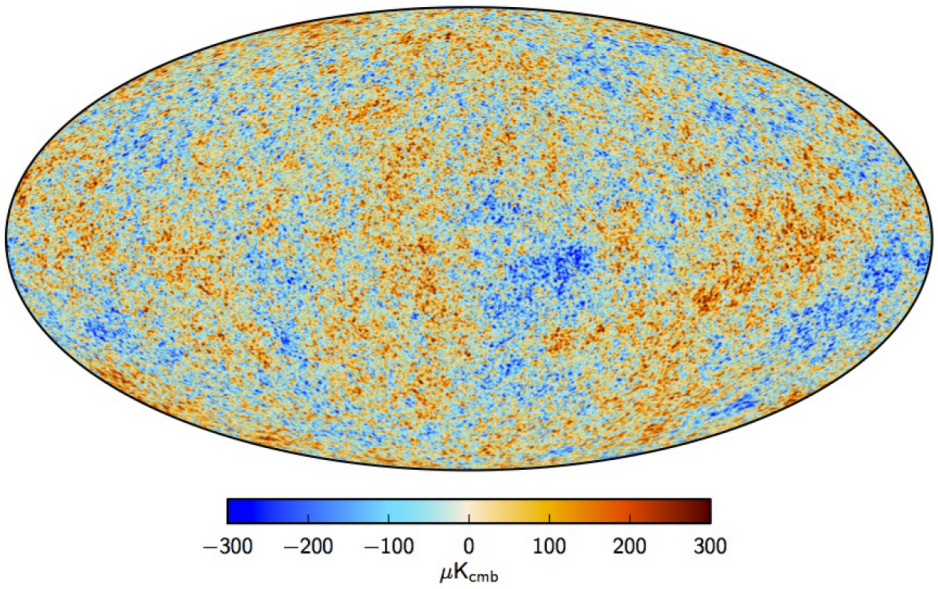

Figure 1.6: Map of CMB temperature anisotropies, from Planck collaboration [13].

domain walls in a ferromagnet. In any case, the gravitational infall of the cosmic fluid into potential wells generates compressional or acoustic waves. Because compression raises the temperature, this results in temperature oscillations that are visible still today.

From observations of the anisotropies, one can thus extract information on the early Universe (the parameters describing the cosmological fluids and the dynamics of the expansion) as well as on the origin of its perturbations. In particular, the angular power spectrum of the CMB (see Fig. 1.7) contains information about the Universe composition and evolution, and thus its study provides a powerful method to extract a remarkable wealth of cosmological information, including a precise estimate of the density of dark and baryonic matter.

The CMB temperature field is typically represented through a spherical harmonic expansion:

$$T(\theta,\phi) = \sum_{\ell=0}^{+\infty} \sum_{m=-\ell}^{+\ell} a_{\ell m} Y_{\ell m}(\theta,\phi), \tag{1.18}$$

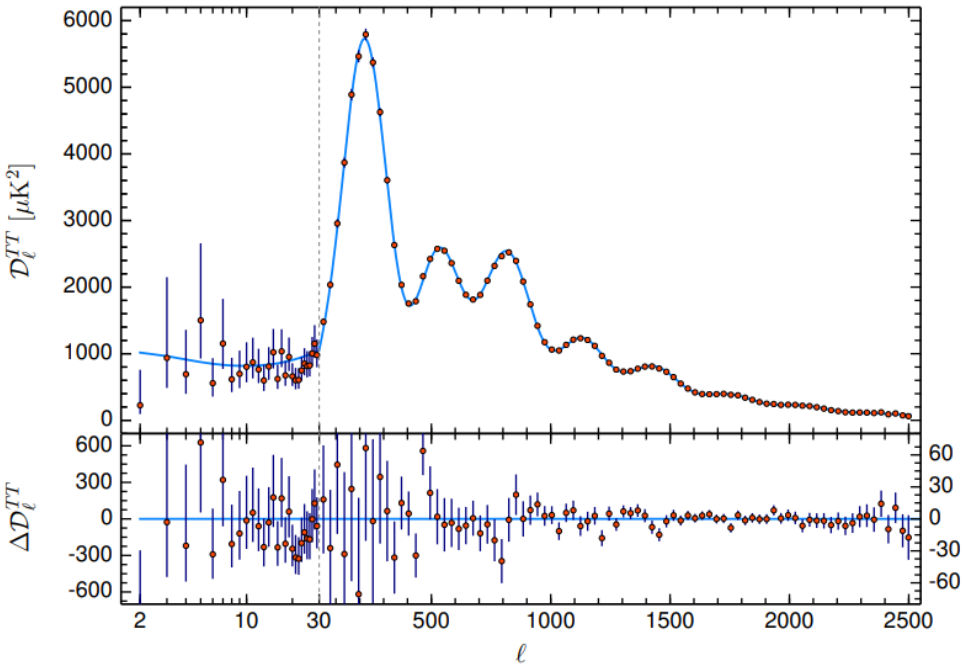

Figure 1.7: Planck 2018 [18] temperature power spectrum. The base-ΛCDM theoretical spectrum best fit to the Planck likelihoods is plotted in light blue in the upper panel. Residuals with respect to this model are shown in the lower panel. The error bars show $\pm 1\sigma$ diagonal uncertainties, including cosmic variance (approximated as Gaussian) and not including uncertainties in the foreground model at ≥ 30. Note that the vertical scale changes at $l = 30$, where the horizontal axis switches from logarithmic to linear.

where $Y_{\ell m}(\theta, \phi)$ are the spherical harmonics and $a_{\ell m}$ are the corresponding multipole coefficients. The coefficients of the angular power spectrum are then defined as:

$$C_\ell = \frac{1}{2\ell + 1} \sum_{m=-\ell}^{+\ell} |a_{\ell m}|^2. \tag{1.19}$$

Angular power spectrum coefficients represent the distribution of temperature anisotropies as a function of angular scale.

The CMB has a measured mean temperature $T_\gamma = 2.7255 \pm 0.0006$ K (1σ) [2], which corresponds to the monopole component associated to the coefficient a_{00}, or equivalently to C_0. The largest anisotropy observed in the CMB corresponds to the

dipole component of the spherical harmonic expansion associated to the coefficient C_1. Its measured amplitude is 3.3621 ± 0.0010 mK [18], and it is interpreted as a Doppler-induced anisotropy, resulting from the motion of the Solar System with respect to the nearly isotropic blackbody rest frame of the CMB.

The temperature fluctuations in the CMB at higher multipoles ($\ell \geq 2$) are primarily interpreted as the result of primordial density fluctuations in the early Universe at the epoch of last scattering, when the CMB photons decoupled from matter. Perturbations inside the horizon at last scattering were able to evolve causally and produce anisotropy which reflects this evolution.

Fig.1.7 shows the CMB angular power spectrum measured by the Planck experiment [18]. From the positions and heights of the peaks in the angular spectrum one can estimate the density of DM, separating it from baryonic matter. Odd-numbered peaks correspond to compressions of the primordial plasma, while even-numbered peaks correspond to rarefaction of the plasma. The amount of DM determines the relative height of the odd-numbered peaks, as DM affects the depth of gravitational potential wells. The amount of baryons determines the difference between even and odd-numbered peaks, as they are involved in the oscillations of the primary cosmic fluid. The angular position of the first peak ($\ell \approx 220$) is related to the geometry and scale of the acoustic horizon, which represents the maximum distance a sound wave (in the photon-baryon fluid) can have traveled from the Big Bang until the time of decoupling.

A fit of the data allows an evaluation of the cosmological parameters of the ΛCDM model [19][4]. In particular, the fit provides the values of the baryon density $\Omega_b h^2 = 0.0224 \pm 0.0001$ and of the DM density $\Omega_c h^2 = 0.120 \pm 0.001$, where $h = 0.674 \pm 0.005$ is the Hubble constant [18]. These data confirm, within the framework of ΛCDM model, that our Universe is composed only by a small fraction of visible baryonic matter ($\sim 4.9\%$), while the largest part consists of dark matter ($\sim 26.4\%$) and dark energy ($\sim 68.7\%$).

[4]The ΛCDM model is the simplest model that fits almost all cosmological data, treating the Universe as composed mostly of dark energy (with density proportional to the cosmological constant Λ) and cold dark matter (CDM), plus a small fraction of ordinary matter and radiation.

1.2.2 Big Bang Nucleosynthesis (BBN)

The density of normal matter inferred from global fits to CMB data is in excellent agreement with the independent, high-precision estimates obtained from Big Bang Nucleosynthesis (BBN) data. BBN is the theoretical framework that explains the formation of light elements in the early Universe, primarily deuterium (D), helium-4 (^4He), and significant amounts of helium-3 (^3He) and lithium-7 (^7Li), from the primordial plasma of free protons and neutrons. This process is particularly sensitive to the baryon-to-photon ratio, $\eta = n_b/n_\gamma$, since photons can disrupt nuclei and thereby delay the onset of nucleosynthesis to lower temperatures. According to recent measurements $\eta = (6.2 \pm 0.4)10^{-10}$, implying a baryon density $\Omega_{\rm b}h^2 = 0.022 \pm 0.002$ [2], consistent with that obtained from CMB measurements (see Sec.1.2.1).

This agreement between BBN and CMB determinations of the baryon density is considered a major success of the standard cosmological model, enforcing the view that the Universe evolution is well described within this framework. In addition, most importantly, BBN probes an earlier epoch when the Universe was at temperatures around $T \sim$ MeV, compared to the CMB, which corresponds to $T \sim$ eV.

The fact that the baryon density $\Omega_b h^2$ is significantly less than the total matter density $\Omega_{\rm m}h^2 \simeq 0.30$ provides strong evidence for the existence of DM. Since this missing component cannot be baryonic, it must consist of non-baryonic matter. Historically, the BBN result on the baryon density played a crucial role, particularly before the CMB and large-scale structure (LSS) observations reached the precision needed to independently constrain the relative fractions of baryonic matter and DM.

1.3 Particle candidates for dark matter

As a consequence of what stated in sec. 1.1.4, "dark" baryons (e.g. MACHOs) cannot account for all the unseen mass content of the Universe, making them not viable candidates to settle the problem of DM identity. In addition, DM cannot

be composed of baryonic matter, because that would be in conflict with the yield from BBN and the results from CMB fluctuation analyses [19], which point strongly towards DM existence and its non-baryonic nature.

In this regard, DM uniquely bridges the fields of cosmology, particle physics, and astrophysics like no other scientific challenge. Within the current ΛCDM paradigm, DM is considered non-relativistic since the time of its decoupling and is modeled as a collisionless fluid whose particles interact primarily through gravity and only very weakly with Standard Model particles. Consequently, these particles must lie beyond the known zoo of the Standard Model.

However, since there is no experimental evidence constraining their mass, many possible candidates exist. Nevertheless, a few properties of these candidates can be constrained based on current observational evidence. First and foremost, DM must be electrically neutral, otherwise it would have been detected through electromagnetic interactions via conventional astronomical observations and spectroscopic methods. Furthermore, the non-baryonic nature of DM implies that it must also be color-neutral, meaning DM particles do not participate in strong interactions. As a consequence, DM particle interactions with ordinary matter should be preferably weak, where "weak" is intended in a broad sense, i.e. either weak interactions or just a weak but non-negligible coupling to the Standard Model particles.

Finally, the DM particles should be either absolutely stable or extremely long-lived compared to the cosmological time scale, otherwise we would already have detected them [20]. This also strengthens the idea of their color neutrality, otherwise they would have been very unstable and the proofs of their decay would be quite noticeable.

There are several possible DM candidates which satisfy these properties. In this section we will give some generalities about them, providing an overview of the currently most credited ones, focusing on WIMPs, since they are the candidates searched in the analysis work presented in the next chapters.

1.3.1 "Sterile" neutrinos

Based on the properties discussed at the end of Sec1.1, neutrinos are natural DM candidates: non-baryonic, neutral and only weakly interacting. The only problem is related to their very low mass, that could account for the DM amount only if in huge quantities, which are currently not observed. Neutrinos from different astrophysical sources are deeply studied for several reasons, but they do not seem likely to fill the gaps correctly within the unsolved DM puzzle.

A possible DM candidate is the so-called "sterile" neutrino. In contrast to other left-handed fermions, which have corresponding right-handed partners, right-handed neutrinos have not yet been observed. Neutrinos have all fixed chirality: neutrinos are left-handed, while antineutrinos are right-handed. Thus, for instance, right-handed neutrinos have never been observed (the same applies for left-handed antineutrinos). Sterile (right-handed) neutrinos with masses in the $\mathrm{keV} - \mathrm{MeV}$ range are among the proposed candidates for DM [9] since they would also solve the puzzle of the apparent particle-antiparticle asymmetry in the neutrino sector. The $\mathrm{keV} - \mathrm{MeV}$ range is motivated by the currently accepted neutrino mass values (the upper limits are at of $\sim 1\,\mathrm{eV}$ for the electron neutrino, of $\sim 200\,\mathrm{keV}$ for the muon neutrino and of $\sim 20\,\mathrm{MeV}$ for the tau neutrino respectively [2]), but also by the fact that this would lead to a specific *warm dark matter* scenario, resulting in a structure formation that may offer some advantages with respect to the standard hot and cold DM models [21].

In general, the neutrino flavor eigenstates (ν_α with $\alpha = e, \mu, \tau, s$, with 's' as the new hypothetical 'sterile' flavor) are linear combinations of mass eigenstates, and the sterile neutrino should have very small mixing with active neutrinos. A heavier neutrino mass eigenstate is proposed to radiate a photon and decay to a lighter mass state ($\nu_2 \to \nu_1 + \gamma$). Since the sterile neutrino is predominantly composed of ν_2 mass eigenstates, in this scenario this process is often described as its decay into an active neutrino. This decay produces a photon line at half of the sterile neutrino mass and is therefore expected to yield a line signal feature in X-rays.

Recently, a hint of an unidentified emission line around $3.55\,\mathrm{keV}$ was found in the X-ray spectra of galaxy clusters [22]. Fig. 1.8 shows the X-ray spectra

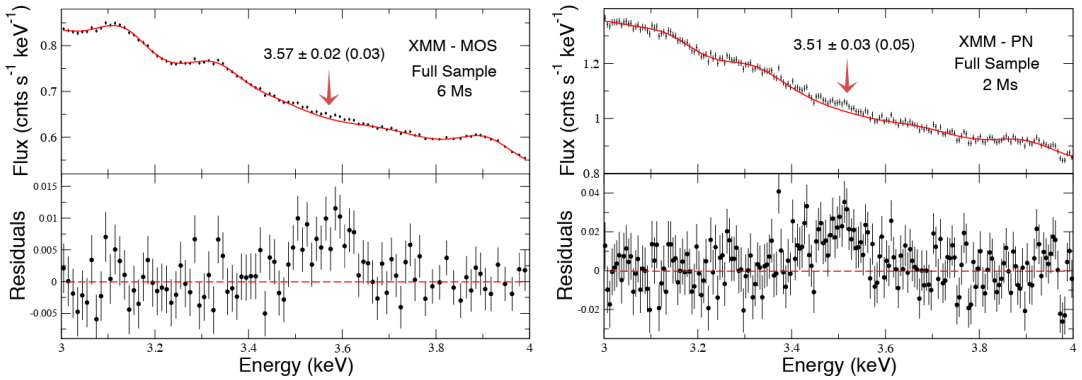

Figure 1.8: X-ray spectra in the 3–4 keV energy band measured by the MOS (left panel) and PN (right panel) cameras of the EPIC instrument onboard XMM-Newton. The plot is taken from ref. [22] and refers to the stacked analysis of 73 galaxy clusters.

obtained from the XMM-Newton telescope data stacking data from 73 different galaxy clusters, at different redshifts. Each source spectrum was thus blueshifted to the source frame using the best X-ray redshift of each observation determined from the bright Fe lines at 6.7 keV. The data show an excess with respect to the models in the region around 3.55 keV. This line has been discussed as a possible decay signature of a 7.1 keV sterile neutrino, which has been proposed as a DM candidate. However, no definitive answer can be given, since the most significant flux upper limit has been resized to 1.5σ in an independent search that analyzed a CHANDRA dataset from the Galactic bulge [23]. Other scenarios seem to give more convincing explanations of the line also in a DM context [24].

The debate is still ongoing and intense: results in a recent work by NuSTAR Collaboration [25] seem to strongly disfavor a ~ 7 keV sterile neutrino decaying into a 3.5 keV photon.

1.3.2 Axions and axion-like particles (ALPs)

The *axion* is a hypothetical light pseudoscalar particle (with spin-parity 0^+) originally proposed to solve the so-called strong CP problem (for details, see the review in ref. [26]). Although there is no compelling theoretical reason for CP symmetry to be preserved in the QCD Lagrangian, experimental observations

indicate that, unlike in weak interactions, CP (and consequently T) is conserved in strong interactions. To address this discrepancy, Peccei and Quinn(PQ) [27] proposed in 1977 a new global symmetry called $U(1)_{PQ}$, which is spontaneously broken at a very high energy scale. Indeed, the term of the Lagrangian corresponding to CP violation can be written in the form:

$$\mathcal{L}_{\theta_{QCD}} = \theta_{QCD} \frac{g^2}{32\pi^2} G^a_{\mu\nu} \tilde{G}^{\mu\nu}_a \tag{1.20}$$

where θ_{QCD} is a phase parameter of QCD, G is the gluon field strength tensor, a stands for trace summation over the SU(3) colors, and g^2 is the QCD coupling constant ($\theta_{\mathrm{QCD}} = 0$ in case of no CP violation, nullifying the term).

The introduction of the axion field can make the term in Eq. 1.20 negligible. The axion mass is given by:

$$m_a \simeq 6 \times 10^{-6}\mathrm{eV} \left(\frac{10^{12}\mathrm{GeV}}{f_a} \right) \tag{1.21}$$

where f_a is a decay constant related to its coupling strength g and in the original model was predicted to be of the order of 100 keV.

At present, after many unsuccessful searches for axions, the axion model was extended to a wider group of particles, called Axion-Like Particles (ALPs), in which the decay constant is no longer coupled with the axion mass, in contrast with the original axion. More recently, axions and ALPs were proposed as viable DM particle candidates. The reason for this relies upon their small mass, combined with a possibly large decay constant $f_a \sim 10^{12}\,\mathrm{GeV}$.

Experimental techniques to search for ALPs are based on their predicted property to convert into photons and vice versa. ALPs emitted from a source and travelling through a region with an intense magnetic field can convert into photons, that can be detected at Earth. Similarly, photons passing through a magnetic field region can convert into ALPs. Therefore ALPs can be detected in two different ways: the first consists in trying to detect photon excesses due to ALP conversions, and requires a source of ALPs and a region with strong magnetic fields where the conversion probability is enhanced; the second consists in searching for

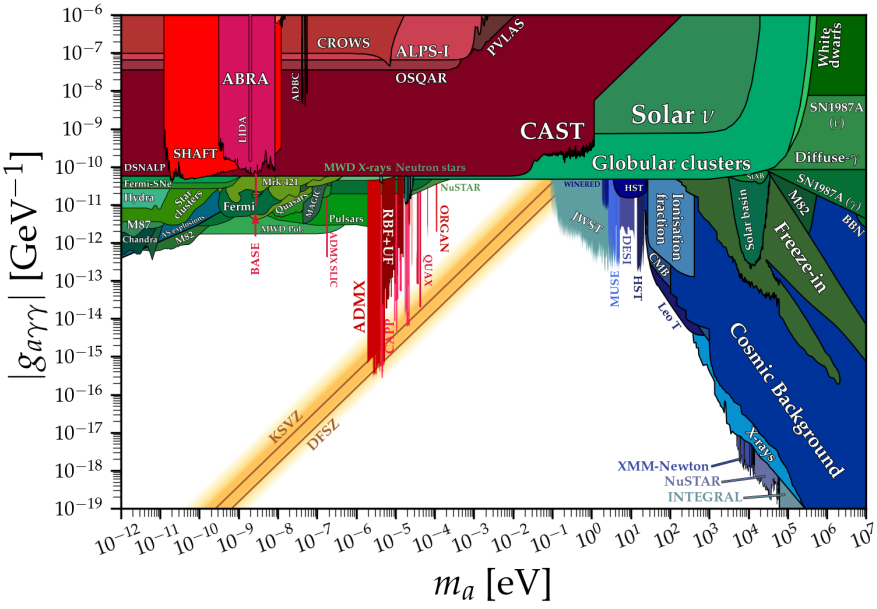

Figure 1.9: ALP parameter space with the most recent constraints (July 2020) [28]. The golden band represents the current target parameter space, given by the QCD axion model: KSVZ and DFSZ are two benchmark models with different coupling strengths [29]. Dark red contours represent parameter space exclusion regions from laboratory experiments, green regions from astrophysical observations of stellar environments, blue regions from cosmological observations.

photon deficits due to conversion into ALPs, and requires a photon source and a region with a strong magnetic field.

Axion and ALP searches can be performed either directly or indirectly. Direct searches are performed with the following techniques:

1. Light-shining-through-a-wall: a laser beam travels through a region of high magnetic field, allowing the possible conversion of photons into axions or ALPs. These particles can then pass through a wall and, when on the other side, can be converted back into photons in another magnetic field region;

2. Detection of solar axions: the CAST (CERN Axion Solar Telescope) [30] experiment looks for X rays that would result from the conversion of solar axions in the superconducting magnet of the detector. Solar axions might be produced in the Sun's core when X rays scatter off electrons and protons in the presence of strong electric fields.

On the other hand, for indirect searches there are three effects that can be exploited:

1. Birefringence of vacuum in high magnetic fields due to photon–axion mixing: the magnitude of this birefringence[5] could be enhanced by the presence of an axion field that could provide more photons and, thus, more virtual e^+e^- pairs contributing to vacuum polarization, as reported in Ref. [31], where the authors set constraints on ALPs coupling constant using the PVLAS ellipsometer.

2. Possible anomalies in the cooling times of cataclysmic stars: stars produce huge quantities of weakly interacting particles, like neutrinos and possibly hypothetical gravitons, axions, and other unknown particles. Usually, neutron stars reach a slower cooling rate after $\sim 10^5$ years, when neutrino dominated cooling reaches an end. A faster cooling rate may be a hint of ALP production (see ref. [32]) that, after being produced at the core of the star, escape undetected, carrying a significant part of the star energy budget and resulting in a higher cooling rate of the star.

3. ALPs can also directly affect the propagation of photons from astrophysical sources, by mixing to them, thus enhancing the universe transparency to VHE photons ($0.1 - 1000$ TeV) by partially preventing absorption caused by the extragalactic background light.

All these searches have yielded negative results, but have limited the region of masses and couplings allowed for ALPs and axions (Fig.1.9).

1.3.3 The "WIMP Miracle"

The candidates shown so far, excluding ALPs that can be also very heavy, involve quite low-mass particles that are easier to find in a high kinetic energy state, which is in contrast with the usual picture of the ΛCDM model, that requires DM to be

[5] A QED-predicted effect where strong electromagnetic fields cause empty space (the vacuum) to act like a birefringent material because of polarization of virtual e^+e^- pairs.

"cold", i.e. basically at rest, since its decoupling from radiation. This is why the identification of DM with WIMPs (Weakly Interacting Massive Particles) is still one of the most credited hypothesis.

WIMPs were originally proposed in theories beyond the Standard Model (SM) within the framework of Supersymmetry (SUSY). SUSY is a theoretical framework that extends the symmetries of quantum field theory by introducing a new symmetry that relates bosons and fermions, allowing for transformations between the two. In contrast to the SM, which does not predict bosonic counterparts for fermions (and vice versa), SUSY posits such pairings. Later on, once the required properties for DM particle candidates emerged, it appeared how such proposed object could bridge gracefully cosmologically-motivated properties with ones required in solving SM limitations. Over time, a consensus was formed over the so called "WIMP paradigm", mainly because WIMPs are predicted to be produced with a relic abundance that closely matches the DM density inferred from observations. This remarkable coincidence is commonly known as the "WIMP miracle".

At the beginning, the early Universe was dense and hot, and all particles were in thermal equilibrium. The DM species χ are assumed to be stable and to interact only through the annihilation processes $\chi\chi \leftrightarrow X\bar{X}$, where X indicates any SM particles. In this scenario, the χ particles are assumed to be of Majorana type, meaning that particle and antiparticle states coincide. The time evolution of DM particles is described quantitatively by the Boltzmann equation:

$$\frac{dn}{dt} = -3Hn - \langle\sigma_{ann}v\rangle(n^2 - {n_{eq}}^2) \tag{1.22}$$

where n is the number density of DM particles χ, H is the Hubble parameter, $\langle\sigma_{ann}v\rangle$ is the velocity-averaged annihilation cross section, and n_{eq} is the DM number density at thermal equilibrium. The term $-3Hn$ in the r.h.s. of eq. 1.22 takes into account the Universe expansion. It depends on Hubble parameter, and therefore quantifies the dilution of DM as the Universe expands. The term $\langle\sigma_{ann}v\rangle(n^2 - {n_{eq}}^2)$ describes the annihilation processes in which DM particles are created or destroyed.

As the Universe expanded and its temperature T dropped, the rates of WIMP annihilation and production remained in equilibrium as long as $T \gg m_\chi$. However, once the temperature fell below the WIMP mass ($T < m_\chi$), WIMPs began to decouple from the thermal plasma, and their abundance started to decline due to ongoing annihilation.

Boltzmann equation 1.22 can be solved numerically. An approximate solution is given by [20]:

$$n_{\chi,eq} \approx g \left(\frac{m_\chi T}{2\pi} \right)^{3/2} e^{-m_\chi/T} \tag{1.23}$$

where g is the number of degrees of freedom for the DM particle.

When the expansion rate of the Universe, H, exceeded the WIMP annihilation rate, $n_\chi \langle \sigma_{ann} v \rangle$, the abundance of WIMPs effectively froze out, meaning that their production and annihilation ceased to occur at significant rates. After the freeze-out temperature was reached, the number density of DM particles remained essentially constant, leading to the present-day relic abundance. From eq. 1.23 we get:

$$n_f \sim (m_\chi T_f)^{3/2} e^{-m_\chi/T_f} \tag{1.24}$$

where the subscripts f denote quantities at freeze out.

The evolution of the thermal relic's number density is shown in Fig. 1.10. The behavior of the solution of the Boltzmann equation shows that the DM relic density is basically set by the inverse value of the velocity-averaged cross section $\langle \sigma_{ann} v \rangle$ calculated at the freeze-out temperature. The larger is $\langle \sigma_{ann} v \rangle$ at freeze-out, the longer WIMPs χ can stay in thermal equilibrium. Therefore lower annihilation cross sections lead to larger relic densities $\Omega_\chi h^2$ [33].

The value of $x_f = m_\chi / T_f$ can be estimated by assuming that around freeze-out the number density of WIMP DM is equal to the DM equilibrium number density [20] and is in the range $20 - 50$ for DM masses $10\,\mathrm{GeV} < m_\chi < 10\,\mathrm{TeV}$. This value is matched by a value of the velocity-averaged annihilation cross section of the order of $\langle \sigma_{ann} v \rangle \sim 10^{-26}\,\mathrm{cm}^3 s^{-1}$ [33], that is consistent with a weak scale cross section for particles in a mass range $10\,\mathrm{GeV} - 1\,\mathrm{TeV}$.

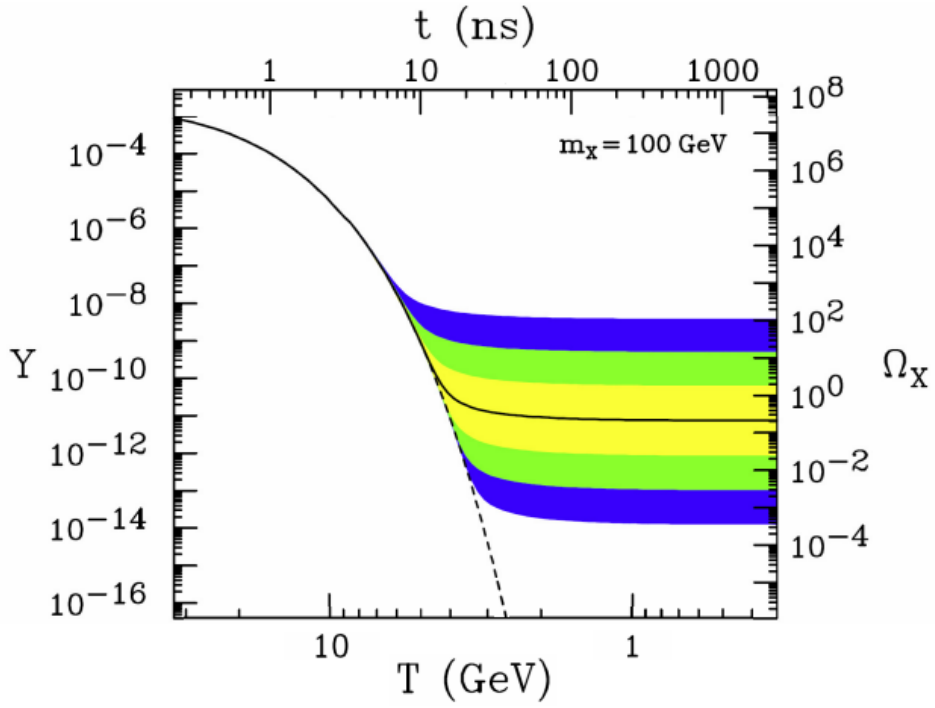

Figure 1.10: Comoving number density Y (left y-axis) and thermal relic density (right y-axis) of a $100\,\mathrm{GeV}$ annihilating DM particle as a function of temperature T (bottom x-axis) and of time t (top x-axis). The solid contour is for an annihilation cross section that yields the correct relic density, while the shaded regions are for cross sections that differ by 10, 10^2, and 10^3 from this value. The dashed contour is the number density of a DM particle remaining in thermal equilibrium. The plot is taken from ref. [34].

Among the promising DM candidates in the SUSY framework are neutralinos. These hypothetic particle states possess properties consistent with the WIMP paradigm. According to the Minimal Supersymmetric Standard Model (MSSM), neutralinos can either self-annihilate into gamma rays or decay directly into photons, enabling gamma-ray photons as potential probes to test the WIMP DM scenario.

Chapter 2

Indirect dark matter searches: an overview

In this chapter we will give an overview on the DM indirect searches using three possible messengers: gamma rays, neutrinos and antiparticles. In particular, the chapter contains a survey of searches with the Fermi LAT in gamma rays and from other gamma-ray telescopes, both ground-based and satellite-borne.

2.1 Possible probes for indirect dark matter search

Indirect searches for DM aim to detect Standard Model (SM) particles that could result from processes involving DM candidates, such as those discussed in Sec. 1.3.3. In particular, these include scenarios where WIMPs can decay or self-annihilate into photons, which are the primary focus of the analysis carried out in this thesis.

Fig. 2.1 outlines all possible probes for DM and the processes in which they can be produced. Among the possible decay or annihilation products of DM are gamma rays, neutrinos, and antimatter. Gamma rays, in particular, serve as effective probes, since they propagate through space without being deflected by galactic magnetic fields, thereby enabling the identification of their sources. Furthermore,

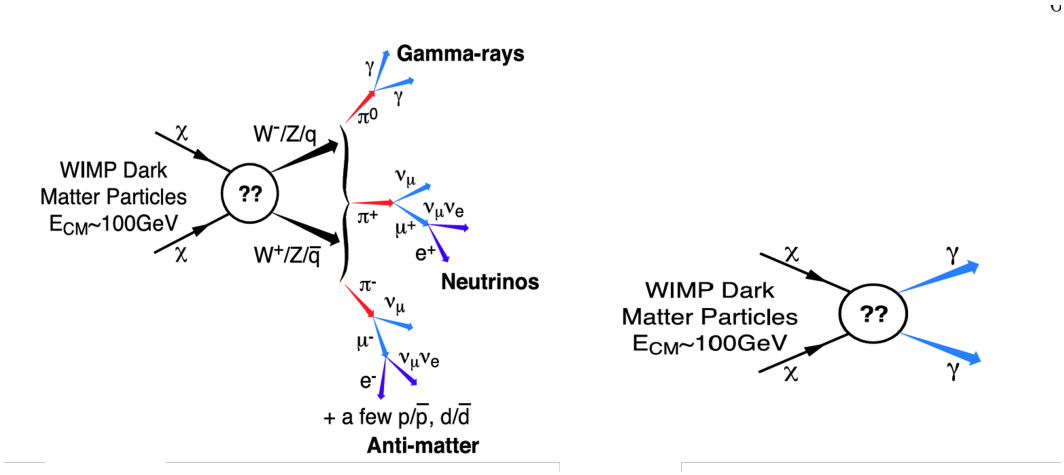

Figure 2.1: Left: possible WIMP annihilation processes into W, Z, or quark pairs that hadronize creating secondary gamma rays, neutrinos, electrons, and antimatter. Right: direct production of gamma rays in the case of self-annihilation. The same particles are expected to be produced in the WIMP decay processes.

their energy spectra encode valuable information that can help to characterize the properties of the parent DM particles, should a signal be observed. On the other hand, charged cosmic rays and antiparticles do not retain information on their sources because the galactic magnetic field randomizes their directions. However they are easy to detect, and anomalous abundances could hint at possible processes involving DM in our vicinity (see left panel of Fig. 2.2). Finally, neutrinos, like gamma rays, are neutral and do not suffer from randomization due to magnetic fields; however their detection is a much more challenging endeavor, but it is worthy since neutrinos can come from much farther sources, as the universe is substantially transparent to them.

Unlike neutrinos, gamma rays may interact with different components along their path, depending on their energy. The right panel of Fig. 2.2 shows the gamma-ray mean free path as a function of energy. At energies below $\sim 10^{14}$ eV, the absorption of gamma rays is mainly due to the interactions with the Extragalactic Background Light (EBL)[1], which is made up of a distribution of soft

[1]Sum of starlight emitted by galaxies throughout their whole cosmic history, plus possible additional contributions, like, e.g., light from hypothetical first stars that formed before galaxies were assembled [35].

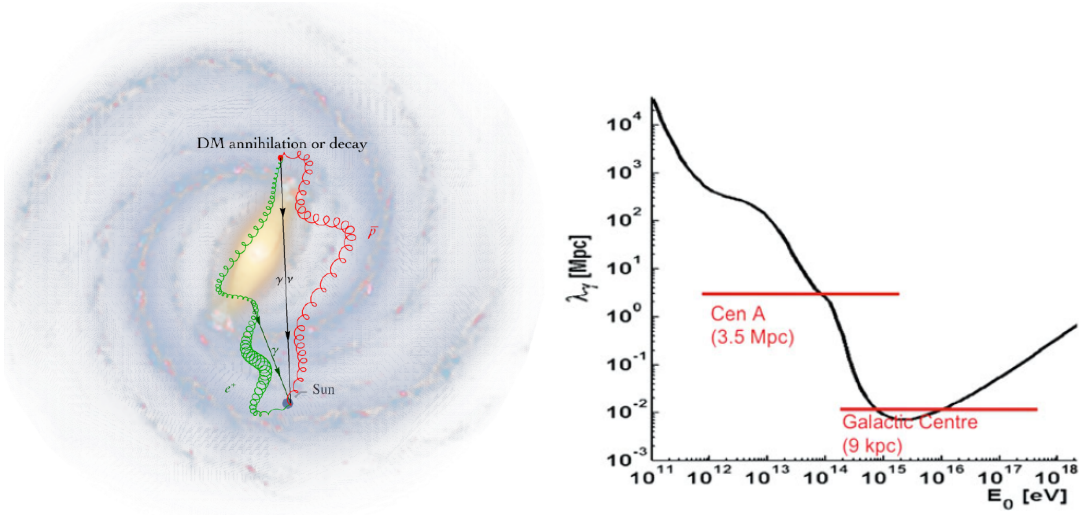

Figure 2.2: Left panel: DM annihilations or decays in the Milky Way produce SM particles that reach the observer in the solar system, possibly producing an excess in the energy spectrum of cosmic rays over the observed astrophysical background. Charged probes do not point to their source because of the randomization of their direction due to magnetic fields, differently from neutrinos and gamma rays (figure from Ref. [1]). Right panel: Mean free path λ_γ as a function of the photon energy. (plot from Ref. [35]).

photons that can be $10^2 - 10^3$ times less dense than CMB, enabling gamma rays from extragalactic sources like Centaurus A, the nearest active galaxy at 3.5 Mpc, to reach the Earth. Higher energy photons may start to interact with the CMB soft photons. The minimum in the gamma-ray mean free path λ_γ is found around 10^{15} eV, corresponding to a horizon of just a few kpc, implying that gamma rays in this energy range from extragalactic sources cannot reach the Earth. Finally, photons with energies above of $\sim 10^{16}$ eV can interact with the radio background, and the transparency start to rise again due to the lower density of this population of soft photons.

2.1.1 Dark matter distribution inside galaxies

As discussed in the previous sections, DM clumps into halos. Various theoretically well-founded models have been developed to characterize the distribution of DM density within galaxies. In this section, we present a selection of these models, which will be pertinent to the data analysis carried out in Chapter 4.

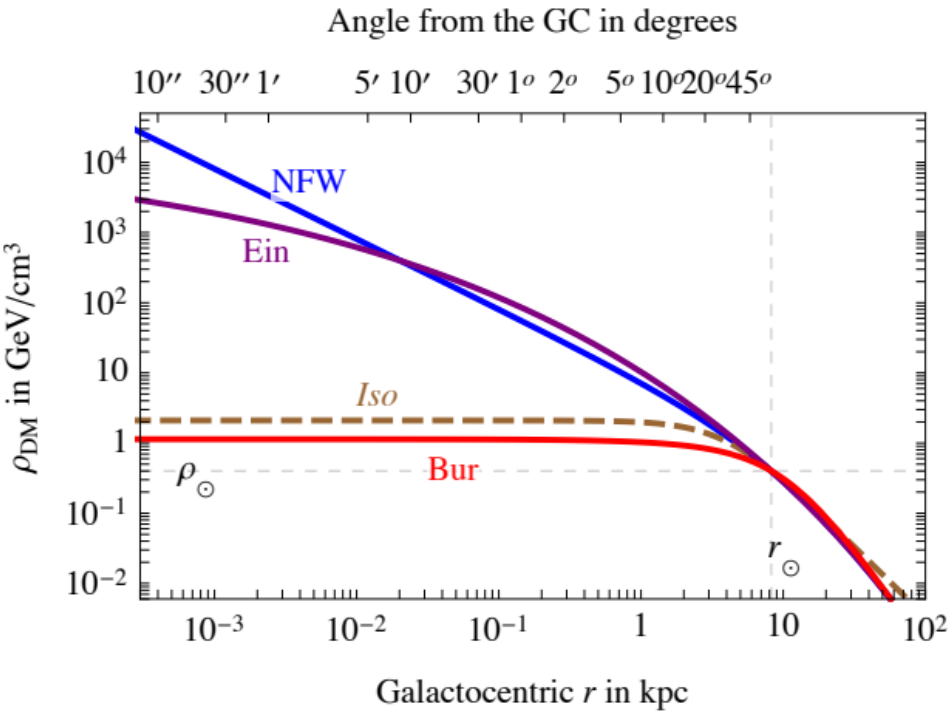

Figure 2.3: Comparison among the four different DM density profiles [1] for the Milky Way. All the curves are normalized by setting the value of the DM density at the Sun position ($R_\odot = 8.5\,\mathrm{kpc}$) to $\rho_\odot = 0.4\,\mathrm{GeV/cm^3}$.

Cored isothermal profile

The stellar structure of a galaxy is commonly modeled as a combination of a disk and a central bulge. However, to account for the observed rotation curves (see Sec. 1.1.1), the presence of an additional DM halo is required. This halo must be approximately spherical, similar to the stellar bulge, and the majority of its mass must be concentrated within an appropriate radius (e.g. of about $\simeq 5kpc$ from the Galactic center in the case of the Milky Way).

In the isothermal model [36], the DM density profile is described by the following equation:

$$\rho_{iso}(r) = \frac{\rho_0}{1 + (r/r_s)^2} \tag{2.1}$$

where $r_s = 5\,\mathrm{kpc}$ is the core radius. In this profile, the DM density is roughly constant for $r < r_s$ and then decreases as r^{-2}.

Basically, this is maybe the most natural model stemming from the observations of galactic rotational velocity anomalies in spiral galaxies (see sec.1.1.1). However, as noted in ref. [37], the isothermal distribution provides a good approximation only when averaged over radial distances. Indeed, the DM density tends to be more centrally peaked than predicted by the isothermal model, and at large radii, it falls off slightly more steeply than r^{-2}. Despite these limitations, the isothermal profile is still considered a suitable choice for describing the DM density in the innermost regions of dwarf galaxies.

NFW and NFWc profiles

N-body simulations carried out in the late 1990s revealed that a 2-parameter model describes density profiles of DM halos across a broad spectrum of halo masses and astrophysical systems, including dwarf galaxies and galaxy clusters, more accurately compared to cored isothermal profiles. This density distribution, known as the Navarro-Frenk-White (NFW) profile [37], is given by the following expression:

$$\rho_{NFW}(r) = \frac{\rho_0}{(r/r_s)\,(1 + r/r_s)^2} \tag{2.2}$$

where r is the distance from the center of the halo, r_s is a scale radius (for the Milky Way $r_s \simeq 20\,\mathrm{kpc}$) and ρ_0 is a scale DM density (for the Milky Way the DM density at Earth is used, $\rho_0 \simeq 0.4\ \mathrm{GeV/cm^3}$)

This is the most well-known DM density profile used, since, as outlined by the authors of ref. [37], it emerges universally in CDM simulations, regardless of halo mass or cosmological parameters. It still serves as a sort of benchmark model with respect to other models, like the Einasto (see Sec. 2.1.1) or the Burkert models.

Subsequent simulations and observational evidence indicate that the inner slopes of DM halos may deviate from the original NFW profile. Various mechanisms have been proposed to account for these deviations, particularly

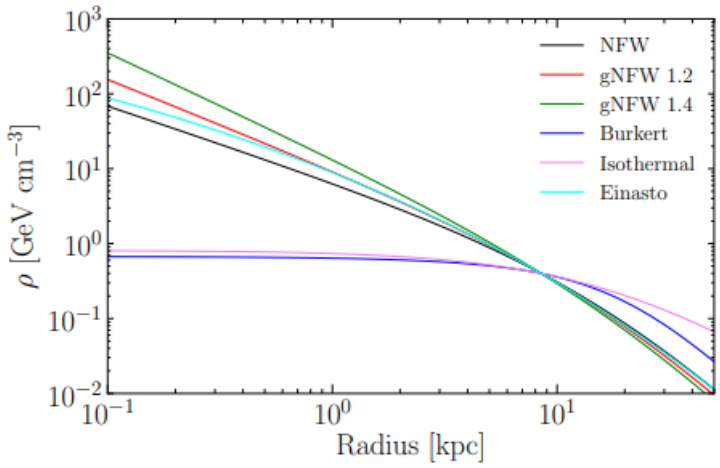

Figure 2.4: DM density as a function of Galactocentric radius reporting different modified NFW profiles. Other profiles are also reported. From ref. [39].

those involving interactions with baryonic matter. A notable example is adiabatic contraction, in which the gravitational influence of baryons draws DM inward, leading to a steeper profile. To accommodate such effects, the NFW profile can be generalized by introducing a variable inner slope γ, as shown below:

$$\rho_{NFWc}(r) = \frac{\rho_0}{(r/r_s)^{\gamma}\,(1 + r/r_s)^{3-\gamma}} \tag{2.3}$$

The parameter $\gamma = 1$ corresponds to the original NFW profile, while $\gamma > 1$ represents an adiabatically contracted NFW profile (NFWc) (see ref. [38]). This profile with $\gamma = 1.3$ can accurately model the DM density in the Galactic center region. Fig. 2.4 reports some modified NFW profiles from ref. [39], where they use the term 'generalized-NFW', or 'gNFW'.

Einasto profile

Subsequent high-precision N-body simulations performed by the Aquarius Project[2] found that the DM density profile in the innermost regions of the halo should deviate from a simple power law behavior. In the Einasto DM profile [41] the logarithmic slope of the DM density changes with the radial distance. The Einasto profile is described by the following equation:

$$\rho_{Ein}(r) = \rho_0 \exp\left\{\left(\frac{2}{\alpha}\right)\left[\left(\frac{r}{r_s}\right)^{\alpha} - 1\right]\right\} \tag{2.4}$$

where, for the Milky Way, $\alpha = 0.17$ and $r_s \simeq 20\,\mathrm{kpc}$.

Burkert profile

In Ref. [42], A. Burkert discusses a phenomenological profile that addresses the problem of flat central density profiles, like the cored isothermal one discussed in Sec. 2.1.1. All other profiles also reported here from cosmological simulations with non-baryonic DM predict central density cusps, suggesting the possibility that the cusp feature may be a signature of DM non-barionicity. This brought someone to the conclusion that DM could actually be baryonic, since observations from dwarf spiral galaxies report a flatter density profile, similar to the isothermal one.

However, Burkert shows how to modify the cored isothermal profile described by Eq. 2.1 to describe a flat central density that rules out a possible barionicity of DM. The observed universal mass profiles from dwarf spirals can be fitted nicely over the whole observed radius range by the following, purely phenomenological density distribution:

$$\rho_{bur}(r) = \frac{\rho_0}{(1 + r/r_s)\left(1 + (r/r_s)^2\right)} \tag{2.5}$$

This excludes barionicity because it can be obtained by assuming that all the haloes formed from density fluctuations with the same primordial amplitude,

[2]The Aquarius Project is a large-scale collaborative programme to simulate structure formation in the universe using ΛCDM cosmology, simulating a Milky Way-sized dark matter halo [40] resolving very precisely the subhalo structures.

ruling out scenarios where the at halo cores formed subsequently through violent dynamical processes in the baryonic component. In this case, ρ_0 and r_s are free parameters representing central density and scale radius respectively.

For the Milky Way, as an example, a recent study [43] found $r_s = 7.8 \pm 0.4$ kpc and $\rho_0 = 0.48 \pm 0.05$ GeV cm^{-3}, though deeming Burkert profile not the best option for the Milky Way specifically.

2.2 Gamma-ray signals from dark matter

2.2.1 Astrophysical backgrounds to tackle

All DM searches via gamma rays must account for backgrounds arising from numerous astrophysical sources. The impact of these backgrounds varies depending on the position and extent of the DM search target, as well as the specific methodology employed in the search strategy. In all cases, the endeavor is to search for very faint signal features consisting in excesses in gamma-ray spectra of various nature, depending on the hypothesized DM scenario producing them. These spectral features should appear together with known and much stronger astrophysical backgrounds which, therefore, need to be correctly modeled. There are mainly five sources of astrophysical backgrounds:

1. ***Milky Way diffuse emission*** (see middle left panel of Fig.2.5). It is an emission associated to the interstellar medium (ISM)[3] and the interstellar radiation field (ISRF)[4] in the Milky Way. Production processes involve inelastic collisions between cosmic-ray nuclei and nuclei of the ISM, resulting in gamma-ray emission primarily through the production and subsequent decay of neutral mesons such as the π^0. Additional contributions arise from bremsstrahlung of cosmic-ray electrons and positrons interacting with gas nuclei, as well as from inverse-Compton scattering of these leptons off

[3]The InterStellar Medium (ISM) is the matter and radiation that fills the space between star systems in a galaxy.

[4]The InterStellar Radiation Field (ISRF) is the energy present within the space between stars in a galaxy in the form of electromagnetic radiation.

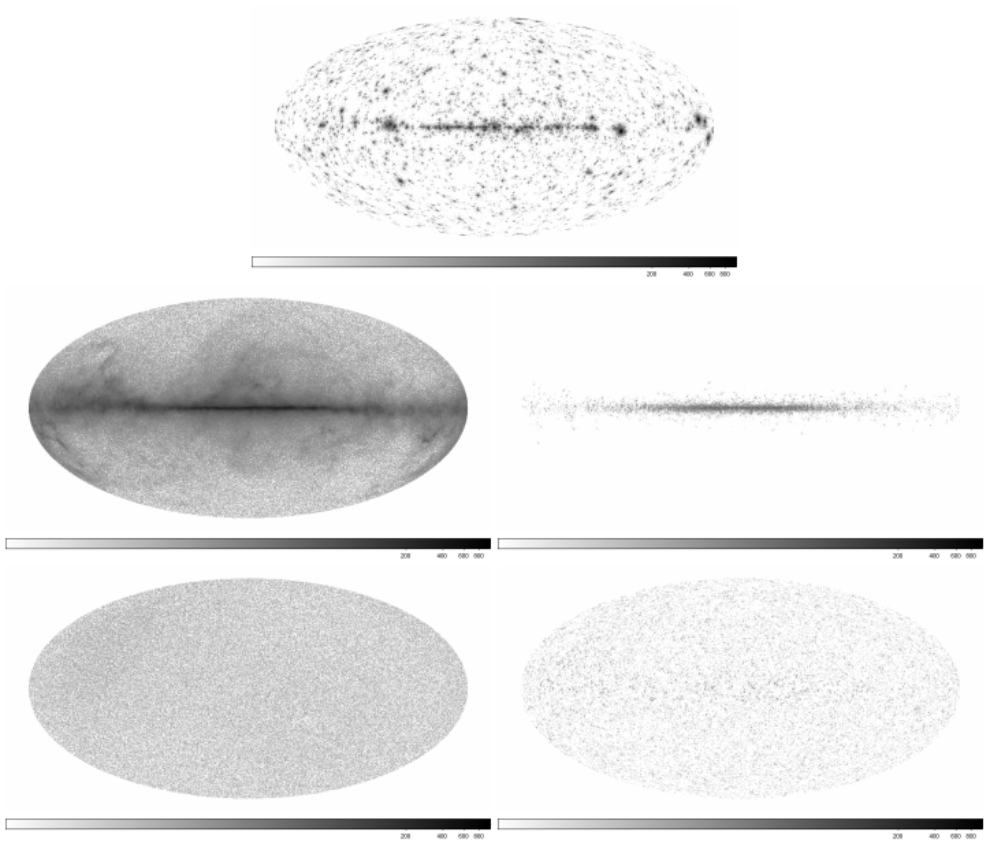

Figure 2.5: Count maps of all gamma rays with reconstructed energies above $1\,\mathrm{GeV}$ are shown for 15 years of simulated $Fermi$-LAT data using the P8R2 SOURCE event class (see Sec. 3.5 for details on *Fermi*-LAT data products). The maps are displayed in Galactic coordinates using a Hammer-Aitoff projection, with pixel sizes of $1^\circ \times 1^\circ$. Individual panels represent the contributions from cataloged sources (top panel), diffuse Galactic emissions (middle left), unresolved Galactic sources (middle right), isotropic background emission (bottom left), and unresolved extragalactic sources (bottom right). All maps use the same grayscale range to allow for direct comparison. Figures adapted from [39].

interstellar photons spanning the radio to optical/UV spectrum.

2. ***Isotropic Background and Extragalactic Source Populations.*** The isotropic gamma-ray background (IGRB) consists of all extragalactic emissions that are either too faint or too diffuse to be individually resolved in a given observation, along with any residual Galactic foregrounds that appear approximately isotropic (see lower left panel of Fig.2.5). In contrast,

the extragalactic gamma-ray background (EGB) encompasses the IGRB in addition to the contributions from resolved extragalactic point sources (see lower right panel of Fig.2.5).

3. ***Cataloged Sources.*** This is the known emission from both galactic and extragalactic gamma-ray sources (see top panel of Fig.2.5). This emission needs to be accurately modeled to avoid misinterpreting a possible candidate gamma-ray excess as a DM signal feature rather than an incorrectly modeled known source. This can be achieved in two ways, depending on the kind of analysis. For analyses with a full-sky coverage, like the line and box search reported in Chapter 4, it is preferable to directly mask regions where most of known sources are located (i.e. the Galactic Plane, GP), basically assuming that DM would not be detectable in regions overwhelmed by known astrophysical emission; on the other hand, for analyses of smaller regions of the sky, it is crucial to correctly fit the parameters of all known sources to build up a complete background model in which the possible signal feature will be added and its existence will be tested.

4. ***Unresolved Galactic Source Populations*** (see middle right panel of Fig. 2.5). Not all gamma-ray sources have been *resolved*. For most DM searches this is not a relevant background, with the exception of Galactic Center searches (and analogous searches in the centers of other galaxies), where possible unidentified pulsar populations pose a particular challenge, as their gamma-ray spectra are similar to the expected DM signal for a region of the parameter space.

5. ***Residual Charged-Particle Backgrounds.*** Most gamma-ray telescopes suffer from misidentification of gamma-ray events which are actually produced by cosmic rays impinging on the detectors. To reduce this contamination at most, they are usually equipped with an anticoincidence system that rejects all events where a charged impinging radiation is identified, regardless of what produced in the actual detectors (like in the *Fermi* LAT and DAMPE). However, a small fraction of misidentified charged

particles persists and this can affect DM searches since they involve such faint signal features.

2.2.2 Gamma-ray spectral excesses as DM signatures

Gamma rays from DM particle candidates can be produced in different processes:

1. annihilation or decay into other particles that eventually produce gamma rays either through π^0 production and subsequent decay into photons ("soft" channels, quark and gauge-boson final states $b\bar{b}$, $t\bar{t}$, W^+W^- ...) or final state bremsstrahlung and inverse Compton from leptonic channels ("hard" channels $e^+e^-, \mu^+\mu^-, \tau^+\tau^-$) resulting in a continuous spectrum;

2. direct annihilation or decay into γX, where X is usually another neutral particle (Z_0, H_0 or another γ), resulting in a spectral line.

The expected differential gamma-ray flux due to DM interactions from a sky region covering a solid angle $\Delta\Omega$ centered on a DM source can be calculated from the following equations:

$$\left(\frac{d\Phi}{dE}\right)_{ann} = \frac{1}{4\pi}\frac{\langle\sigma v\rangle}{2m^2_\chi}\left(\frac{dN_\gamma}{dE}\right)_{ann} J_{ann}(\Delta\Omega) \tag{2.6}$$

$$\left(\frac{d\Phi}{dE}\right)_{decay} = \frac{1}{4\pi}\frac{1}{m_\chi \tau}\left(\frac{dN_\gamma}{dE}\right)_{decay} J_{decay}(\Delta\Omega) \tag{2.7}$$

Eqs. 2.6 and 2.7 hold respectively for the annihilation and decay processes. The annihilation yield of DM is evaluated under the assumption that the DM particle χ is of Majorana type, i.e. coincides with its antiparticle; otherwise, an additional factor 1/2 should be included in eq. 2.6.

In both cases, the gamma-ray flux can be seen as the product of two different factors:

1. A "particle physics term", involving either the velocity-averaged annihilation cross section $\langle\sigma v\rangle$ or the inverse of the decay time $1/\tau$, the DM particle mass

m_χ and the differential spectrum of photons emitted in each annihilation or decay, given by:

$$\frac{dN_\gamma}{dE} = \sum_f B_f \frac{dN_{\gamma,f}}{dE} \tag{2.8}$$

where B_f and $(dN_{\gamma,f}/dE)$ are the branching ratio and the spectra of gamma rays in the final state f respectively;

2. An "astrophysics term" $J(\Delta\Omega)$ called "J-factor", which is proportional to the expected intensity of gamma-ray emission from DM annihilations or decays in a given angular region $\Delta\Omega$, which depends on the DM density profile $\rho(r)$. For the annihilation and decay processes the J-factors are respectively given by:

$$J_{ann}(\Delta\Omega) = \int_{\Delta\Omega} d\Omega \int_{l.o.s.} dl \rho^2(l) \tag{2.9}$$

$$J_{decay}(\Delta\Omega) = \int_{\Delta\Omega} d\Omega \int_{l.o.s.} dl \rho(l) \tag{2.10}$$

where the integrals are computed over the solid angle $\Delta\Omega$ and along the line of sight ($l.o.s.$) from the observer to the sky region under investigation.

Particular care should be taken in computing integrals along the $l.o.s.$, since the DM density ρ is a function of the distance from the galactic center r. Fig. 2.6 represents the geometry involved in the calculation of the J-factor: the distance along the $l.o.s.$ and the galactocentric distance are related by Carnot's theorem:

$$r^2 = l^2 + R^2 - 2lRcos\psi \tag{2.11}$$

where R is the distance of the observer (Earth) from the GC and $cos\psi = cos\lambda cos\beta$, where λ and β are the galactic coordinates of the generic point along the line of sight.

From eqs. 2.6 and 2.7, it is evident that larger J-factors correspond to higher expected gamma-ray fluxes from DM. Nevertheless, the most suitable targets for DM searches are those that maximize the signal-to-noise ratio. Hence, a high J-factor must also be accompanied by minimal backgrounds from known astrophysical sources.

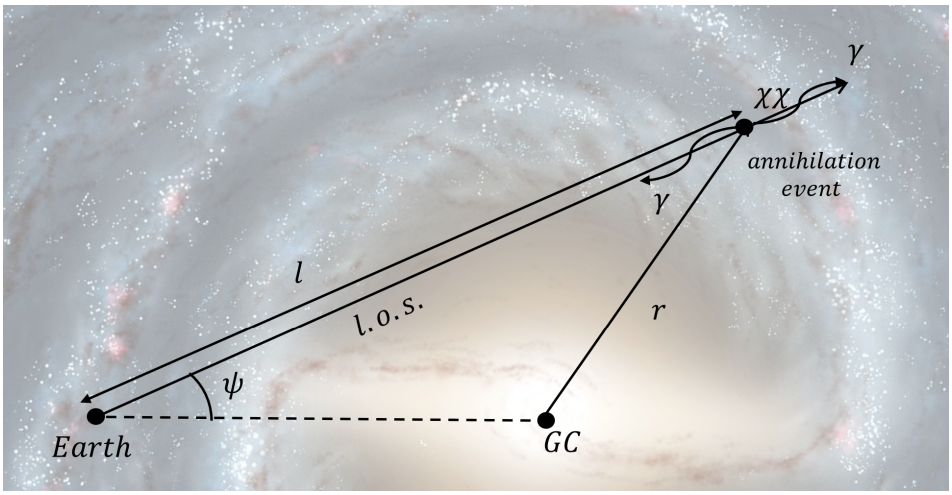

Figure 2.6: Scheme representing the geometry involved in the integration along the $l.o.s.$ to calculate the J-factor. A WIMP annihilation event is reported, but the same considerations can be made with a decay event.

Although the Galactic Center possesses the highest J-factor, it is a challenging environment for DM searches due to intense astrophysical backgrounds. This complexity arises from the high density of gamma-ray sources and the strong diffuse emission originating from interstellar gas. In contrast, Milky Way satellite galaxies offer a much cleaner observational window, albeit with lower J-factors. However, this drawback can be mitigated by performing a joint analysis across multiple satellites.

Galaxy clusters are generally considered less favorable targets due to their relatively modest expected signals. Yet, significant uncertainties in their J-factors, primarily due to the presence of substructures, suggest that the gamma-ray flux may be considerably enhanced, especially at larger radii from the cluster center. Lastly, DM subhalos in the Milky Way that lack a visible stellar component may be detectable either as isolated sources or through their cumulative contribution to the diffuse gamma-ray background.

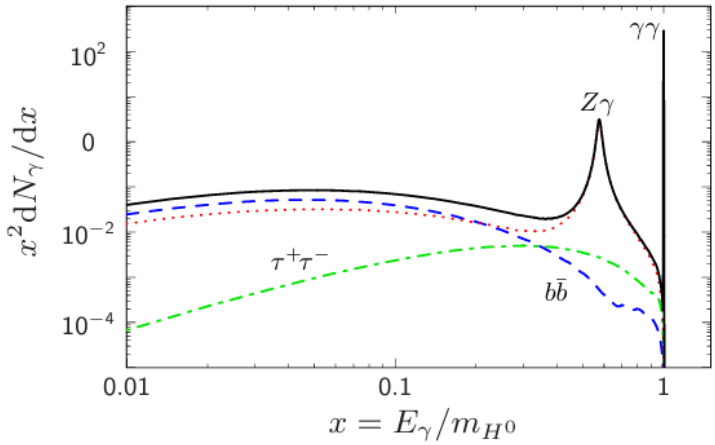

Figure 2.7: The simulated total differential gamma-ray distribution resulting from the annihilation of a WIMP particle (in this case a inert Higgs H^0, with $m_{H^0} \sim 135GeV$) is shown by the solid line. Individual contributions are displayed separately: $\chi\chi \to b\bar{b}$ (dashed line), $\chi\chi \to \tau^+\tau^-$ (dash-dotted line), and $\chi\chi \to Z\gamma$ (dotted line). The monochromatic line feature would visibly stand out with respect to other channels which affect the spectral distribution broadly. Figure from Ref. [44].

2.2.3 WIMP searches in gamma rays

WIMPs are the most natural DM candidate when a Cold Dark Matter scenario (CDM) is assumed (see Sec. 1.3.3). In this framework, DM particles are basically at rest, clumping around galaxies and massive objects, including the Milky Way or even the Sun and the Moon. Assuming that these particles may annihilate or directly decay into gamma rays, searching for them using gamma rays as a probe means looking for spectral excesses in possible targets.

Spectral lines from WIMPs

The differential flux dN_γ/dE incorporates the information on the physics of the DM annihilation process. In the simplest case, it is a *monochromatic spectral line* corresponding to a particular energy value, i.e. a Dirac delta-like feature:

$$\frac{dN_\gamma}{dE} = 2\delta(E - E_{line}) \tag{2.12}$$

where the factor 2 denotes that for each annihilation event 2 gamma photons

are produced, if we are considering the process $\chi\chi \to \gamma\gamma$.

In general, however, in the process $\chi\chi \to \gamma X$, photons are expected to be monochromatic, with their energy in the rest frame given by:

$$E_\gamma = m_\chi \left(1 - \frac{m_X^2}{4m_\chi^2}\right). \tag{2.13}$$

In writing eq. 2.13 it is assumed that both WIMPs annihilate at rest. This assumption holds for non-relativistic ($v/c \sim 10^{-3}$) WIMPs annihilating in the Milky Way halo. Similarly, in the case of the decay process $\chi \to \gamma X$, photons from non-relativistic decaying WIMPs are still expected to be monochromatic, but with half of the energy in eq. 2.13. As a result, a monochromatic line feature is expected to appear in the gamma-ray spectra at as well.

In particular, if the particle X is a second photon, the gamma-ray line from annihilation would appear at the mass of the DM particle, while in the case of a decay the line is expected to appear at $m_\chi/2$.

The detection of a gamma-ray line would serve as a "smoking gun" for WIMPs as DM candidates, since, in the energy range from a few MeV to a few hundred GeV, no known standard astrophysical processes are capable of producing monochromatic gamma-ray emission.

However, most theoretical models describing WIMP couplings with SM particles predict that processes leading to gamma-ray lines are loop-suppressed, resulting in branching ratios as low as $\sim 10^{-4}$–10^{-1} [44–48].

To date, no gamma-ray line has been definitively observed. Although a hint of a line-like feature at around 130 GeV was reported in an analysis of the *Fermi* LAT data from the Galactic Center [49], a thorough investigation by the *Fermi*-LAT Collaboration found no statistically significant evidence for such a feature [50, 51].

Box-like spectral features from WIMPs

WIMPs may also annihilate into metastable mediators, which subsequently decay away from their production site. Gamma rays can be produced in the mediator decays and can be detected by instruments like the *Fermi* LAT, yielding box-

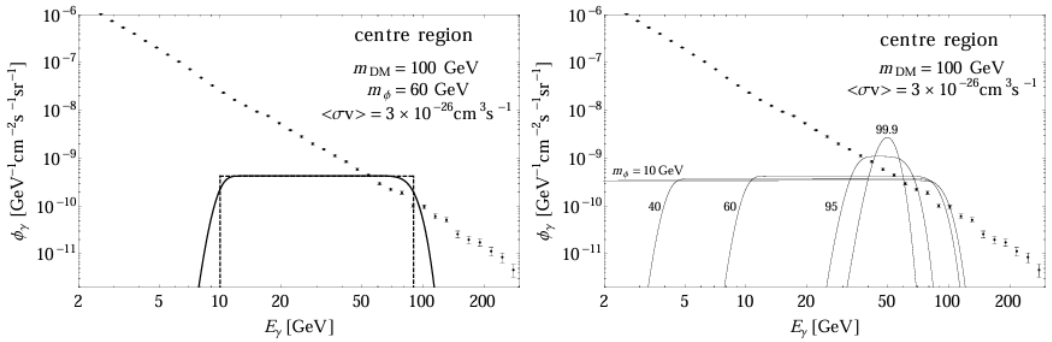

Figure 2.8: Spectra of box-shaped gamma-ray features. The left panel shows both the unconvoluted (dashed) and the convoluted (solid) with *Fermi* LAT energy resolution box spectra for $m_\chi = 100$ GeV, $m_\phi = 60$ GeV, and $\langle\sigma v\rangle = 3 \times 10^{-26}$ cm^3/s, overlaid on the 2-year *Fermi* LAT data (adapted from [49]) for the Galactic Center region. The right panel displays the convoluted box spectra for $m_\chi = 100$ GeV, $\langle\sigma v\rangle = 3 \times 10^{-26}$ cm^3/s, and various values of m_ϕ. Figures from Ref. [52].

shaped features in the energy spectrum [52]. The detailed calculation of the prompt gamma-ray flux resulting from mediator decays is discussed extensively in the literature, for instance in ref. [52,53], and here we will give only an essential overview.

In this scenario, a pair of non-relativistic DM particles χ annihilate into a pair of scalars ϕ ($\chi\chi \to \phi\phi$), that in turn decay into a pair of photons ($\phi \to \gamma\gamma$). In this way, each annihilation event produces four photons, with each photon carrying an energy $E_0 = m_\phi/2$ in the rest frame of the parent ϕ. In the laboratory frame, where DM particles are nearly at rest, the scalars carry an energy $E_\phi = m_{\rm DM}$. The energy of their daughter photons is given by:

$$E_\gamma = \frac{m_{DM}}{2}\left(1 + \cos\theta\sqrt{1 - \frac{m_\phi^2}{m_{\rm DM}^2}}\right), \tag{2.14}$$

where θ denotes the angle between the outgoing photon and the momentum of the parent scalar in the laboratory frame.

From this relation, one can see that the photon spectrum has sharp endpoints determined by the parameters $m_{\rm DM}$ and m_ϕ. The maximum (minimum) photon energy corresponds to emission at $\theta = 0°$ ($180°$) with respect to the parent particle

momentum. Since the photon emission is isotropic in the ϕ rest frame, the resulting spectrum in the laboratory frame is flat between the endpoints, with a box-shaped profile:

$$\frac{dN}{dE} = \frac{4}{\Delta E}\,\Theta(E - E_-)\,\Theta(E_+ - E), \tag{2.15}$$

where Θ is the Heaviside function, $\Delta E = E_+ - E_- = \sqrt{m_{\rm DM}^2 - m_\phi^2}$ denotes the box width, and the edges of the spectrum are given by:

$$E_\pm = \frac{m_{\rm DM}}{2}\left(1 \pm \sqrt{1 - \frac{m_\phi^2}{m_{\rm DM}^2}}\right). \tag{2.16}$$

The factor 4 is related to the fact that 4 photons are produced for each annihilation event.

In the case where a single DM particle decays into a pair of scalars, the above expressions are still valid with the replacement $m_{\rm DM} \to m_{\rm DM}/2$.

In Fig. 2.8 some examples of box-like spectral features are shown are shown. From the plot in the right panel we see that, as the value of m_Φ increases, the box-like feature becomes narrower and narrower, eventually reducing to a line-like feature in the limit $m_\Phi \to m_{DM}$. On the other hand, if $m_\Phi \to 0$, the box feature encompasses a larger energy interval, eventually extending from 0 to m_{DM}. This limit is also the one explored in the main analysis contained in this thesis (see Sec. 4.6.1.)

The production of metastable mediators has also an impact on the J-factor as well, as gamma rays are produced after the mediator decays. In the limit $m_\phi \ll m_\chi$ gamma rays are produced in the same direction of the parent ϕ (in the lab frame). In the calculation of the J-factor one should take into that gamma rays from a point P at distance l along the line-of-sight are produced by mediators decaying at distances l' from the given point, as shown in the scheme of Fig. 2.9. Therefore, in computing the J-factor integral along the $l.o.s.$, one should include the contributions from the mediators produced in all possible distances from P up to $l' = +\infty$, each weighted with the corresponding mediator survival probability

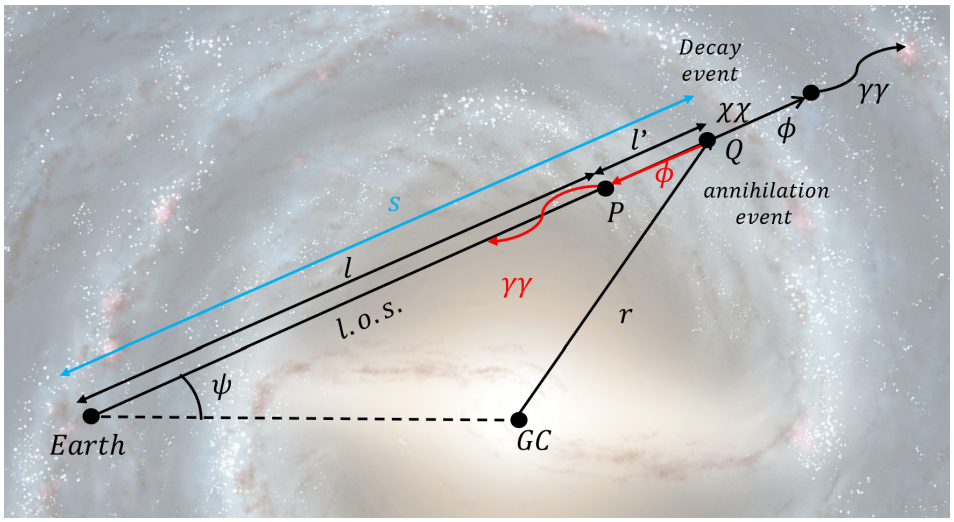

Figure 2.9: Scheme representing the geometry to calculate the J-factor in the case of a metastable mediator scenario produced in WIMP annihilation. Assuming that the gamma ray is produced in an arbitrary point P along the $l.o.s.$ at distance l from Earth, the annihilation event can be occurred at any the point Q at a distance $l' > 0$ from P.

$\frac{e^{-l'/l_d}}{l_d}$, where l_d is the mediator decay length. Therefore, the formula for the J-factor becomes:

$$J_{eff}(\Delta\Omega) = \int_{\Delta\Omega} d\Omega \int_0^{+\infty} dl \int_0^{+\infty} dl' \rho^2(l+l') \frac{e^{-l'/l_d}}{l_d} \tag{2.17}$$

With the substitution $s = l + l'$ the previous integral becomes:

$$J_{eff}(\Delta\Omega) = \int_{\Delta\Omega} d\Omega \int_0^{+\infty} ds \int_0^{s} dl' \rho^2(s) \frac{e^{-l'/l_d}}{l_d} = \int_{\Delta\Omega} d\Omega \int_0^{+\infty} ds \rho^2(s) \left[1 - e^{-\frac{s}{l_d}}\right]. \tag{2.18}$$

In the limit $l_d \to 0$, the effective J-factor J_{eff} can be assumed to coincide with the conventional J-factor defined in Eq. 2.9.

Dedicated box-like feature searches up to now focus on nearby extended gamma-ray sources like the Sun (see Ref. [54], also discussed in 2.3.1), and on galaxy clusters (see Ref. [55]).

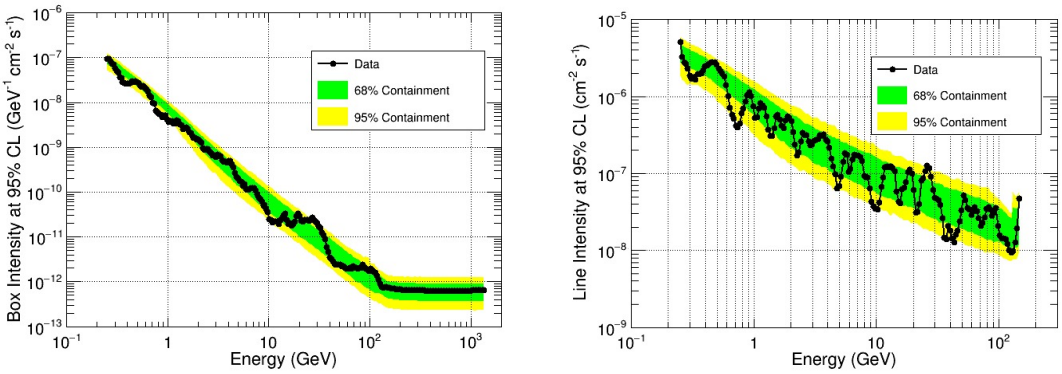

Figure 2.10: Upper limit at 95% confidence level on the intensity of a possible feature in the solar gamma-ray spectrum. Left panel: box model; Right panel: line model. The green and yellow regions indicate the central 68% and 95% expectation bands for the 95% CL limits evaluated from the pseudo-experiments [54].

2.3 Main targets for DM searches in gamma rays

2.3.1 The Sun

Due to its proximity, the Sun is a promising target for indirect DM searches. In fact, in leading theoretical models, it is considered a potential trap for galactic DM, which may be confined either within its core or in bound orbits [56–62]. DM particles are expected to become gravitationally bound to the Sun after being slowed down through elastic scattering with solar nuclei. An alternative scenario involves a sequence of inelastic interactions with Standard Model particles inside the Sun, ultimately resulting in the gravitational capture of DM particles. In this case, the particles do not thermalize but instead enter stable orbits around the Sun.

If DM particles are capable of annihilation, a dynamic equilibrium may be established between their capture and annihilation rates. The resulting annihilation products can include gamma rays, which in principle could reach Earth and be detected by instruments like Fermi. However, if annihilations occur in the solar core, only low-energy neutrinos ($E_\nu < 1$ TeV) are able to escape and reach Earth, due to the dense solar environment. An alternative scenario, proposed by some authors [63], suggests that DM particles may annihilate into long-lived

mediator particles. These mediators could escape the Sun before decaying into gamma rays, which would then be able to reach Earth and serve as detectable signatures of DM.

However, the Sun itself is a gamma ray source, characterized by a steady and a transient emission (solar flares[5]). The main known mechanism that originate the steady solar gamma-ray emission consists in the interactions of charged cosmic rays in the solar environment, which includes two main components [64–69]:

1. A contribution from the disk, originating from the interactions of hadronic CRs with the solar atmosphere, which yield hadronic cascades with their gamma-ray component;

2. A diffuse contribution, due to the interactions of cosmic-ray electrons and positrons with the optical solar photons in the heliosphere, in which gamma rays are produced by inverse Compton scattering.

Background modeling is crucial to attempt a disentanglement of potential faint DM signal features from known physical mechanisms of emission.

In 2020, the Fermi-LAT collaboration investigated the gamma-ray emission from the Sun to search for possible features in the spectra, indicating DM annihilation: a box-shaped feature, characteristic of the mediator scenario, and a line-shaped feature, which would be expected if DM particles annihilate directly into gamma rays outside the solar environment. In Fig. 2.10 the upper limits at 95% CL on the intensities of these possible features are shown.

The limits on the box intensities can be converted into limits on the DM-nucleon scattering cross sections in both the spin-dependent and spin-independent case. Fig. 2.11 shows these limits and compares them to those obtained in direct search experiments: PICO-60 [70] 90% CL limits for spin-independent scattering (cyan line) and XENON1T [71] 90% CL limits for spin-independent scattering (blue line). The limits from the indirect search appear to be consistent with those from direct search.

[5]Sudden releases of magnetic energy from the Sun that accelerates particles to relativistic energies, producing high-energy photons (from hundreds of keV to GeV) through bremsstrahlung, nuclear interactions, and pion decay.

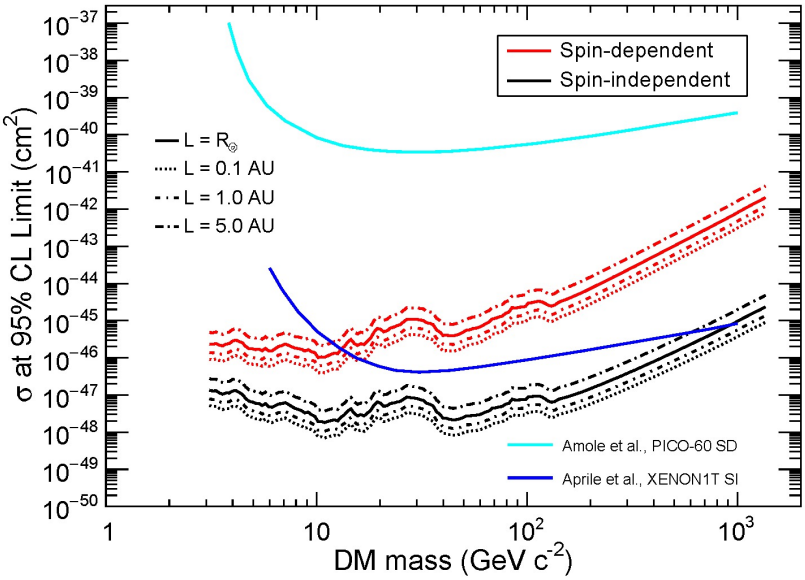

Figure 2.11: Limits at 95% CL on the DM-nucleon cross section via long-lived mediator for four different decay lengths $L = R_\odot, 0.1, 1$ and $5\,\mathrm{AU}$. The plots also show the limits at 90% CL from the PICO-60 experiment [70] in the case of spin-dependent (SD) scattering (cyan line) and from the XENON1T experiment [71] in the case of spin-independent (SI) scattering (blue line). From Ref. [54].

2.3.2 The Galactic Center

The region surrounding the Galactic Center (GC) is among the most complex and intense in the gamma-ray sky. Gamma-ray emission from this area arises from a combination of mechanisms, including the interactions of cosmic rays with interstellar gas, via inelastic nucleon-nucleon collisions and bremsstrahlung from electrons and positrons, and with interstellar radiation fields through inverse Compton scattering. In addition, the GC hosts numerous individual gamma-ray sources such as pulsars, binary systems, and supernova remnants. On top of all these possible mechanisms, a further excess in gamma-rays could be the signal of WIMP annihilation, which is expected to be the brightest towards the GC [73]. Several independent groups have reported the detection of an excess gamma-ray emission at energies of a few GeV near the Galactic Center, observed on top of various models of interstellar emission and point sources [74–83].

The Fermi-LAT Collaboration carried out a comprehensive analysis of the

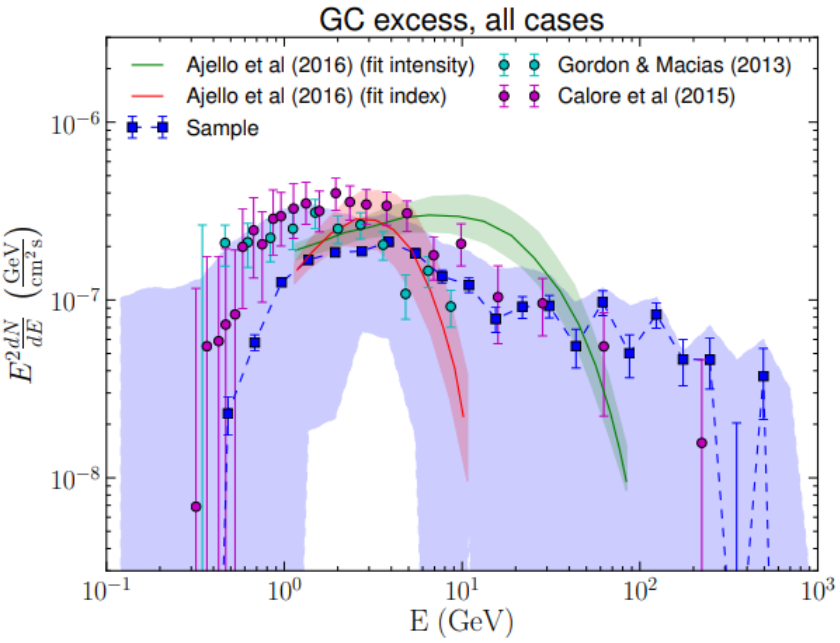

Figure 2.12: Spectrum of the Galactic Center excess as reported in Ref. [72]. Blue points are derived using the Sample Model described in [72], where the *Fermi*-LAT emission components are fitted using parameters obtained by GALPROP code (used to model CRs propagation and produce spatial models for gamma-ray subsequent emission) and source templates obtained from Fermi 3FGL catalog. The "excess" part of the model makes use of a gNFW (see Sec. 2.1.1) annihilation template with $\gamma = 1.25$. The effects of systematics are represented by the blue band. These results are compared to previous determinations of the GC excess spectrum from the literature.

gamma-ray emission towards the Galactic Center (GC), conclusively reporting the presence of an excess component that peaks at approximately 3 GeV [72]. Fig. 2.12 illustrates the spectrum of this GC excess along with its associated uncertainty band (in blue), which reflects the full range of systematics arising from variations in the modeling of point sources and interstellar emission. This modeling is based on various emission components, compiled in a "Sample Model" that uses GALPROP[6]-computed spatial maps for gamma-ray diffuse emission originated by cosmic-ray transport in the Galaxy and source catalog-based parameters to model

[6]GALPROP is a numerical code for calculating the propagation of relativistic charged particles and the diffuse emissions produced during their propagation, see `https://galprop.stanford.edu/`.

point sources (*Fermi* 3FGL in particular). On top of all these known mechanisms, the "excess" part of the model makes use of a gNFW (see Sec. 2.1.1) annihilation template with $\gamma = 1.25$.

The spectral and morphological properties of the excess are not straightforwardly compatible with the expectations from DM annihilation, and instead suggest the presence of an underlying astrophysical contribution in addition to a possible DM component. Therefore, stringent constraints on the annihilation cross section of DM particle candidates are set by requiring that the predicted DM-induced signal does not exceed the upper bound of the GC excess spectrum, as determined from variations in conventional emission models plus 95% statistical confidence.

Nevertheless, even if the GC excess is found, its nature remains elusive: a fraction of the excess emission may originate from the Fermi Bubbles[7], cosmic-ray interactions near the GC, or an unresolved population of sources such as millisecond pulsars. All these possible explanations make the DM interpretation of the GCE not conclusive.

In addition, this DM interpretation is increasingly challenged by growing evidence that the morphology of the excess is more consistent with expectations from a population of MSP-like sources residing in the Galactic bulge, as in the analysis of Ref. [85], which finds that an emission profile tracing stellar mass in the bulge is preferred over conventional DM profiles (e.g. NFW and Einasto). This scenario is further investigated in a more recent work [86], in which a machine-learning multiclass classification of *Fermi*-LAT sources within 10° around the GC points to the conclusion that the resulting spectral energy distribution, spatial morphology, and source count distribution are all consistent with those expected from a population of MSPs capable of accounting for the observed gamma-ray excess.

The GC region remained an interesting target for DM searches also in other

[7]The *Fermi Bubbles* are large, bilobate structures extending roughly 50° above and below the Galactic Center, discovered in gamma-ray data from the *Fermi*-LAT. They are believed to originate from past energetic events, such as outflows from the central supermassive black hole [84].

recent works that do not address the identification of the GC excess as a main task, rather searching for other spectral features, such as monochromatic spectral lines.

In the *Fermi*-LAT Collaboration line search of 2013 [50], a suspect line-like feature at around 133 GeV was reported with a local significance of 3.3σ in a Region Of Interest (ROI) encircling the GC (R3, see Sec. 2.2.3). However, with two additional years of data and the new event reconstruction and selection algorithms, the significance of the possible feature decreased. The "fractional signal" decreased from $f(133\,\mathrm{GeV})_{R3} = 0.61$[8] in the 3.7-year data set to $f(133\,\mathrm{GeV})_{R3} = 0.07$ in the 5.8-year dataset. With the whole 5.8 year dataset, the local significance drops to 0.72σ [51], which is consistent with the hypothesis that most of the original feature originated from a statistical fluctuation.

2.3.3 The Milky Way Halo

The Milky Way galaxy is thought to be embedded in a halo of DM, and is not a special case. As emerged from the discussion in Sec. 2.3.2, even though DM is expected to be relatively abundant in the GC region, its predicted signature features tackle with strong astrophysical gamma-ray emission mechanisms that make the search for these faint features very challenging. Moving progressively away from the GC and searching for possible DM annihilation events in the halo may be more viable, even though the predicted DM density becomes lower and lower, mainly because of the drastic reduction in known emission mechanisms potentially masking signal features.

WIMP annihilations in the Galactic halo may produce gamma rays detectable by the LAT. The processes $\chi\chi \to \gamma\gamma, \gamma Z^0, \gamma H^0$ should produce a narrow, sharp spectral feature ("line"). The *Fermi*-LAT Collaboration has performed several different searches for a possible DM line signal from our Galaxy [50, 51, 88, 89]. This thesis work will illustrate an update of this search. The main features of the LAT analysis are the same as in this work, and will be explained in detail in

[8] The fractional signal f is defined as $f = n_{sig}/b_{eff}$ [51], where n_{sig} and b_{eff} are the signal counts and the effective background counts.

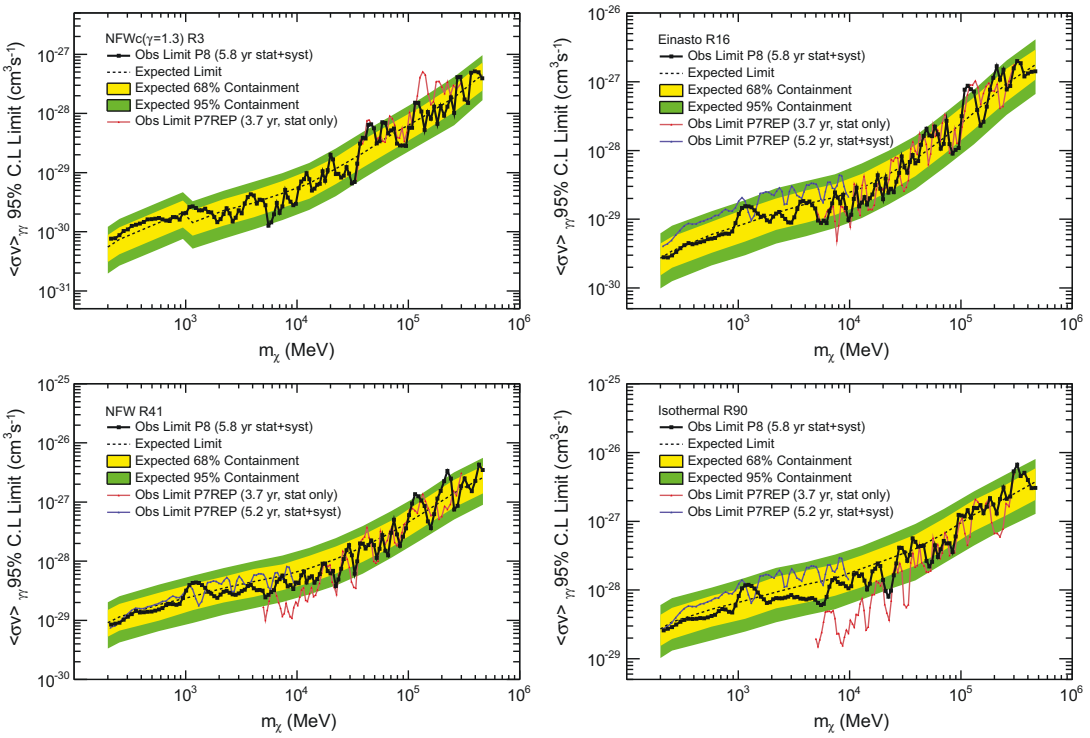

Figure 2.13: Upper limits at 95% confidence level on $\langle \sigma v \rangle_{\gamma\gamma}$ for each DM profile considered in the corresponding optimized ROI. Yellow (green) bands show the 68% (95%) expected containment bands derived from 1000 no-DM MC simulations. The black dashed lines show the median expected limits from those simulations. Also shown are the limits obtained in a previous 3.7-year line search [50] and 5.2-year line search [87] when the assumed DM profiles were the same. Plots taken from Ref. [51].

Chap. 3.

The latest line search analysis in galactic gamma-rays from the *Fermi*-LAT Collaboration [51] was performed selecting gamma rays from different Regions Of Interest (ROIs). Each ROI is defined as a circular region centered on the GC. The galactic plane, which is rich of bright gamma-ray sources, is masked, with the exception of a $12° \times 10°$ box centered on the GC. The ROIs are optimized for the different DM density profiles discussed in sec. 2.1.1. The following RoIs are used:

1. R3, which is a cone centered on the GC with an aperture of 3° and is optimized for a cored NFW profile; this is the only ROI that does not include

the GP mask;

2. R16, which is a cone centered on the GC with an aperture of 16° and is optimized for the Einasto profile;

3. R41, which is a cone centered on the GC with an aperture of 41°, optimized for the NFW profile;

4. R90, which is a cone centered on the GC with an aperture of 90° and is optimized for the isothermal profile;

5. R180, which corresponds to the whole Galaxy, and is optimized for the search of gamma rays from DM decays events, with a NFW DM density profile.

In the end, no signatures of lines were found, and therefore upper limits on the line intensity were evaluated. These limits, with the same procedure that will be explained in Chapter 4, are converted into upper limits on the velocity-averaged annihilation cross section $\langle \sigma v \rangle_{\gamma\gamma}$ and into lower limits on the decay time τ_χ. Fig. 2.13 shows upper limits on $\langle \sigma v \rangle_{\gamma\gamma}$ for the 4 RoIs for which annihilation events are expected to take place (R3, R16, R41, R90). Also yellow and green bands of 68% and 95% containment respectively are superimposed and, coherently with the lack of observation of line-like features in the spectra, the measured limits lie within these bands. Hence all fluctuations can be considered due to statistical effects.

This line of research is followed also by researchers working on the data from other gamma-ray telescopes, like DAMPE. The DArk Matter Particle Explorer (DAMPE) is a space borne high-energy particle detector launched on 2015, December 17^{th}. Its goal is to measure charged cosmic rays and gamma rays in a very wide energy range [90] (5 GeV - 10 TeV for electrons and gamma rays, 50 GeV - 100 TeV for protons and heavier nuclei).

Although its acceptance is ∼10 times smaller than that of the *Fermi* LAT, thanks to its better energy resolution, DAMPE is suitable to perform searches for possible line-like features in the gamma-ray spectra. This search was performed and, like in the case of the LAT, it yielded negative results.

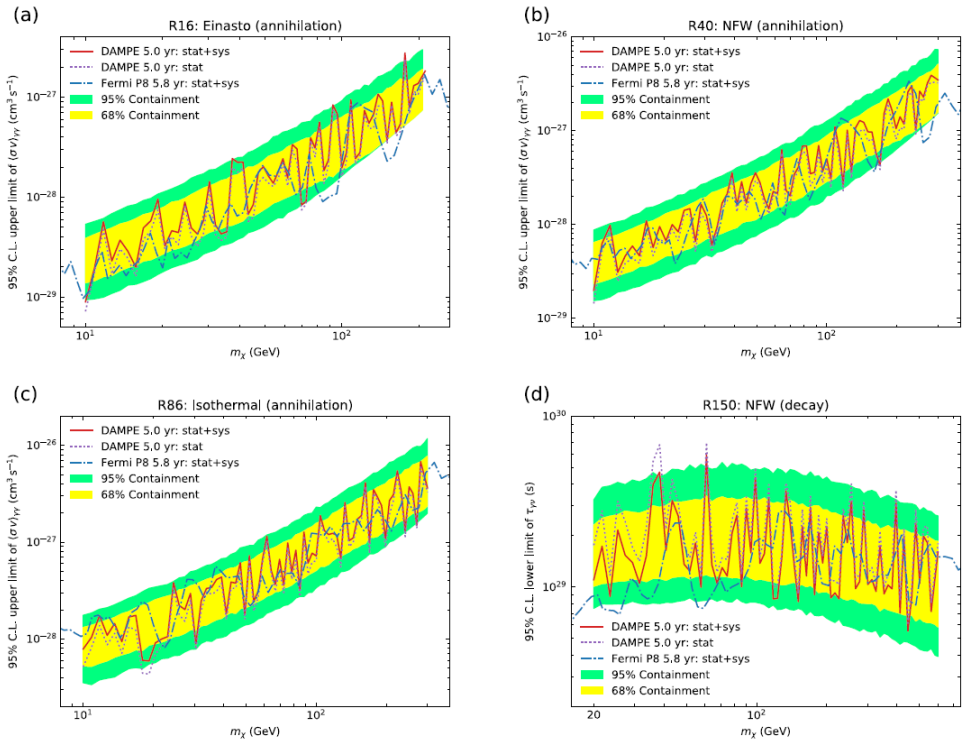

Figure 2.14: Constraints at 95% confidence level for different DM density profiles obtained from the analysis of a 5-years DAMPE dataset. The top-left, top-right and bottom-left panels show the upper limits on $\langle\sigma_{ann}v\rangle$ assuming the Einasto, NFW and isothermal profiles respectively; the bottom-right panel shows the lower limit on the decay time $\tau_{\gamma\nu}$ assuming the NFW profile. Yellow (green) bands show the 68% (95%) expected containment bands obtained from 1000 simulations of background emission with systematic uncertainties involved. The red solid and purple dotted lines are the results with and without the systematic uncertainties respectively. The blue dot-dashed lines show the 5.8-year Fermi-LAT constraints from [51]. The plots are taken from Ref. [91]

The DAMPE Collaboration has performed its search for possible line-like features using the data collected by DAMPE in its first 5 years of operation [91]. The methodology followed in this analysis has strong similarities with the one adopted by the *Fermi*-LAT Collaboration, with a different choice of the ROIs. In this analysis all ROIs are defined as circular areas of radius $R_{\rm GC}$ centered on the Galactic Center, with the rectangular region $|l| \geq \Delta l$ and $|b| \leq 5^\circ$ masked. For annihilating DM, the optimal $(R_{\rm GC}, \Delta l)$ values are $(16^\circ, 5^\circ)$, $(40^\circ, 9^\circ)$, and $(86^\circ, 0^\circ)$ for the Einasto, NFW, and isothermal profiles, respectively, while for decaying DM,

the optimal values are $(150°, 0°)$.

Fig. 2.14 shows the constraints obtained by DAMPE for the velocity-averaged DM annihilation cross section and for the DM decay time. Again, since no signature of lines were found, upper limits are given on the line intensity parameter and then converted into constraints on $\langle\sigma_{ann}v\rangle$ and on τ_χ. The limits lie within the expected containment bands, obtained from Monte Carlo simulations of background-only events and are consistent with those obtained by the Fermi LAT.

2.3.4 Dwarf Spheroidal Galaxies

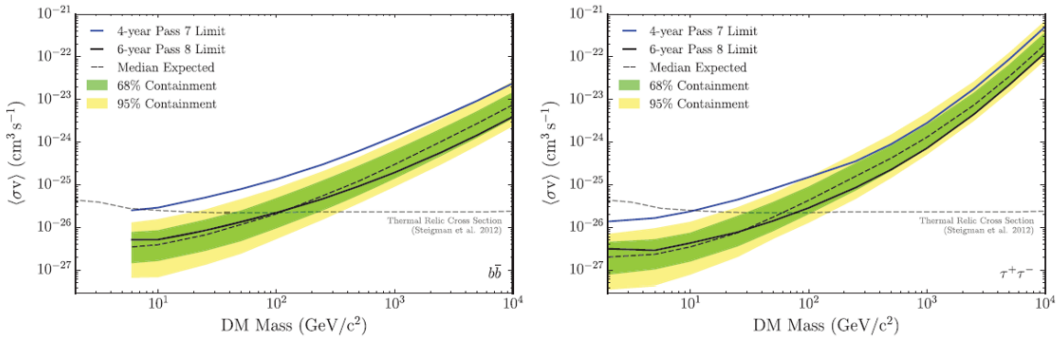

Figure 2.15: Constraints on the DM velocity-averaged annihilation cross section $\langle\sigma_{ann}v\rangle$ at 95% confidence level for the $b\bar{b}$ (left) and $\tau^+\tau^-$ (right) channels derived from a combined analysis of 15 dSphs with 6 years of PASS8 data. The blue curve shows the limits derived from a previous analysis of a four-year PASS7 data set with the same sample of 15 dSphs [92]; the gray curve corresponds to the thermal relic cross section in Ref. [93]. The plots are taken from Ref. [94].

The dwarf spheroidal (dSph) satellite galaxies of the Milky Way are among the most DM-dominated systems known. Their high DM content, relative proximity, and minimal astrophysical background make them ideal targets for the indirect detection of DM through gamma-ray observations. The *Fermi*-LAT Collaboration has conducted several searches for DM signals from dSph galaxies, all of which have so far yielded null results [92,94,100,101]. Nonetheless, these studies have produced some of the most stringent constraints on the thermally averaged annihilation cross section $\langle\sigma_{ann}v\rangle$, particularly when data from multiple galaxies are combined using a joint likelihood analysis.

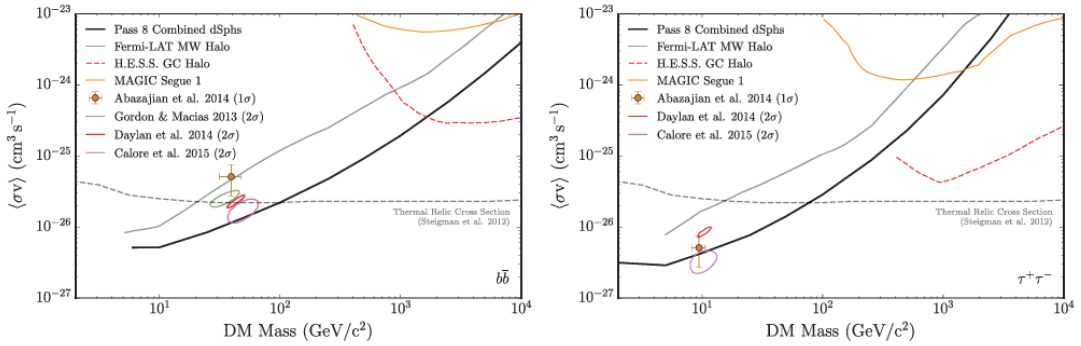

Figure 2.16: Comparison of constraints on the DM annihilation cross section for the $b\bar{b}$ (left) and $\tau^+\tau^-$(right) channels from [94] with previously published constraints from LAT analysis of the Milky Way halo (3σ limit) [95], 112 hours of observations of the Galactic center with H.E.S.S. [96], and 157.9 hours of observations of Segue 1 with MAGIC [97]. Pure annihilation channel limits for the Galactic center H.E.S.S. observations come from Ref. [98]. Closed contours and the marker with error bars show the best-fit cross section and mass from several studies of the GC excess [79, 80, 99]

In 2015, The Fermi-LAT collaboration analyzed a sample of 25 Milky Way dSphs (the same sample analyzed in 2014 [92]) using a data sample collected by the LAT in its first 6 years of operation. A joint analysis was performed on a set of 15 dSphs, without finding significant gamma-ray excess associated to these objects. Fig. 2.15) shows the upper limits at 95% confidence level on the velocity-averaged annihilation cross section obtained when considering DM annihilations in the channels $b\bar{b}$ and $\tau^+\tau^-$ for WIMPs with mass between 2 GeV and 10 TeV (see sec. 2.2) [94]. These limits exclude the thermal relic annihilation cross section for WIMPs with $m_\chi < 100$ GeV annihilating through the b-quark and τ-lepton channels.

These constraints from dSph can be combined with limits from Galactic DM halo searches and results from GCE. This combination results in an allowed region in DM parameter space ($\langle\sigma_{ann}v\rangle$ - m_{DM}) . Fig. 2.16 reports these allowed regions taking advantage of the combination of all the mentioned constraints. Assuming a $b\bar{b}$ final state, the best-fit models are located in a region of parameter space slightly exceeding the 95% confidence level upper limits, with an annihilation cross section in the range $(1\text{–}3) \times 10^{-26}$ cm^3 s^{-1} and dark matter masses between 25 and

50 GeV. However, significant uncertainties in both the structure of the Galactic DM distribution and the modeling of the diffuse Galactic gamma-ray background can substantially broaden the range of viable values for $\langle\sigma_{ann}v\rangle$, the annihilation channel, and m_{DM}.

2.3.5 Galaxy clusters

Galaxy clusters are the largest gravitationally bound structures in the Universe and are expected to be predominantly composed of DM. In the case of DM decay, they are predicted to produce the highest gamma-ray fluxes among all standard targets. For DM annihilation, the expected flux from clusters can be comparable to that from dSph galaxies, provided that the contribution from DM substructures is properly included in the J-factor evaluation.

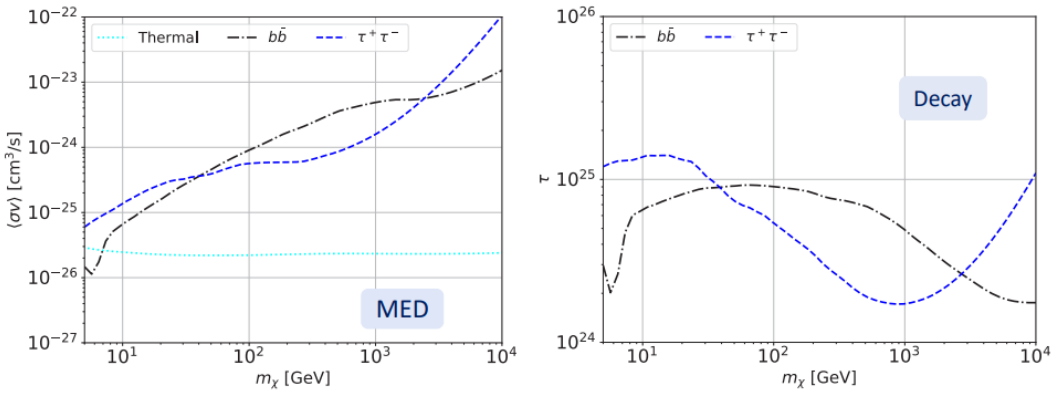

Figure 2.17: Upper limits at 95% confidence level on $\langle\sigma v\rangle$ (left) and lower limits on τ (right) as a function of m_χ obtained in the analysis in Ref. [102]. MED refers to the state-of-the-art estimate of the effect of substructures on the J-factor evaluation.

In Ref. [102], 12 years of *Fermi*-LAT data in the direction of 49 clusters are used to set competitive constraints on the velocity-averaged annihilation cross section of WIMPs and their decay time. The expected population of substructures within these objects is investigated and benchmark models to assess the uncertainties in their contribution to the annihilation flux are given. The combined analysis revealed a signal with a significance of $2.5 - 3.0\,\sigma$, which could be interpreted as

either a DM-induced signature or a gamma-ray emission from CR interactions in the intracluster medium.

2.4 Neutrino signals from WIMPs

2.4.1 Solar neutrinos

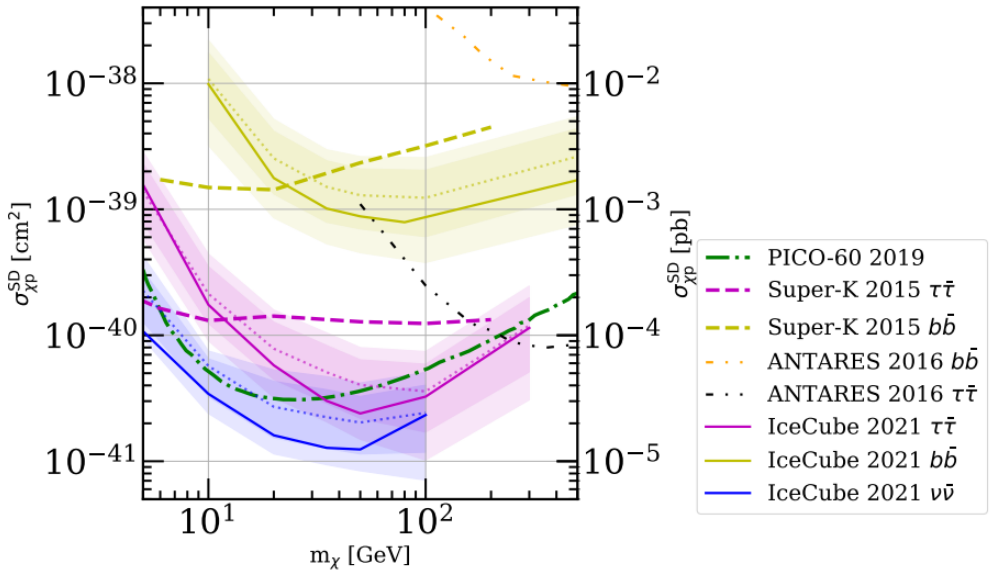

Figure 2.18: Upper limits at 90% confidence level (solid curves) and expected sensitivities (dotted curves) on the spin-dependent scattering cross-section as a function of the WIMP mass derived from seven years of IceCube data on solar neutrinos (Ref. [103]). The dark and light shaded regions indicate the central 68% and 95% expectatiob bands, respectively. Limits from the Super-K [104], PICO-60 and ANTARES [105] experiments are also shown. Plot taken from Ref. [103].

Interactions between WIMPs and baryonic matter inside the Sun are thought to yield not only detectable features in the solar gamma-ray emission, but also to produce an excess in the neutrino flux. Indeed, the solar gamma-ray steady emission, as outlined in Sec. 2.3.1, exhibits a potentially overwhelming background. This fact makes neutrinos a very popular alternative probe to gamma rays for a possible solar DM signal. A solar DM signature would yield an excess in

the solar neutrino flux. Various experiments, including Super-Kamiokande [106], IceCube [103,107] and ANTARES [108] have searched for a possible excess of solar neutrinos, still with negative results.

The neutrinos observed towards the Sun by these experiments were found to be always consistent with background expectations of the Sun as a point-like source emitting steadily neutrinos as a result of both nuclear reactions happening inside the star and CRs interacting with solar protons.

Nevertheless, constraints on physical quantities of interest can be extracted, like the WIMP-proton cross section as a function of the WIMP mass. The scenario here is the same as in the search for DM gamma-ray signals from the Sun, illustrated in Sec. 2.3.1. The sun is considered a potential capture site for galactic DM particles and gravitational binding can occur if DM loses energy through elastic scattering with solar protons, leading to confinement within the solar core. Confined DM can therefore decay into SM particles, including neutrinos with energies 1 GeV$< E_\nu <$ 1 TeV, which are the only particles expected to escape the solar environment by themselves, without requiring long-lived mediators or other mechanisms. The non-detection of excess flux in solar neutrinos allows the setting of competitive constraints on WIMP-proton cross sections.

Fig.2.18 shows the upper limits on the spin-dependent DM-proton scattering cross section obtained by the IceCube Collaboration [103] with a 7 years data sample. The data exclude scattering with cross-sections down to a $10^{-41} \div 10^{-40}\,\mathrm{cm}^2$ for DM masses in the range $5 - 100$ GeV, under the assumption of capture-annihilation equilibrium, with annihilation occurring into neutrinos and antineutrinos.

2.4.2 Neutrinos from the Galactic Center

Due to its proximity, the GC is expected to yield the highest flux of DM annihilation products, including neutrinos. However, differently from the gamma-ray case (see Sec. 2.3.2), no hints of neutrino excesses from this region were found. However, the possible neutrino excess from the GC is expected in the same energy range as the gamma-ray excess, from 1 to 10 GeV, where the sensitivities of current

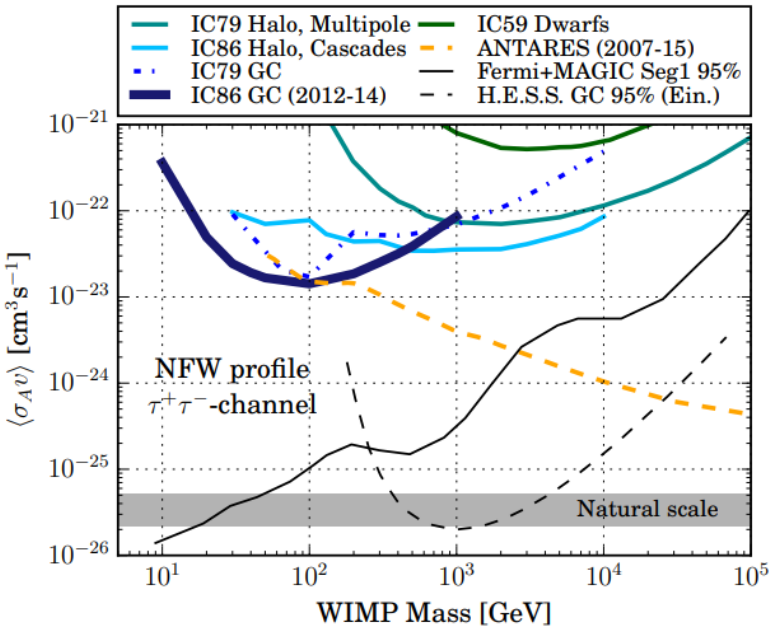

Figure 2.19: Upper limits on $\langle\sigma_A v\rangle$ as a function of WIMP mass for annihilation into neutrinos via the $\tau^+\tau^-$ channel, assuming an NFW halo profile. Results from the IceCube Galactic Center search (IC86, $2012-2014$ [109]) are compared with previous IceCube [110–113] and ANTARES [114] analyses, as well as gamma-ray limits from Segue 1 (*Fermi*-LAT+MAGIC [115]) and the Galactic Center (H.E.S.S. [116]). The "natural scale" denotes the $\langle\sigma_A v\rangle$ expected for thermal relic WIMPs [93]. Plot from Ref. [109].

and past instruments are low[9]. Indeed the lack of a neutrino counterpart to the gamma-ray excess from the GC would be a further evidence in favor of its non-DM nature, making the millisecond pulsar scenario more viable. Nevertheless, searching for DM neutrinos from this region yields meaningful constraints in the DM parameter space: the IceCube Collaboration conducted a search for an excess of muon (anti)neutrinos from DM annihilation in the GC [109, 112], exploiting the position of the detector at the South Pole, where the GC remains continuously above the horizon. In particular, the analysis at Ref. [109], which uses 3 years of IceCube data, sets the strongest constraints on a neutrino signal from DM in the mass range $10-100\,\mathrm{GeV}$, excluding self-annihilation cross-sections down to

[9] As an example, the lower bound of the IceCube energy range is ~ 10 GeV [117], while the lower bound of the ANTARES energy range is $\sim 20-30$ GeV [118].

$1.18 \times 10^{-23}\,\mathrm{cm}^3\,\mathrm{s}^{-1}$ for 100 GeV DM particles annihilating through the $\tau^+\tau^-$ channel, under the assumption of a NFW profile. These limits are reported in Fig. 2.19, with a comparison of constraints on $\langle\sigma_A v\rangle$ from gamma-ray data as well, showing that the latter are still much more competitive, mainly because of the larger statistics available.

2.4.3 Search for spectral lines in the Galactic neutrino spectra

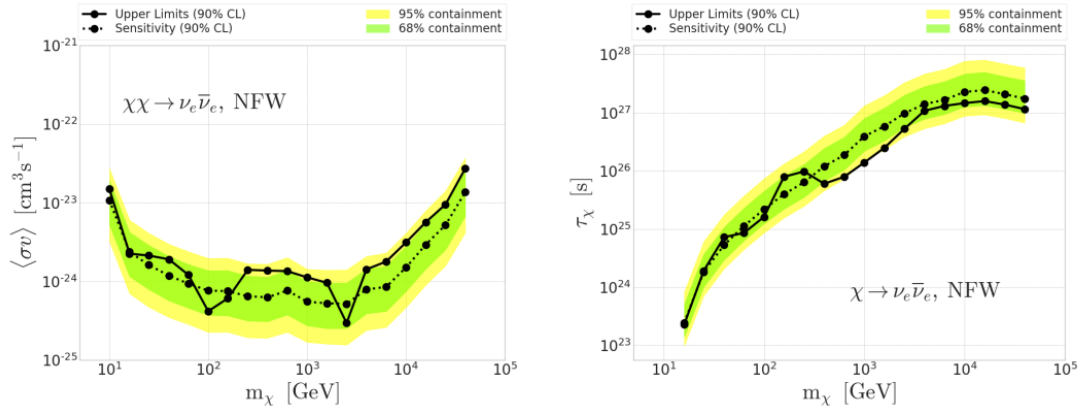

Figure 2.20: Constraints on DM from galactic neutrinos in Ref. [119]. Left panel: upper limits (solid line) and sensitivity (dotted line) at 90% C.L. on the thermally averaged self-annihilation cross section of the $\nu_e\bar{\nu}_e$ channel and NFW profile. Right panel: lower limits (solid line) and sensitivity (dotted line) at 90% C.L. on the decaying DM lifetime of the $\nu_e\bar{\nu}_e$ channel and NFW profile. Constraints are plotted as functions of the DM mass, together with the 1σ (green) and 2σ (yellow) containment bands representing the expected sensitivity. Plots from Ref. [119].

Similarly to gamma rays, a spectral line-like feature can be searched in the spectra of galactic neutrinos. The mechanism originating this feature is the same illustrated in the case of gamma rays (see Sec. 2.3.3). Like gamma rays, neutrinos are not deflected by magnetic fields, and point back to their sources. In addition, they undergo much less absorption with respect to gamma rays, especially at very high energies. Therefore neutrinos are a powerful probe to detect distant sources, even though they are embedded in dense environments.

In the work at Ref. [119], a total of five years of IceCube DeepCore data were analyzed to probe DM masses in the range from 10 GeV to 40 TeV. No significant neutrino excess was observed, and upper limits on the annihilation cross section as well as lower limits on the DM lifetime were derived, as shown in Fig. 2.20. The constraints obtained reach values down to $10^{-25} \div 10^{-24}$ cm^3 s^{-1} for the velocity-averaged DM annihilation cross section and up to 10^{27} s for the DM lifetime.

2.4.4 Neutrinos from galaxy clusters and dwarf spheroidal galaxies

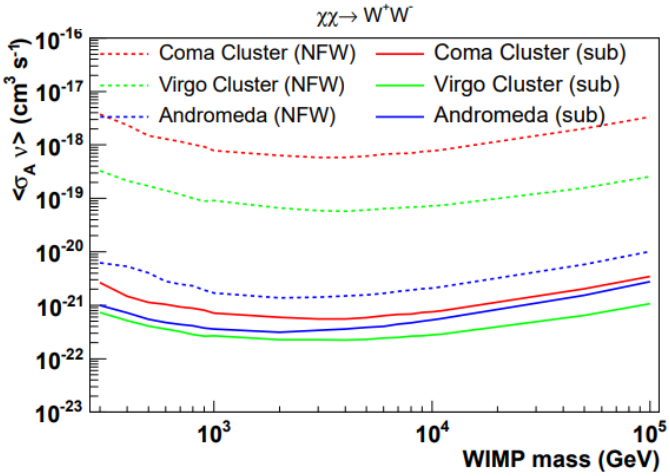

Figure 2.21: 95% CL Upper limits on annihilation into W^+W^- for the Coma and Virgo clusters and for the Andromeda galaxy. Dashed lines assume pure NFW profiles, while solid lines include subhalo contributions (denoted with "sub"); sensitivity curves differ from the limits by multiplicative factors given in Ref. [120]

.

As discussed above, both galaxy clusters and dSphs are considered to be attractive targets for DM indirect search because of their predicted high DM densities, low intrinsic luminosity, and the lack of known background processes capable of generating high-energy neutrinos. At energies above 100 TeV the gamma-ray horizon is limited at a few kpc due to absorption; on the other hand, neutrinos can travel for much longer distances, allowing to probe even very distant

sources.

In a 2013 work [120], the IceCube collaboration performed a search for DM in three types of astrophysical targets: dwarf galaxies, galaxy clusters and the Andromeda spiral galaxy, whose DM halo is well understood [121] and could provide insights about our own galaxy. Upper limits are obtained on the annihilation cross-section as a function of WIMP mass in the range from 300 GeV to 100 TeV, for the annihilation channels $b\bar{b}$, W^+W^-, $\tau^+\tau^-$, $\mu^+\mu^-$, and $\nu\bar{\nu}$. Fig. 2.21 shows upper limits on annihilation into W^+W^- for the Coma and Virgo clusters and the Andromeda galaxy, highlighting the impact of incorporating subhalo boost factors, which account for DM substructures in the halo with a standard parametrization of the J-factor (also mentioned in Sec. 2.3.5) for galaxy clusters searches for DM, with the strongest constraint obtained for the Virgo cluster, followed by Andromeda.

2.5 Searching dark matter in cosmic rays: The rising positron fraction

Local cosmic-ray fluxes exhibit an anomalous rise in the positron fraction $n_{e^+}/(n_{e^+} + n_{e^-})$ from 10 GeV to at least 100 GeV. This feature was first observed in the PAMELA data [123], and subsequently confirmed by the Fermi LAT [124] and by AMS-02 [122].

The rise in the positron fraction is not expected by the conventional models describing secondary Galactic CRs, which predict a drop in the positron fraction above 10 GeV. A possible explanation is that of a nearby source injecting high-energy positrons. DM annihilations or decays are among the possible options, although pulsars have also been proposed as the responsible of the e^+ excess [125]. Both DM clumps and pulsars, indeed, are thought to be sources of e^+ e^- pairs injection, and both should be located sufficiently close to Earth to account for the observed high-energy positrons.

However, a DM origin of the positron excess would imply a cut-off in the

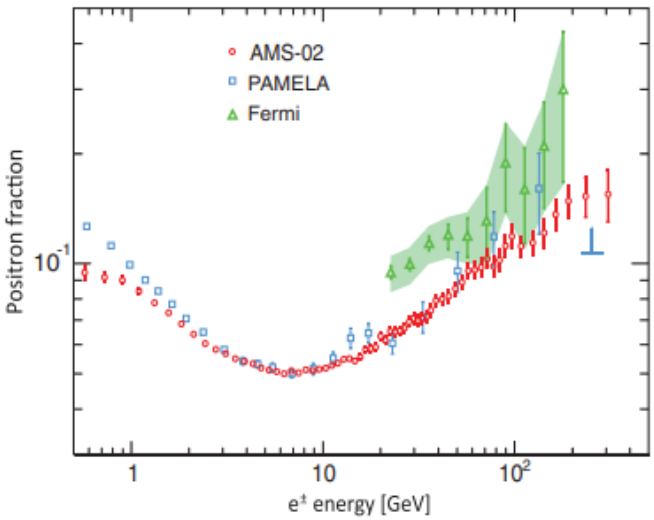

Figure 2.22: Positron fraction measured by AMS-02 [122], PAMELA [123] and Fermi-LAT [124].

energy spectrum of the cosmic-ray positrons[10]at the DM particle mass (or half mass in the case of decay); on the other hand, if multiple pulsars are the source of the additional positrons, several spectral features would be expected, due to the different cut-offs in the spectra of individual pulsars. These features should be observed, but the results of the researches mentioned above are inconclusive as far as settling the origin of the excess is concerned.

A possible way to identify the sources of the positron excess is the detection of anisotropies in the arrival directions of both positrons and electrons. Indeed, as it was pointed out in the work from the *Fermi*-LAT collaboration at Ref. [124], if a single nearby source (like a pulsar) was the only responsible of the positron excess, despite significant loss of directional information due to diffusion, an anisotropy should be observed in the angular distribution of the positron (or electron and positron) fluxes. Such an anisotropy might appear even in the case of multiple sources, dominated by the nearest, strongest one. If the excess was generated by a

[10]DM annihilation or decay injects equally e^- and e^+, however while electrons have primary injection sources in many objects like SNRs, pulsars etc., positrons are produced mainly in hadronic interactions of cosmic-ray protons and nuclei with the ISM.

DM clump near our planet, only a very small anisotropy would be detected in the direction of the GC[11], while a pulsar-induced anisotropy could be much stronger and in any direction. The upper limits set by the *Fermi*-LAT collaboration in Ref. [124] cannot exclude neither the pulsar origin nor the DM origin.

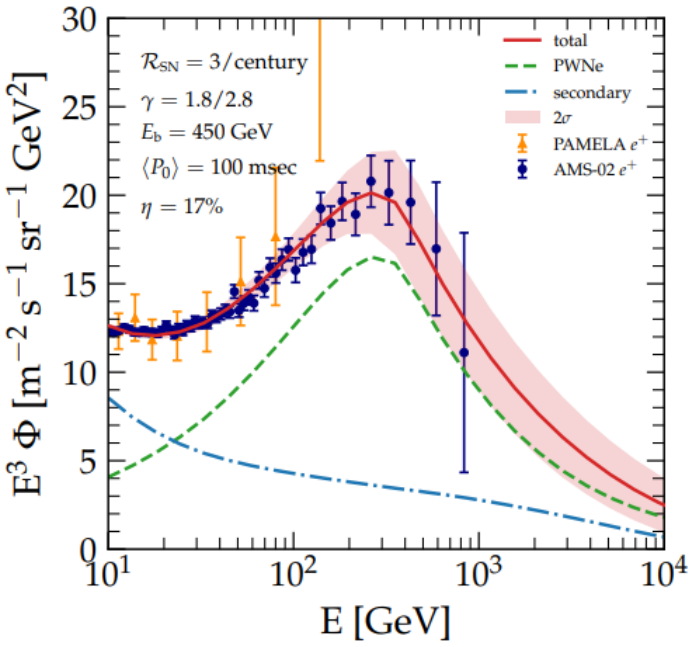

Figure 2.23: Positron spectrum from the combined contribution of all Galactic PWNe with a broken power-law injection ($\gamma = 1.8$ below and $\gamma = 2.8$ above $E_b = 450$ GeV). Secondary positrons are shown separately (dash-dotted blue line). The total spectrum is given by the solid red line. Plot from Ref. [127].

More recent studies seem to support more the pulsar-origin scenario, such as in Ref. [127]. In Fig. 2.23, the flux of positrons resulting from the superposition of stochastically generated pulsars following the spiral structure of the Galaxy is reported. The position of the break very well agrees with what deduced from observations of nonthermal emission from Pulsar Wind Nebulae (PWNe), accommodating the possibility that the rising positron fraction may be due to positron injection from PWNe, whose wind is indeed made up of e^+e^- pairs. In

[11] A local clump embedded within the larger DM halo would remain nearly isotropic, with at most a subtle alignment toward regions of higher DM density, i.e. the GC [126].

conclusion, the authors claim that the spectrum of positrons is very well described by the contribution of pulsars and the rising positron fraction originates naturally.

Chapter 3

Spaceborne gamma-ray telescopes and the *Fermi* Mission

In this chapter, some of the past, current and future spaceborne gamma-ray instruments are illustrated, with a particular focus on the *Fermi* Large Area Telescope (LAT), since it collected the data analyzed in this thesis. Therefore, most of the information reported in this chapter has been adapted from the Fermi Science Support Center (FSSC) website [128].

3.1 A bit of history: Vela and EGRET

The first recorded instrument to consistently perform measurements of gamma rays on board of a satellite was installed on the *Explorer-11* [129] launched in 1961, and enabled the measurement of the intense gamma-ray emission from Earth's atmosphere. Then, the counter telescope on the *Orbiting Solar Observatory-3 (OSO-3)* [130], launched in 1967, succeeded in demonstrating gamma-ray emission above 50 MeV from the galactic disk.

The subsequent generation of high-energy telescopes were not only able of just recording the passage of e^+e^- pairs in scintillators, but featured detectors to image the interactions of incoming photons and their secondary particles in greater detail

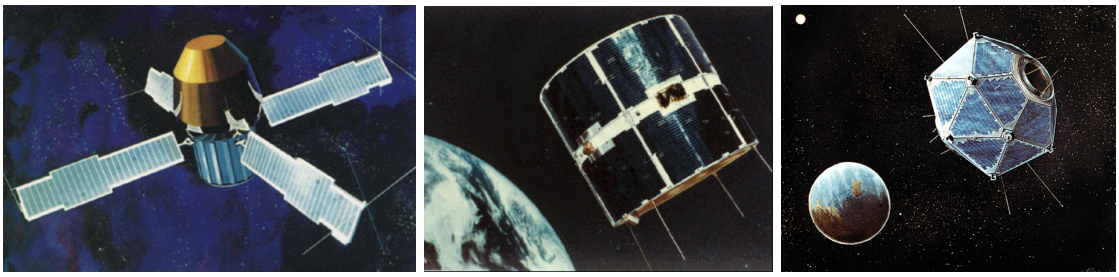

Figure 3.1: Artistic renditions of the SAS-2 (left), COS-B (center) and one of the VELA satellites, VELA-5B (right). Images from NASA and ESA

by means of digital wire spark chambers. Such telescopes were the one onboard of the *Small Astronomy Satellite-2 (SAS-2)* [131], launched in 1972, and the one onboard the *Celestial Observation Satellite-B (COS-B)* [132], launched in 1975, artistically rendered in the first 2 panels of Fig. 3.1.

It is worth to remark here that the early developments of gamma-ray astronomy were mainly driven by strategic motivations. In fact, when the Nuclear Test Ban Treaty negotiated by USA, USSR and Great Britain was signed in 1963, the US started the *Vela* (spanish for "Watchman") project, which consisted of a series of satellites carrying X-ray and gamma-ray detectors to observe possible signatures of nuclear explosions, monitoring the compliance with the treaty. In July 1967, Vela 4 detected a flash of mysterious gamma rays, but it was not able to deduce the exact origin of this radiation. The main concern was to assess whether the signature was identifiable with a nuclear detonation, which was not, but its nature remained a mystery for a while. However, the detectors onboard Vela-5A and B (1969) and Vela-6A and B (1970) had the timing accuracy necessary to reconstruct the source direction through differences in the arrival photon times, and excluded the Earth, the Moon and the Sun as possible sources. It was then understood, by the observation of further similar events [133], that the event of July 1967 was a GRB, the first ever detected.

Launched in 1991, NASA's Compton Gamma Ray Observatory (CGRO) [134] marked a pivotal point in gamma astronomy history. This spacecraft mounted 4 different instruments, each one specialized in different bandwidths of the electromagnetic spectrum. Particularly relevant is the gamma-ray telescope

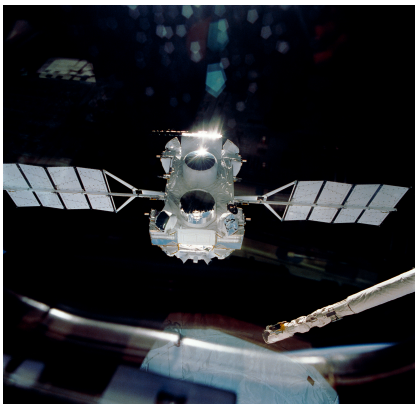

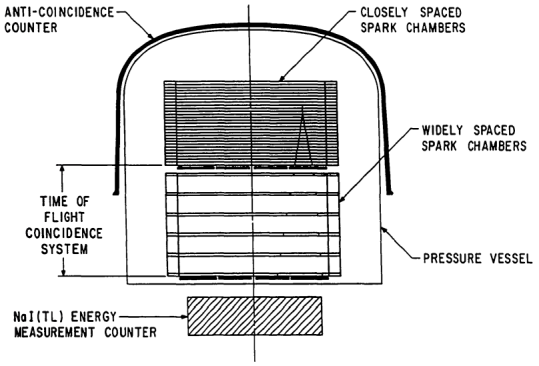

Figure 3.2: NASA'S CGRO (Credits: NASA), with a schematic view of EGRET instrument (right), taken from [135].

which was mounted onboard the CGRO, the Energetic Gamma Ray Experiment Telescope (EGRET) [135].

EGRET is a multilevel spark chamber telescope designed for gamma-ray detection above approximately 20 MeV, with an acceptance for incident photons up to $\sim 40°$ from the detector axis. The instrument employs a scintillator-based coincidence trigger system and uses a large NaI(Tl) Total Absorption Shower Counter (TASC) as its primary device for energy measurement. In its operational concept, EGRET builds upon the successful design of earlier gamma-ray missions such as SAS-2 [131] and COS B [132], but features a significantly larger and more advanced configuration.

Gamma rays are detected via pair production in the active region of the instrument. Incident photons do not interact with the outer anticoincidence scintillator shield. If a photon converts into an e^+e^- pair within one of the tantalum foils, interleaved among the upper spark chamber modules, the resulting charged particles may trigger the internal coincidence system. This system comprises a 4×4 array of plastic scintillator tiles located both mid-chamber and at the bottom. A valid trigger requires a preset combination of tile activations along with a time-of-flight signature consistent with downward-traveling particles. When these conditions are met, a high-voltage pulse is applied to the spark chamber, initiating both the spatial track readout and energy data acquisition. EGRET,

in particular, carried out the first all-sky survey at energies above 50 MeV and achieved breakthrough observations of high-energy gamma-ray phenomena, including blazars, pulsars, delayed emission from gamma-ray bursts (GRBs), high-energy solar flares, and diffuse radiation from both our Galaxy and extragalactic sources [135]. BATSE [136], on the other hand, focused on the detection of Gamma-Ray Bursts (GRBs).

3.2 From GLAST to *Fermi*

Scientific motivations for what would become *Fermi* mission root in the impressive goals achieved by EGRET and BATSE instruments onboard the Compton Gamma Ray Observatory spacecraft (CGRO) [134]. A substantial fraction of the sources detected by EGRET was still unidentified by the end of its operational life, hence the need for an observatory that not only could identify them, but also give a full coverage of the gamma-ray sky in a few hours.

On June 11^{th} 2008, the *Fermi* satellite was launched from Cape Canaveral with a Delta 2920H-10 (also known as a Delta II "Heavy") rocket. This date marks the beginning of the *Fermi* mission and of present day gamma-ray astronomy. At the beginning, the mission was named "*Gamma-ray Large Area Space Telescope (GLAST)*". Once all systems proved to be operational, in August of the same year, the official data-taking started and the mission was renamed *Fermi Gamma-ray Space Telescope (FGST)*, honoring Enrico Fermi's unvaluable contributions to high-energy astrophysics. The mission was designed for a lifetime of at least of 5 years, with a goal of 10 years. Actually, Fermi is still taking data and the mission has been extended more than once because of its remarkable scientific results. *Fermi* is orbiting around the Earth at an altitude of 565 km (Low-Earth Orbit, LEO), with an inclination of 25.6° from the Equator and an orbital period of about 90 minutes.

Fermi observes gamma-ray emission across the entire celestial sphere, with a sensitivity more than 30 times greater than that of previous gamma-ray missions, allowing for a significantly deeper survey of the high-energy sky. The mission

Figure 3.3: Top left panel: Fermi being prepared for launch at Cape Canaveral. Top right panel: schematic view of the Fermi satellite components and instruments. Lower Panel: artistic representation of *Fermi* spacecraft, Credit: NASA's Goddard Space Flight Center/Chris Smith (USRA/GESTAR), taken from [137]

has enabled major advances in high-energy gamma-ray astrophysics, thanks to substantial improvements in angular and energy resolution, timing accuracy, effective area, field of view (FOV), and energy coverage with respect to its predecessors.

The *Fermi* observatory is equipped with two primary instruments: the Large Area Telescope (LAT) and the Gamma-ray Burst Monitor (GBM). Both instruments feature exceptionally wide fields of view (FOVs): 2.4 sr at ~ 1 GeV

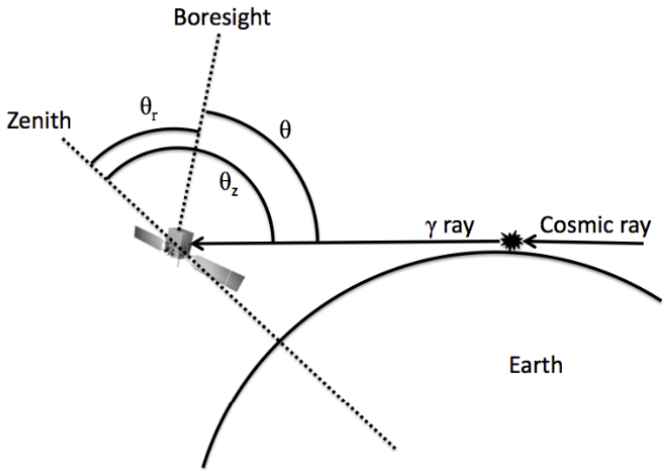

Figure 3.4: Sketch representing the Earth's limb gamma-ray emission where both the zenith angle θ_Z and rocking angle θ_r are shown. Taken from [50].

for the LAT [138], which corresponds to $\sim 55°$ on the celestial sphere, and > 8 sr for the GBM [139], meaning $> 106°$ on the celestial sphere, enabling broad sky coverage. The mission was originally designed with a high degree of flexibility in its pointing capabilities; however, this functionality has been partially constrained since 2018 due to the failure of a solar-array drive motor (see Sec. 3.2.1).

The Earth imposes an observational constraint on the pointing direction of the *Fermi* observatory. As the Earth itself is a significant source of gamma rays, the LAT FOV must generally avoid Earth occultation (see Fig. 3.4). Nonetheless, observations of the Earth's limb are occasionally performed for the detection of albedo gamma rays or for instrument calibration purposes.

Additional constraints arise from engineering considerations, including thermal requirements for the LAT cooling radiators, the battery radiators, and the orientation of the solar panels, particularly during slewing maneuvers.

Moreover, no scientific data are collected while the spacecraft passes through the South Atlantic Anomaly (SAA)[1], as the instruments reduce the voltage on the

[1]The SAA is a region above the South Atlantic where the Earth magnetic field is weaker, resulting in an increased flux of trapped charged particles. At the *Fermi* orbital altitude and 25.6° inclination, SAA crossings lead to a loss of approximately 15% of the potential observing time for both LAT and GBM instruments.

photomultiplier tubes (PMTs) to protect sensitive components.

The *Fermi* spacecraft is capable of operating in multiple observational modes, among which the two most relevant are the sky-survey mode and the Target Of Opportunity (TOO) pointing mode. Transitions between these modes can be initiated either via ground commands or autonomously by the spacecraft.

Before 2018, the LAT was able to autonomously trigger a repointing of the spacecraft in response to the detection of a gamma-ray burst (GRB), switching to TOO mode in order to monitor the burst location and capture follow-up emission. However, following the failure of a solar-array drive motor in 2018, this autonomous repointing functionality has been severely restricted and is no longer employed in current operations. Nevertheless, it is important to note that, when scientifically justified, the LAT retains the ability to perform pointed observations towards a specific target. Although the 2018 solar-array drive anomaly did not eliminate this capability, it has made such operations more resource-intensive and less efficient. Pointed mode operations may be preferable in some contexts, such as pulsar timing studies, where minimizing the impact of rotational period variations is critical, or in cases where rapidly accumulating exposure on a target within a limited time frame is essential.

In survey mode, which currently accounts for virtually all of the *Fermi* observing time, the LAT maintains its pointing relative to the zenith direction (i.e., away from the Earth), resulting in a continuously changing orientation with respect to the celestial sphere. To ensure uniform sky exposure, the spacecraft employs a *rocking* strategy, in which the LAT's pointing is alternately tilted perpendicular to the orbital plane. Under the default configuration, the instrument axis is rocked by approximately 50° north of the orbital plane during one orbit, and by 50° south during the next, producing a two-orbit periodic pattern. However, following the 2018 solar-array drive anomaly, modified rocking strategies with asymmetrical profiles have been adopted. These include increased rocking angles, up to a maximum of 60°, to maintain acceptable solar illumination on the panels. The primary figure of merit used to optimize a given rocking strategy is the uniformity of sky exposure. Nonetheless, this criterion may be adjusted as mission priorities

evolve.

3.2.1 The -Y SADA anomaly and related observation strategies

During the first decade of its mission, the *Fermi* satellite primarily operated in sky-survey mode, with the LAT pointing direction alternating between rocking angles of $+50°$ and $-50°$ relative to the zenith and perpendicular to the orbital plane—northward for one orbit, then southward for the next. This strategy enabled uniform sky coverage, allowing the entire celestial sphere to be observed approximately every 90 minutes. Less frequent Target of Opportunity (TOO) observations were interleaved within this baseline strategy.

On March 16^{th}, 2018, the Solar Array Drive Assembly (SADA) associated with the $-Y$ solar array—one of two solar panels onboard *Fermi*—experienced a malfunction (for a description of the spacecraft reference frame, see Sec. 3.4 and Fig. 3.11). Although the array itself remains operational, the drive mechanism can no longer rotate the panel.

To maintain a balance between adequate power generation and thermal stability, *Fermi*'s observing strategy was subsequently revised. The current operational mode depends on the angle β between the Sun and the orbital plane (see left panel of Fig. 3.5). This angle evolves both annually and with a periodicity of approximately 46 days, driven by the precession of *Fermi*'s orbit (right panel of Fig. 3.5).

At present day, *Fermi* operates under three distinct observing configurations, depending on the value of the β angle:

1. When $\beta < 14°$, the pre-anomaly sky-survey mode is still adopted. In this mode, the LAT rocking angle alternates symmetrically above and below the orbital plane, with a two-orbit repeat cycle.

2. For intermediate angles, i.e. $14° < \beta < 24°$, an asymmetric rocking pattern is employed: the LAT alternates between offsets of $50°$ in one direction and $60°$ in the other.

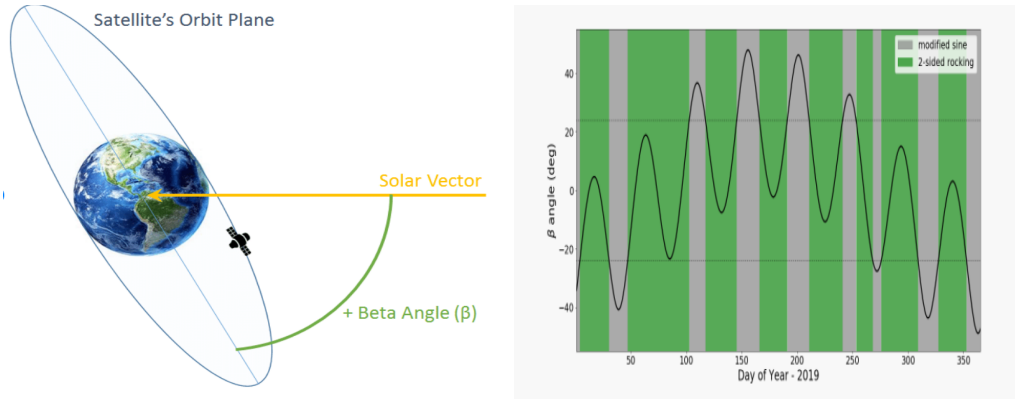

Figure 3.5: Left panel: diagram representing the β angle, i.e. the angle between the solar vector and the orbital plane of the satellite. Right panel: beta angle of the *Fermi* spacecraft during 2019 (taken from [140]). The β angle varies continuously, following both an annual cycle and the $\sim$ 46-day orbital precession period. The angle spans a range of nearly $\pm 50°$. The color scale indicates the observing mode in use: green for the symmetric two-sided rocking profile (used over two orbits), and grey for the asymmetric mode with sinusoidal rocking during orbital day and fixed offset during orbital night.

3. When $\beta > 24°$, a more complex rocking profile is implemented. During spacecraft day, the rocking angle follows a sinusoidal-like pattern relative to the orbital plane, reaching a maximum offset of 50° at orbit noon and decreasing to 0° near orbit "6 AM" and "6 PM". The sign of the rocking offset matches the sign of the β angle. During orbital night, the LAT maintains a fixed offset of 50° in the opposite direction to that used during orbital day. Unlike the pre-anomaly profile, this configuration has a one-orbit periodicity.

The exposure maps corresponding to the three observing modes are presented in Fig. 3.6. In modes 1 and 2, the sky coverage remains comparable to the pre-anomaly configuration. However, in mode 3, some regions of the sky exhibit reduced exposure. As a result, complete sky coverage can still be achieved approximately every three hours (i.e., two spacecraft orbits) under observing modes 1 and 2. In contrast, when operating in mode 3, full sky coverage is no longer attainable on such short timescales and typically requires up to one week to be completed.

Under these circumstances, it is expected that most Target of Opportunity (TOO) observations will no longer be feasible under the current operational regime.

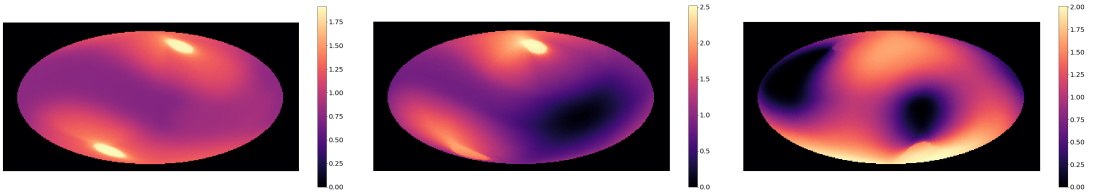

Figure 3.6: Exposure maps corresponding to the 3 possible rocking profiles of *Fermi* spacecraft. All maps report an exposure normalized to the average, projected onto an AITOFF coordinate system.**Left panel**: exposure map corresponding to the symmetric $\pm 50°$ rocking profile, which characterized the majority of the *Fermi* mission and enables complete sky coverage within approximately three hours. **Middle panel**: exposure map for the asymmetric $+50°/-60°$ profile, which maintains full-sky coverage within two orbits, though the maximum exposure reaches only about 85% of the uniform coverage. **Right panel**: exposure map obtained using the partial sinusoidal $50°$ rocking profile, associated with the post-anomaly mode 3 configuration. Maps taken from [141].

3.3 The Gamma-ray Burst Monitor (GBM) instrument

The Gamma-ray Burst monitor (GBM), which consists of 12 NaI(Tl) and 2 BGO crystal scintillators (see Fig. 3.7), is mainly aimed to the observations of transient sources in the $8\,\mathrm{keV} - 40\,\mathrm{MeV}$ energy range [139].

The NaI(Tl) detectors, depicted in the left panel of Fig. 3.7 are designed to measure low-energy gamma-ray spectra in the range from $8\,\mathrm{keV}$ to $1\,\mathrm{MeV}$ and are employed to determine the directions of gamma-ray bursts (GRBs). Each detector consists of a thallium-doped sodium iodide crystal disk with a diameter of $12.7\,\mathrm{cm}$ and a thickness of $1.27\,\mathrm{cm}$. The crystals are enclosed in hermetically sealed, light-tight aluminum housings to prevent moisture absorption, as NaI is highly hygroscopic. A $0.6\,\mathrm{cm}$ thick NBK-7 glass window with a diameter of $12.7\,\mathrm{cm}$ is attached to the housing to accommodate the photomultiplier tube (PMT), secured using white Araldite adhesive. The detector entrance window consists of a $0.2\,\mathrm{mm}$ thick beryllium sheet to ensure sensitivity at low photon energies. For mechanical stability, an additional $0.7\,\mathrm{mm}$ thick silicone layer is positioned in front of the crystal, setting the effective low-energy detection threshold at approximately $8\,\mathrm{keV}$. To maximize light collection efficiency, the crystals are wrapped in a

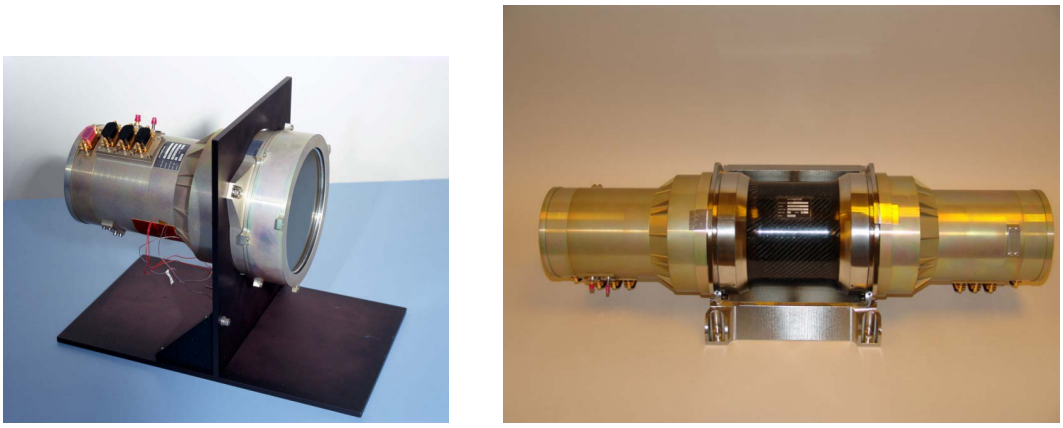

Figure 3.7: Left: NaI(Tl) crystal scintillator unit. Right: BGO crystal scintillator unit. The photos are taken from ref. [139]

reflective coating—Tetratec on the entrance-window side and Teflon around the circumference.

The BGO detectors, depicted in the right panel of Fig. 3.7, operate over an energy range from approximately 200 keV to 40 MeV, overlapping with the NaI(Tl) detectors at low energies and with the LAT at higher energies. This overlap enables effective cross-calibration across instruments. Each BGO crystal is a cylinder with a diameter and length of 12.7 cm. The circular end faces of the crystal are polished to ensure optical quality, while the cylindrical surface is deliberately roughened to enhance diffuse reflection of the scintillation photons. The crystals are enclosed in a carbon-fiber reinforced plastic (CFRP) housing, which ensures both mechanical robustness and light tightness. The housing is held in place by two titanium support rings. Titanium is used due to its thermal expansion coefficient being closely matched to that of BGO, minimizing thermal stress. PMTs are mounted at both ends of each crystal, coupled via the titanium rings. This dual-PMT configuration enhances light collection efficiency and provides redundancy in case of component failure. The whole BGO assembly is mounted within a titanium shell-type holding structure that secures the detectors to the spacecraft frame.

The primary goal of the GBM is the joint analysis of energy spectra and time histories of Gamma Ray Bursts (GRBs). Further objectives include provision

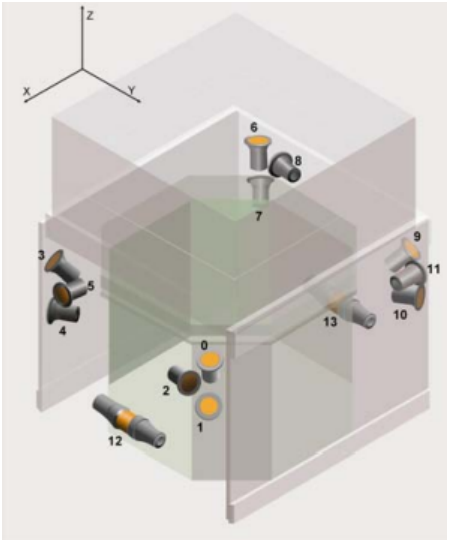

Figure 3.8: Schematic of the GBM detectors positioning on *Fermi* observatory. From [139].

of real time burst locations onboard to enable repointing of the spacecraft to allow LAT observations of delayed emission (afterglow), and to rapidly share the burst locations to the community of ground-based observers, in synergy with the Gamma-ray Coordinates Network (GCN) [142].

The ability of GBM in localizing transient phenomena relies on the positioning of the scintillators (see Fig. 3.8). The axes of the NaI detectors are oriented such that the positions of GRBs can be derived from the measured relative counting rates, a technique previously employed by BATSE [136]. The BGO detectors are positioned on opposite sides of the spacecraft so that any burst above the horizon will be visible by at least one of them.

The physical response of the GBM instrument, encompassing both the individual detector characteristics and the structural influence of the *Fermi* spacecraft, is characterized through detailed Monte Carlo simulations [139], complemented and validated by on-ground calibration campaigns. Extensive calibration and characterization of all flight and spare detectors were carried out at the Max Planck Institute for Extraterrestrial Physics (MPE) in 2005. During these campaigns, the detectors were irradiated in the laboratory using calibrated radioactive sources spanning an energy range from 14 keV to 4.43 MeV [143].

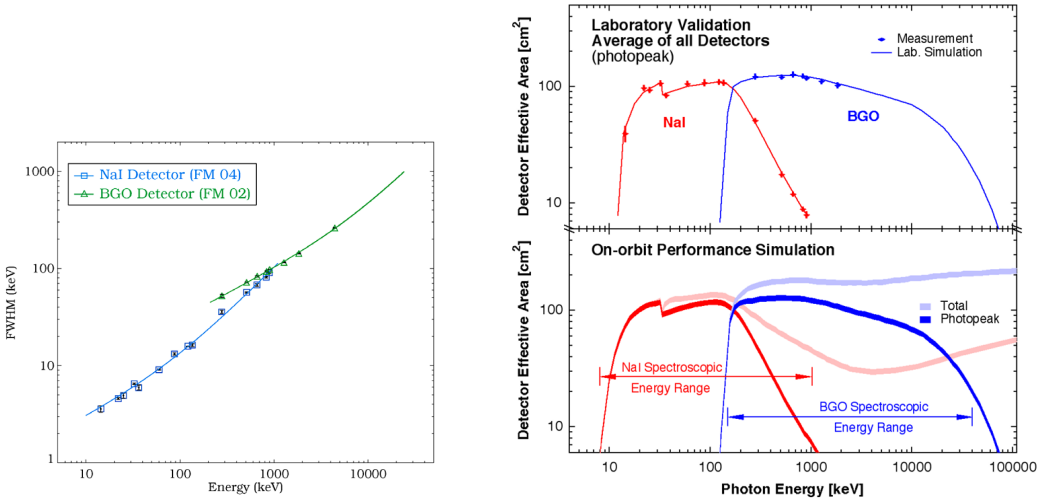

Figure 3.9: Left panel: Energy resolution as a function of photon energy for the NaI detector (square markers) and the BGO detector (triangle markers). **Right panel:** Effective area as a function of photon energy at normal incidence for both detector types. The plot in the lower-right part illustrates the simulated impact of the spacecraft structure on the response of a representative detector. Plots from [139].

Due to the limited number of emission lines from standard radioactive sources below 100 keV, additional calibration data in the 10–60 keV range were acquired in collaboration with the X-ray radiometry group of the Physikalisch-Technische Bundesanstalt (PTB) at the BESSY synchrotron facility in Berlin.

The left panel of Fig. 3.9 illustrates the energy resolution as a function of photon energy for representative NaI and BGO detectors. The energy dependence of the effective area at normal incidence is presented in the right panel of Fig. 3.9 for both detector types, together with the corresponding simulated responses. The on-orbit simulations account for the effects of spacecraft obstruction and photon scattering. In certain energy ranges above a few hundred keV, the total effective area is noticeably enhanced due to photons that are scattered off the spacecraft structure into the detectors.

3.4 The Large Area Telescope (LAT)

The Large Area Telescope (LAT) is the primary instrument onboard the *Fermi* satellite. It is a pair-conversion gamma-ray telescope capable of detecting photons with energies ranging from approximately 20 MeV to beyond 300 GeV [138].

The LAT is composed of a 4×4 array of identical towers, each consisting of a converter-tracker (TKR, see Sec. 3.4.1) and a calorimeter (CAL, see Sec. 3.4.2). Surrounding the tower array is a segmented anticoincidence detector (ACD, see Sec. 3.4.3) made of plastic scintillator tiles, which provides rejection of the charged cosmic-ray background. The overall dimensions of the instrument are $1.8\,\mathrm{m} \times 1.8\,\mathrm{m} \times 0.72\,\mathrm{m}$. Its wide field of view (FoV), approximately 2.4 sr, primarily results from its favorable aspect ratio (height-to-width ~ 0.4).

The detection system is equipped with a dedicated data acquisition system (DAQ, see Sec. 3.4.4), which manages onboard triggering and performs preliminary data filtering. Data are downlinked to Earth approximately every three hours, corresponding to two full satellite orbits.

A major advantage of the LAT over previous gamma-ray instruments lies in its long-term operational reliability. Earlier detectors such as EGRET relied on a noble gas-hydrocarbon mixture for the spark chamber detector, which not only needed to be changed almost every year to limit performance degradation, but also slowly escaped from the pressurized chamber hosting the instrument. Its operational life lasted nine years [135]. The LAT was designed without the need of any components subject to draining up, replacing the spark chamber tracker with a solid state detector, which enabled it to remain fully operational for over 17 years.

Figure 3.10 provides an exploded view of a TKR tower and a CAL tower. The ACD tiles, shown in grey, are enclosed by a thermal blanket, which is rendered in yellow. In an ideal detection scenario, an incoming gamma ray passes through the ACD and undergoes pair production in the TKR, generating an electron-positron pair. This pair then enters the CAL, where it triggers an electromagnetic shower.

Figure 3.11 illustrates the local reference frame of the LAT. The xy-plane coincides with the base of the TKR, with its origin at the center of the instrument.

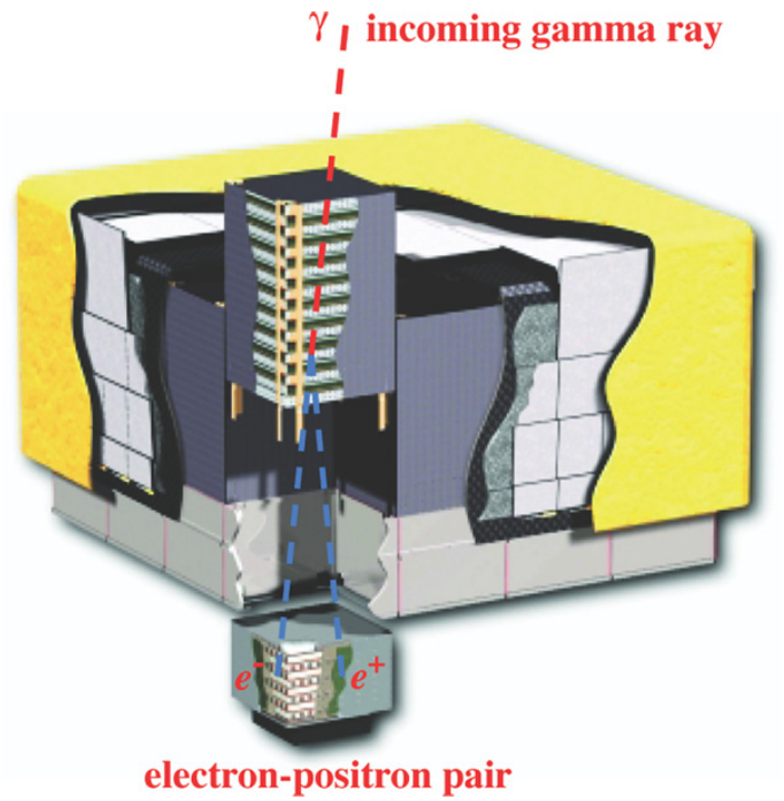

Figure 3.10: Schematic view of the Large Area Telescope (taken from [138]). Gamma-rays pass through the ACD, convert in the TKR, and produce electromagnetic showers in the CAL.

The x-axis is oriented perpendicular to the spacecraft's solar panels and typically points toward the Sun. The angle θ denotes the off-axis angle between the incident photon direction and the z-axis, whereas ϕ represents the azimuthal angle, i.e., the angular separation between the projection of the incident direction onto the xy-plane and the x-axis [144].

3.4.1 The pair conversion tracker system (TKR)

The Tracker-Converter (TKR) subsystem of the LAT consists of 16 identical towers, each with a cross-section of 37.3 cm × 37.3 cm and a height of 66 cm. Within these modules, high-energy gamma rays primarily interact via pair production, resulting in the creation of e^+e^- pairs [145]. Fig. 3.12 shows the schematic of a pair production event inside a TKR tower, that is also depicted on the right

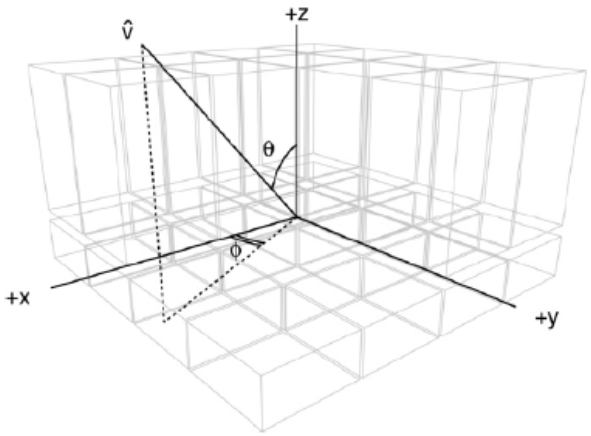

Figure 3.11: LAT coordinate system. θ is the off-axis angle with respect to the z-axis, and ϕ is the azimuthal angle in the xy-plane relative to the x-axis (oriented toward the Sun). The solar panels lie along the y-axis. (taken from Ref. [144]).

panel of the same figure, where one of the shield panels was removed to display the readout electronics arrangement.

Each module in the TKR system is designed to optimize the conversion of incoming gamma rays into e^+e^- pairs and track them to reconstruct the impinging photon direction. To enhance pair production, each module includes 16 tungsten foils, which is a high Z material.

The trajectory of these charged particles is reconstructed using 18 tracking planes, each consisting of two orthogonal layers of single-sided silicon strip detectors (SSDs).

Each SSD plane is composed of 16 *wafers*, each with an active area of $8.95 \times 8.95\,\mathrm{cm}^2$ and a thickness of $400\,\mu$m. The wafers are segmented into 384 strips, each $56\,\mu$m wide, with a strip pitch of $228\,\mu$m. Four wafers are bonded together edge-to-edge using epoxy glue and interconnected via wire bonding to form so-called *ladders*, allowing a single readout channel to collect signals from strips approximately 36 cm long. Each plane consists of four such ladders, separated by 0.2 mm gaps.

The SSD layers and tungsten foils are assembled within support panels known as *trays*. Each tray is a rigid, lightweight carbon-composite panel, 3 cm thick, with SSDs mounted on both its upper and lower surfaces, oriented such that the strips

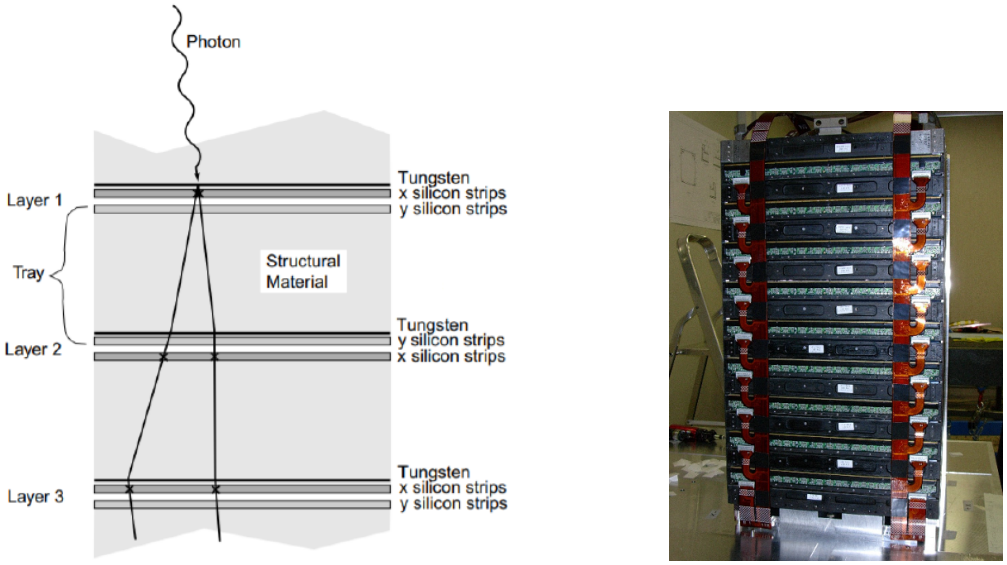

Figure 3.12: Left panel: schematic of a pair conversion inside the TKR . **Right panel**: photo of a TKR tower during its assembly. Taken from [138].

on opposite sides are aligned. A TKR tower consists of 19 stacked trays, with the strip orientation alternating by 90° from one tray to the next. The top tray contains only a lower SSD layer, while the bottom tray has only an upper SSD layer, resulting in a total of 18 xy detection planes per tower. Carbon-composite sidewalls provide thermal stability and mechanical strength to each tray.

To optimize performance across a broad energy range, the converter foils are arranged in sections of varying thickness. The upper 12 trays (the *front* section) include thin tungsten layers, each corresponding to 0.03 radiation lengths, minimizing multiple Coulomb scattering and enhancing angular resolution at low energies. The following 4 trays (the *back* section) use thicker converters (0.18 radiation lengths each) to increase the conversion efficiency for higher-energy photons. The final two trays are left without converter material to reduce scattering and improve the precision of the particle's entry point into the CAL.

As illustrated in Fig. 3.12, incoming gamma rays are most likely to convert into e^+e^- pairs within the tungsten foils, while the SSDs detect and track the resulting charged particles. The use of SSDs also grants the TKR subsystem a

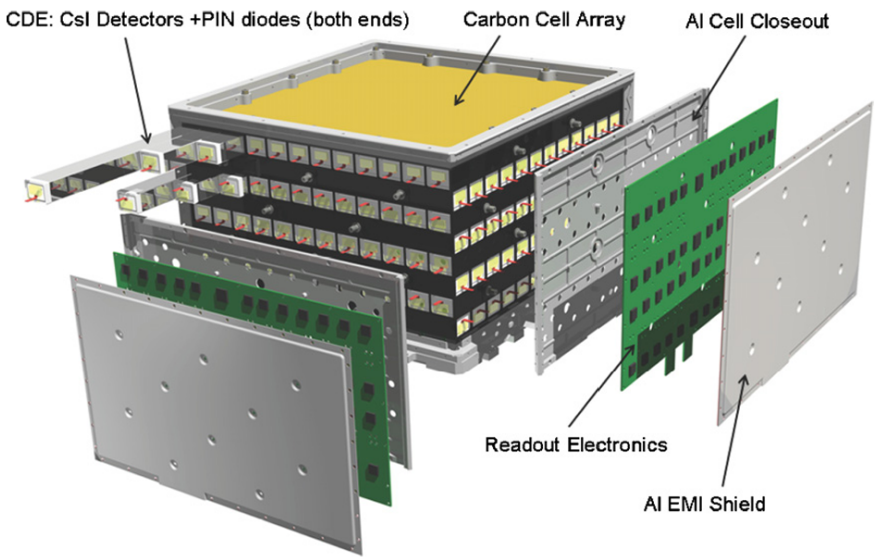

Figure 3.13: Exploded view of a CAL tower. Taken from [138].

self-triggering capability: one of the Level-1 triggers is activated by a coincidence of signals in at least three consecutive x and y planes.

3.4.2 The hodoscopic electromagnetic calorimeter (CAL)

The CAL is composed by 16 identical towers, each equipped with 96 CsI(Tl) crystal bars, of 2.7 cm × 2.0 cm × 32.6 cm size, hodoscopically arranged in 8 layers of 12 crystals. Fig. 3.13 shows an exploded view of the CAL subsystem, showing the implementation of the Alluminum ElectroMagnetic Interference (EMI) shield and the PCBs for readout electronics as well. The crystals are suitably sized to ensure good imaging of the electromagnetic showers (the CsI radiation length and Moliere radius are respectively 1.85 cm and 3.8 cm). The total on-axis thickness of the CAL is of about 8.5 radiation lengths. To achieve 3D imaging, the crystals are arranged in layers with the bars in each layer disposed perpendicularly to those in the adjacent layers (see Fig. 3.13).

The scintillation light produced by the charged particles in each crystal is collected by PIN photodiodes placed at both sides of the bar. Each end is equipped with two photodiodes, with areas of 147 mm^2 and 25 mm^2 respectively, which

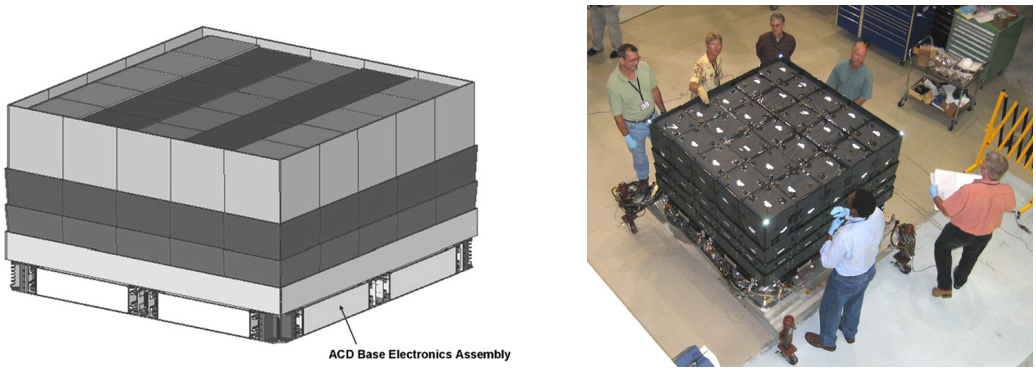

Figure 3.14: Left panel: Schematic of *Fermi*-LAT ACD subsystem , taken from ref. [138]. **Right panel**: photo of the ACD, freshly completed, taken from [146].

provide two readout channels to ensure coverage of the large dynamic range of energy depositions in the crystal. The position resolution achieved from the ratio of light collected at the two ends of a crystal scales with the deposited energy and ranges from a few mm for low-energy depositions ($\sim 10\,\mathrm{MeV}$) to a few hundred μm for large energy depositions (above 1 GeV).

3.4.3 The Anticoincidence Detector (ACD)

The ACD subsystem is aimed at discriminating photons from the large background of charged cosmic rays which continuously impinge on the apparatus. It consists of 89 plastic scintillator tiles surrounding the TKR and the uppermost layers of the CAL, with a total active area of $8.3\,\mathrm{m}^2$, arranged in a 5×5 array on the top face and in four arrays of 16 tiles on each side, as shown in Fig. 3.14.

Each scintillator tile is equipped with a read-out system consisting of wavelength shifting fibers embedded in the scintillator and connected to two photomultiplier tubes (PMTs) at both their ends. This arrangement enables a uniform collection of light that is typically better than 95% over each tile (except near the edges, where the uniformity drops to 75% at $1 - 2$ cm from them).

The tiles are overlapped in one dimension to achieve the minimization of the dead zones; in the other dimension, gaps between tiles are covered by flexible scintillating fiber ribbons with more than 90% detection efficiency.

In a typical gamma-ray event, the photon will pass through the ACD without

yielding any signal, and then will produce an e^+e^- pair inside the TKR system. The e^+e^- will then enter the CAL, where the electromagnetic shower will develop. Thus, a typical gamma-ray event yields signals in the TKR and CAL systems, but not in the ACD. Any event with a signal in the ACD could be, in principle, rejected since signals in the scintillators are originated by charged particles. However, showers initiated by high-energy gamma rays can include secondary charged particles entering in the ACD ("backsplash" effect), therefore issuing a veto on genuine gamma-ray events. This effect is relevant for high-energy photons ($E > 10\,\mathrm{GeV}$) and could affect the gamma-ray detection efficiency. The segmentation of the ACD allows to reduce the efficiency losses due to this effect: in fact, a veto is issued only if a signal is found in the ACD tiles near to the track of a photon candidate.

The ACD can reject background cosmic-ray events with 99.97% efficiency [146]. Furthermore, it can also be used for the identification of charged nuclei, since the energy loss (and consequently the scintillation light produced in the scintillators) depends on the charge as Z^2.

3.4.4 The Data Acquisition System (DAQ)

All subsystems produce a considerable amount of data collected by the DAQ system, which also provides onboard multilevel triggering and filtering, optimizing the downlinked event rate at $\sim 500\,\mathrm{Hz}$. This arrangement enables the management of the data analysis pipeline in such a way to handle a rapid search for transients effectively. Its hierarchical architecture is outlined in Fig. 3.15.

At the base level, each of the 16 Tower Electronics Modules (TEMs) interfaces with the TKR and CAL within a tower. Each TEM generates trigger primitives from the TKR and CAL signals, buffers event data, and communicates with the Event Builder Module (EBM), which is part of the Global-trigger/ACD/Signal-distribution Unit (GASU).

The GASU includes: (1) the Command Response Unit (CRU), responsible for command handling and clock distribution; (2) the Global-Trigger Electronics Module (GEM), which issues LAT-wide trigger decisions based on input from

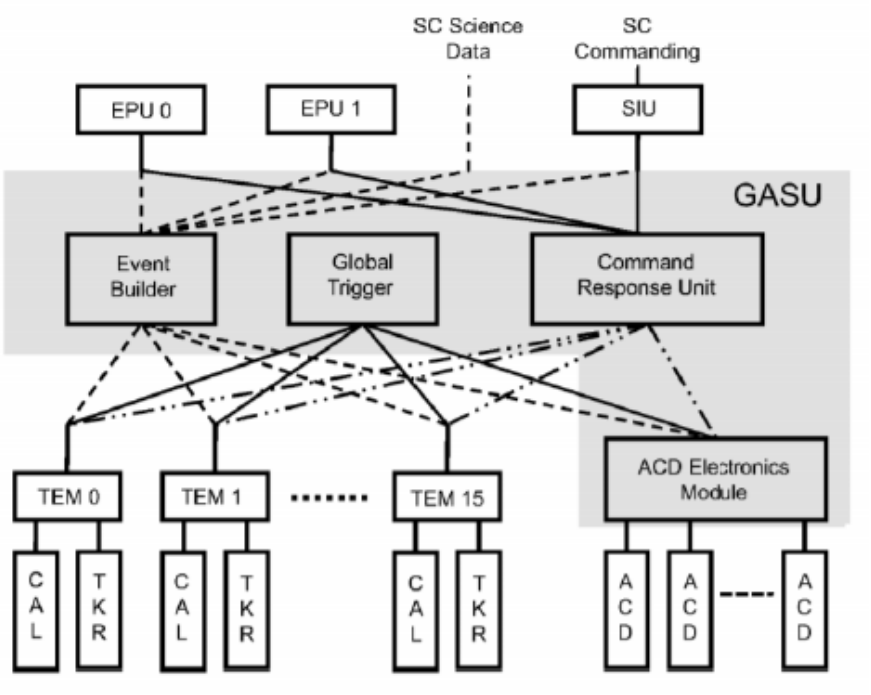

Figure 3.15: Schematic of the *Fermi*-LAT DAQ system architecture. From ref. [138]

the TEMs and the ACD; (3) the ACD Electronics Module (AEM), which works similarly to a TEM but for the ACD; and (4) the EBM, which builds complete LAT events from the TEMs and AEM and routes them to the Event Processing Units (EPUs).

Two EPUs are active and apply onboard filters to reduce the raw event rate of $2 \div 4$ kHz down to ~ 400 Hz for downlink. These filters suppress background events (mainly charged particles) while preserving gamma-ray signals. Both the EPUs and the Spacecraft Interface Unit (SIU), which handles LAT control and spacecraft communication, make use of RAD750 Compact PCI processors running at 115.5 MHz, delivering $80 - 90$ million instructions per second (MIPS). Flight software operates exclusively on the EPUs and SIU. TEMs and GASU components include software-controlled trigger and mode registers.

The DAQ system includes redundant units for fault tolerance: primary and backup EPUs, SIUs, and GASU units, along with a redundant Power Distribution

Unit (PDU). The PDU supplies power to the TEMs, EPUs, and GASU. The spacecraft powers the SIUs directly. TEMs control power to the tracker and calorimeter modules, while the GASU powers the ACD.

A trigger accept message (TAM) is issued by the GEM when its logic is satisfied within a programmable time window. The TAM is immediately broadcast to all TEMs and the AEM. Upon receiving the TAM, a Trigger Acknowledge (TACK) signal is issued after a configurable delay to the TKR and CAL front-ends (and similarly from AEM to the ACD), initiating readout of TKR hit addresses, CAL pulse heights (across 3072 channels), and ACD data (216 channels).

Triggers can originate in several ways: (i) when a TKR channel exceeds threshold, the TEM checks for a valid pattern, typically requiring hits in three consecutive (x, y) planes—and, if met, sends a trigger request to the GEM; (ii) if energy deposited in a CAL crystal surpasses preset low-energy (CAL-LO) or high-energy (CAL-HI) thresholds, the CAL module also sends a trigger to the GEM.

The ACD sends two types of prompt signals to the GEM: (i) a nominal 0.4 MIP threshold from each of the 97 scintillators (used to veto TKR-based triggers), and (ii) a high-level 20 MIP threshold signal from highly ionizing cosmic-ray nuclei (e.g., CNO group), primarily for calibration. The GEM can define up to 16 Regions of Interest (ROIs) from ACD tiles/ribbons for localized veto logic.

In addition to detector-based triggers, the GEM supports calibration and diagnostics through (i) periodic signals from the LAT system clock (20 MHz) or the spacecraft's 1 Hz GPS clock (accurate to $\pm 1.5\mu$s), and (ii) solicited trigger inputs for manual operation. The GEM internal time base is synchronized with the spacecraft clock for accurate event time-stamping.

The time delay between a particle interaction and the TKR discriminator latching is $2.3 \div 2.4$ μs, mostly due to analog rise times. CAL and ACD latching are similarly delayed (~ 2.5 μs) to match signal peaking. The minimum LAT readout dead time is 26.5 μs, dominated by GEM-to-EBM data transfer. Additional dead time may occur if full-range calorimeter readout is enabled. During any readout, active modules send "busy" signals to the GEM, which uses this information to

record and tag the dead time for each event.

The onboard event filtering is managed by two parallel EPUs, which perform real-time background rejection and γ-ray selection before data downlink. Each event is subjected to a series of veto tests that evaluate its consistency with the expected topology of a true gamma-ray interaction. Events failing any of these criteria are flagged for rejection, while those consistent with photon-induced pair production are retained for further processing. To implement these veto tests, the following onboard filters have been designed:

- **GAMMA:** selects γ-ray candidates and all events depositing more than 20 GeV in the CAL. This filter also accepts high-energy cosmic-ray electrons, yielding an average output rate of approximately 350 Hz;

- **Heavy Ions:** identifies heavy-ion candidates producing large energy deposits in the ACD, with an output rate of about 10 Hz;

- **MIP:** selects non-showering particles, primarily protons, for calibration purposes. This filter remains disabled during nominal science operations;

- **Diagnostic:** extracts an unbiased event sample used for performance monitoring and calibration of the onboard filters. The selected events are pre-scaled by a factor of 250.

Events passing the onboard filtering are subsequently downlinked for detailed ground-based reconstruction and analysis. To ensure full acceptance of genuine high-energy photons, all events depositing a total raw energy in the CAL exceeding 20 GeV are automatically accepted for downlink, bypassing the veto logic. These veto criteria were optimized through Monte Carlo simulations and extensive pre-launch calibration to balance efficient background suppression with maximum gamma-ray detection efficiency [138].

3.5 Pass 8 event reconstruction and classification

This section gives an essential description of the event reconstruction chain implemented by the *Fermi*-LAT collaboration. Detailed information can be found on the FSSC website [128] and in refs. [144] and [147]. The aim of the event reconstruction chain is to process raw data from the various subsystems into higher level data. The data available for the scientific community include a detailed event classification, based on the energy resolution, on the angular resolution and on other characteristics. The event-level analysis framework was designed and largely developed before launch, by means of Monte Carlo simulations, through a series of iterations called *"Passes"*: on-orbit experience has given the opportunity for several improvements with the purpose of greatly extend the LAT science capabilities, including the most updated data Pass, *Pass 8*. The newest version

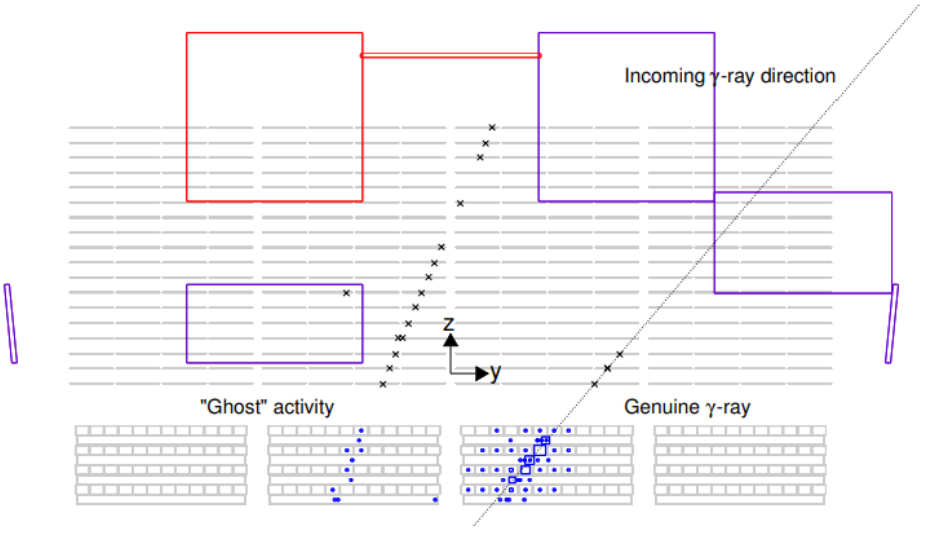

Figure 3.16: Example of a "ghost event" in the LAT (y–z view). In addition to an 8.5 GeV gamma-ray candidate (on the right) there is additional activity in all the three LAT subsystems, with the remnants of a charged-particle track crossing the ACD, TKR and CAL. The small crosses represent the clusters (i.e., groups of adjacent hit strips) in the TKR, while the variable-size squares indicate the reconstructed location of the energy deposition for every hit crystal in the CAL (the side of the square being proportional to the magnitude of the energy release) [144].

(Pass 8) of LAT data provides a number of improvements over the reprocessed

Pass 7 data: the main one consists in a detailed evaluation of the quality of the measurement of both direction and energy. This allows the user to select a subset of the events if it is thought to be appropriate to improve analysis results. The main purpose of Pass 8 redesign was to handle the so called *"ghost events"*. Indeed, soon after launch in 2008, it became apparent that the LAT was recording events that included the remnants of the signals from particles that traversed the detector a few μs before the particle issuing the trigger. An example of such an event is shown in Fig. 3.16. Data taking and processing follows a series of selections and cuts performed first on board of the observatory and then on ground, within the infrastructures which participate in the mission. *Fermi* sends data to the ground by means of the Tracking and Data Relay Satellite System (TDRSS). We can refer to the data at each passage with a tier number, i.e. "Level 0" data is the data sent by the spacecraft to the Mission Operation Center (MOC) hosted at Goddard Space Flight Center (GSFC) and managed by the Flight Operations Team (FOT). The MOC "cleans up" the telemetry, monitors the spacecraft through the housekeeping portion of the telemetry, and transmits it to the other ground system elements, i.e. the Instrument Operation Center (IOC) associated to the instrument onboard. Indeed, the LAT and the GBM have two different IOCs: the former is called LISOC (LAT Instrument Science and Operation Center) and is located at SLAC.

The IOC monitors the conditions of the instrument in real time and processes the data, creating event lists. This processing, in the case of LAT, is quite extensive: it starts with event reconstruction from the "hits" in the different LAT detectors and ends with a characterization of these events. These data are called "Level 1" data, and are publicly available on the FSSC website. Finally, the data can be processed by scientists using the "Science Tools" developed by the *Fermi*-LAT Collaboration and publicly available, obtaining "Level 2" data. As LAT data are public, the FSSC creates and posts count and exposure maps on weekly, monthly, and yearly timescales. Catalogs and compendia of "Level 2" data are considered "Level 3" products.

3.5.1 Track reconstruction

The track reconstruction code up to Pass 7 used a track-by-track combinatorial pattern-recognition algorithm to find and fit the two tracks representing the electron-positron pair in the TKR, and then combined them to form a vertex representing the photon conversion point. This approach turned out to be problematic for several reasons: one in particular, which is exacerbated by the presence of ghost events, is that the track-following algorithm needs an initial direction to start the track following and hit attachment. To reduce the number of potential hit combinations, it uses the reconstructed CAL energy centroid and the axis of energy flow to choose the initial hits, and this makes the efficiency of the track finding dependent on the accuracy of the CAL reconstruction: if the CAL reconstruction fails, because it is not correlated to the correct event but rather to ghost activity, this procedure yields incorrect results.

This and other features combine to produce three main effects: the loss of events for which reconstruction is failed, the migration of events from the core of the Point-Spread Function (PSF) to the tails, because of poorly reconstructed tracks, and increased confusion often resulting in mislabeling good gamma-ray events as background.

The Pass 8 reconstruction addresses these issues by introducing a global approach, called tree-based tracking, which looks at the conversion in the TKR as the start of a shower and attempts to model this process by linking hits together into one or more tree-like structures. Once the tree has been built, its axis can be found by calculating the moments of inertia of the associated hits.

Tests with Monte Carlo simulations and flight data show that the new tracker pattern recognition has significantly reduced the fraction of mistracked events and has provided a 15–20% increase of the high-energy acceptance, with an even larger improvement in the off-axis effective area, especially for photons converting in the lower part of the tracker [147].

3.5.2 Event classification

The next step of the event-level analysis is the event classification, which gives the different typologies of data handled in the analysis. Classification Trees (CTs) are used to select candidate gamma rays on the basis of the outputs yielded by the reconstruction procedures. Particle identification CTs are trained using variables from all the three LAT subsystems.

Events are classified according to their photon probability and the quality of their reconstruction. This classification separates events into classes, with each class characterized by its own set of Instrument Response Functions (IRFs). Events within a class are divided in types, according to their individual topologies. Event classes are nested, with higher probability photon selections having small effective areas, narrower Point Spread Functions (PSFs) and lower contamination of background events. In the present set of Pass 8 data (called P8R3 by the LAT team) the background contamination in each class is calibrated to the best-fit power-law parameterization of the Isotropic Diffuse Gamma-Ray Background (IGRB) emission from ref. [148].

The TRANSIENT class has the loosest selection criteria, as it is designed to study localized short duration events, such as gamma-ray bursts that, being localized, can tolerate higher backgrounds, and for timing studies for which a very high photon statistics is needed. The SOURCE class is most favorable for analysis of moderately extended sources and point sources on medium to long timescales, while the CLEAN class is better for energies above 5 GeV. Finally, the ULTRACLEAN and ULTRACLEANVETO classes are the most restrictive selections, ideal for the analysis of large regions that are more sensitive to spectral features caused by instrumental backgrounds.

Within each event class, events are partitioned in the following types:

1. PSF event types: it is a classification which describes the accuracy of the reconstructed direction. Data are divided into quartiles, from the lowest quality quartile (PSF0) to the best quality quartile (PSF3);

2. EDISP event types: is a classification which describes the accuracy of the

energy reconstruction (thus "Energy DISPersion"). Similarly to the PSF, data are divided into quartiles, from the lowest quality quartile (EDISP0) to the best quality quartile (EDISP3).

A further classification is provided by FRONT and BACK event types, depending on the position of the TKR in which the photon conversion occurred.

3.6 *Fermi*-LAT Instrument Response Functions

The LAT performance is described in terms of the so called Instrument Response Functions (IRFs), which are provided by the *Fermi*-LAT Collaboration. Further details can be found in the *Fermi* LAT performance website [149] and in the appropriate section of the FSSC [150].

The LAT performance is determined essentially by three factors:

1. LAT hardware design;
2. Event reconstruction algorithms;
3. Background selections and event quality selections.

The IRFs consist in the mapping between the incoming photon flux and the detected events, where "detection" depends not only on the LAT hardware but also on the data processing that calculates the event parameters from the observables and assigns probabilities that an event is an actual gamma ray.

The differential gamma-ray count rate measured by LAT per unit energy and solid angle can be expressed by folding the "true" differential flux per unit area at the detector with the IRFs:

$$\frac{dN}{dtdEd\hat{u}}(E,t,\hat{u}) = \int dE'd\hat{u}'\mathcal{R}(E,\hat{u}|E',\hat{u}',t)\frac{dN}{dtdE'd\hat{u}'dS}(E',\hat{u}',t) \tag{3.1}$$

where E' and $\hat{u}'$ are the true photon energy and direction respectively, while E and $\hat{u}$ are the corresponding quantities "seen" by the instrument. The function

$\mathcal{R}(E, \hat{u}|E', \hat{u}', t)$ is the IRF, which bridges the true quantities with the measured ones.

The IRF can be thought as composed of three factors:

$$\mathcal{R}(E, \hat{u}|E', \hat{u}', t) = \mathcal{A}(E', \hat{u}') \times \mathcal{P}(\hat{u}|E', \hat{u}') \times \mathcal{D}(E|E', \hat{u}'). \tag{3.2}$$

In eq.3.2 $\mathcal{A}(E', \hat{u}')$ is the *"effective area"*, i.e. the detection efficiency for photons of true energy E' and true direction $\hat{u}'$, expressed as an area; $\mathcal{P}(\hat{u}|E', \hat{u}')$ is the *"point spread function"*, i.e. the probability that a photon of true energy E' and true direction of arrival $\hat{u}'$ is reconstructed with direction $\hat{u}$; $\mathcal{D}(E|E', \hat{u}')$ is the *"energy dispersion"*, i.e. the probability for a photon of true energy E' and true direction $\hat{u}'$ to be reconstructed with energy E. In writing eq.3.2 we have neglected the time dependence or the IRF.

To evaluate the IRFs, a dedicated Monte Carlo simulation is needed. A large number of gamma-ray events is simulated to cover all possible photon inclination angles and energies with good statistics. The simulation is based on the best available representation of the physics interactions, of the instrument, and of the onboard and ground processing (see refs. [138] and [144]).

3.6.1 Effective area

The effective area has a strong dependence not only on the energy of the incoming photon, but also on its direction, which is conveniently described in LAT reference frame (see Figure 3.11) by the *off-axis angle* θ and the *azimuthal angle* Φ.

Fig. 3.17 shows the LAT effective area as a function of the photon energy for the SOURCE event class and for photons with normal incidence ($\theta = 0$). In the energy range from 10 MeV to 1 GeV the effective area increases with energy, following the increase of the pair conversion cross section. At energies of a few hundred GeV, the backsplash effect (see section 3.4.3) reduces the detection efficiency and the effective area as well.

Fig. 3.18 shows the effective area for 10 GeV photons of the SOURCE event class as a function of the off-axis angle θ.

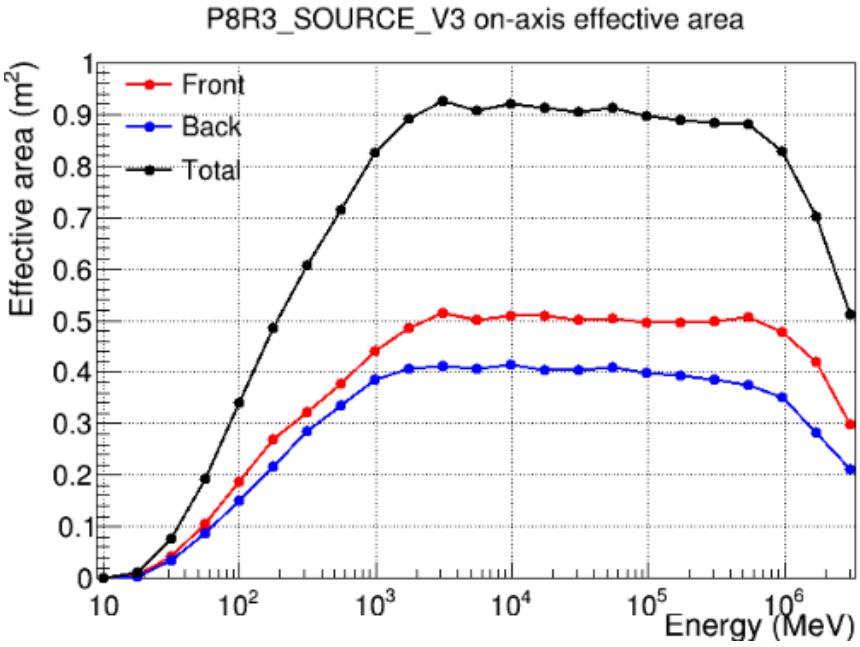

Figure 3.17: Effective area for the SOURCE event class as a function of energy for normal incidence photons (θ=0). The red curve corresponds to photon converting in the front section of the detector, while the blue one to photons converting in the back section. The black curve corresponds to all the photon events [149].

Finally, Fig. 3.19 shows a comparison among the effective areas for different event classes, for photons with normal incidence. We see that the increasing quality of reconstructed photons is achieved at the expense of the detection efficiency.

3.6.2 Acceptance and field of view

The "*acceptance*" of the instrument is evaluated by integrating the effective area on the possible directions of incoming photons. The acceptance is proportional to the detection efficiency of photons of true energy E' coming from any direction. It is defined as:

$$A(E) = \int_0^{\frac{\pi}{2}} d\theta \int_0^{2\pi} d\phi \mathcal{A}(E,\theta,\phi) sin\theta \tag{3.3}$$

where $\mathcal{A}(E,\theta,\phi)$ is the effective area.

The top panel of Fig. 3.20 shows the acceptance of the LAT as a function of

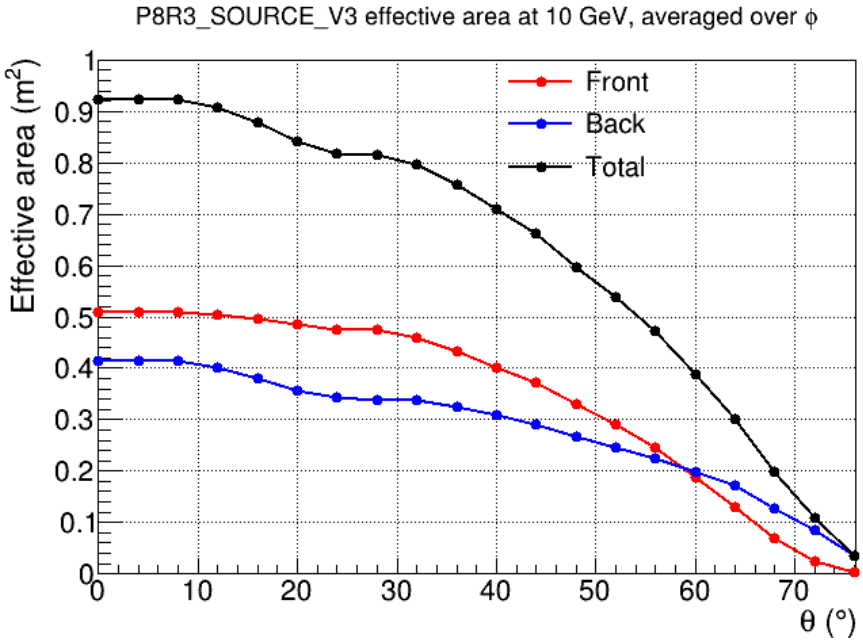

Figure 3.18: LAT effective area for the SOURCE event class as a function of the incidence angle for 10 GeV photons. The curves correspond to photons converting in the front section of the TKR (red), in the back section (blue) and to all photon events (black) [149].

energy for gamma-rays of the SOURCE event class. The bottom panel of Fig. 3.20 shows a comparison among the acceptances of the different event classes.

Since the effective area depends on the off-axis angle, the acceptance for a given analysis is given by weighting the effective area with the fraction of time that the LAT spends observing a given direction at a given off-axis angle during the spacecraft orbital history (usually compiled into a "spacecraft file"): this is what is usually referred to as "exposure".

A quantity strictly related to the acceptance is the "*Field of View*" (FoV), which is defined as the ratio between the acceptance and the on-axis effective area:

$$FoV(E) = \frac{A(E)}{\mathcal{A}_{peak}} = \frac{\int \mathcal{A}(E,\Omega)d\Omega}{\mathcal{A}(E,\phi,\theta=0^{\circ})} \tag{3.4}$$

The FoV represents the fraction of sky to which the detector is exposed at any given time and depends on the detector geometry. In particular, the aspect ratio

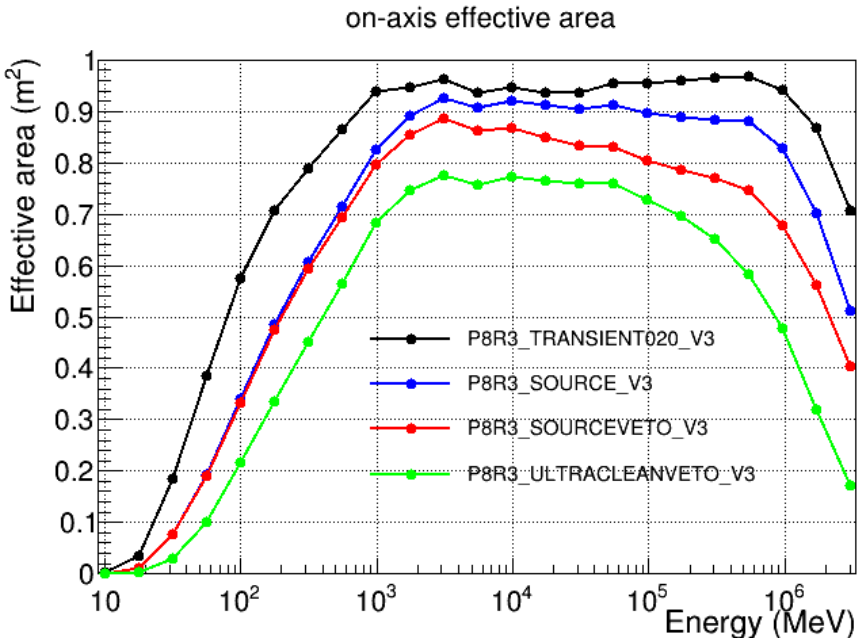

Figure 3.19: Comparison of the on-axis effective area as a function of the energy for different event classes [149].

h/w (where h is the height and w is the width of the apparatus) plays a pivotal role in determining the FoV. Indeed, if an assumption of planar geometry is made, meaning $h \ll w$, the effective area can be approximated by $\mathcal{A}_{peak} cos\theta$, and FoV(E) in equation 3.4 becomes:

$$FoV(E) = \frac{\int_0^{2\pi} d\phi \int_0^{\frac{\pi}{2}} \mathcal{A}_{peak} cos\theta sin\theta d\theta}{\mathcal{A}_{peak}} = \frac{2\pi}{2} = \pi \tag{3.5}$$

Consequently, a low aspect ratio is therefore highly desirable as far as the field of view is concerned, since the telescope is exposed to approximately 1/4 of the sky (π sr) at any given time.

3.6.3 Point Spread Functions

The PSF describes the LAT angular resolution and is derived from Monte Carlo simulations. Starting from simulated data, it is possible to evaluate the angular separation between the real photon direction $\hat{u}$ and the reconstructed one $\hat{u}'$. From

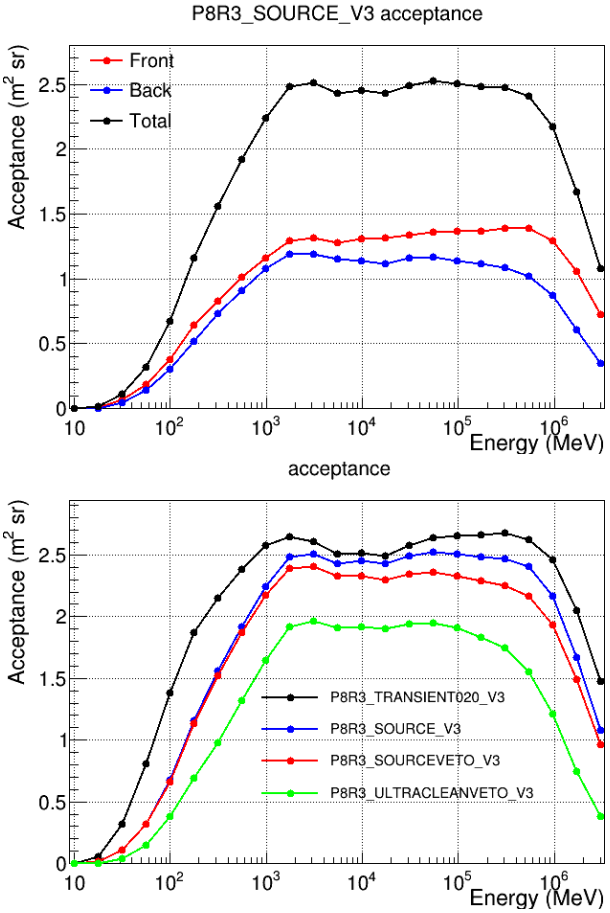

Figure 3.20: Top: LAT acceptance as a function of energy. The curves correspond to photons converting in the front section of the TKR (red), in the back section (blue) and to all photon events (black). Bottom: comparison of the acceptance as a function of energy for different event classes (total) [149].

the distribution of angular separations, it is possible to estimate the 68% and 95% event containment angles (i.e. the 68% and 95% quantiles of the distribution), that are shown in the top panel of Fig. 3.21 as a function of the photon energy for SOURCE events. At low energies, the PSF is limited by the multiple Coulomb scattering affecting the electron and positron trajectories inside the TKR. As the photon energy increases, the multiple scattering becomes negligible, but the PSF is limited by the finite spatial resolution of the SSDs in the TKR ($\sim 0.1^\circ$ at normal incidence). The bottom panel of Fig. 3.21 shows a comparison of the 68% containment angles for the four PSF event types.

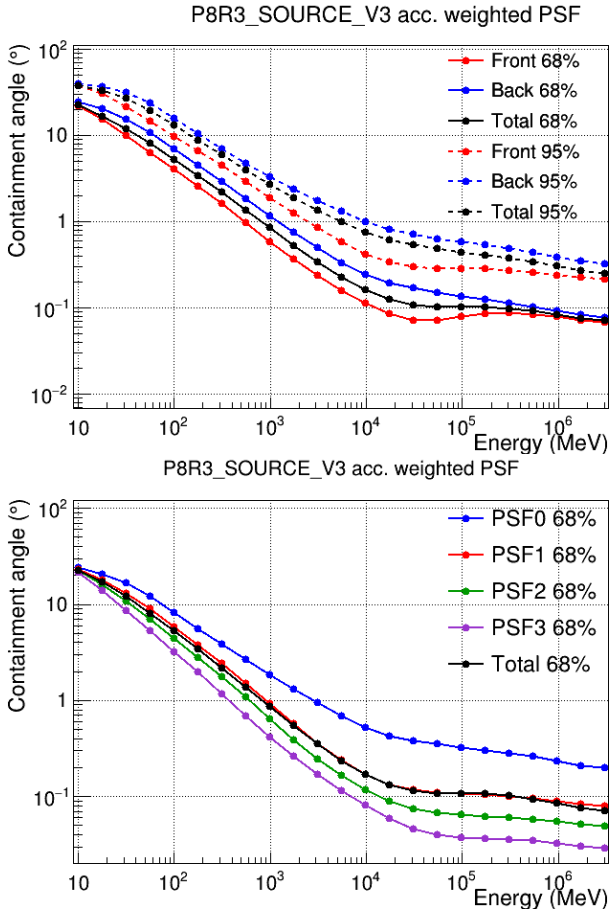

Figure 3.21: Top: 68% and 95% containment angles as a function of energy for SOURCE class photons. The curves correspond to photons converting in the front section of the TKR (red), in the back section (blue) and to all photon events (black). Bottom: Comparison of the 68% containment angle as a function of energy for different PSF event types [149].

3.6.4 Energy dispersion

The other fundamental figure of merit of the LAT evaluated with Monte Carlo simulations is the energy resolution, defined as:

$$\frac{\Delta E}{E'} = \frac{|E - E'|}{E'} \tag{3.6}$$

where E is the measured energy and E' is the true energy.

Similarly to the PSF, the energy dispersion is evaluated from the quantiles

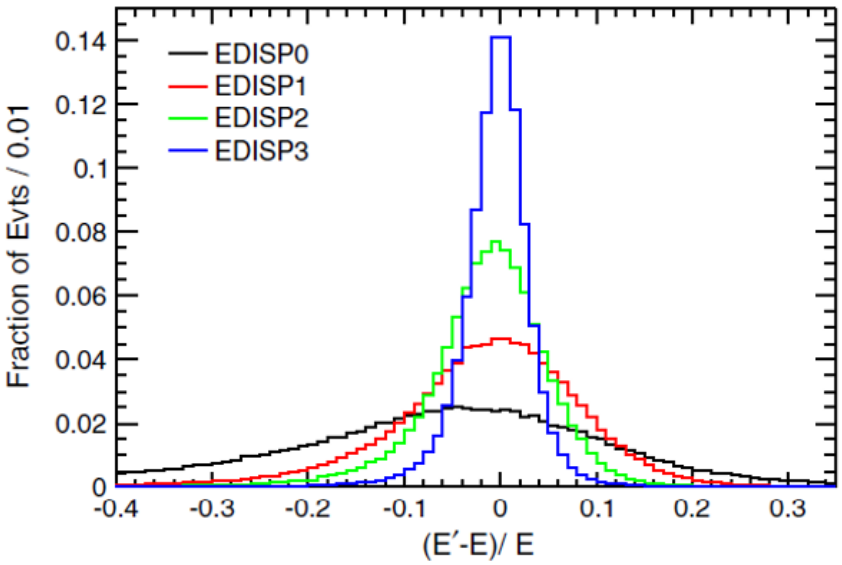

Figure 3.22: Distributions of $\Delta E/E'$ for the different event types of SOURCE class photons with 100 GeV true energy [149].

of the distributions of $\Delta E/E'$. Fig. 3.22 shows these distributions for 100 GeV photons of the SOURCE class, obtained considering the different event types. We see that the distributions become broader (and consequently the energy dispersion worsens) as the event type shifts from EDISP3 to EDISP0.

The top panel of Fig. 3.23 shows the energy dispersion as a function of the photon energy for SOURCE class photons. The energy dispersion is better than 15% over a broad energy range. At low energies the dispersion is limited because of the high fraction of energy losses in the TKR, while at high energies it deteriorates due to the partial containment of the particle showers in the CAL and to the saturation of the response of most of its crystals. Finally, the bottom panel of Fig. 3.23 shows a comparison between the energy resolution of the different event types.

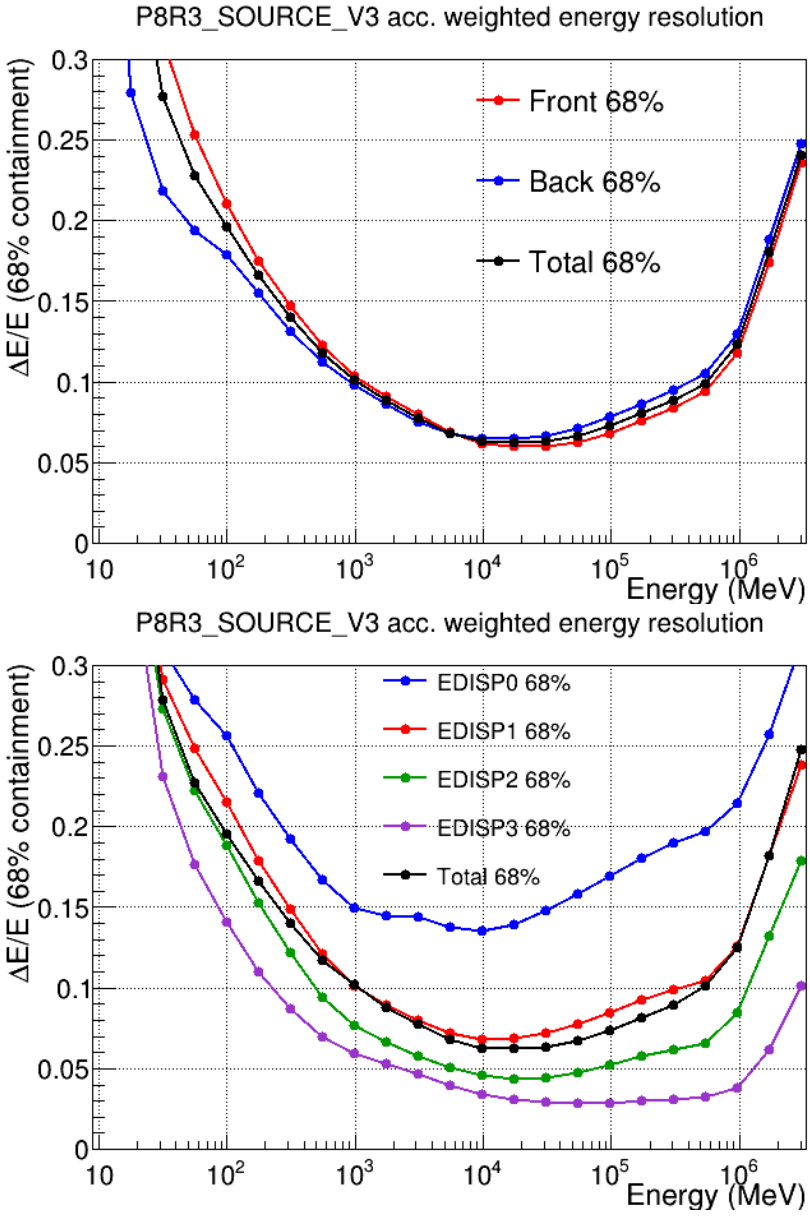

Figure 3.23: Top: Energy resolution ΔE/E, defined as the 68% containment region of the reconstructed photon energy as a function of energy. The curves correspond to photons converting in the front section of the TKR (red), in the back section (blue) and to all photon events (black). Bottom: Comparison of the 68% containment region of the reconstructed photon energy as a function of energy for different energy dispersions [149].

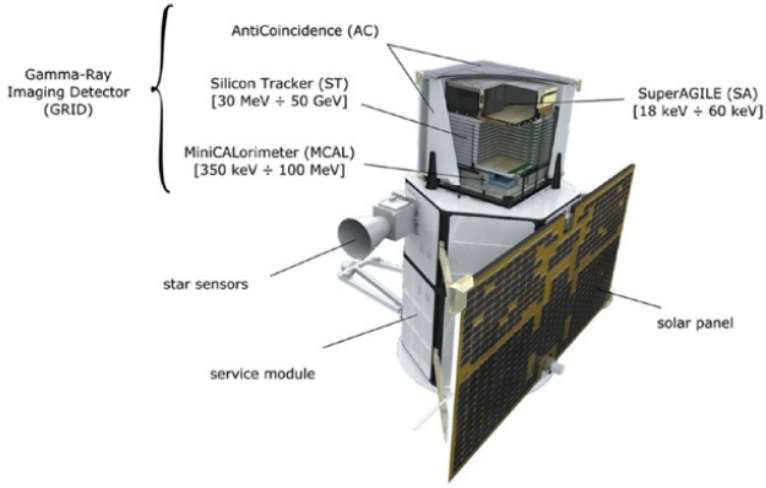

Figure 3.24: Schematic of all subsystems onboard AGILE spacecraft. Taken from Ref. [151].

3.7 Current gamma-ray space missions

3.7.1 The AGILE mission

The AGILE space mission [152] (*Astro-rivelatore Gamma a Immagini LEggero*) was a high-energy astrophysics program led by the Italian Space Agency (ASI), with scientific and technical contributions from INAF, INFN, CNR, ENEA, and several Italian universities that has been recently deorbited on January 18th 2024 [151]. The AGILE spacecraft, launched more than one year earlier than *Fermi*, addressed the same scientific goals born as the aftermath of EGRET results and was designed to be complementary not only with *Fermi*, but also with other X-ray missions (CHANDRA, INTEGRAL, RXTE, XMM-NEWTON, SWIFT, SUSAXU, RHESSI).

AGILE produced a vast amount of gamma-ray data during its 17 years of operation, which contributed to progress remarkably our knowledge of the gamma-ray sky, for example with the discovery of the Crab Nebula fast variability in gamma rays [153], with the first evidence of cosmic-ray acceleration from supernova remnants [154, 155] related to W44 and with the detection of transient gamma-ray emission from microquasars [156].

The AGILE mission featured a highly innovative payload, pioneering the combined use of a gamma-ray imager based on solid-state silicon technology alongside a hard X-ray imaging system. The full payload, compactly designed as a cube measuring approximately 60 cm per side and weighing around 100 kg, was composed of four independent instruments, schematized in Fig. 3.24:

1. **Gamma-Ray Imaging Detector (GRID):** composed of a silicon-tungsten tracker, a cesium iodide mini-calorimeter (MCAL), and a segmented plastic scintillator anticoincidence system (ACS). These components operated in concert to detect gamma rays in the energy range from 30 MeV to 30 GeV, offering a large field of view of approximately 2.5 sr. Its architecture was very similar to the *Fermi*-LAT, but with a smaller field of view and a reduced energy range of operation.

2. **Super-AGILE:** a hard X-ray imager located on the top of the payload, sensitive to photons in the 18˘60 keV range and featuring a field of view of roughly 1 sr;

The payload was complemented by a Data Handling (DH) unit equipped with advanced onboard processing capabilities, as well as a dedicated power supply unit.

3.7.2 The DAMPE mission

The *DArk Matter Particle Explorer* (DAMPE) [90] is one of the four scientific space missions developed under the Strategic Pioneer Program on Space Science of the Chinese Academy of Sciences. Although not a dedicated gamma-ray mission, DAMPE works as a general-purpose high-energy observatory for cosmic rays and gamma rays as well. It was successfully launched on December 17^{th}, 2015, from the Jiuquan Satellite Launch Center. The primary scientific goals of DAMPE include the investigation of galactic cosmic rays, extending up to ~ 10 TeV for electrons and gamma rays, and up to several hundred TeV for nuclei, as well as the search for potential DM signatures in their energy spectra.

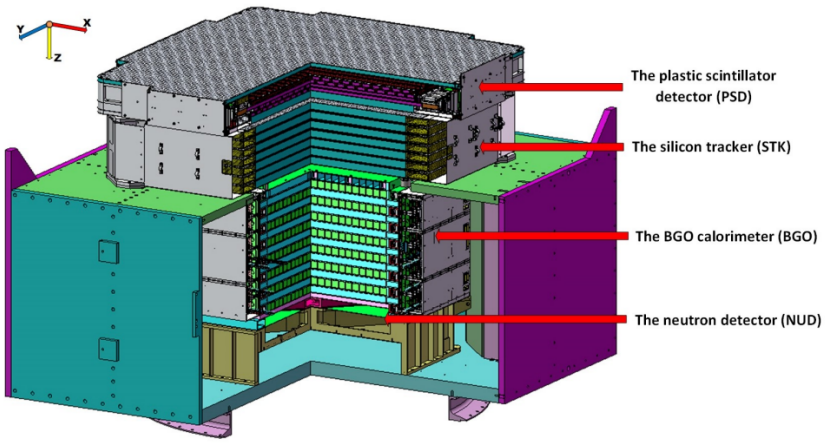

Figure 3.25: DAMPE particle detector. Its four subdetectors are visible: the Plastic Scintillator Detector (PSD), the Silicon-Tungsten Tracker (STK), the BGO Calorimeter (CALO) and the NeUtron Detector (NUD). Taken from ref. [90].

This first purely astronomical satellite from China brought remarkable results mainly related to cosmic-rays, such as the direct detection of a break at TeV energies in the spectrum of cosmic-ray electrons and positrons [157].

Fig. 3.25 shows the DAMPE experimental apparatus, which consists of four main subdetectors:

1. A **plastic scintillator detector (PSD)**, which performs the same task as the ACD for the *Fermi*-LAT: it is the anticoincidence system to enable gamma-ray measurement. In addition, since DAMPE is not only a gamma-ray telescope, but also a detector of charged cosmic rays, it provides the information about the charge of incoming particles. The PSD has a double layer configuration, and is composed of 82 modules, each one consisting of a plastic scintillator bar 884 mm long, with a 28 mm × 10 mm cross section, readout by two PMTs coupled to the ends of the bar.

2. The **Silicon-Tungsten Tracker (STK)** is the analogous of the *Fermi*-LAT TKR subsystem. It includes 6 position-sensitive double (X and Y) planes of silicon detectors with a total area of about 7 m^2, each one consisting of two layers of single-sided silicon micro-strip detectors. It can measure the

two orthogonal coordinates perpendicular to the pointing direction of the detector, enabling track reconstruction with a resolution better than 80 μm for most incidence angles. Three layers of tungsten plates of 1 mm thickness are inserted in front of the tracking layers 2,3 and 4, to enhance the photon conversion probability, while keeping negligible the multiple scattering of electron/positron pairs (above $\sim$ 5 GeV). The STK detector is equipped with a total of 768 single-sided AC-coupled silicon micro-strip detectors (SSD). Four SSDs are assembled together with a wire bonded strip-to-strip connection to form a silicon detector ladder. The total strip length along a ladder is about 37 cm. The ladders are glued on the seven support trays to form the 12 STK silicon layers. Each silicon layer consists of 16 ladders. The inter-distance between two consecutive silicon layers is $\sim$ 3 mm. This subsystem is designed not only to track electron-positron pairs from impinging gamma rays and charged cosmic rays, but also to perform charge identification of nuclei up to oxygen.

3. The **BGO ($Bi_4Ge_3O_{12}$) Calorimeter** is composed of 308 BGO crystal bars with dimension of 2.5 cm $\times$ 2.5 cm $\times$ 60 cm each. It is an electromagnetic calorimeter, whose total on-axis depth corresponds to $\sim$ 32 radiation lengths X_0, thus allowing electrons/positrons and gamma rays with energies below 200 GeV to deposit almost 100% of their energy. This deep calorimeter ensures the best performance in terms of energy resolution and allows energy measurements up to 10 TeV.

4. The **NeUtron Detector (NUD)** is located below the BGO and consists of four 1 cm-thick boron-doped plastic scintillator plates, of dimensions 19.5 cm$\times$19.5 cm, each one readout by a PMT. These scintillators can capture neutrons with a probability inversely proportional to the neutron speed. The neutrons produced in hadron-induced showers are thermalized in the BGO calorimeter, in a few μs. For the NUD, neutron captures become the dominant source of photon generation beginning 2 μs after the initial shower in the calorimeter; therefore, with a suitable trigger logic, neutrons can be

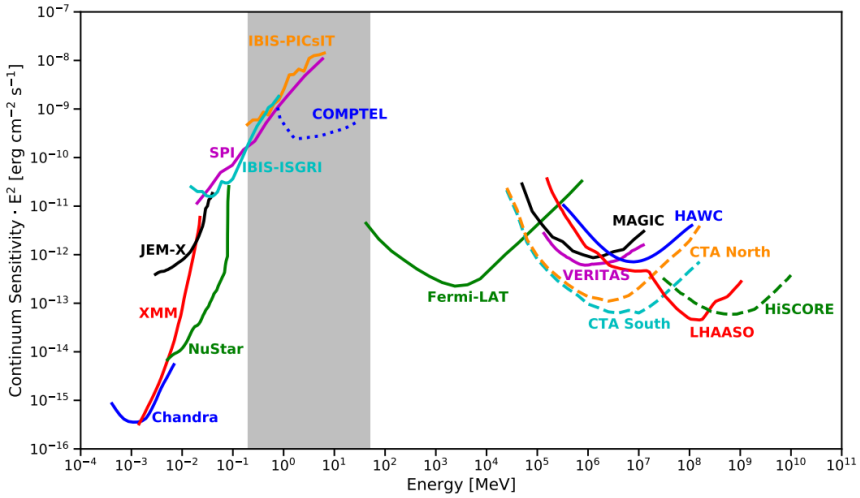

Figure 3.26: Continuum sensitivity of different X-ray and gamma-ray instruments as evaluated in Ref. [158]. Past missions are shown in dotted lines, currently operating instruments in solid lines and future planned missions in dashed lines. An energy range spanning from $\sim 200\,\mathrm{keV}$ to $\sim 50\,\mathrm{MeV}$ appears as the least explored now.

detected.

3.8 Future gamma-ray space missions

We conclude this section dedicated to gamma-ray space borne telescopes with some perspectives on future missions. Most of these designs focus on enhancing sensitivity in the MeV range, since current instruments are either completely blind or not performative in this energy range, as outlined in Fig. 3.26.

The COMPTEL instrument onboard CGRO [134] was the only one dedicated to explore the MeV energy range, but it is not anymore operational and can not give insight on transient processes such as soft GRBs, which have been observed associated with neutron stars mergers like in the joint Gravitational Wave-Gamma Ray Burst detection of 2017 [159], or studying nucleosynthesis gamma-ray lines that would enable a better understanding of Type Ia SNe. The current design challenge consists in devising a performative instrument both in Compton and pair production regimes, since these two mechanisms have comparable probability

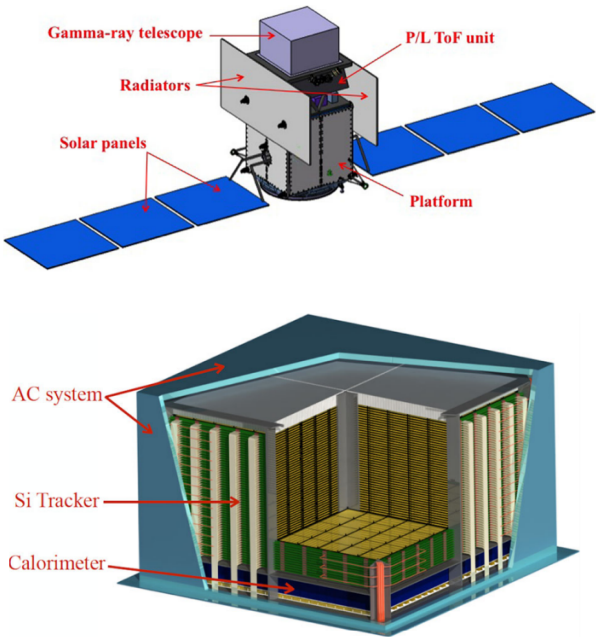

Figure 3.27: Top panel: e-ASTROGAM spacecraft in deployed configuration. **Bottom panel:** Overview of the e-ASTROGAM payload showing the silicon Tracker, the Calorimeter and the Anticoincidence system. Taken from [160].

to occur at this energy range.

3.8.1 e-ASTROGAM

e-ASTROGAM [160] is a gamma-ray mission concept proposed in response to the European Space Agency's (ESA) Call for the fifth Medium-size mission (M5) under the Cosmic Vision Science Programme, with a planned launch date in 2029.

The payload is designed to include:

- a **Tracker** composed of 56 layers of double-sided silicon strip detectors (DSSDs), each with a total area of approximately $1\,\mathrm{m}^2$, enabling the detection of gamma rays via Compton scattering or pair production;

- a **Calorimeter** consisting of an array of CsI(Tl) scintillator bars ($5 \times 5 \times 80\,\mathrm{mm}^3$), providing an energy resolution of about 4.5% at 662 keV;

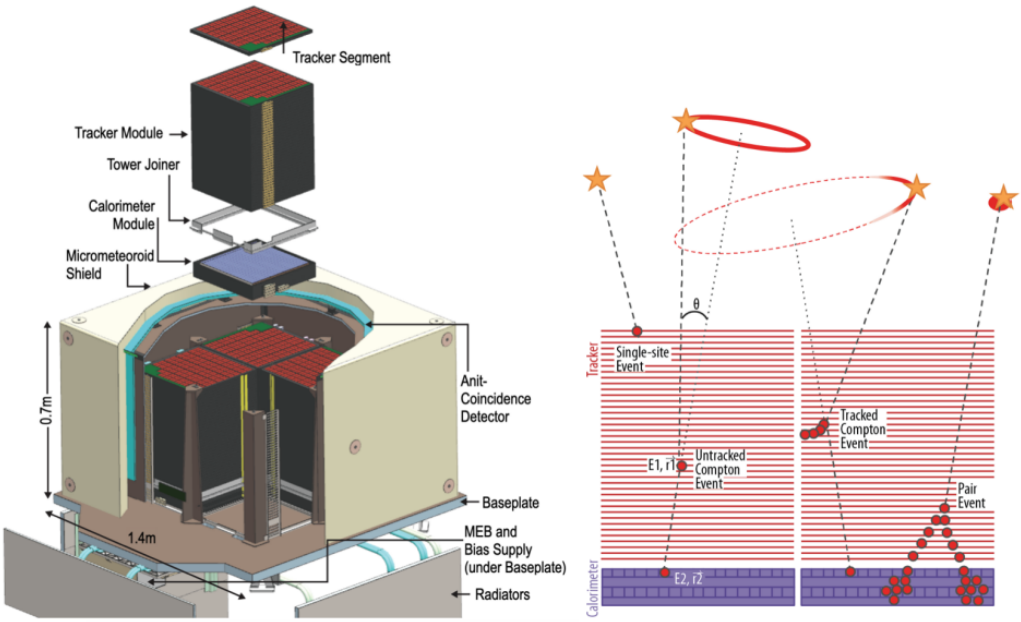

Figure 3.28: Left panel: Exploded view of the Gamma-Ray Telescope aboard AMEGO-X. The Tracker (red) and Calorimeter (purple) work together to characterize incoming gamma rays through multiple detection techniques. **Right panel:** Illustration of the three detection techniques: single-site events enhance sensitivity and response below 100 keV, particularly for transient sources; Compton events (both untracked and tracked) enable imaging below 10 MeV by reconstructing the Compton scattering angle θ from energy (E) and position ($\vec{r}$) measurements; pair-production events enable imaging above 10 MeV, employing techniques similar to those used by *Fermi*-LAT.

- an **Anticoincidence (AC) system**, which includes plastic scintillator shielding and a Time-of-Flight (ToF) system to suppress the charged-particle background.

If selected, *e-ASTROGAM* will be launched in the era of advanced gravitational wave and multimessenger astrophysics, offering unprecedented opportunities for synergistic observations.

3.8.2 AMEGO

The All-sky Medium Energy Gamma-ray Observatory eXplorer (AMEGO-X) [161] is a wide-field survey telescope designed to detect and characterize gamma-

ray emission from multi-messenger sources through imaging, spectroscopy, and polarization measurements. Over its three-year primary mission, AMEGO-X will operate in the critical 100 keV to 1 GeV energy range, surveying nearly the entire sky every two orbits and producing a deep all-sky map of both point sources and diffuse emission. The instrument will provide instantaneous coverage of over 50% of the sky below 10 MeV and over 20% above 10 MeV, enabling prompt detection of transients and rapid dissemination of alerts to the broader astrophysics community.

The Gamma-Ray Telescope (GRT) is the only scientific instrument aboard the AMEGO-X mission, designed as a wide-field survey telescope for the detection and characterization of gamma-ray emission from multimessenger sources through imaging, spectroscopy, and polarization. The GRT consists of two primary detector subsystems: the Gamma-Ray Detector (GRD) and the Anti-Coincidence Detector (ACD), all housed within a Micro-Meteoroid Shield (MMS), as illustrated in the left panel of Fig. 3.28. The GRD integrates a Tracker, including 40 layers of silicon CMOS Monolithic Active Pixel Sensors (MAPS), and a Calorimeter composed of four layers of Cesium Iodide (CsI) scintillator bars. Together, these components allow for the detection and characterization of gamma rays over a broad energy range from 100 keV (or down to 25 keV for transient events) up to 1 GeV.

The MeV energy range spans three primary photon–matter interaction regimes, each requiring a different detection method, as shown in right panel of Fig. 3.28.

For energies < 100 keV, below the Compton regime, photons are primarily absorbed via the photoelectric effect within a single pixel of the Tracker. Although these *single-site events* lack imaging capability, they are useful for identifying transient sources by analyzing aggregate signal patterns.

In the ~ 100 keV to ~ 10 MeV range, gamma rays primarily undergo Compton scattering. When both the energy and position of the initial Compton interaction and subsequent absorption are measured, the incoming photon direction can be constrained geometrically and kinematically to a circle on the sky (these are referred to as *untracked Compton events*).

Due to the angular dependence of Compton scattering, these events are

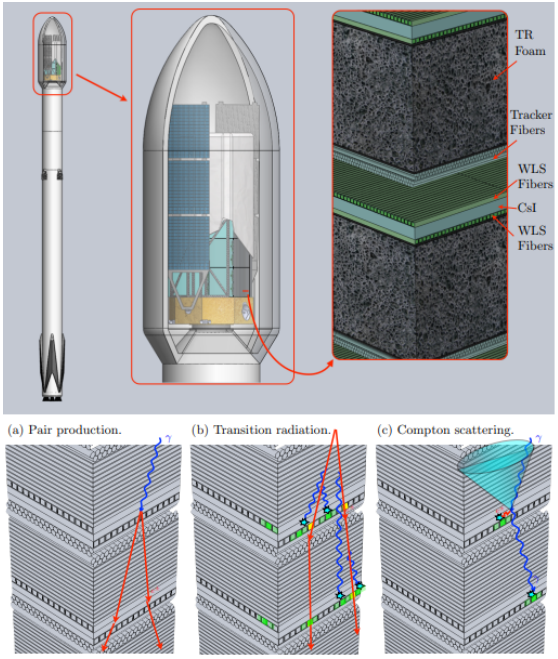

Figure 3.29: **Top panel:** APT instrument configuration shown inside the Falcon 9 payload fairing. **Bottom panel:** Overview of the primary APT detection modes across the relevant energy ranges.

inherently sensitive to the polarization of the incoming radiation, with linearly polarized photons producing a sinusoidal modulation in the scattering angle distribution. If the Tracker is able to measure the direction of the first Compton-scattered electron, the photon direction can be further constrained to an arc, enhancing imaging performance and improving background rejection (these are *tracked Compton events*).

At higher energies (> 10 MeV), gamma rays primarily convert to electron-positron pairs. The Tracker reconstructs the direction of the incident photon from the resulting ionization tracks, while the Calorimeter measures the total deposited energy via the resulting electromagnetic shower(s).

3.9 The APT mission

The Advanced Particle-astrophysics Telescope (APT) [162] project was conceived to address two fundamental questions: determining the nature of DM and understanding the physics of neutron star mergers, including their role in the synthesis of heavy elements.

Achieving these scientific goals requires improving the γ-ray sensitivity from MeV to GeV energies by at least one order of magnitude compared to existing instruments, without a proportional increase in mission cost. This performance can only be realized through a novel technical approach for a large-area Compton and pair telescope.

APT employs scintillating fibers read out by Silicon Photomultipliers (SiPMs) together with a distributed imaging CsI calorimeter (ICC), enabling more than an order of magnitude increase in effective area and twice the field of view (FOV) of the *Fermi* LAT, while keeping comparable mission costs. The main scientific goals of the mission are described in the decadal survey white paper [162].

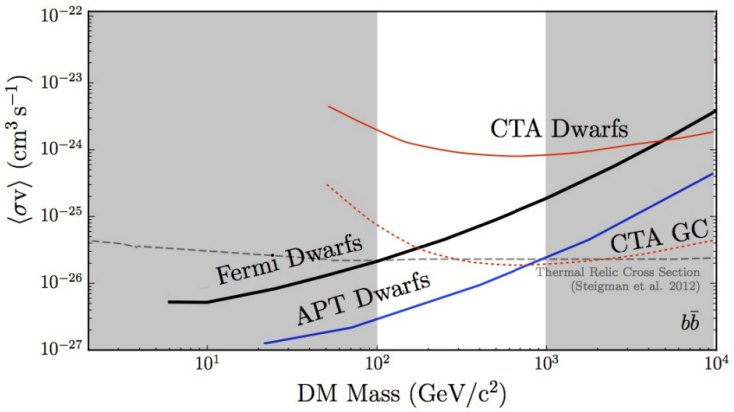

Figure 3.30: Estimated sensitivity of APT to DM from the measurements on dSph Galaxies. From Ref. [162]

Although optimized for gamma-ray observations, APT is conceived as a comprehensive particle-astrophysics observatory capable of performing complementary gamma-ray and cosmic-ray (CR) measurements to address the same overarching questions. In the MeV– TeV range, APT is expected to improve

upper limits on DM annihilation cross sections by an order of magnitude with respect to the *Fermi* LAT, through stacked dwarf galaxy analyses, as reported in Fig. 3.30. APT would thus be capable of either detecting a DM signal or excluding the entire natural parameter space of a thermal WIMP up to the TeV mass scale. In parallel, high-energy CR measurements, such as the Boron-to-Carbon ratio and isotopic abundances of light nuclei, would provide crucial constraints on CR propagation models, essential for interpreting possible DM-induced anomalies. Thanks to its high sensitivity, nearly all-sky instantaneous FOV ($\sim 4\pi$ sr for multi-Compton events), and sub-degree localization accuracy in the MeV range, APT would deliver real-time alerts for multimessenger follow-ups of gravitational wave events and short gamma-ray bursts (GRBs). Its proposed Sun–Earth Lagrange orbit and symmetric multilayer design effectively double the GeV FOV compared to *Fermi*. In addition, APT would measure elemental abundances of rare, ultra-heavy cosmic-ray nuclei produced via the r-process, providing key insights into whether these elements originate predominantly from supernovae or neutron star mergers.

The use of low-cost scintillators and SiPMs allows the construction of an instrument with a very large effective area. Operating from a Sun–Earth Lagrange orbit minimizes Earth occultation and maximizes exposure, while the symmetric calorimeter geometry yields roughly twice the instantaneous FOV of conventional bottom-mounted calorimeter designs such as that of the *Fermi* LAT. To reach such an orbit, the electromagnetic calorimeter must remain relatively shallow (less than six radiation lengths) to keep a reduced instrument mass. Despite its size, APT would be compatible with a *Falcon 9 Heavy* (or equivalent) launcher to reach a Lagrange orbit.

For MeV observations, this orbit would largely eliminate background contamination from the Earth's limb, which limits the FOV of low-Earth Compton telescopes. Although the per-event Compton reconstruction of APT is less precise than that of Germanium-based instruments like *COSI* [163], its vastly larger effective area would enable superior localization of transient events. The detection of gravitational waves from a neutron star merger by the

LIGO Collaboration [164] has already demonstrated the crucial role of wide-field instruments in multimessenger astrophysics.

Instantaneous all-sky coverage and near real-time event reconstruction are therefore critical for detecting and promptly reporting these transient phenomena. The gamma-ray band is one of the few regions of the electromagnetic spectrum where such coverage is feasible. APT's large effective area, spanning the MeV–multi-GeV range, would be ideally suited for detecting short GRBs and gamma-ray counterparts of gravitational wave events. In this context, APT would greatly surpass the *Fermi* LAT, which has so far detected only the brightest GRBs near the high end of the fluence distribution.

Chapter 4

Search for line-like and box-like features with the *Fermi*-LAT data

In this chapter the main data analysis effort of this thesis is presented: a maximum likelihood analysis approach in sliding energy windows is adopted to set upper limits on the intensity of possible spectral features that could arise from WIMP DM self-annihilation or decay. The limits on the velocity-averaged DM annihilation cross section $\langle \sigma_{ann} v \rangle$ and on the DM decay time τ_χ are evaluated, obtaining more stringent constraints with respect to those previously quoted by the Fermi-LAT Collaboration [51].

4.1 Data access and event selection

The Fermi-LAT data have been publicly available starting one year after the mission began. This means that all researchers, as well as the general public, can access the files necessary for scientific analysis (from "Level 1" products onwards, according to the tier system introduced in Sec. 3.5). Moreover, both the analysis tools and the recommended procedures are freely accessible on the FSSC website [128], and are explained in detail through a comprehensive step-by-step guide. This open-access policy has allowed the Fermi-LAT collaboration to

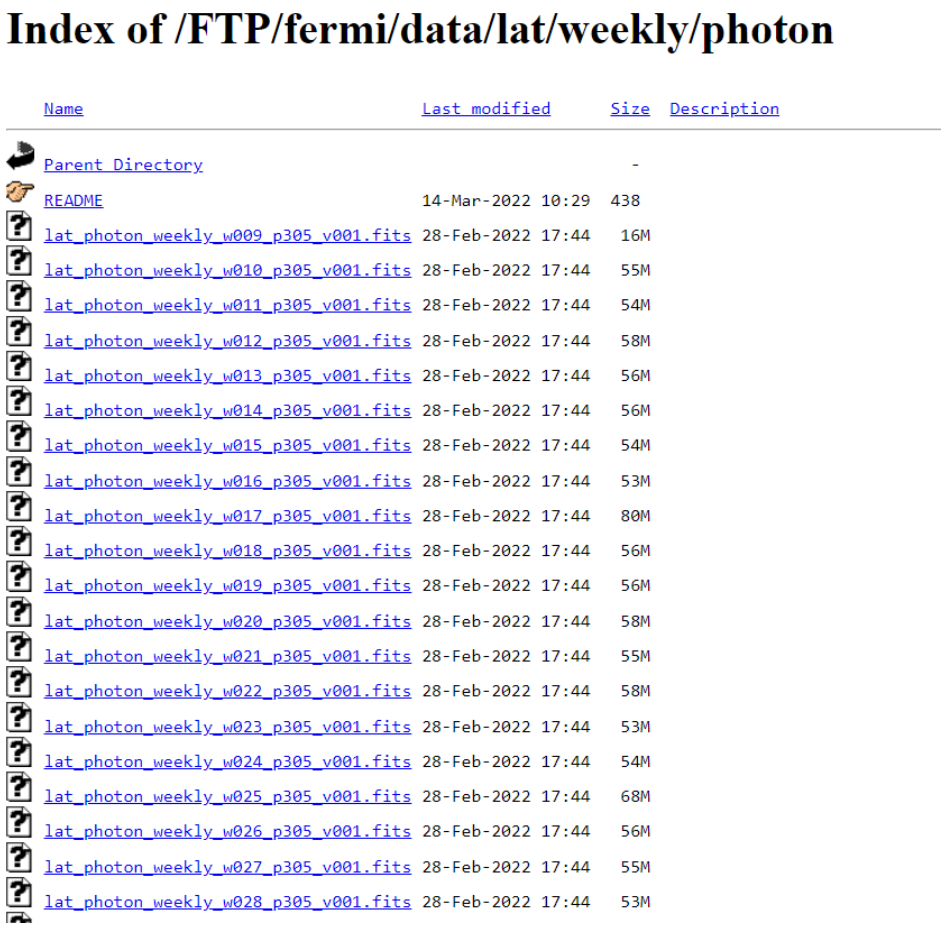

Index of /FTP/fermi/data/lat/weekly/photon

Name	Last modified	Size	Description
Parent Directory		-	
README	14-Mar-2022 10:29	438	
lat_photon_weekly_w009_p305_v001.fits	28-Feb-2022 17:44	16M	
lat_photon_weekly_w010_p305_v001.fits	28-Feb-2022 17:44	55M	
lat_photon_weekly_w011_p305_v001.fits	28-Feb-2022 17:44	54M	
lat_photon_weekly_w012_p305_v001.fits	28-Feb-2022 17:44	58M	
lat_photon_weekly_w013_p305_v001.fits	28-Feb-2022 17:44	56M	
lat_photon_weekly_w014_p305_v001.fits	28-Feb-2022 17:44	56M	
lat_photon_weekly_w015_p305_v001.fits	28-Feb-2022 17:44	54M	
lat_photon_weekly_w016_p305_v001.fits	28-Feb-2022 17:44	53M	
lat_photon_weekly_w017_p305_v001.fits	28-Feb-2022 17:44	80M	
lat_photon_weekly_w018_p305_v001.fits	28-Feb-2022 17:44	56M	
lat_photon_weekly_w019_p305_v001.fits	28-Feb-2022 17:44	56M	
lat_photon_weekly_w020_p305_v001.fits	28-Feb-2022 17:44	58M	
lat_photon_weekly_w021_p305_v001.fits	28-Feb-2022 17:44	55M	
lat_photon_weekly_w022_p305_v001.fits	28-Feb-2022 17:44	58M	
lat_photon_weekly_w023_p305_v001.fits	28-Feb-2022 17:44	53M	
lat_photon_weekly_w024_p305_v001.fits	28-Feb-2022 17:44	54M	
lat_photon_weekly_w025_p305_v001.fits	28-Feb-2022 17:44	68M	
lat_photon_weekly_w026_p305_v001.fits	28-Feb-2022 17:44	56M	
lat_photon_weekly_w027_p305_v001.fits	28-Feb-2022 17:44	55M	
lat_photon_weekly_w028_p305_v001.fits	28-Feb-2022 17:44	53M	

Figure 4.1: Overview of the Weekly-All-sky files listed on the HEASARC website [165]. The dataset used in this thesis spans the period from August, 4^{th} 2008 to December, 31^{st} 2023, for a total of 185 months of data.

enhance the scientific output of the instrument by leveraging contributions from the broader scientific community beyond the collaboration itself.

The data employed in this work were retrieved from the HEASARC website [165], which provides Weekly All-Sky Files. These datasets are particularly suitable for analyses requiring photon events collected across the entire sky, as is the case in this study.

As illustrated in Fig. 4.1, the photon event files ("FT1" files) are distributed in the ".fits" format, which stands for "Flexible Image Transport System", i.e. a standard format in astronomy designed for efficiently storing and transferring

image and event data. Equally essential to the analysis are the "spacecraft" files ("FT2" files), also provided in the ".fits" format. These files contain key information regarding the position of the *Fermi* spacecraft, the LAT livetime, its pointing history, and orientation.

In all the files, time information is recorded using the "Mission Elapsed Time" (MET) format, which represents the number of seconds elapsed since the start of the mission, starting from January 1st, 2001 at 00:00:00 Coordinated Universal Time (UTC).

The dataset used in the present analysis encompasses 185 months of Pass 8 data, spanning the period from August 4th, 2008 to December 31st, 2023. It includes photons of the CLEAN event class in the energy range between 100 MeV and 2 TeV, with conversions occurring either in the front or back sections of the tracker (F+B). The data were retrieved as 185 individual files per type (FT1 and FT2), corresponding to one per month, and subsequently merged into a single file following the application of selection cuts using the *gtselect* and *gtmktime* tools [166].

The tool *gtselect* is employed to apply selection cuts on the event data file based on various parameters, which may include those already used during the data query. The *gtmktime* tool, on the other hand, performs cuts based on spacecraft-related quantities contained in the FT2 file. Specifically, it defines the "Good Time Intervals" (GTIs), i.e. the time intervals during which the data can be considered valid based on the operational status and pointing conditions of the spacecraft during data acquisition. In summary, *gtmktime* processes the spacecraft file and, based on a set of user-defined filters and selection criteria, builds the GTIs corresponding to time intervals during which the spacecraft conditions are deemed suitable for scientific analysis. These newly generated GTIs are then combined with the existing GTIs in the event data file through a logical AND operation. Consequently, all events falling outside the resulting valid time intervals are excluded from the dataset.

Table 4.1 summarizes the selection cuts applied in the present analysis. In particular, a zenith angle cut of 100° was imposed to exclude events

Observation time	August 2008 - December 2023
Energy Range	[10 MeV - 2 TeV]
Maximum zenith angle θ_Z	100°
Event class	256 (CLEAN)
Conversion point	Front + Back
Event type	`EDISP0`, `EDISP1`, `EDISP2`, and `EDISP3`
Data quality	DATA_QUAL==1 LAT_CONFIG==1 IN_SAA!=T

Table 4.1: Summary of the cuts applied in the data selection.

originating from the bright Earth's limb[1]. In the present work I implemented an analysis of the whole event sample as well as of the four individual subsamples corresponding to the different event types classified according to the quality of energy reconstructions (`EDISP0`, `EDISP1`, `EDISP2`, and `EDISP3`, see Sec. 3.6.4). Finally, to fully exploit the information on the reconstructed energy, I performed a combined analysis of all the subsamples.

Further data quality filters are also applied by means of the following cuts:

1. DATA QUAL==1: is a quality flag given by LAT instrument team to data which corresponds to good data;

2. LAT CONFIG==1: is a flag that corresponds to data taken during standard science configuration of LAT;

3. IN SAA!=T: selects time intervals when the spacecraft is outside the South Atlantic Anomaly.

4.2 Regions of Interest (ROIs)

A Region of Interest (ROI) defines a specific portion of the sky to be analyzed, typically selected based on the scientific motivations. In the present analysis I have

[1]The Earth's limb gamma-ray emission arises from high-energy photons produced by interactions between charged cosmic rays and the upper atmosphere.

selected five ROIs, following the approach in Ref. [51]. Each ROI corresponds to a cone centered on the Galactic Center (GC), but with different angular apertures: R3 (3° aperture), R16 (16°), R41 (41°), R90 (90°), and R180 (180°), the latter encompassing the entire sky.

Because of the strong background produced by the numerous gamma-ray sources and by the interactions of charged cosmic rays with the interstellar gas in the Galactic Plane (GP), a mask was applied to exclude the GP region from all ROIs, with the exception of R3. The mask is defined by the region with galactic latitude $|b| < 5°$ and galactic longitude $|l| > 6°$. This procedure effectively mitigates the impact of background emission originating from astrophysical sources.

The angular radii of each ROI were chosen to optimize the signal-to-noise ratio (S/N) for each of the different DM density profiles illustrated in sec. 2.1.1. The S/N ratio is defined as:

$$S/N_{RoI} = \frac{\int_{RoI}\int_{FOV} d\Omega_{\hat{v}} d\Omega S(\hat{p})\varepsilon(\hat{p})}{\int_{RoI}\int_{FOV} d\Omega_{\hat{v}} d\Omega B(\hat{p})\varepsilon(\hat{p})} \tag{4.1}$$

where $S(\hat{p})$ and $B(\hat{p})$ are the intensities of gamma rays in the direction $\hat{p}$ from DM and from the diffuse background respectively [50], $\varepsilon(\hat{p})$ is the exposure at direction $\hat{p}$, $\hat{v}$ represents the unit vector in the instrument reference frame along the line of sight of a single pixel and $d\Omega_{\hat{v}}$ is the infinitesimal element of solid angle in the instrument frame associated to it.

In ref. [89] it was shown that the optimal ROIs for annihilation searches are R3, R16, R41 and R90 if the DM distributions follows the NFWc profile (eq. 2.3 with gamma= 1.3), the Einasto profile (eq. 2.4), the NFW profile (eq. 2.2) and the isothermal profile (eq. 2.1) respectively. Finally, R180 is optimized for the search of gamma rays from DM decays if a NFW profile is also assumed, like for R41.

The top panel of Fig. 4.2 displays a gamma-ray counts map in Galactic coordinates obtained by selecting photons with energies above 100 MeV. The map was generated using the Mollweide projection implemented in the HEALPix package [167]. The full sky is pixelized with $n_{\rm side} = 128$, corresponding to a total of 196,608 pixels (12×128^2). This pixelization divides the spherical surface into

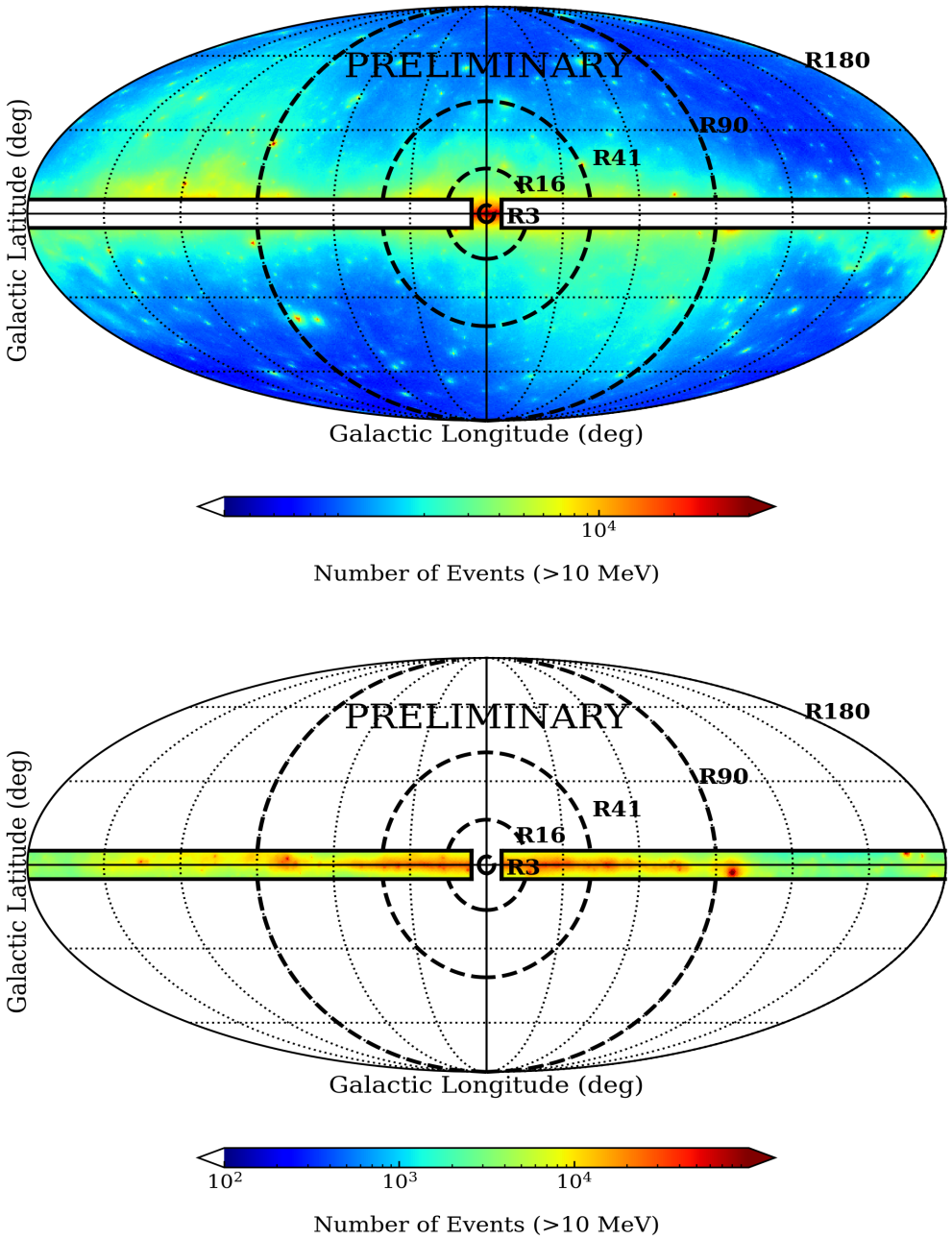

Figure 4.2: All sky count map with the different ROIs highlighted (top panel) and for the GP (bottom panel). This map was generated from the dataset analyzed in the present thesis.

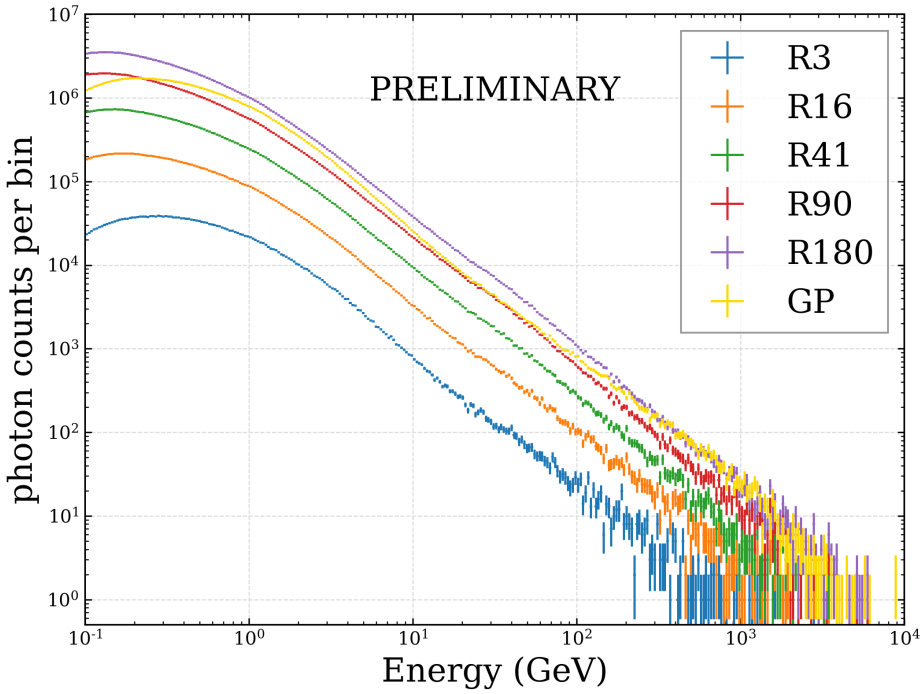

Figure 4.3: Photon counts spectra for the different ROIs used in the analysis. The spectra have been built selecting all events, with 64 bin per decade, meaning that each bin is $3.66\% \times E$ wide, where E is the central energy of the bin, for a total of 339 bins.

pixels of equal area, each covering a solid angle of $\Omega_{\rm pixel} = 6.39 \times 10^{-5}$ sr. The contours of the ROIs defined for the present analysis are overlaid on the map. The bottom panel of Fig. 4.2 shows a zoomed photon counts map of the GP region, which is adopted as a control region in the analysis (see Sec. 4.4).

Fig. 4.3 shows the overall photon count spectra in all the ROIs selected for the analysis. As expected, the number of counts in all energy bins increases with the size of the ROI.

4.3 Livetime, exposure and expected counts

For each ROI, the data were selected by applying the cuts described in Sec. 4.1. The first step of the analysis consists in evaluating the *livetime* and the average

exposure within the ROI. The livetime is defined as the time during which the LAT observed a given sky position; it depends on the off-axis angle θ as well as on the instrument's orientation history ("pointing history"). This quantity is computed using the *gtltcube* tool, which is part of the Fermitools suite [166].

The tool *gtltcube* computes the livetime over a user-defined grid of inclination angles for any direction in the sky, using the information contained in the FT2 files together with the GTIs previously selected (see Sec. 4.1). In this analysis, the off-axis angle was binned with a step size of $\Delta\sqrt{1-\cos\theta} = 0.025$, and the sky was partitioned into 49,152 pixels using the HEALPix scheme with $n_{\rm side} = 64$. Livetime cubes were first evaluated for individual pixels on a monthly basis, and subsequently merged into a single cumulative cube using the Fermitool *gtltsum* [166], corresponding to the 185 months of data for each pixel.

The livetime of a given ROI is then computed as

$$\mathcal{T}_{\rm ROI}(\cos\theta) = \sum_{i\in{\rm ROI}} w_i\,\mathcal{T}_i(\cos\theta), \tag{4.2}$$

where the sum extends over all pixels within the ROI and the weights w_i account for the contribution of each pixel to the ROI livetime distribution. Figure 4.4 shows the integrated livetime for R3 as a function of $\cos\theta$.

The *exposure* of a given ROI is defined as the integral over the solid angle of the effective area multiplied by the livetime and is given by:

$$\mathcal{E}_{ROI}(E|E') = \sum_{cos\theta} \mathcal{A}(E|E', cos\theta)\mathcal{T}_{ROI}(cos\theta) \tag{4.3}$$

where E and E' are the observed and true energies respectively, $\mathcal{A}(E|E', cos\theta)$ is the IRF, $\mathcal{T}_{ROI}(cos\theta)$ is the livetime evaluated for each ROI as discussed above (an example is shown in Fig.4.4 for R3). In the previous formula, the integral over the entire solid angle is replaced with the sum over the $\cos\theta$ bins. Fig. 4.5 reports the exposure for $R180$ and `EDISP3` events.

For a fixed true energy E', one can extract from the exposure matrix a one-dimensional histogram, such as the example shown in Fig. 4.6, which represents

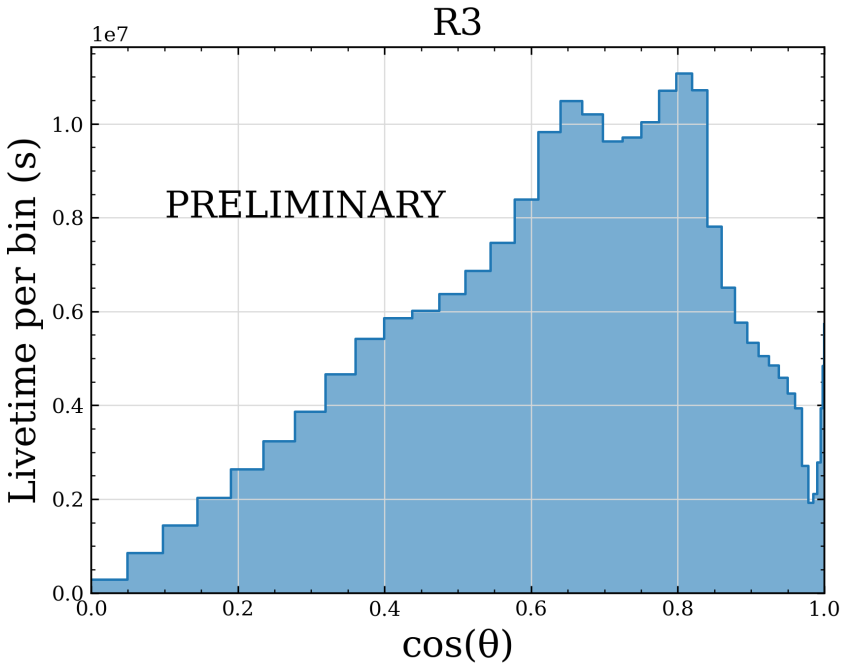

Figure 4.4: Integrated livetime vs cosθ for R3, where θ is the off-axis angle (see fig.3.4). The histogram is divided in 40 bins, with ($\Delta\sqrt{1-cos\theta} = 0.025$).

the exposure as a function of the reconstructed energy for photons of the different `EDISP` types with true energy $E' = 1$ GeV and $E' = 100$ GeV. The energy dispersion can then be estimated by evaluating the quantiles of these distributions.

Fig. 4.7 shows the energy dispersion in R180 as a function of the true energy. The dispersion was evaluated for all event types combined as well as for individual event types. The energy resolution improves when moving from `EDISP0` to `EDISP3` events. The resolution obtained by considering all events lies within the range defined by the curves of the individual event types. In particular, `EDISP3` events exhibit an energy resolution (at 68% containment) between 10% and 15% across the entire energy range, whereas `EDISP0` events show a poorer resolution, ranging from 20% to 25%. A similar trend is observed in the other ROIs, with only minor variations among them due to differences in exposure.

The exposure allows the reconstruction of the expected counts for a given photon flux. Indicating with $\Phi(E')$ the photon flux at true energy E' in the ROI,

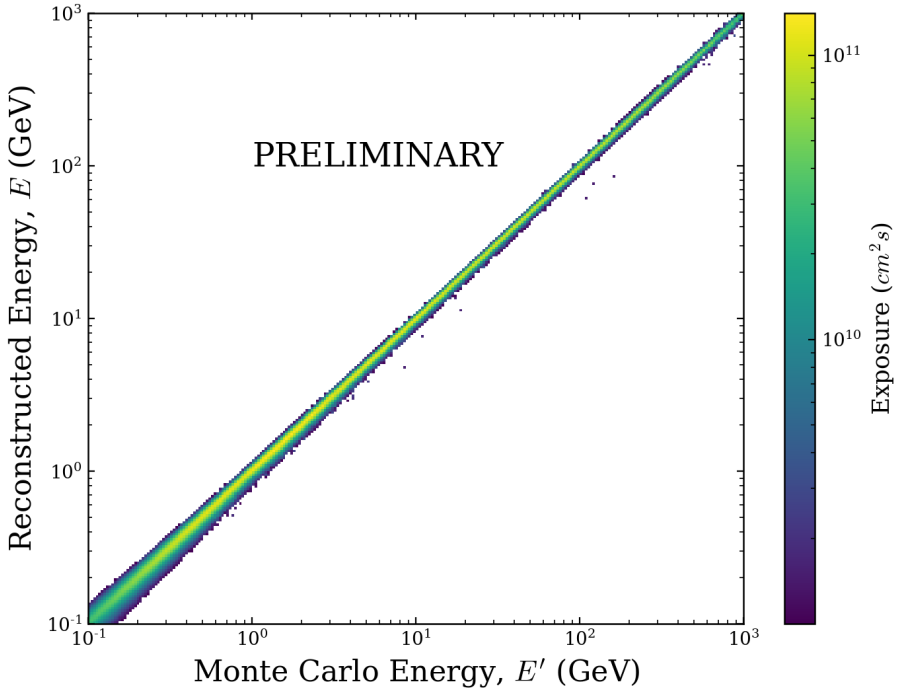

Figure 4.5: Exposure $\mathcal{E}(E|E')$ in R180 for EDISP3 events. The true energy is on the x-axis, while the observed energy is on the y-axis.

the expected counts in the j-th bin of observed energy in the pixel can be evaluated as:

$$\mu(E_j) \equiv \mu_j = \int dE' \; \mathcal{E}_{ROI}(E|E') \; \Phi(E') \tag{4.4}$$

where the integration is carried out over the whole true energy range.

The photon flux in each ROI can be seen as the sum of a background flux, due to the sources, to the diffuse emission and to possible systematic effects, and of the possible signal flux originated from DM, as will be shown in the next sections.

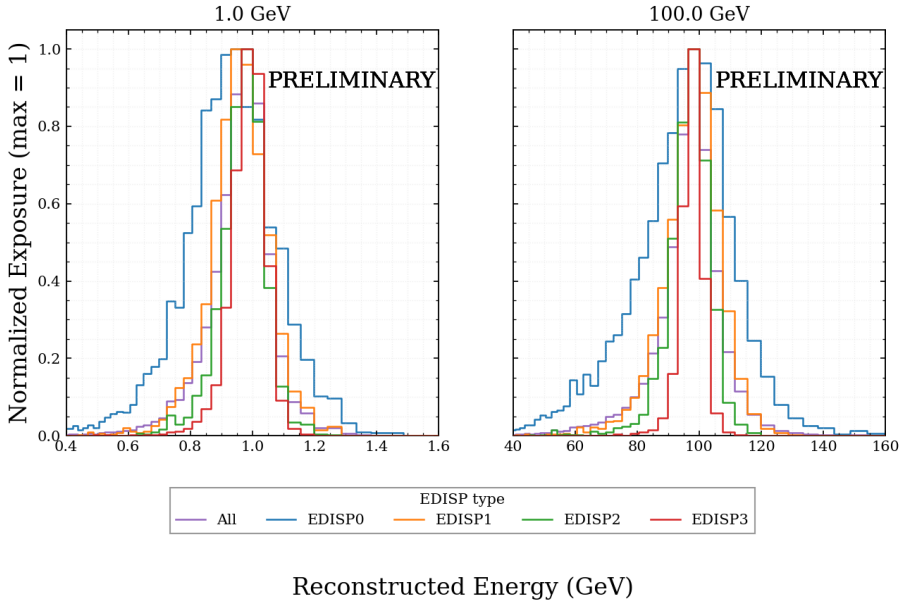

Figure 4.6: Projection of the exposure matrix corresponding to R180 (shown in Fig. 4.5), along the y-axis (observed energy), at fixed true energies of 1 and 100 GeV. The energy dispersion corresponds to the width of the distribution. Each EDISP type exhibits a broader distribution according to dispersion in energy reconstruction quality, as outlined in Fig. 3.22.

4.4 Fit procedure

A maximum likelihood fit procedure in sliding energy windows was implemented to search for potential line-like and box-like spectral features in the gamma-ray emission from the various ROIs. The fits were performed over the energy range from 1 GeV to 1 TeV. For each ROI, the full event sample was analyzed, and individual analyses of the subsamples corresponding to the event types `EDISP0`, `EDISP1`,`EDISP2` and `EDISP3` were performed. Additionally, a combined analysis including all four event types was performed.

The sliding window corresponding to the fit energy E is defined as the interval $[E(1-w), E(1+w)]$, where wE is the width of the window. In the present work, windows with different sizes have been analyzed, and precisely $w = 0.40$, 0.50 and 0.60. These values are larger than the energy resolution of the LAT, which is at most $\sim 30\%$ in the worst case. In fact, as shown in Fig. 4.7, the worst case is

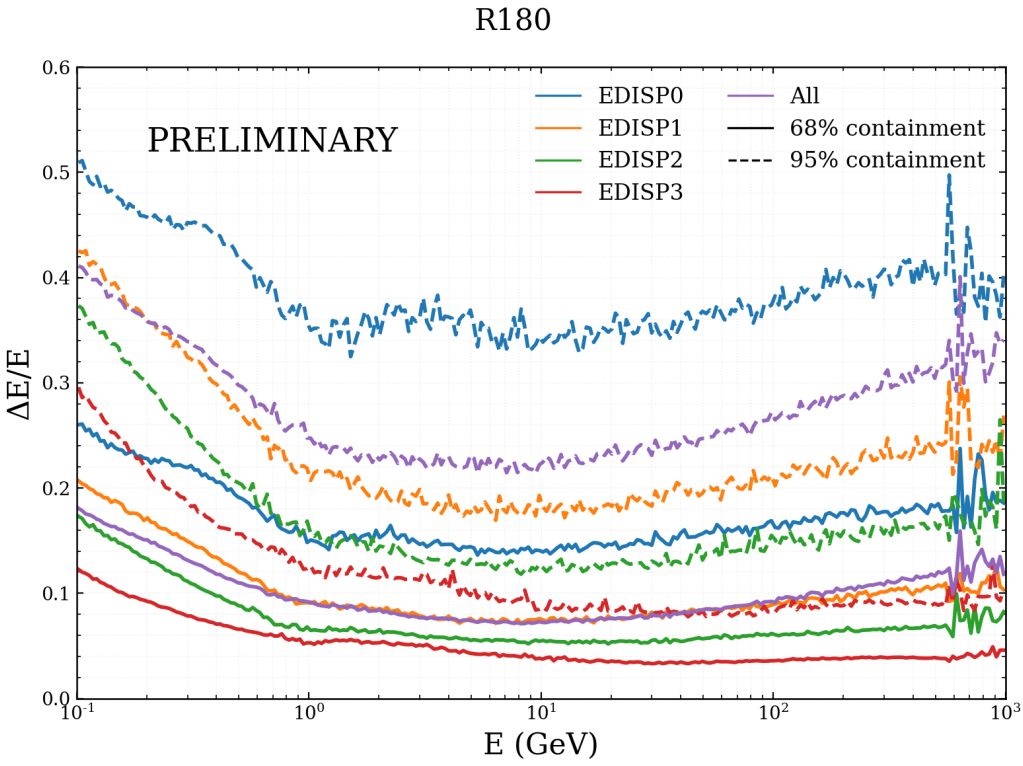

Figure 4.7: Energy resolution curves corresponding to 68% (full lines) and 95% containment (dashed lines), relative to all different event types in R180. The curves were obtained from the projections along the observed energy axis of the exposure matrix, scanning the true energies. These curves are compatible with the ones declared in *Fermi*-LAT performance (Fig. 3.23).

around 36% for the `EDISP0` event type at 1 GeV. A possible gamma-ray line at energy E is expected to yield a signal spread over an energy interval with the size of the energy resolution. Even in the worst case, this signal will therefore lie within one of the sliding windows.

The energy range from 1 GeV to 1 TeV was binned into 64 bins per decade, equally spaced in logarithmic scale, to ensure adequate sampling of the energy dispersion and spectral features. The line search was conducted over the same range, selecting 32 logarithmically equally spaced fit energies per decade as central energies of the sliding windows. This sampling is motivated by theoretical models of WIMP DM, which commonly predict DM particle masses in the range of a few hundred GeV. A similar strategy was adopted for the search of box-like spectral

features, where the upper edge of the box plays a role analogous to the line energy. As in the case of lines, energy dispersion effects broaden the observed shape of the feature, smoothing the upper edge of the box, which must be fully contained within the sliding energy window to enable reliable detection.

For each ROI, up to 96 sliding-window fits were performed, depending on the coverage of the energy range. In fact, when fewer than 10 photon counts were found in the interval above the central energy of a given window, the corresponding fit was discarded due to insufficient statistics. For instance, in the case of R3, this count threshold is reached at energies around 300 GeV.

4.4.1 Flux models and likelihood function

The photon flux from a given ROI is modeled as:

$$\Phi_{\rm tot}(E' \,|\, \vec{\theta}) = \Phi_{\rm bkg}(E' \,|\, \vec{\theta}_b) + \Phi_{\rm sig}(E' \,|\, \vec{\theta}_s) \tag{4.5}$$

where $\vec{\theta} = (\vec{\theta}_b, \vec{\theta}_s)$ denotes the full set of model parameters. The terms $\Phi_{\rm sig}(E' \,|\, \vec{\theta}_s)$ and $\Phi_{\rm bkg}(E' \,|\, \vec{\theta}_b)$ represent the signal and background flux components, respectively. The signal flux corresponds to a potential line-like or box-like feature arising from DM interactions.

The background flux can be decomposed into two components: a "smooth" contribution, $\Phi_{\rm bkg,smooth}(E')$, accounting for the continuous gamma-ray emission from known astrophysical processes, and a possible feature-like component, $\Phi_{\rm bkg,feature}(E')$, which could mimic a DM signal and may originate from instrumental systematics.

The smooth component of the background flux is modeled using a log-parabola function below 10 GeV and a simple power law above that threshold:

$$\Phi_{\rm bkg,smooth}(E') = \begin{cases} k \left(\dfrac{E'}{E_0} \right)^{-\Gamma - \beta \log\left(\frac{E'}{E_0}\right)} & \text{for } E' < 10 \text{ GeV}, \\ k \left(\dfrac{E'}{E_0} \right)^{-\Gamma} & \text{for } E' \geq 10 \text{ GeV}, \end{cases} \tag{4.6}$$

where $E_0 = 1$ GeV is a reference energy scale. The log-parabola form accounts for the spectral curvature typically observed in gamma-ray fluxes at energies ≤ 1 GeV, which cannot be reproduced by a simple power law. In this model, the spectral index is energy-dependent due to the additional logarithmic term in the exponent, unlike the constant index in the pure power-law case.

As will be illustrated in the discussion of the results, this modeling choice represents one of the key methodological improvements in the present analysis, enabling stronger constraints to be retrieved, particularly in the lower energy range ($1 - 10$ GeV), in the context of the line search.

The line-like signal and background components are described by Dirac-delta distributions:

$$\Phi_{\rm sig}(E'|s) = s\,\delta(E' - E_{line}) \tag{4.7}$$

$$\Phi_{\rm bkg,line}(E'|b) = b\,\delta(E' - E_{line}) \tag{4.8}$$

while in the box search case a Heaviside step function is used in place of the Dirac-delta function:

$$\Phi_{\rm sig}(E'|s) = \frac{s}{E_{box}} H(E_{box} - E') \tag{4.9}$$

$$\Phi_{\rm bkg,box}(E'|b) = \frac{b}{E_{box}} H(E_{box} - E') \tag{4.10}$$

In both cases, the parameters s and b describe the strength of the spectral features. The parameter b can take either positive or negative values, as it accounts for possible background features arising from instrumental effects or systematic uncertainties. In contrast, the parameter s, associated with the potential DM signal, is constrained to be non-negative. The line energy, E_{line}, and the upper edge of the box, E_{box}, correspond either to m_χ in the DM self-annihilation scenario or to $m_\chi/2$ in the DM decay scenario.

The factor E_{box} in the denominator of Eqs. 4.9 and 4.10 is introduced to give the parameters s and b the same physical meaning as in Eqs. 4.7 and 4.8. In the case of the line-like features, the total fluxes from the signal line and from

the background line, evaluated integrating Eqs. 4.9 and 4.10 on true energy, are given by s and b respectively; similarly, in the case of the box-like features, s and b correspond to the integral fluxes from the signal and background boxes respectively.

To disentangle potential systematic features from a true DM-induced signal, a control region was also defined, corresponding to the portion of the Galactic Plane that was excluded from the ROIs with the masking procedure (see Sec. 4.2).

The gamma-ray flux in a signal ROI is therefore given by:

$$\Phi_{\mathrm{ROI}}(E') = \Phi_{\mathrm{sig}}(E') + \Phi_{\mathrm{ROI,\,smooth}}(E') + \Phi_{\mathrm{bkg,\,feature}}(E'), \tag{4.11}$$

while the flux in the control region is given by:

$$\Phi_{\mathrm{GP}}(E') = \Phi_{\mathrm{GP,\,smooth}}(E') + \Phi_{\mathrm{bkg,\,feature}}(E'). \tag{4.12}$$

The corresponding expected photon counts are evaluated by folding the fluxes with the exposures, $\mathcal{E}_{\mathrm{ROI}}$ and $\mathcal{E}_{\mathrm{GP}}$.

In the null hypothesis H_0, the observed counts in both the signal ROI and the control region are assumed to arise from a background-only model, i.e., $\Phi_{\mathrm{sig}} = 0$, which corresponds to $s = 0$. Under the alternative hypothesis H_1, the presence of a signal is assumed, i.e., $\Phi_{\mathrm{sig}} > 0$, or equivalently $s > 0$.

For each hypothesis, a Poisson likelihood function is defined as:

$$\mathcal{L}(\vec{n}\,|\,\vec{\theta}) = \prod_j e^{-\mu_j}\,\frac{\mu_j^{n_j}}{n_j!}, \tag{4.13}$$

where $\vec{n} = (n_1, n_2, \ldots)$ denotes the vector of observed photon counts in each energy bin, and $\vec{\mu}(\vec{\theta}) = (\mu_1(\vec{\theta}), \mu_2(\vec{\theta}), \ldots)$ is the corresponding vector of expected counts, dependent on the model parameters $\vec{\theta}$, evaluated as indicated by Eq. 4.4. The index j in the product in the r.h.s. of Eq. 4.13 runs over all energy bins within the fit window, in both the signal ROI and in the control region. The set of free parameters of the model is given by:

$$\vec{\theta} = (k_{\rm ROI}, \Gamma_{\rm ROI}, \beta_{\rm ROI}, k_{\rm GP}, \Gamma_{\rm GP}, \beta_{\rm GP}, b, s), \tag{4.14}$$

where the first six parameters describe the smooth spectral components in the ROI and in the Galactic Plane (GP) control region, while b and s correspond to the feature-like background and signal intensities, respectively. The null hypothesis is nested within the alternative hypothesis, as it can be obtained by setting $s = 0$ in the general model.

The best-fit values of the parameters are determined by maximizing the likelihood function. This is equivalent to maximizing the likelihood ratio, defined as:

$$\lambda(\vec{\theta}) = \frac{\mathcal{L}(\vec{n}\,|\,\vec{\theta})}{\mathcal{L}(\vec{n}\,|\,\vec{n})} = \frac{\prod_j e^{-\mu_j}\,\mu_j^{n_j}/n_j!}{\prod_j e^{-n_j}\,n_j^{n_j}/n_j!}, \tag{4.15}$$

where $\mathcal{L}(\vec{n}\,|\,\vec{n})$ is the likelihood of the "saturated" model, in which the expected counts are set equal to the observed counts in each bin, i.e., $\mu_j = n_j$. The values of $\vec{\theta}$ that maximize $\mathcal{L}$ are the same that maximize λ. For computational purposes it is useful to work on the logarithm of the likelihood ratio:

$$-2\ln\lambda(\vec{\theta}) = -2\sum_j \Big[-\mu_j + n_j - n_j ln\Big(\frac{n_j}{\mu_j}\Big)\Big] \tag{4.16}$$

where for bins with $n_j = 0$, the last term is assumed to be zero. From the definitions we see that the maximization of the likelihood ratio corresponds to the minimization of the function $-2\ln\lambda(\vec{\theta})$.

According to Wilks' theorem [2], the quantity $-2\ln\lambda(\vec{\theta})$ obeys a χ^2 distribution with $N-m$ degrees of freedom, where N is the number of independent data points and m is the number of free parameters in the model. This result holds in the asymptotic limit, meaning that the approximation to the χ^2 distribution becomes valid when the sample size is sufficiently large, i.e. when the number of expected counts per bin is $\gtrsim 10$, such that the Poisson distribution of the data can be approximated by a Gaussian, and the likelihood surface becomes well-behaved

near its maximum. In the present analysis, N corresponds to the total number of energy bins within the fit windows of both the signal ROI and the Galactic Plane control region, while m is the total number of model parameters to be fitted.

4.4.2 Local significance

The test of the alternative hypothesis H_1 with respect to the null hypothesis H_0 is performed using the likelihood functions defined in the previous sections. The fitted signal line strength is the value of s corresponding to the maximum of λ_1. Indicating with λ_0 and λ_1 the likelihood ratios corresponding to H_0 and H_1, the test statistics is defined as:

$$TS = 2[ln\lambda_{1,max} - ln\lambda_{0,max}] \tag{4.17}$$

where $\lambda_{0,max}$ and $\lambda_{1,max}$ are the maximum likelihood ratios for the hypothesis H_0 and H_1 respectively. Since λ_1 contains one additional parameter with respect to λ_0, the TS is expected to follow a χ^2 distribution with 1 degree of freedom.

The local significance S_{local} of the fit can be evaluated from the TS as:

$$S_{local} = \sqrt{TS_{min}}. \tag{4.18}$$

where TS_{min} is the minimum value of the TS. It is "local" since it refers to a fit performed in an individual window. Since the TS obeys a χ^2 distribution with 1 degree of freedom, the upper limits (ULs) at 95% confidence level on the parameter s can be evaluated by searching the value of s for which $TS = TS_{min} + 2.71$

A procedure has been also implemented to combine the likelihood functions corresponding to the different event type sub-samples, `EDISP0`, `EDISP1`,`EDISP2` and `EDISP3`. For a given ROI, the "combined likelihood" is defined as the product of the individual likelihood functions associated with each event type sub-sample:

$$\lambda_{\text{combined}}(s) = \prod_i \lambda_i(s), \tag{4.19}$$

where i indexes the event types. As in the individual analyses, the quantity

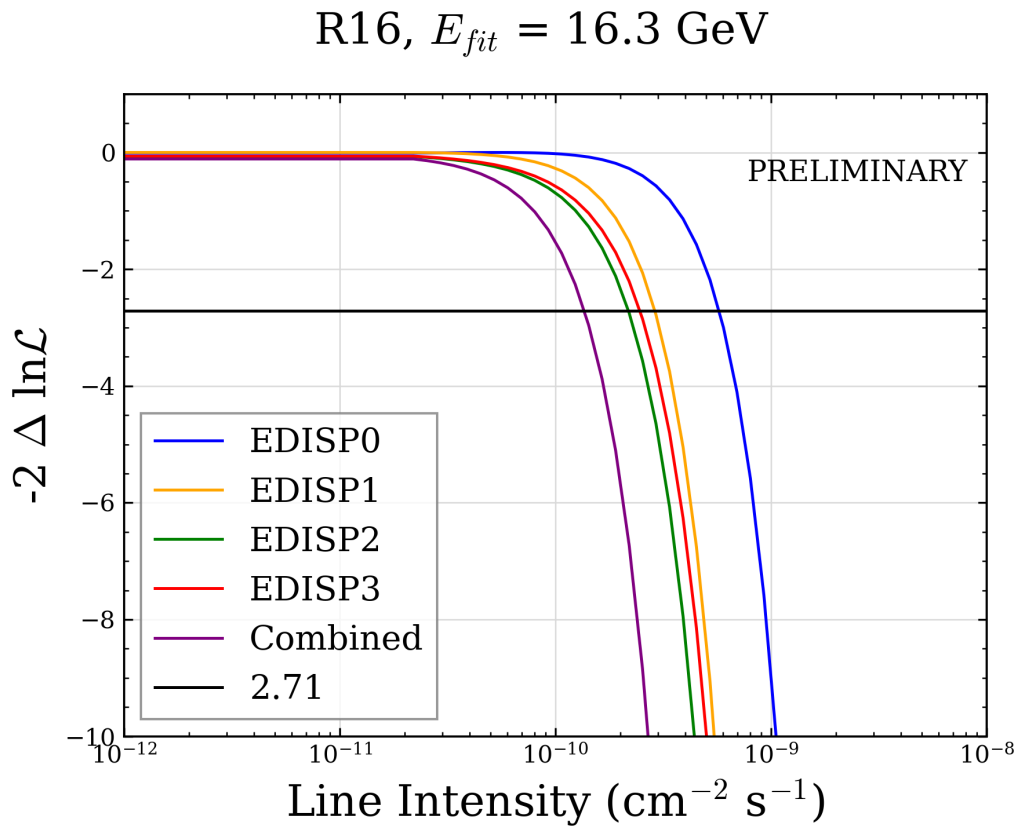

Figure 4.8: Profile of the function $-2\Delta ln\mathcal{L}$, evaluated for the different event types as a function line flux at $E_{line} = 16.3\,\mathrm{GeV}$, in R16. The ULs at 95% CL are determined by the intersection of the curves with the horizontal black line at $-2\Delta ln\mathcal{L} = -2.71$. The combined procedure yields stronger constraints (purple line) with respect to the analyses of individual event types.

$-2\ln\lambda_{\mathrm{combined}}$ is used as the test statistics for the hypothesis test. An example of this approach is shown in Fig. 4.8, which compares the profile likelihood functions obtained separately for each event type and for the combined analysis in the case of a line search. In this example, the tested line energy is $E_{\mathrm{line}} = 16.3$ GeV, in $R16$. The curve corresponding to the combined analysis falls more steeply than those of the individual components, indicating tighter constraints on the line flux.

4.4.3 Global significance

The TS as evaluated in Eq. 4.17 is a local significance indicator, referring to an individual energy window. However, since the energy windows are overlapping, the fits in different windows are correlated. Therefore, a global significance indicator is needed, that accounts for all energies results at the same time. To build it, I have first performed a set of background-only Monte Carlo simulations (pseudoexperiments) and compared the results of the analysis with the expectations from the simulations for both line and box features searches.

In the present work I have simulated a set of 1000 pseudoexperiments for each feature search. Each pseudoexperiment is generated starting from a template of the count distributions corresponding to the null hypothesis. The counts in each energy bin are extracted from a Poisson distribution with its average value taken from the template model. The same analysis chain as for real data has then been applied to the simulated data. The distributions of the ULs on the line intensities and of the TS values obtained from the pseudoexperiments for each value of the line energy have then been studied.

For each pseudoexperiment, the maximum value TS_{max} of the local TS is retrieved and the distribution of these maximum TS values is built. This distribution gives an indication of how the TS can fluctuate in absence of a signal. Assuming that TS_{max} obeys a (half) normal distribution, one can convert the observed values of TS_{max} into sigma units, thus obtaining the global significance.

4.5 Results for the monochromatic line search

Fig. 4.9 shows an example of the fit procedure in an individual energy window centered at 113 GeV. The fit has been performed in $R180$ combining all event types. The observed photon counts are well reproduced by the fitted counts, as it can be seen from the residuals, which are defined as the fractional deviations of data from the model and do not exceed 25%. The contribution of the signal line feature to the fitted model is also shown in the plot. The spectral shape is not a sharp Dirac delta function, but is instead broadened due to the finite energy

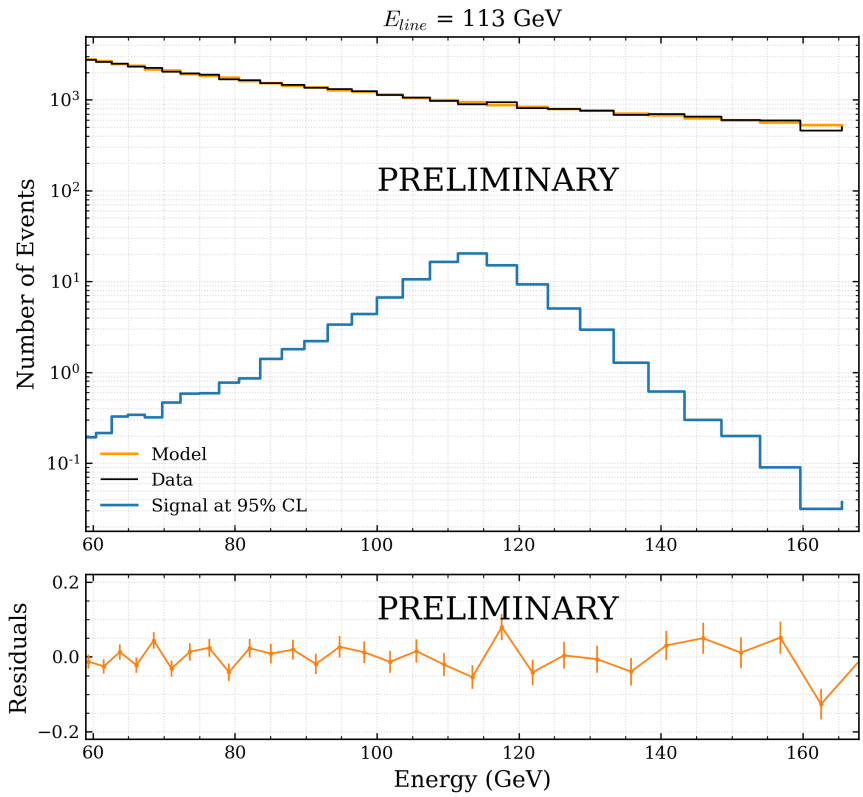

Figure 4.9: Photon counts as observed in the data (black points) and as predicted by the best-fit model including the signal component (blue line) for a single window centered at 113 GeV. The lower inset shows the fractional residuals, defined as (data − model)/model, which typically remain within a 25% range across other fit windows as well.

resolution of the LAT. In this case, the counts originated from the line are less than 1% of the total model counts in all energy bins.

Fig.. 4.10 shows a summary of the fit results. The colored lines show the contributions of the fitted line components to the observed photon counts in $R180$ at different energies. Figure 4.11 shows the test statistic TS as a function of the line energy for the analysis performed by combining the four event-type subsamples, `EDISP0`, `EDISP1`, `EDISP2` and `EDISP3`. The results are shown for the five different ROIs defined in the analysis. For each ROI, the fits were repeated using energy windows of varying widths, chosen as multiples of the central energy: $0.4 \cdot E_{\rm fit}$, $0.5 \cdot E_{\rm fit}$, and $0.6 \cdot E_{\rm fit}$. The resulting TS values exhibit very little variation with

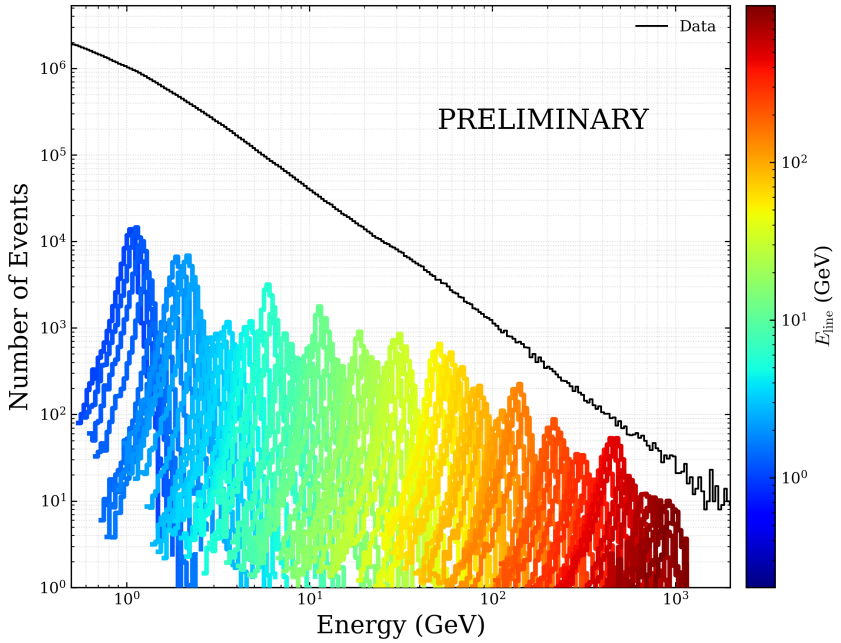

Figure 4.10: Example of the results from the line feature search using a sliding energy window (width 0.5) fit in $R180$ using all event types combined. Fitted signal features counts superimposed on the photon count spectra.

respect to the choice of energy window width, indicating that the analysis is robust against this selection.

In all ROIs and for all window configurations, the TS remains below 25 across the whole scanned energy range. This implies that any observed spectral feature corresponds to a local significance below 5σ. Similar conclusions are obtained when performing the analysis on individual event-type subsamples or on the full unpartitioned event sample. No significant line-like excess is observed in any of the cases considered.

Since no significant excesses in the TS are detected, I have evaluated the upper limits (ULs) on line signal strength parameter s. In Fig. 4.12, the 95% confidence level (CL) ULs on the intensity of a possible DM-induced gamma-ray line are reported as a function of the line energy. The analysis combines the four event-type subsamples (`EDISP0`, `EDISP1`, `EDISP2` and `EDISP3`), and results are provided for the five ROIs using different energy window widths. The constraints are nearly

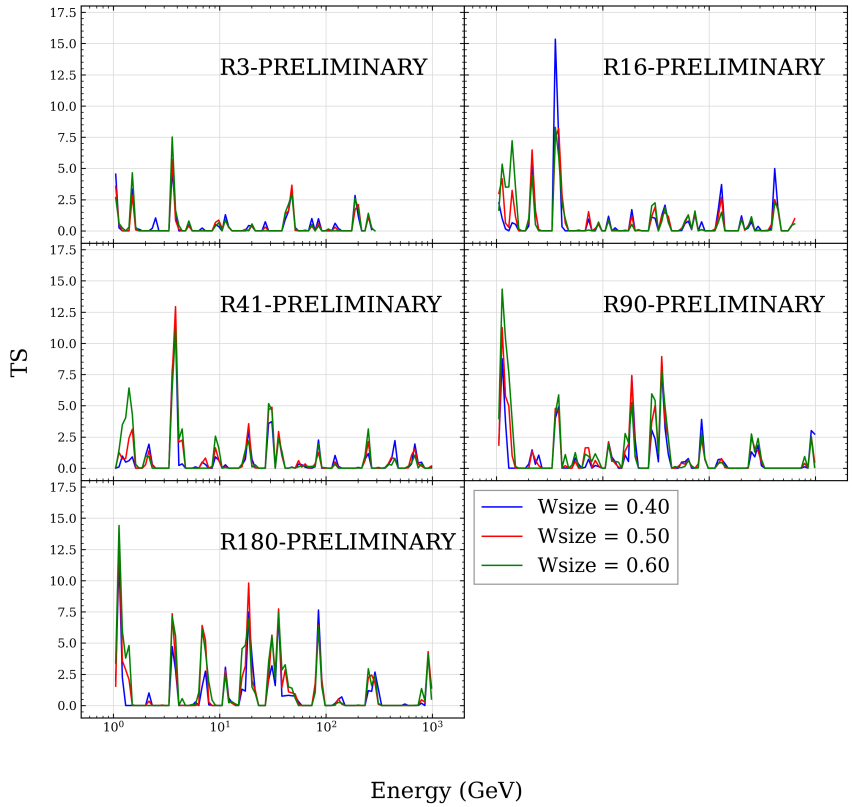

Figure 4.11: TS as a function of energy for the combined analysis of the four subsamples corresponding to the different event types EDISP0, EDISP1, EDISP2, EDISP3, calculated for the five different ROIs. The colored lines correspond to different energy window size with w of 0.4, 0.5 and 0.6, respectively. No peculiar excesses are found.

independent of the chosen window size, indicating the robustness of the results with respect to this selection. A comparison is also made with the limits derived by the Fermi-LAT Collaboration in Ref. [51]. Across the entire energy range, the constraints obtained in the present work are more stringent. In particular, at low energies the improvement reaches a factor of ~ 250, while at higher energies the current limits remain slightly stronger. This improvement, especially in the low-energy regime, is attributed not only to the use of a combined likelihood analysis across event types, but also to a more accurate modeling of the smooth background component. While Ref. [51] employed a power-law model over the full

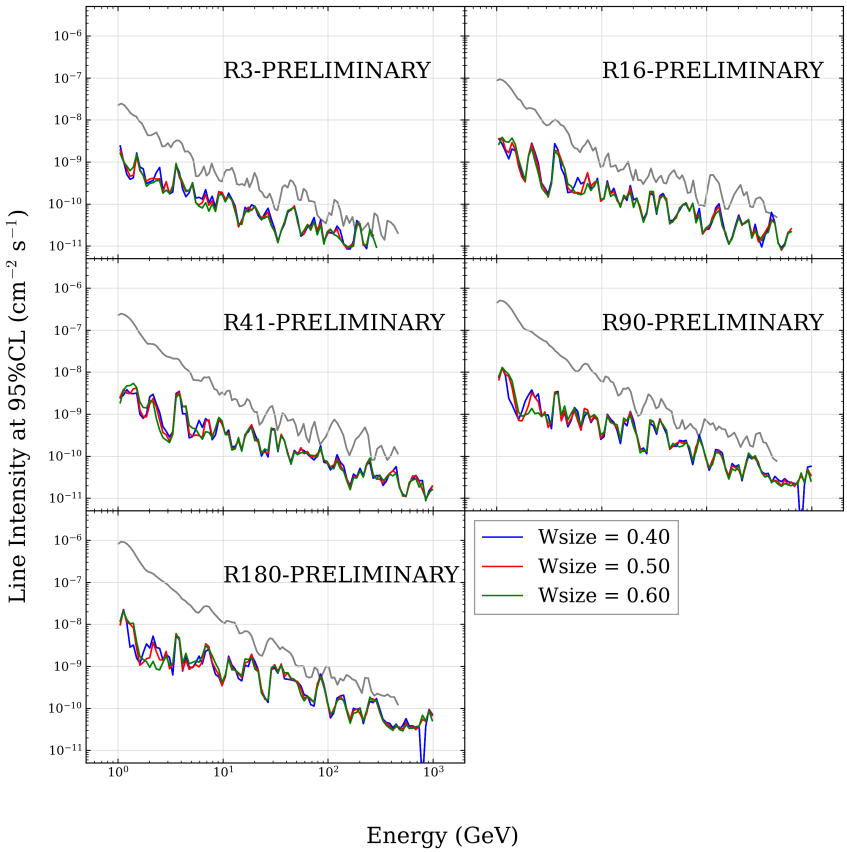

Figure 4.12: ULs at 95% CL on the line flux as a function of energy for the combined analysis of the four subsamples corresponding to the different event types `EDISP0`, `EDISP1`, `EDISP2` and `EDISP3`, calculated for the five different ROIs. The colored lines correspond to different energy window sizes, with $w = 0.4$, 0.5 and 0.6, respectively. The grey lines indicate the limits in Ref. [51].

energy range, the present analysis uses a log-parabola model below 10 GeV, which better accounts for the spectral curvature observed in this region (see Fig. 4.3). In addition, the LAT energy dispersion is used in the best-fit procedure for both smooth and feature components.

Since both TS and ULs exhibit a remarkable insensitivity to the choice of window size, we deem $w = 0.50$ to be the best choice for the window size. In all subsequent steps of this analysis to search for line-like features, we will assume this width.

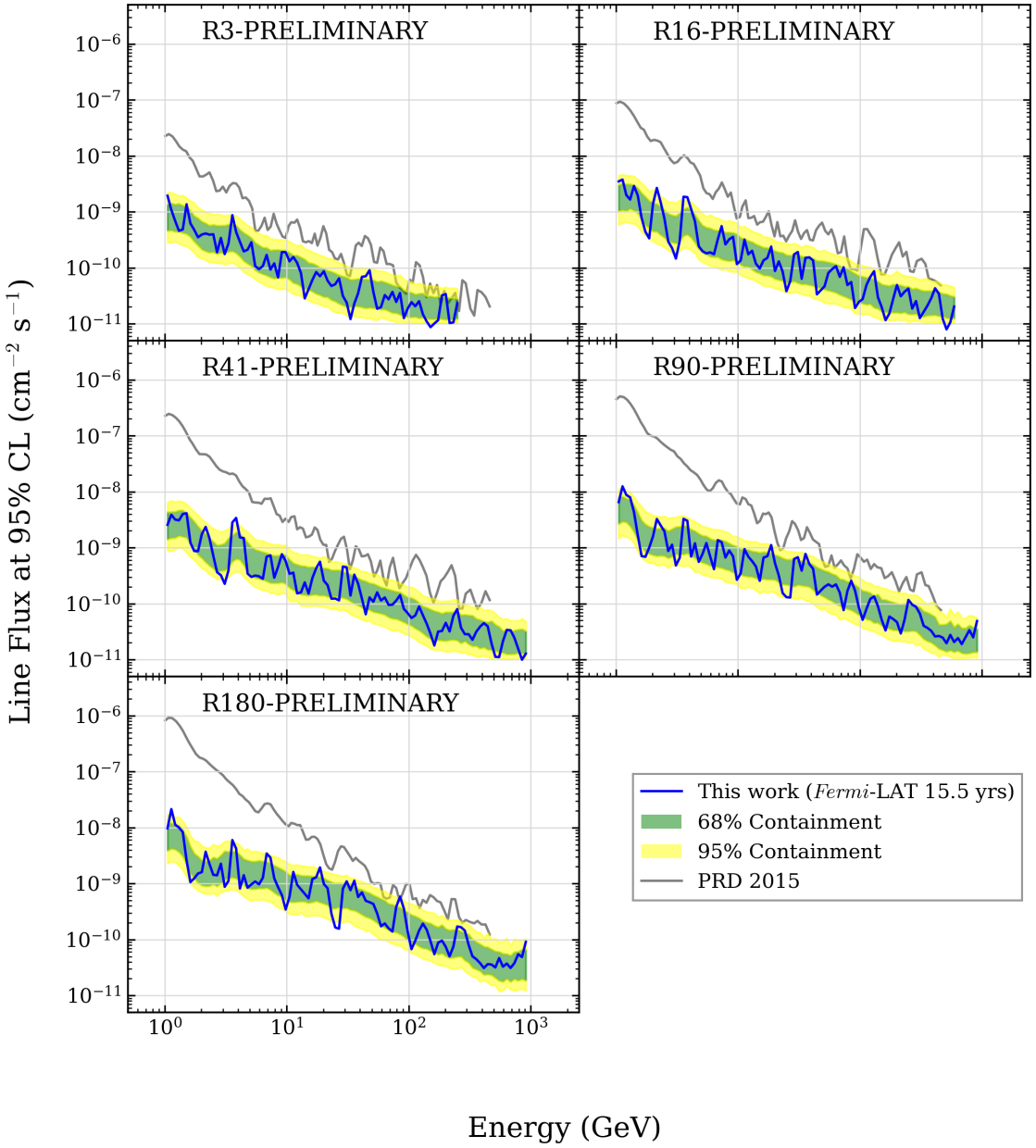

Figure 4.13: line flux ULs at 95% CL in R3, R16, R41 and R180 for the combined analysis. The green and yellow bands show the 68% and 95% expected containment bands derived from 1000 background-only Monte Carlo simulations. The limits obtained in Ref. [51] in the same ROIs are also shown (grey line).

4.5.1 Sensitivity to the null hypothesis in the line search

Fig. 4.13 shows a comparison of the ULs at 95% CL on the line flux obtained in the combined analysis of the four subsamples corresponding to the different event types with the predictions from the pseudoexperiments, as explained in Sec. 4.4.3. The data shown are those of the analysis performed selecting a window size $w = 0.50$. The green and yellow bands represent the central 68% and 95% containment bands, evaluated from the quantiles of the distributions of the ULs from the pseudoexperiments. The lower and upper bounds of the green (yellow) band correspond to the 16% and 84% (2.5% and 97.5%) quantiles of the distributions of the ULs at 95% CL evaluated in the pseudoexperiments. The measured values lie within the containment bands, and are therefore consistent with the expectations for the null hypothesis. The ULs on the parameter s can be converted into ULs on the velocity-averaged annihilation cross section $\langle\sigma_{ann}v\rangle$ or into lower limits (LLs) on the DM decay time τ using eqs. 2.6 and 2.7 in Sec. 2.2.2, replacing the differential gamma-ray spectrum $\frac{dN_\gamma}{dE}$ with the spectrum of a line at the energy E_{line}, i.e. $2\delta(E - E_{line})$ in the annihilation case and $\delta(E - E_{line})$ in the decay case. Taking into account that in the annihilation scenario $E_{line} = m_\chi$, while in the decay case $E_{line} = m_\chi/2$, when integrating with respect to energy, we obtain the following equations:

$$\Phi_{ann}(E_{line}) = \frac{1}{4\pi}\frac{\langle\sigma_{ann}v\rangle_{\gamma\gamma}}{{m^2}_\chi}J_{ann}(RoI) \tag{4.20}$$

$$\Phi_{dec}(E_{line}) = \frac{1}{4\pi}\frac{1}{m_\chi\tau_\chi}J_{dec}(RoI) \tag{4.21}$$

Plugging in the equations the upper limits at 95% CL on the line flux in each ROI, (s_{95}), one can obtain the corresponding upper/lower limits on $\langle\sigma_{ann}v\rangle$ or τ_χ:

$$\langle\sigma_{ann}v\rangle_{\gamma\gamma} \leq \frac{4\pi m_\chi^2}{J_{ann}(RoI)}s_{95} \tag{4.22}$$

$$\tau_\chi \geq \frac{J_{dec}(RoI)}{4\pi m_\chi}\frac{1}{s_{95}} \tag{4.23}$$

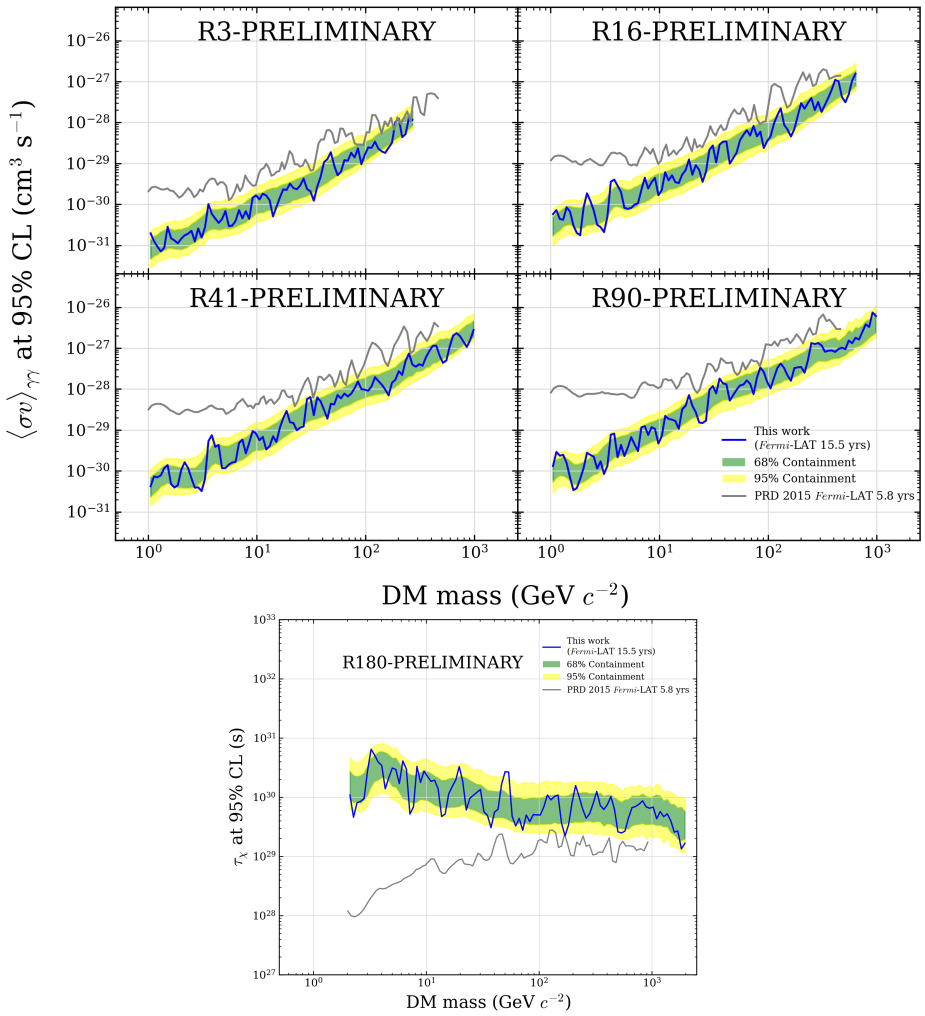

Figure 4.14: **Upper panel**: Upper limit at 95% CL on the velocity-averaged cross section $\langle\sigma_{ann}v\rangle$ as a function of energy from the analysis of R3, R16, R41 and R90 with $w = 0.5$. **Lower panel**: Lower limit at 95% CL on the decay time τ_χ as a function of energy from the analysis of R180 with $w = 0.5$. The green and yellow bands show the 68% and 95% expected central containment bands derived from 1000 background-only Monte Carlo simulations. The limits have been obtained from the combined analysis of the subsamples corresponding to the different event types. The grey lines indicate the limits in Ref. [50].

To convert the constraints on the line intensities into constraints on the physical quantities $\langle\sigma v\rangle_{\gamma\gamma}$ and τ_χ the values of the J-factors are needed. They are reported in Table 4.2 and are extracted from Ref. [51]. Fig. 4.14 shows the containment bands obtained for both the velocity-averaged annihilation cross section and the

Annihilation		
RoI	**Profile**	**J-factor** [10^{22} GeV^2 cm^{-5}]
R3	NFWc	13.9
R16	Einasto	8.48
R41	NFW	8.53
R90	Isothermal	6.94
Decay		
RoI	**Profile**	**J-factor** [10^{23} GeV cm^{-2}]
R180	NFW	2.46

Table 4.2: J-factors of the different ROIs considered in the analysis. They have been evaluated for the DM profiles for which each ROI is optimized and for both WIMP annihilation and decay. The same values were used in previous researches of *Fermi*-LAT collaboration [50].

decay time for the ROIs for which these are optimized. Superimposed on the bands, the upper limits on $\langle\sigma_{ann}v\rangle_{\gamma\gamma}$ and lower limits on τ_χ at 95% CL for the analysis performed with $w = 0.50$ are shown. The constraints from the present analysis are stronger than those in Ref. [51] and are within the expectation bands for the null hypothesis. Fig. 4.15 shows a comparison of the TS obtained in the combined analysis of the different event types with the expectations from the pseudoexperiments. Similarly to the case of the ULs, the 68% and 95% containment bands are evaluated from the quantiles of the TS distributions. Since $TS \geq 0$, the lower bound of both bands is zero, while the upper bounds are the 68% and 95% quantiles of the TS distributions respectively. Almost all the measured TS values lie within the expectation bands from the pseudoexperiments, with a few outliers.

To check whether there is at least a significant feature in the whole energy range scanned, since the energy windows are overlapping, the correlation among the analyses of different energy windows should be taken into account. This is done by evaluating the global significance, as discussed in section 4.4.3. The global significance as a function of the maximum TS is evaluated from the simulated pseudoexperiments. Fig. 4.16 shows the conversion curves obtained for the maximum TS distributions in all the ROIs together with the points corresponding to the measurements performed in this work. Even the most locally significant

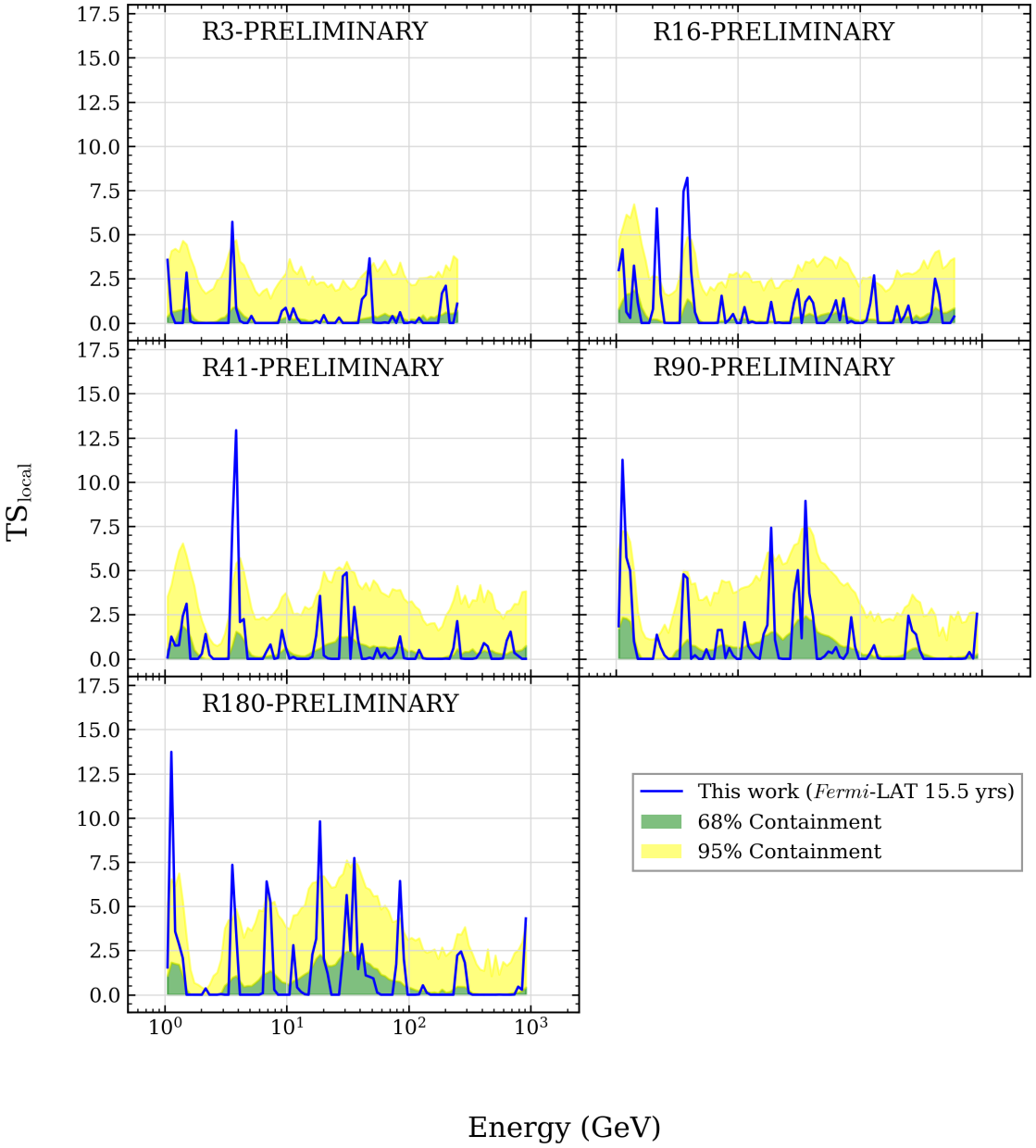

Figure 4.15: TS as a function of energy in R3, R16, R41 and R180 for the combined analysis in the line search case. The green and yellow bands show the 68% and 95% expected containment bands derived from 1000 background-only Monte Carlo simulations. A few outliers can be spotted: in R3, R16 and R41 features with TS of ~ 6, ~ 8 and ~ 13 respectively at $\sim 4\,\mathrm{GeV}$. In any case outliers are quite far from 25.

features turns out to be globally insignificant, as their global significance is $< 0.6\sigma$.

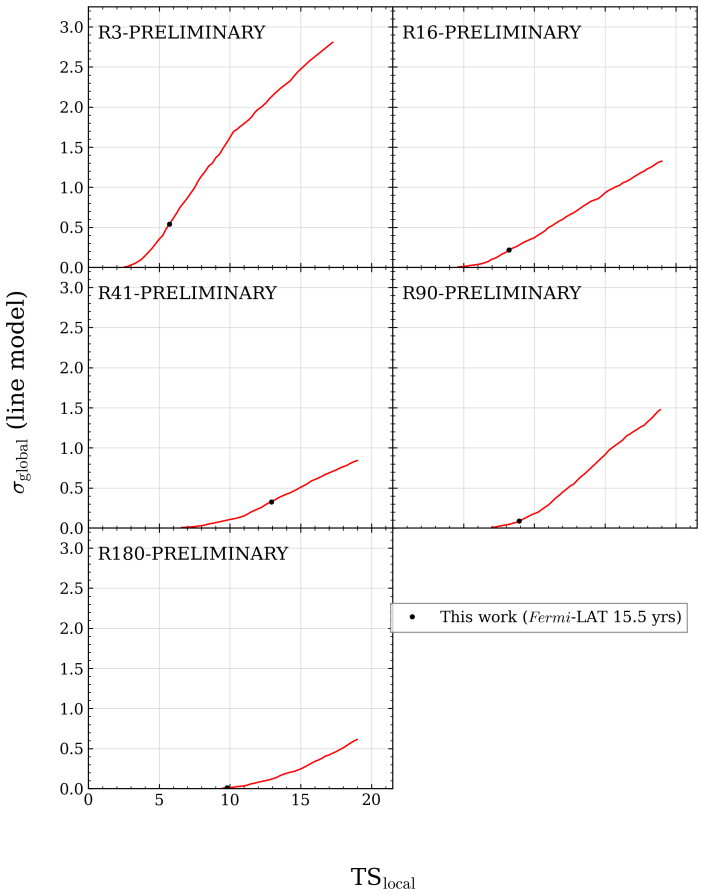

Figure 4.16: Global significance s_{global} as a function of the local TS in R3, R16, R41 and R180 in the line search case. The black dots represent the maximum TS values coming from our data set analysis.

4.6 Search for box features in galactic gamma-ray spectra

Following the considerations of Sec. 2.2.3, we can assume that low-mass mediators produced by self-annihilating DM particles may decay not too far from their production site, possibly affecting the resulting gamma-ray flux at Earth and producing box-shaped spectral features. Moreover, as reported in Eq. 2.18,

assuming that the decay length of the mediators is small with respect to galactic size ($\ll\sim 20-30$ kpc), the effective J-factor reduces to its canonical definition, allowing the use of the same J-factors in Tab. 4.2 as for direct annihilation in gamma rays in the case of line search.

4.6.1 Analysis procedure

Thanks to the assumptions of Sec. 2.2.3, the analysis approach does not differ substantially from the one described in Sec. 4.4: it is a maximum-likelihood fit procedure in sliding energy windows with a different model for the signal and the background features as shown in Eqs. 4.9 and 4.10, where a Heaviside function replaces the Dirac delta in the true energy space.

As before, s and b are the parameters describing the intensities of the box-like features: the former is the actual signal parameter and can be strictly positive, while the latter can be either positive or negative to account for possible systematic effects. The same 185 months dataset described in Sec. 4.1 is used, with the same 5 ROIs and EDISP types, enabling also in this case a combined-likelihood technique.

4.6.2 Results for box-shaped features search

From the fitted flux parameters, one can evaluate the photon count spectra. Fig. 4.17 shows the fit results from $R180$, including all event types, as an example of the employed procedure.

Fig. 4.18 reports how the box feature appears and compares to the photon count data and those of the model (with feature).

Analogous considerations as in Sec.4.5 can be made on the substantial independence on the upper limits on box flux from the window size used. Again, in the present section I will discuss the results obtained with $w = 0.50$.

Also in this case a set of 1000 pseudoexperiments is simulated with the background-only hypothesis to which the same analysis chain as for real data is applied. Fig. 4.19 shows a comparison of the ULs at 95% CL on the box flux obtained in the combined analysis of the different event types with the

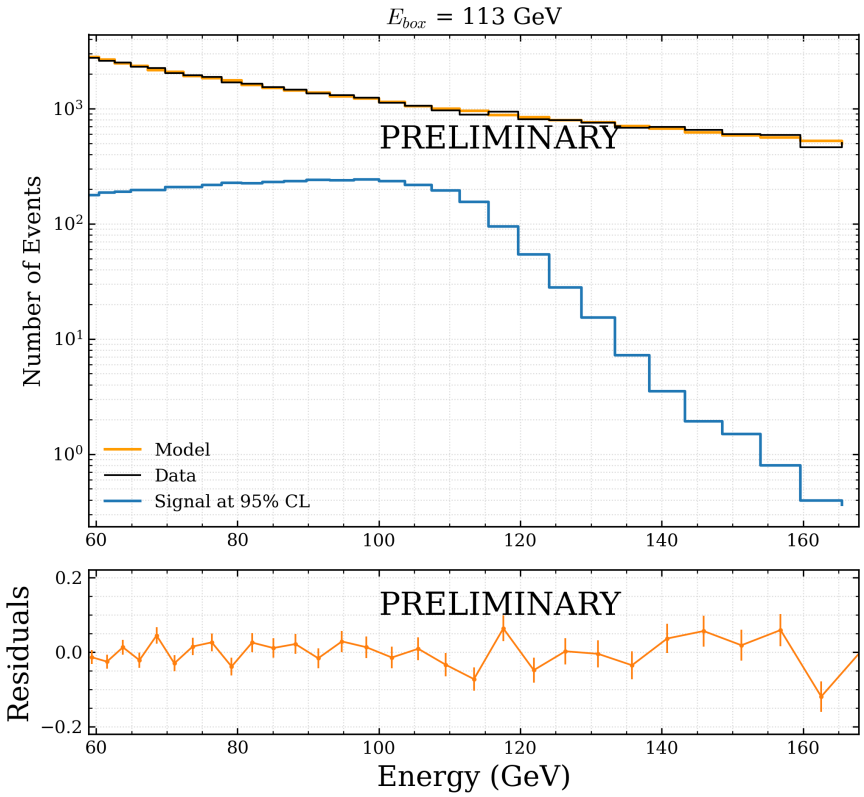

Figure 4.17: Photon counts as observed in the data (black points) and as predicted by the best-fit model including the box-like signal component (blue line) for a single window centered at 113 GeV. The lower inset displays the fractional residuals, defined as (data−model)/model, which typically remain within a 25% range across the scanned energy windows.

predictions from the pseudoexperiments. The lower and upper bounds of the green (yellow) band correspond to the 16% and 84% (2.5% and 97.5%) quantiles of the distributions of the ULs at 95% CL evaluated in the pseudoexperiments. The measured values lie within the containment bands, and are therefore consistent with the expectations for the null hypothesis.

Figure 4.20 shows a comparison of the TS obtained in the box-search using the combined analysis of the different event types with the expectations from the pseudoexperiments. Similarly to the case of the ULs, the 68% and 95% containment bands are evaluated from the quantiles of the TS distributions. Since $TS \geq 0$, the lower bound of both bands is zero, while the upper bounds are the 68%

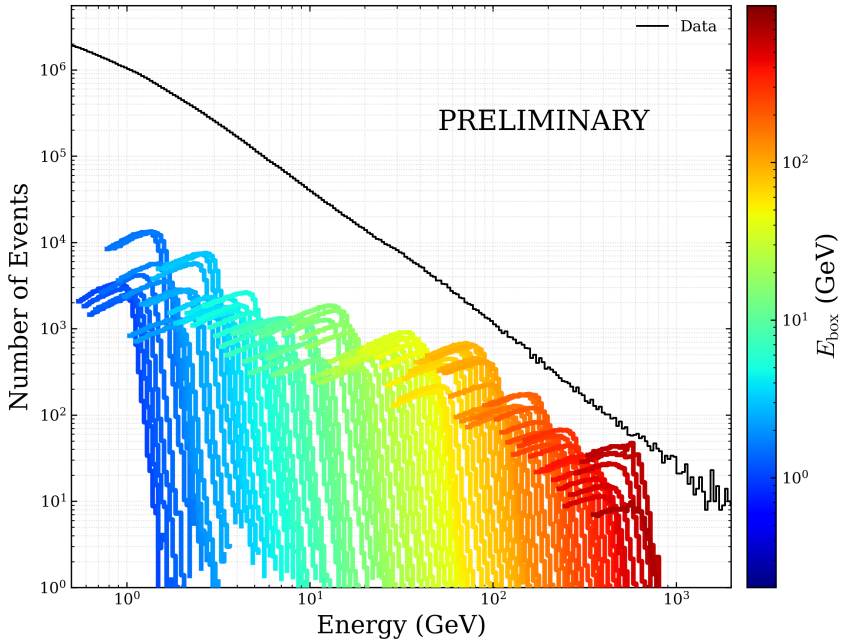

Figure 4.18: Example of the results of the box-shaped feature search using a sliding energy window fit in $R180$, with all event types combined, with fitted box-like features overlaid on the photon count spectra.

and 95% quantiles of the TS distributions respectively. Almost all the measured TS values lie within the expectation bands from the pseudoexperiments, with a few outliers especially in R90 and R180 in the energy interval from 10 GeV to 100 GeV, that in any case do not reach relevant local significance ($TS > 25$).

These limits can be converted into constraints on the annihilation cross section in similar fashion to the line search case. However, there are some substantial differences. First of all, the velocity-averaged annihilation cross section in this case involves DM particles converting into low-mass mediators. These particles are produced back-to-back, we then assume that all of them decay into gamma-rays, thus the one mediator that decays in a direction towards Earth produces 2 gamma-rays. Therefore, as illustrated by Ref. [52] that describes this scenario, we should be able to detect an excess as a box-shaped spectral feature, recovering the same initial and final state that we explore in the line case: from 2 DM particles we get 2 gamma-ray photons. In this way, the formula by means of which we can

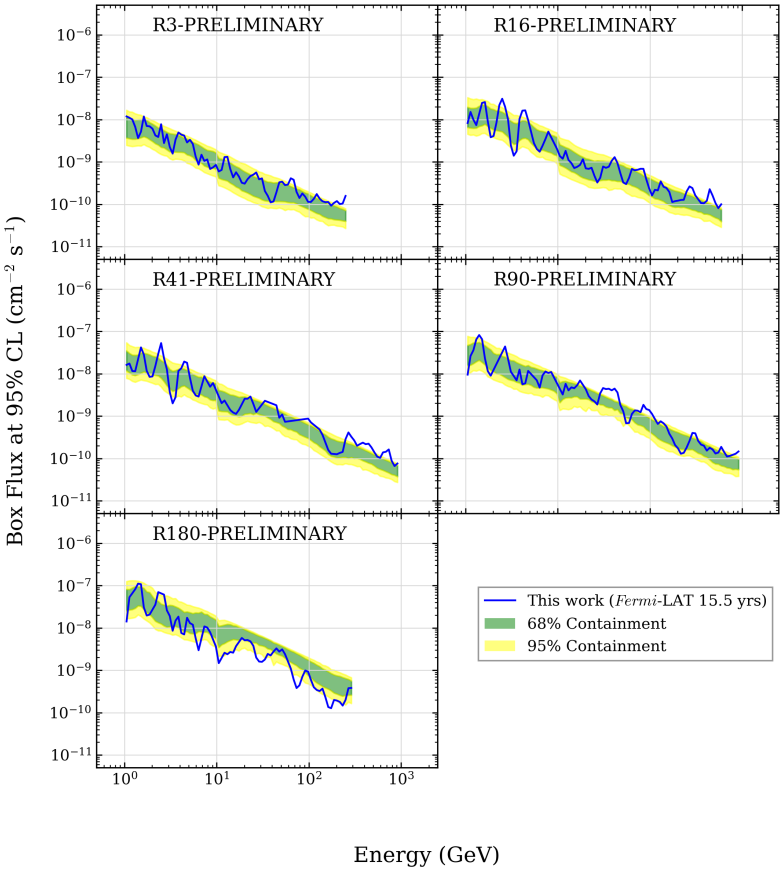

Figure 4.19: box flux at 95% CL in R3, R16, R41 and R180 for the combined analysis. The green and yellow bands show the 68% and 95% expected containment bands derived from 1000 background-only Monte Carlo simulations.

extract constraints on the annihilation cross section is very similar to the one of the line case (Eq. 4.20):

$$\Phi_{ann}(E_{box}) = \frac{1}{4\pi} \frac{\langle \sigma_{ann} v \rangle_{\Phi\Phi}}{E^2{}_{box}} J_{ann}(ROI) \tag{4.24}$$

where the J-factors used in each ROI are the same reported in Table 4.2. From Eq. 4.25, the relation for the upper limit on $\langle \sigma_{ann} v \rangle_{\Phi\Phi}$ is:

$$\langle \sigma_{ann} v \rangle_{\Phi\Phi} \leq \frac{4\pi m_\chi^2}{J_{ann}(RoI)} s_{95} \tag{4.25}$$

where we also considered that $E_{box} = m_\chi$

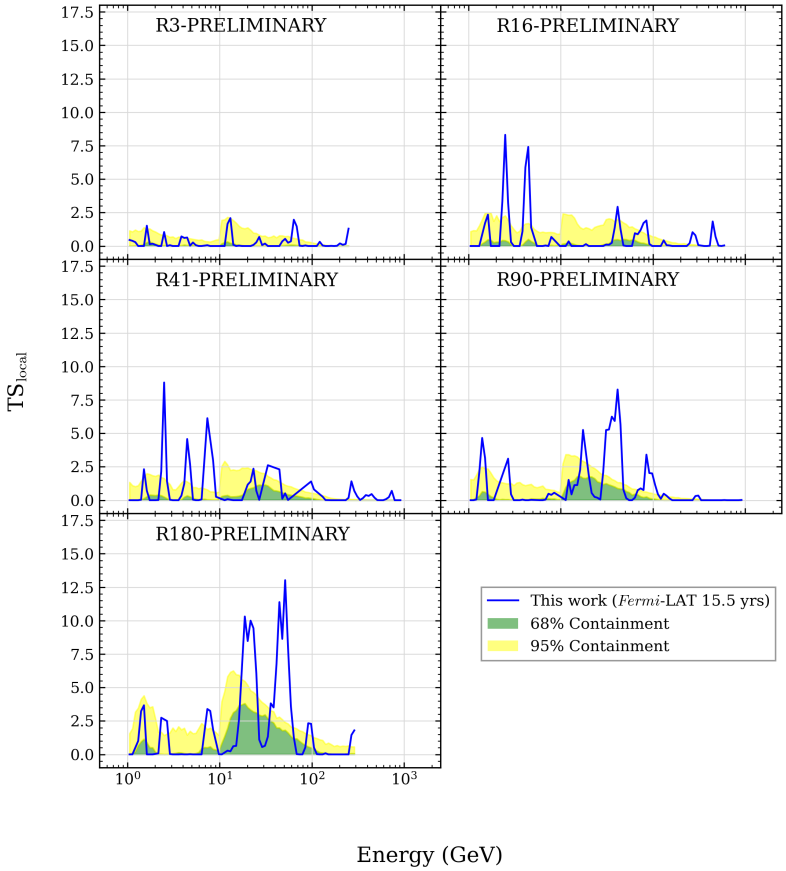

Figure 4.20: TS as a function of energy in R3, R16, R41 and R180 for the combined analysis in the box search case. The green and yellow bands show the 68% and 95% expected containment bands derived from 1000 background-only Monte Carlo simulations. A few outliers can be spotted: in R90 and R180 features with TS of ~ 7.5 and ~ 12.5, albeit still not locally significant.

Fig. 4.21 shows the containment bands obtained for the velocity-averaged annihilation cross section for the first 4 ROIs for which these are optimized. Superimposed on the bands, the upper limits on $\langle \sigma_{ann} v \rangle_{\Phi\Phi}$ at 95% CL for 0.50 window size are shown. These upper limits are compatible with the idea that DM is a thermal relic.

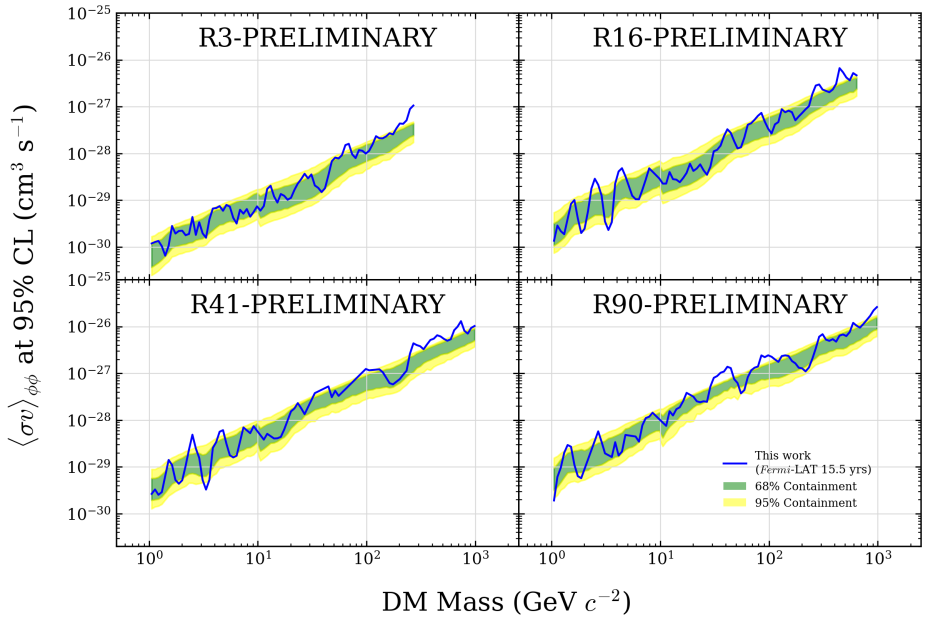

Figure 4.21: Upper limit extracted from the box search at 95% CL on the $\langle\sigma_{ann}v\rangle$ annihilation cross section as a function of energy for 0.50 energy window only, from the analysis of R3, R16, R41 and R90.

4.6.3 Global significance

Using the TS distributions obtained in the 1000 pseudoexperiments in the box search case, we use the same approach shown in Sec.4.5.1 to extract the containment bands reported in Figs.4.19, 4.20, 4.21 and to retrieve a global significance indicator assuming the TS distribution from the pseudoexperiments follow a half-normal distribution. Fig. 4.22 reports all the conversion curves for each ROI. The most globally significant potential features appear in R90 and R180. Since no TS values from our analysis correspond to a global significance value exceeding 2σ, we can conclude that the results are consistent with the null hypothesis.

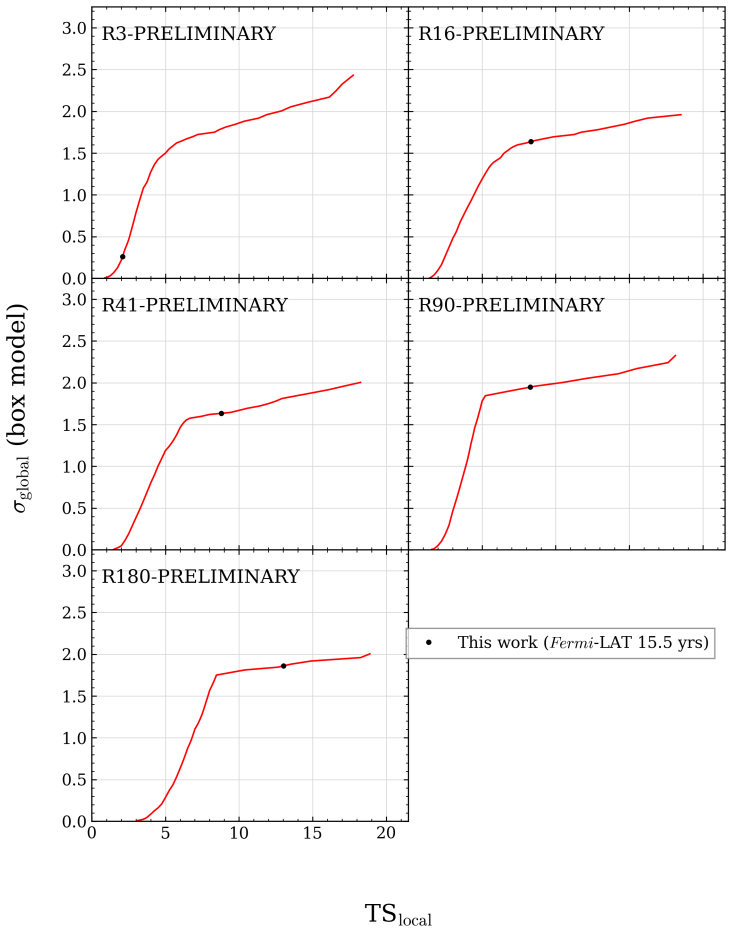

Figure 4.22: Global significance s_{global} as a function of the local TS in R3, R16, R41 and R180. The black dots represent the maximum TS values coming from our data set analysis.

4.7 A cross-check study with an Earth Limb photons dataset

To test the robustness of the analysis procedure presented in this work, I have used a dataset consisting of Earth's limb photons. Earth's limb photons are the result of the interactions of charged cosmic rays entering the atmosphere near grazing incidence: their interactions with atmospheric nuclei produce forward hadronic showers with a fraction of neutral pions, which notoriously decay into gamma rays, resulting in a remarkably bright gamma-ray signal from the Earth's limb as seen from orbit. Even though our planet is expected to be embedded

Observation time	August 2008 - December 2023
Energy Range	$[10\,\mathrm{MeV} - 2\,\mathrm{TeV}]$
Maximum zenith angle θ_Z	$[105^\circ - 115^\circ]$
Event class	256 (CLEAN)
Event Type	Front + Back
Data quality	DATA_QUAL==1 LAT_CONFIG==1 IN_SAA!=T
Rocking angle cut	$> 70^\circ$
Separation between LAT z-axis and GC	$> 30^\circ$

Table 4.3: Summary of the cuts applied in the data selection for the Earth Limb photons dataset.

in a DM halo as well, we reasonably assume that we can not currently observe significant DM signal features from Earth's Limb gamma-ray emission. Therefore, this population of limb photons may be used to validate our analysis procedure, again verifying consistency with the null hypothesis. Fig. 3.4 shows the geometry scheme of gamma-ray production resulting from cosmic-ray interactions in the Earth's atmosphere. It defines the key observational angles: the zenith angle (θ_z), the spacecraft rocking angle (θ_r), and the gamma-ray incidence angle (θ). From *Fermi*'s orbital altitude (~ 565 km), assuming that the atmosphere extends for 30 km, from geometrical considerations it can be derived that the gamma-ray emission happens at θ_z in the range $\sim 110^\circ$ to 112°. I selected photons with a maximum zenith angle between 105° and 115°: a broader interval to be more confident in including all available statistics for this sample. Moreover, two additional cuts were also required:

1. A cut on the rocking angle to be higher than 70°, to select a photon population whose off-axis angle θ distribution is compatible with that of $R180$, the all-sky ROI of the main analysis. This is reported in Fig. 4.23, where different attempted selections show that a less restricting cut, like rocking angle $> 35^\circ$, selects an off-axis angle distribution that peaks at higher

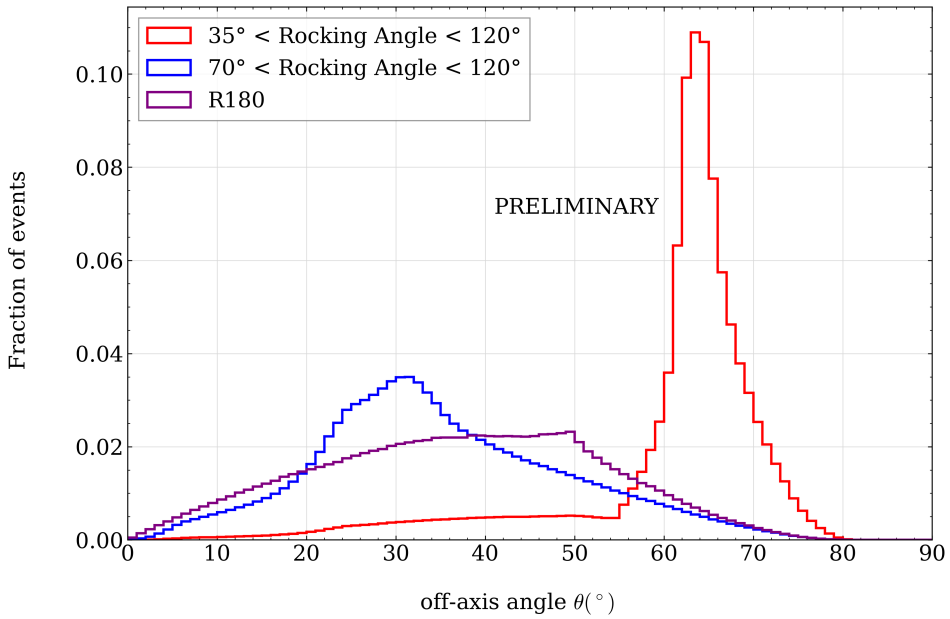

Figure 4.23: Normalized off-axis angle θ distributions of the Earth limb photons without the rocking angle cut (red line) and with the rocking angle cut (blue line) compared with the distribution of R180 (purple line). The peak appearing to be centered around $65°$ is removed selecting events with rocking angles $> 70°$, shaping the final distribution in a similar way to that of R180.

angles;

2. A cut on the angular separation between the LAT z-axis projection onto the celestial sphere and the Galactic Center to be higher than $30°$, to avoid at most possible contamination from the GC emission.

This further requirement on the rocking angle and consequent homogeneity between the off-axis angle distributions ensures that the Earth's limb control sample and the main analysis dataset have the same possible systematic effects related to the off-axis angles.

All these selection requirements are summarized in Table 4.3. The photon limb dataset, once projected onto galactic coordinates, appears as in Fig. 4.24. The Limb ROIs were selected to have the same integral counts as the first two

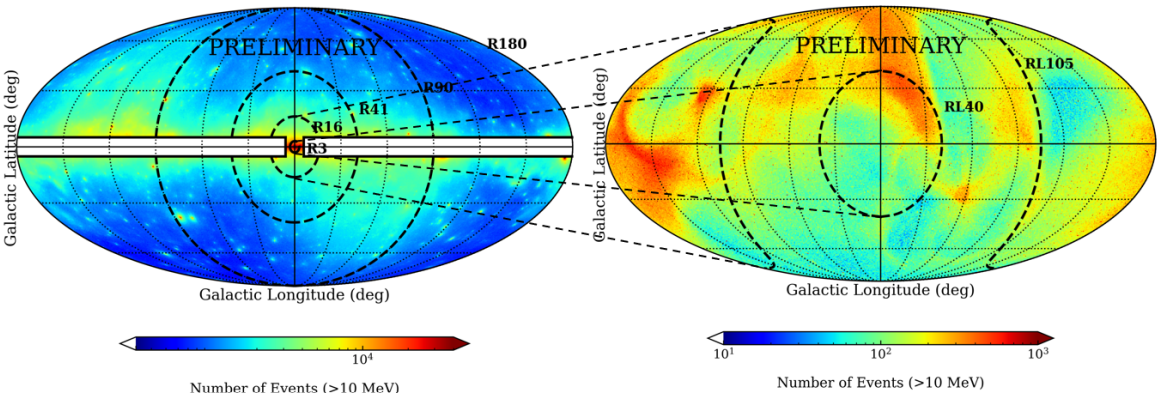

Figure 4.24: Count map of the Galactic dataset with the first 2 ROIs (R3 and R16, left panel) and the corresponding ones in the limb dataset projected onto galactic coordinates, RL40 and RL105 (right panel). Since the total photon counts of the limb dataset is significantly lower, the corresponding ROIs encompass wider regions of the sky.

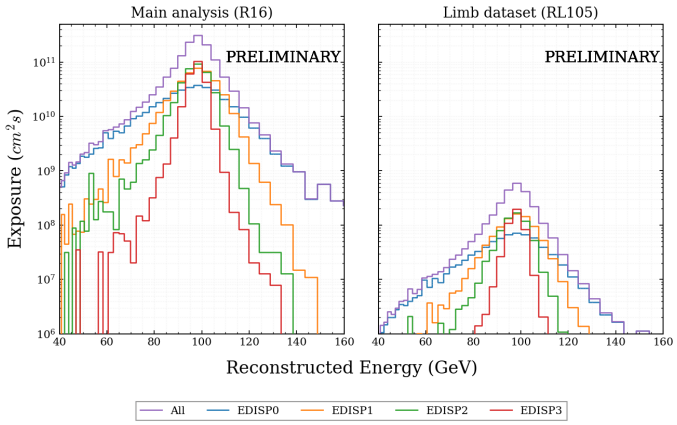

Figure 4.25: Exposure corresponding to R16 and RL105 for the main analysis dataset (left panel) and the limb sample (right panel) respectively vs observed energy for all event types, at fixed true energy of of 100 GeV. The exposure in the ROI differs of a factor of ~ 250 for any event type.

smallest ROIs from the main analysis, $R3$ and $R16$, to have comparable statistics for the consistency check. Since the limb photon counts per pixel are considerably less with respect to the main dataset, the corresponding angular apertures are larger: $RL40$ in the Limb sample corresponds to $R3$ and $RL105$ corresponds to $R16$.

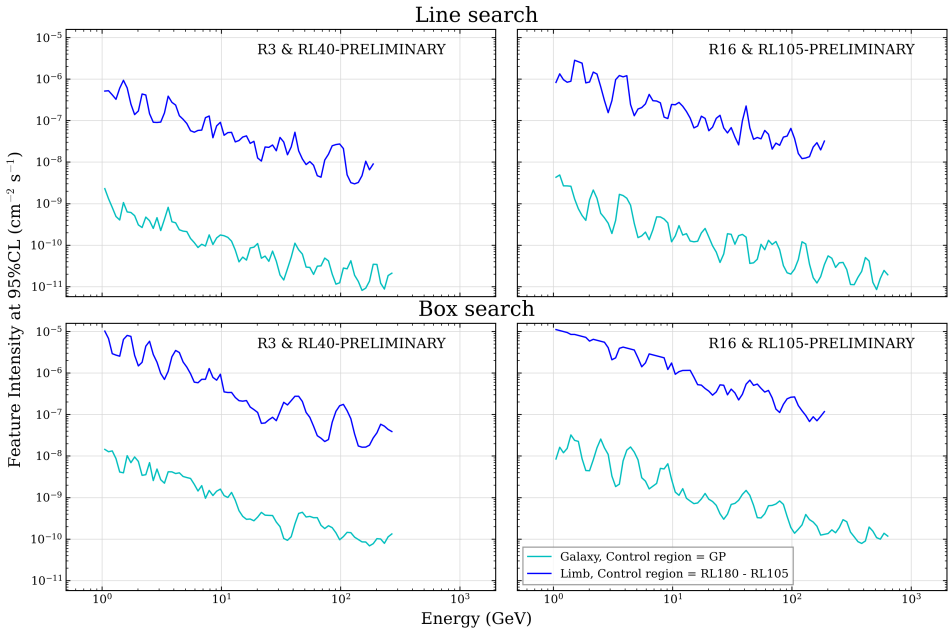

Figure 4.26: Upper limits at 95 % CL on the feature signal intensity for both line and box features searches, comparing the ROIs from the main analysis ($R3$ and $R16$) with the corresponding ones from the limb analysis ($RL40$ and $RL105$ respectively). The limits between the 2 datasets differ of a factor ~ 250, which is the same factor between exposures, as reported in Fig. 4.25.

Applying now the same analysis procedure, since the exposure of the limb dataset is lower, as reported in Fig. 4.25, for the same counts the expected upper limits on the flux value are higher than those from the main analysis. This is required by Eq. 4.4 that states, at fixed expected counts, that if exposure decreases, the associated gamma-ray flux should increase, and so upper limits on signal flux as well.

As a matter of fact, the trend of these limits appears to be consistent, as reported in Fig. 4.26. The limits scale by a factor of ~ 250, which is indeed due to the exposures, that scale of the same quantity. Therefore, to quantitatively compare the limits between the two datasets we used the signal flux fraction, defined as:

$$f = \frac{\Phi_{feature,UL_{95\%CL}}(E_{fit})}{\Phi_{smooth}(E_{fit})} \tag{4.26}$$

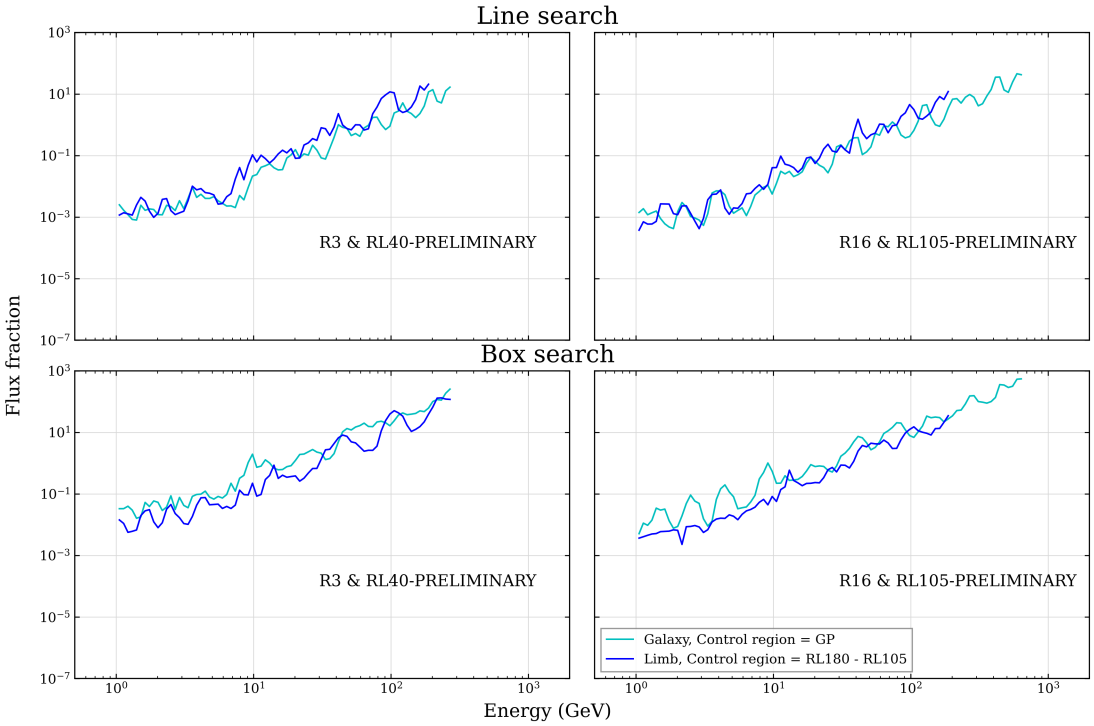

Figure 4.27: Signal flux fraction as defined in Eq. 4.26 in the line case (left panel) and the box case (right panel) in R3 and R16 (RL40 and RL105 for the limb dataset) as a function of observed energy. The sky-blue line represents the galactic datasets limits, while the dark blue one those from the limb dataset. Limb events are characterized by a significantly lower exposure for the same counts, so a comparison is possible only using flux fraction. Signal flux fractions, on the other hand, are consistent between the two datasets in both searches.

where $\Phi_{smooth}(E_{fit})$ comes from the model definition in Eq. 4.6. In this way, a more general quantity is obtained that allows comparison between datasets characterized by different exposure. The signal flux fraction as a function of the fit energy is reported in Fig. 4.27. The values between the two datasets are compatible, and this is an indication of the robustness of the analysis procedure of this work.

4.8 Summary

The analysis here presented benefited from the work carried by the *Fermi*-LAT Collaboration in previous publications [50, 51, 88, 89].

The most relevant novel element is the introduction of a control region to account for possible systematic effects that could mimic a real feature, with a 3-step procedure that employed firstly fitting signal ROIs, then the GP background-only control-ROI and finally a joint fit of all parameters in signal ROIs. In this way the fit procedure accounts for any possible instrumental systematic effect by means of the background feature parameter b.

A more accurate model for the smooth background component has been also used and a combined likelihood function between the different event types has been built, which proved to be crucial in the constraining power of the procedure.

A dedicated fit procedure was applied to search for possible line-like and box-like features in the Galactic gamma-ray spectra in a very wide energy range (from 1 GeV to 1 TeV). Although no evidence of such features were found, constraints were set on the possible signal intensities. The ULs at 95% CL on the signal intensity are found in the range $(10^{-10} - 10^{-8})\,\mathrm{cm}^{-2}\mathrm{s}^{-1}$, and decrease with increasing energy. The corresponding ULs on the velocity-averaged annihilation cross sections $\langle\sigma_{ann}v\rangle$ lie between 10^{-31} and $10^{-27}\,\mathrm{cm}^3\mathrm{s}^{-1}$, while the lower limits on the DM decay times τ_χ are found in the range between 10^{29} and 10^{31} s. The constraints obtained in the present work are stronger than those obtained by the *Fermi*-LAT Collaboration in previous analyses involving line search [50, 51, 88, 89]. This improvement is due not only to the better modeling of the smooth background component of the spectra, but also to the better understanding of systematics and the use of a combined likelihood analysis technique as well.

The present results exclude the existence of spectral features in the galactic gamma-ray spectra in an even wider energy range, since no feature exceeds the global significance of 0.55σ in the line search case, 2.2σ in the box search case. As far as the line search is concerned, we set constraints which are up to two orders of magnitude stronger than those in the Fermi-LAT 2015 analysis. [51].

Finally, this work explores the possibility to search for box-like spectral features using a dataset made up of galactic photons, a scenario that was up to now not deeply explored in works from *Fermi*-LAT collaboration.

Chapter 5

Perspectives of spectral line searches as signature of DM with the future APT detector

In this chapter, moving from the procedure developed to search for line-like and box-like features in the *Fermi*-LAT data, a study on the perspectives of future detectors is presented, and in particular the case of the Advanced Particle-astrophysics Telescope (APT) [162] will be discussed. I will evaluate the sensitivity to DM line-like spectral features in galactic gamma rays of an hypothetic APT-like detector, making considerations on its DM detection capabilities.

5.1 Simulated data sample

As mentioned in Sec. 3.9, the APT detector is designed to have higher FOV and exposure than the *Fermi*-LAT, mainly because of its Sun–Earth Lagrange orbit, which eliminates Earth occultation and all nuisances from the SAA.

APT will have 10 times the on-axis effective area of the *Fermi* LAT, i.e. 10 $m^2\ yr$ and in this study I will assume an hypothetical APT-like detector to have a total exposure of of $\sim 50\ m^2\ yr$. This value is taken to be almost 10 times the

total exposure of the *Fermi*-LAT for the main analysis discussed in Chapter 4, which is $\sim 6.35\ m^2\ yr$.

I estimate that, for an APT-like detector, which has 10 times the average effective area of the *Fermi* LAT, this exposure can be reached in 12.2 years assuming that APT works like the LAT, i.e. observing photons impinging the detector from the front. However, since APT will not have to face Earth occultation, it will be able to operate as two *Fermi* LATs back-to-back, thus halving the time required to reach this exposure.

I take as a template for the sensitivity study the galactic diffuse gamma-ray emission (see Sec. 2.2.1), to avoid contamination from known astrophysical sources. In the standard *Fermi* LAT analysis, the galactic diffuse model is usually provided by the collaboration and consistently used [168]. In order to have an instrument-independent template, whose energy grid is finer and extends beyond the limits of the *Fermi* LAT model, here I take as a reference the `DRAGON2` simulation of galactic gamma-ray diffuse emission described in Ref. [169].

In that work, the authors developed a set of inelastic and inclusive cross sections using the `FLUKA` [170] Monte Carlo nuclear code and validated them against CR data. Subsequently, the cross sections are implemented in the `DRAGON2` [171] code to model the spectra of cosmic-ray nuclei up to $Z = 26$ and to reproduce the secondary-to-primary ratios of B, Be, and Li. Finally, the production cross sections for gamma rays, calculated with `FLUKA` as well, are incorporated into the `Gammasky` code to generate diffuse gamma-ray sky maps and the local H I emissivity spectrum, yielding very good agreement with data from the *Fermi* LAT.

Fig. 5.1 reports the gamma-ray intensity maps obtained from `Gammasky` reported in Ref. [169]. On the lower-right panel, the diffuse gamma-ray model commonly used in *Fermi* LAT analysis is reported as well. This last template provides gamma-ray intensities for just 30 bins in energy from 10 MeV to 500 GeV; thanks to the simulation, this number is extended to 320, from 10 MeV to 1 TeV.

From the template for gamma-ray intensities per pixel at fixed energies, we can

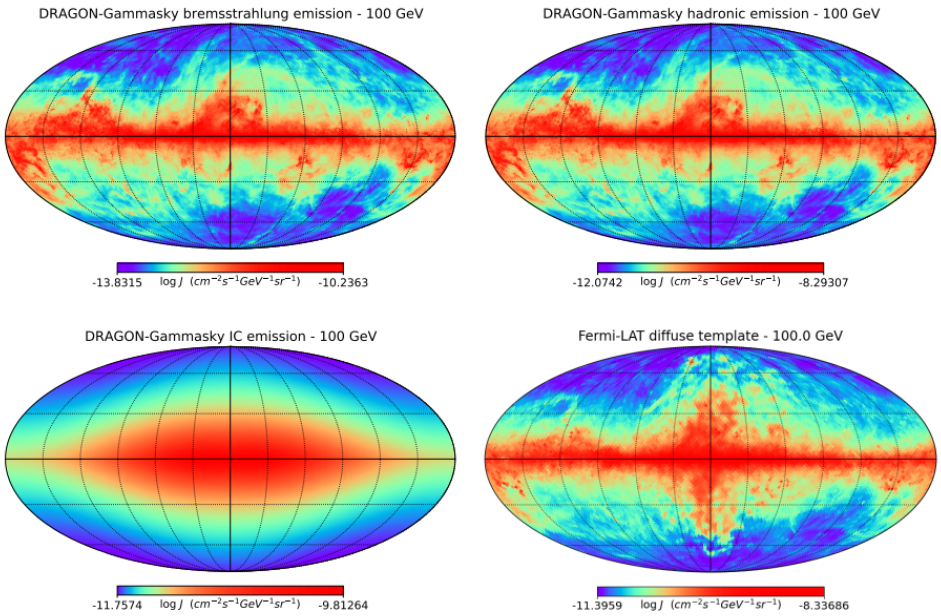

Figure 5.1: Gamma-ray intensity maps of the Galaxy in Mollweide projection, corresponding to the propagation parameters derived from the B/C analysis using the FLUKA cross sections. The upper-left panel shows the bremsstrahlung emission, the upper-right panel displays the gamma-ray emission from π^0 decays, and the lower-left panel presents the inverse Compton (IC) emission. For comparison, the lower-right panel shows the *Fermi*-LAT diffuse emission template, based on the first eight years of data (PASS 8; P8_R3), as provided in `gll_iem_v07.fits` [168]. Plots taken from [169].

retrieve the photon counts distribution in energy per pixel:

$$\mu(E,\psi) = \int dE' \; \mathcal{E}(E',\psi) \; I(E') \; D(E|E') \tag{5.1}$$

where $\mathcal{E}(E',\psi)$ is the exposure per pointing direction angle ψ and I is the gamma ray intensity from the `DRAGON` simulation, plus an isotropic contribution (see IGRB in Sec. 2.2.1) consisting of all unresolved extragalactic emission as well as any residual Galactic foregrounds. This isotropic contribution is homogeneous for every pixel and is calculated using the model in Ref. [172]:

$$I_{IGRB}(E') = I_0 \left(\frac{E'}{0.1GeV}\right)^{-\gamma_{\rm IGRB}} e^{\left(-\frac{E'}{E_{\rm cut}}\right)} \tag{5.2}$$

with $I_0 = 10^{-4}$ cm^{-2} s^{-1} sr^{-1} GeV^{-1}, $\gamma_{IGRB} = 2.28$ and $E_{cut} = 206$ GeV. Finally, $D(E|E')$ is the dispersion relation between true energies E' and observed energies E.

The direction ψ is discretized in pixels in the common `HEALPIX` [167] approach, with `nside` $= 128$, thus dividing all the sky into $196,608$ pixels. The simulated sky gamma-ray map is pictured in Fig. 5.2, where the counts in each pixel are summed over all energy bins.

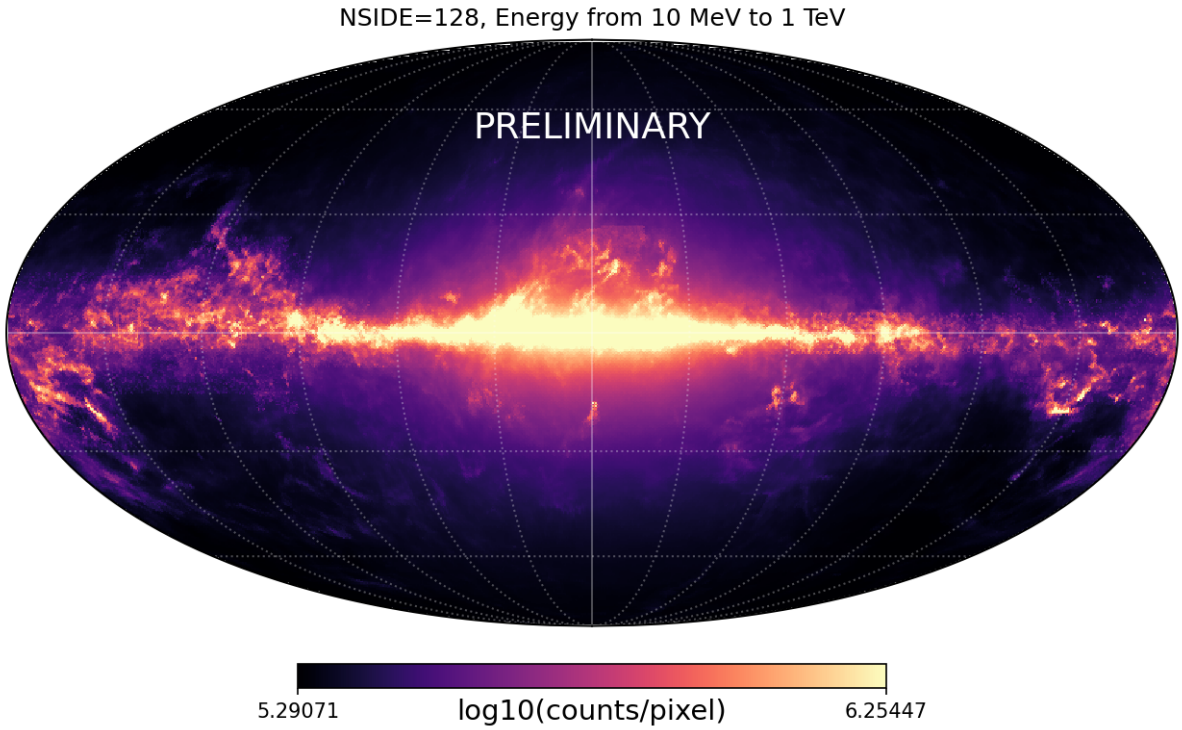

Figure 5.2: Photon count map in galactic coordinates of the gamma-ray sky template used in this sensitivity study. It is an `HEALPIX` map in Mollweide projection with `nside` $= 128$, for a total of $196,608$ pixels.

The integral in Eq. 5.1 is evaluated in true energy space E'. Thus, it is calculated over a grid of reconstructed energies values which conveniently has the same binning of the true energy grid, and for each pixel. Assuming at this level that there is no actual dispersion (that will be implemented in a subsequent step), we have $D(E|E') = \delta(E - E')$.

Since we assumed a flat exposure at all true energies and pixels, the exposure

term can be carried out from the integral, that reduces to a discrete sum of contributions evaluated following the trapezoidal rule as:

$$\mu(E'_j, \psi) = \mathcal{E}\Delta E'_j \frac{I(E'_{j+1}, \psi) + I(E'_j, \psi)}{2} d\Omega \tag{5.3}$$

where at this point each $\mu(E_j, \psi)$ is the template photon count spectrum at each pixel (identified by ψ), in the true energy space. As mentioned, the total exposure is $\mathcal{E} = 50\ m^2\ yr$.

5.2 Sensitivity study with the pseudoexperiments

The counts $\mu(E_j, \psi)$ are used as template distributions to perform, at each pixel, a random poissonian extraction of the photon counts per energy bin. For every pixel and for each energy, I extract a number of counts with a poissonian distribution probability:

$$n(E'_j, \psi) \sim Pois(\mu(E_j, \psi)) \tag{5.4}$$

Then I apply energy dispersion assuming a gaussian smearing: each value $n(E'_j, \psi)$ represents the number of extractions of energies from a gaussian distribution with mean value E'. The energy of each event is given by:

$$E = E'(1 + x\sigma_E) \tag{5.5}$$

where x follows a normal probability distribution, i.e. $x \sim N(0, 1)$ and $\sigma_E = 0.1$, thus assuming an energy resolution of 10%.

Summing the counts for all the pixels in the ROIs, I obtain the random realizations of these spectra, which simulate the observations of diffuse gamma-ray emission from an APT-like detector.

5.3 Fit procedure and results

Each realization yields a photon count spectrum that can be fed to the fitting procedure pipeline described in Chapter 4. In this case no control regions are used. All regions are 'signal' regions and there is no background feature parameter to account for possible instrumental systematics, which here are not modeled. In addition, since in this analysis events are not partitioned in different subsamples characterized by different energy dispersion quality, but a fixed smearing with 10% resolution is applied, no combined likelihood technique is implemented. Finally, to keep calculation simple, I focus only on energies above the 10 GeV, where a power-law model is used to fit the smooth component.

Fig. 5.3 reports the limits obtained from the template spectra at 95% CL with containment bands extracted from the 300 pseudoexperiments. The limits presented in Sec. 4.5 are reported in blue, while the grey line represents the last ones published by *Fermi*-LAT Collaboration [51].

Thanks to the increased exposure, the obtained limits at 95% CL are found in the range $10^{-12} - 10^{-9}\,\mathrm{cm}^{-2}\mathrm{s}^{-1}$, with the limits decreasing as energy increases. These results are stronger than the limits on line feature presented in Sec. 4.5, where the upper limits are higher due to lower exposure. This improvement is direct consequence of the increased statistical power of this simulated dataset.

Moreover, these results also show that an increase of the exposure does not correspond to an improvement of the constraints of the same factor. The constraints obtained in this simulation study, which originate from a hypothetic instrument collecting an amount of data corresponding to ~ 8 times the exposure of the *Fermi* LAT, are a factor $2 \div 3$ stronger than those obtained in Chapter 4. This is somewhat expected, since an increase in the statistics of a factor ~ 8 should correspond to an improvement in the errors of a factor $\sim \sqrt{8}$.

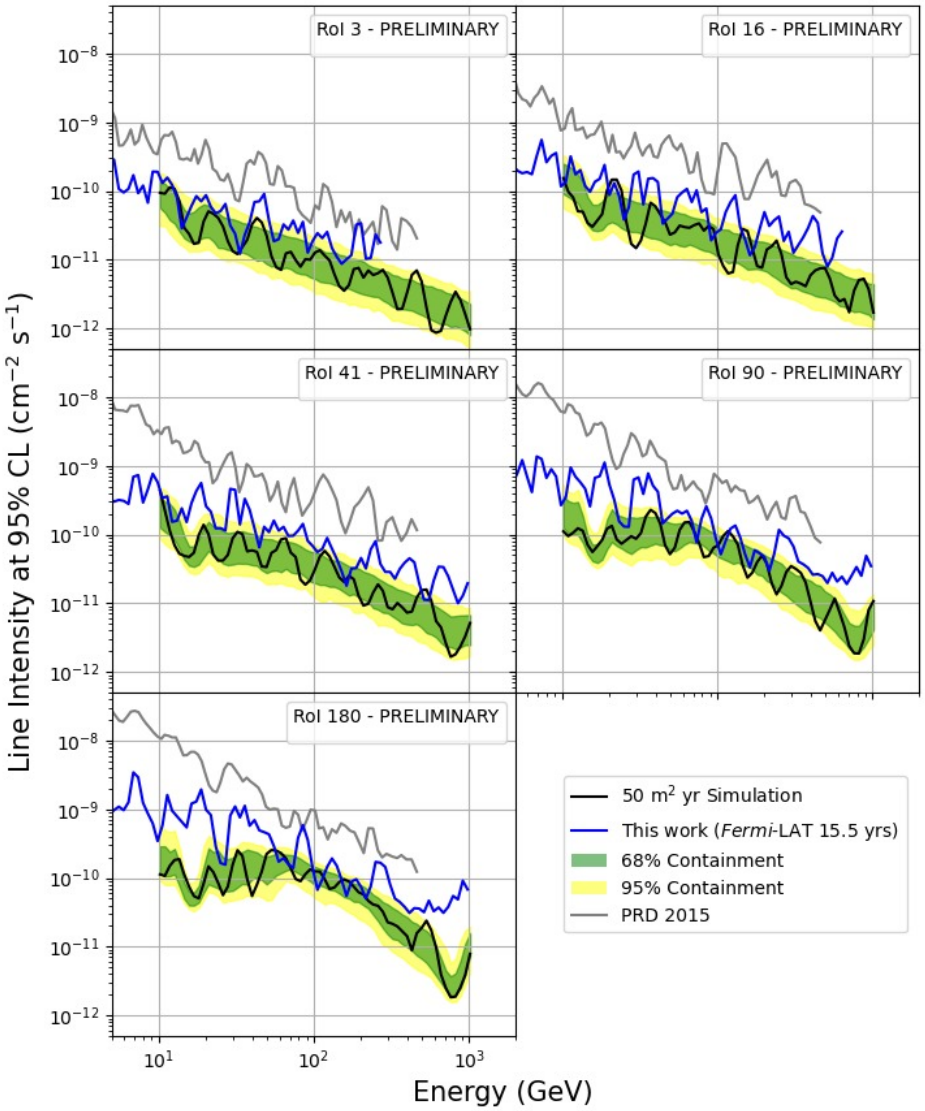

Figure 5.3: Upper limits on line flux at 95% confidence level obtained from the template ROI photon count distributions. Containment bands at 68% (green) and 95% (yellow) CL are extracted from the 300 pseudoexperiments.

Conclusions

The work presented in this thesis started from the analysis techniques developed by the *Fermi*-LAT Collaboration in previous DM searches [50, 51, 89]. The most relevant novel element is the introduction of a control region to account for possible systematic effects that could mimic a real feature. A more accurate model for the smooth background component has been also used and a combined likelihood function between the different event types has been built, giving measurable improvements in the constraints obtained.

A dedicated fit procedure was applied to search for possible spectral features in the Galactic gamma-ray spectra in a very wide energy range (from 1 GeV to 1 TeV). Although no evidence of such features was found, constraints were set on the possible feature flux. The ULs at 95% CL on the feature flux are found in the range $10^{-11} - 10^{-8}\,\mathrm{cm}^{-2}\mathrm{s}^{-1}$ in the case of the line search, and $10^{-10} - 10^{-7}\,\mathrm{cm}^{-2}\mathrm{s}^{-1}$ in the case of the box search, and decrease with increasing energy. The corresponding ULs on the velocity-averaged annihilation cross sections $\langle \sigma_{ann} v \rangle$ lie between 10^{-31} and $10^{-26}\,\mathrm{cm}^3\mathrm{s}^{-1}$ for the line search and 10^{-30} and $10^{-26}\,\mathrm{cm}^3\mathrm{s}^{-1}$ for the box search, while the lower limits on the DM decay times τ_χ are found in the range between 10^{29} and 10^{31} s. The constraints obtained in the present work are stronger than those obtained by the Fermi-LAT Collaboration in their previous line searches [50,51,89]. This improvement is mainly due to the better modeling of the smooth background component of the spectra and to the better handling of systematics. Indeed, as demonstrated in [51] and further discussed in [39], spectral line searches with

the *Fermi*-LAT are limited by systematic uncertainties up to $\sim$ 100 GeV. The present work addresses this challenge by introducing a dedicated control region (the Galactic Plane without the Galactic Center) in which the background flux is fitted independently, including a background feature with the same shape as the signal feature. The background template model obtained with this procedure is more general than a simple power-law model and absorbs potential systematics which can mimic a real signal.

In this work I have also generalized the fit procedure to search for possible box-like spectral features in Milky-Way halo. The analysis approach is the same as for the line search, with the line-like signal and background feature replaced with box-like features. This search represents a novelty and gives competitive constraints on the velocity-averaged DM annihilation cross sections. The box searches fit in a slightly different physics framework than the line searches: while in the line scenario DM particles are assumed to directly annihilate (or decay) into pairs of gamma rays, in the box scenario DM particles are assumed to annihilate into pairs of mediators, which in turn decay into pairs of gamma rays. The limits presented in this work have been obtained under the assumption that the mediator decay times are short enough to allow these particles to decay almost immediately after production. In general, the constraints on the velocity-averaged DM annihilation cross section from the search of possible box-like feature depend on the mediator decay length, since it determines the J-factor. The assumption of a negligible mediator decay length allows the use of the same J-factors evaluated in the line search scenario. On the other hand, including the mediator decay length in the analysis would require a proper calculation of the J-factors.

The obtained limits have meaningful implications for particle DM models. For instance, thermal WIMPs (e.g., Higgs-portal or supersymmetric DM candidates) with cross sections near the canonical thermal relic value ($\sim 3 \times 10^{-26}\ cm^3 s^{-1}$ [93]) are further constrained across a wide mass range (1 GeV $-$1 TeV). The limits presented here, thus, significantly reduce the viable parameter space for these models, since we find upper limits down to $\sim 10^{-30} - 10^{-31}\ cm^3 s^{-1}$ at around 1 GeV (See limits reported in Fig. 4.14). However, a caveat should be taken into

account, since a 100% branching ratio is always assumed to extract the previously discussed constraints, while it is reasonable to assume that WIMP particles could annihilate into many possible channels with different probabilities, thus reducing significantly the projected limit on $\langle \sigma v \rangle$.

Finally, I explored the DM lines detection potential of an APT-like detector. This was achieved assuming that the future APT detector will have 10 times the on-axis effective area of *Fermi*-LAT. Considering a total exposure of 50 $m^2 yr$, which is almost 8 times the one in the main analysis work, I constructed a simulated gamma-ray sky template starting from a `DRAGON2` [169] simulation to which the Isotropic emission model [172] was added. This template was used to perform 300 pseudoexperiments and limits on line flux were extracted with a very close to the main analysis approach. I obtained improved limits with respect to the ones obtained from 15.5 years of *Fermi*-LAT data, proving that the nominal target performance characteristics of APT could produce remarkable improvements in DM line search within a shorter amount of time with respect to the one for the *Fermi*-LAT dataset analyzed in this work.

Looking forward, although no detection has yet been made, the methodology developed in this thesis can be further extended and applied to datasets of future instruments with larger effective area, wider field of view and improved energy resolution. The methodologies developed here can pave the way for next-generation searches that can finally reveal the particle nature of dark matter.

Appendix A

Galactic coordinates

The information of this appendix is adapted from M. Longair textbook [173].

It is not simple to define a coherent coordinate system to locate celestial objects. The main reason for that lies in the fact that the Earth, when moving around the Sun, does not actually follow a perfect elliptical trajectory, since the Moon perturbates continuously its motion, producing significant wobbles.

However, the attempt to assign a set of coordinates to the points of the sky is common practice and several systems are commonly used in astronomy, like *horizontal* and *equatorial* coordinates, which basically consist in an application of the same map used to locate points on the surface of Earth (*latitude* and *longitude*) to locate points on the surface of the *Celestial sphere*, an imaginary surface on which all sky objects are projected, as they appear to us from the surface of the Earth. We do not focus in this appendix in describing these very common coordinate systems, we rather want to give information about a less familiar one which is mentioned in section 4.2, when the different RoIs of our analysis are presented: the *Galactic coordinates*.

The definition of Galactic coordinates is promptly given by Fig. A.1. The pillar of this construction is the definition of the direction of the centre of the Galaxy, namely the solid line that bridges our Sun with the Galactic Center (GC). This direction is accurately determined by means of radio observations (VLBI

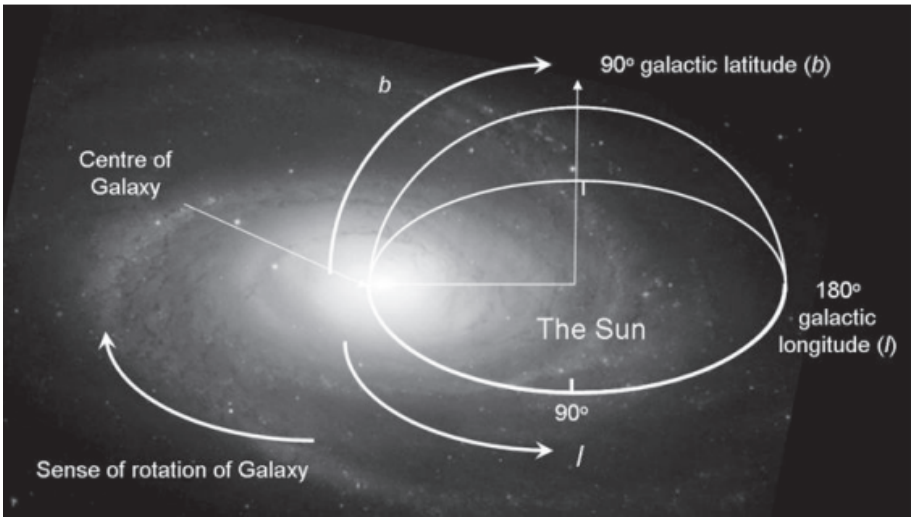

Figure A.1: Definition of the system of Galactic coordinates (l,b). The galaxy M81 has been rotated and inverted to simulate what our Galaxy might look like as seen by an external observer. (Image of M81 courtesy of NASA and the Space Telescope Science Institute.). From [173]

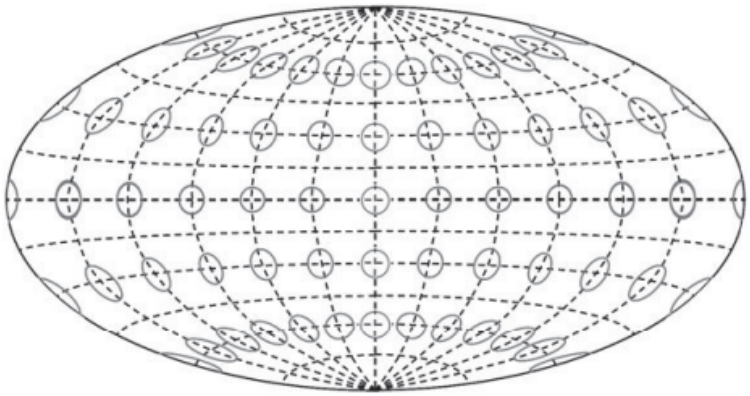

Figure A.2: Distortions of the "Hammer–Aitoff" projection. From [173]

technique [174], the basis of the method that yielded in the end the "photo" of the SMBH at the center of our Galaxy in 2022 [175]), which are made compulsory by the significative presence of dust which creates darkening in all other wavelengths. The GC, and precisely the aforementioned SMBH "Sagittarius A*", is thus taken as the zero of *Galactic latitude* (b) and *longitude* (l). The Galactic equator is taken to be the great circle which passes through the center of the Galactic Plane as seen

in fig. A.2. Galactic longitude conventionally increases in a counter−clockwise direction starting at l = 0° at the Galactic Centre, reaches 180° in the anti−Centre direction and returns to zero after completing a circuit of 360°. The Galactic north pole is defined to be the pole of the Galactic coordinate system which lies in the northern celestial hemisphere at celestial coordinates $\alpha = 12h51m26.282s$; $\delta = +27°0.7'42.01''$ in the 2000.0 coordinate system.

The Galactic equator is at b = 0° and the Galactic north pole at b = +90° the Galactic south pole lies at b = −90°.

The inclination of the Galactic equator to the Earth's equator is 62.9°. The intersection, or node line, of the two equators is at α = 18h 51.4m, $\delta = 0°00'$ or, in Galactic coordinates, at $l = 33°$ degrees,$b = 0°$.

The massive black hole in Sgr A* probably provides the best definition of the dynamical centre of the Galaxy and has galactic coordinates $l = 359°56'39.4''$, $b = -0°2'46.2''$.

The projection which was used to produce the count map in this work (Fig. 4.2) is the *Mollweide projection*. It is a pseudocylindrical projection in which the equator is represented as a straight horizontal line orthogonal to a central meridian whose length is one half of the equatorial one. The other parallels compress near the poles, while the other meridians are equally spaced at the equator. The meridians at 90° east and west form a perfect circle, resulting in the end as a 2 : 1 ellipse. The proportion of the area of the ellipse between any given parallel and the equator is the same as the proportion of the area on the globe between that parallel and the equator, but at the expense of shape distortion, which is significant at the perimeter of the ellipse, although not as severe as in the sinusoidal projection.

List of Figures

1.1 Rotation curves of 21 spiral galaxies studied in ref. [4]. 4

1.2 Rotation curve of the galaxy NGC3196 [5]. The data have been fitted assuming an exponential mass distribution in the disk and a dark matter density profile in the halo described by eq. 1.9. 5

1.3 Gravitational lensing: galaxy clusters can bend light rays passing in their vicinity, in similar fashion to actual lenses, albeit for different reasons. Credit: NASA, ESA and L. Calçad 7

1.4 Left panel: Mass mapping of the Coma Cluster. Red crosses represent the visible matter (brightest galaxies in the cluster). The contours indicate the matter responsible for the gravitational potential. More matter is needed with respect to the observed matter to explain the gravitational potential [8]. Right panel: False-color mosaic of Coma Cluster combining images from the Sloan Digital Sky Survey (optical, shown in blue) with long- and short-wavelength infrared images (shown in red and green, respectively) from NASAs Spitzer Space Telescope. Image credit: NASA / JPL-Caltech / L. Jenkins (GSFC), taken from Ref. [9]. . . 8

1.5 Color image of the merging Bullet Cluster 1E 0657-558 from the Chandra X-ray telescope and weak lensing gravitational potential. The two distributions appear separated: the peaks of the gravitational potential (green contour lines) are different from the peaks of X-ray emission (color scale) [10]. 10

1.6 Map of CMB temperature anisotropies, from Planck collaboration [13]. 13

1.7 Planck 2018 [18] temperature power spectrum. The base-ΛCDM theoretical spectrum best fit to the Planck likelihoods is plotted in light blue in the upper panel. Residuals with respect to this model are shown in the lower panel. The error bars show $\pm 1\sigma$ diagonal uncertainties, including cosmic variance (approximated as Gaussian) and not including uncertainties in the foreground model at ≥ 30. Note that the vertical scale changes at $l = 30$, where the horizontal axis switches from logarithmic to linear. 14

1.8 X-ray spectra in the 3–4 keV energy band measured by the MOS (left panel) and PN (right panel) cameras of the EPIC instrument onboard XMM-Newton. The plot is taken from ref. [22] and refers to the stacked analysis of 73 galaxy clusters. 19

1.9 ALP parameter space with the most recent constraints (July 2020) [28]. The golden band represents the current target parameter space, given by the QCD axion model: KSVZ and DFSZ are two benchmark models with different coupling strengths [29]. Dark red contours represent parameter space exclusion regions from laboratory experiments, green regions from astrophysical observations of stellar environments, blue regions from cosmological observations. 21

1.10 Comoving number density Y (left y-axis) and thermal relic density (right y-axis) of a 100 GeV annihilating DM particle as a function of temperature T (bottom x-axis) and of time t (top x-axis). The solid contour is for an annihilation cross section that yields the correct relic density, while the shaded regions are for cross sections that differ by 10, 10^2, and 10^3 from this value. The dashed contour is the number density of a DM particle remaining in thermal equilibrium. The plot is taken from ref. [34]. 25

2.1 Left: possible WIMP annihilation processes into W, Z, or quark pairs that hadronize creating secondary gamma rays, neutrinos, electrons, and antimatter. Right: direct production of gamma rays in the case of self-annihilation. The same particles are expected to be produced in the WIMP decay processes. 27

2.2 Left panel: DM annihilations or decays in the Milky Way produce SM particles that reach the observer in the solar system, possibly producing an excess in the energy spectrum of cosmic rays over the observed astrophysical background. Charged probes do not point to their source because of the randomization of their direction due to magnetic fields, differently from neutrinos and gamma rays (figure from Ref. [1]). Right panel: Mean free path λ_γ as a function of the photon energy. (plot from Ref. [35]). 28

2.3 Comparison among the four different DM density profiles [1] for the Milky Way. All the curves are normalized by setting the value of the DM density at the Sun position ($R_\odot = 8.5\,\mathrm{kpc}$) to $\rho_\odot = 0.4\,\mathrm{GeV/cm^3}$. 29

2.4 DM density as a function of Galactocentric radius reporting different modified NFW profiles. Other profiles are also reported. From ref. [39]. 31

2.5 Count maps of all gamma rays with reconstructed energies above 1 GeV are shown for 15 years of simulated *Fermi*-LAT data using the P8R2 SOURCE event class (see Sec. 3.5 for details on *Fermi*-LAT data products). The maps are displayed in Galactic coordinates using a Hammer-Aitoff projection, with pixel sizes of $1^\circ \times 1^\circ$. Individual panels represent the contributions from cataloged sources (top panel), diffuse Galactic emissions (middle left), unresolved Galactic sources (middle right), isotropic background emission (bottom left), and unresolved extragalactic sources (bottom right). All maps use the same grayscale range to allow for direct comparison. Figures adapted from [39]. 34

2.6 Scheme representing the geometry involved in the integration along the *l.o.s.* to calculate the *J*-factor. A WIMP annihilation event is reported, but the same considerations can be made with a decay event. 38

2.7 The simulated total differential gamma-ray distribution resulting from the annihilation of a WIMP particle (in this case a inert Higgs H^0, with $m_{H^0} \sim 135GeV$) is shown by the solid line. Individual contributions are displayed separately: $\chi\chi \rightarrow b\bar{b}$ (dashed line), $\chi\chi \rightarrow \tau^+\tau^-$ (dash-dotted line), and $\chi\chi \rightarrow Z\gamma$ (dotted line). The monochromatic line feature would visibly stand out with respect to other channels which affect the spectral distribution broadly. Figure from Ref. [44]. 39

2.8 Spectra of box-shaped gamma-ray features. The left panel shows both the unconvoluted (dashed) and the convoluted (solid) with *Fermi* LAT energy resolution box spectra for $m_\chi = 100$ GeV, $m_\phi = 60$ GeV, and $\langle\sigma v\rangle = 3 \times 10^{-26}$ cm^3/s, overlaid on the 2-year *Fermi* LAT data (adapted from [49]) for the Galactic Center region. The right panel displays the convoluted box spectra for $m_\chi = 100$ GeV, $\langle\sigma v\rangle = 3 \times 10^{-26}$ cm^3/s, and various values of m_ϕ. Figures from Ref. [52]. 41

2.9 Scheme representing the geometry to calculate the J-factor in the case of a metastable mediator scenario produced in WIMP annihilation. Assuming that the gamma ray is produced in an arbitrary point P along the *l.o.s.* at distance l from Earth, the annihilation event can be occurred at any the point Q at a distance $l' > 0$ from P. 43

2.10 Upper limit at 95% confidence level on the intensity of a possible feature in the solar gamma-ray spectrum. Left panel: box model; Right panel: line model. The green and yellow regions indicate the central 68% and 95% expectation bands for the 95% CL limits evaluated from the pseudo-experiments [54]. 44

2.11 Limits at 95% CL on the DM-nucleon cross section via long-lived mediator for four different decay lengths $L = R_\odot, 0.1, 1$ and 5 AU. The plots also show the limits at 90% CL from the PICO-60 experiment [70] in the case of spin-dependent (SD) scattering (cyan line) and from the XENON1T experiment [71] in the case of spin-independent (SI) scattering (blue line). From Ref. [54]. 46

2.12 Spectrum of the Galactic Center excess as reported in Ref. [72]. Blue points are derived using the Sample Model described in [72], where the *Fermi*-LAT emission components are fitted using parameters obtained by GALPROP code (used to model CRs propagation and produce spatial models for gamma-ray subsequent emission) and source templates obtained from Fermi 3FGL catalog. The "excess" part of the model makes use of a gNFW (see Sec. 2.1.1) annihilation template with $\gamma = 1.25$. The effects of systematics are represented by the blue band. These results are compared to previous determinations of the GC excess spectrum from the literature. 47

2.13 Upper limits at 95% confidence level on $\langle \sigma v \rangle_{\gamma\gamma}$ for each DM profile considered in the corresponding optimized ROI. Yellow (green) bands show the 68% (95%) expected containment bands derived from 1000 no-DM MC simulations. The black dashed lines show the median expected limits from those simulations. Also shown are the limits obtained in a previous 3.7-year line search [50] and 5.2-year line search [87] when the assumed DM profiles were the same. Plots taken from Ref. [51]. 50

2.14 Constraints at 95% confidence level for different DM density profiles obtained from the analysis of a 5-years DAMPE dataset. The top-left, top-right and bottom-left panels show the upper limits on $\langle \sigma_{ann} v \rangle$ assuming the Einasto, NFW and isothermal profiles respectively; the bottom-right panel shows the lower limit on the decay time $\tau_{\gamma\nu}$ assuming the NFW profile. Yellow (green) bands show the 68% (95%) expected containment bands obtained from 1000 simulations of background emission with systematic uncertainties involved. The red solid and purple dotted lines are the results with and without the systematic uncertainties respectively. The blue dot-dashed lines show the 5.8-year Fermi-LAT constraints from [51]. The plots are taken from Ref. [91] 52

2.15 Constraints on the DM velocity-averaged annihilation cross section $\langle \sigma_{ann} v \rangle$ at 95% confidence level for the $b\bar{b}$ (left) and $\tau^+\tau^-$ (right) channels derived from a combined analysis of 15 dSphs with 6 years of PASS8 data. The blue curve shows the limits derived from a previous analysis of a four-year PASS7 data set with the same sample of 15 dSphs [92]; the gray curve corresponds to the thermal relic cross section in Ref. [93]. The plots are taken from Ref. [94]. . 53

2.16 Comparison of constraints on the DM annihilation cross section for the $b\bar{b}$ (left) and $\tau^+\tau^-$(right) channels from [94] with previously published constraints from LAT analysis of the Milky Way halo (3σ limit) [95], 112 hours of observations of the Galactic center with H.E.S.S. [96], and 157.9 hours of observations of Segue 1 with MAGIC [97]. Pure annihilation channel limits for the Galactic center H.E.S.S. observations come from Ref. [98]. Closed contours and the marker with error bars show the best-fit cross section and mass from several studies of the GC excess [79, 80, 99] 54

2.17 Upper limits at 95% confidence level on $\langle\sigma v\rangle$ (left) and lower limits on τ (right) as a function of m_χ obtained in the analysis in Ref. [102]. MED refers to the state-of-the-art estimate of the effect of substructures on the J-factor evaluation. 55

2.18 Upper limits at 90% confidence level (solid curves) and expected sensitivities (dotted curves) on the spin-dependent scattering cross-section as a function of the WIMP mass derived from seven years of IceCube data on solar neutrinos (Ref. [103]). The dark and light shaded regions indicate the central 68% and 95% expectatiob bands, respectively. Limits from the Super-K [104], PICO-60 and ANTARES [105] experiments are also shown. Plot taken from Ref. [103]. 56

2.19 Upper limits on $\langle\sigma_A v\rangle$ as a function of WIMP mass for annihilation into neutrinos via the $\tau^+\tau^-$ channel, assuming an NFW halo profile. Results from the IceCube Galactic Center search (IC86, $2012-2014$ [109]) are compared with previous IceCube [110–113] and ANTARES [114] analyses, as well as gamma-ray limits from Segue 1 (*Fermi*-LAT+MAGIC [115]) and the Galactic Center (H.E.S.S. [116]). The "natural scale" denotes the $\langle\sigma_A v\rangle$ expected for thermal relic WIMPs [93]. Plot from Ref. [109]. 58

2.20 Constraints on DM from galactic neutrinos in Ref. [119]. Left panel: upper limits (solid line) and sensitivity (dotted line) at 90% C.L. on the thermally averaged self-annihilation cross section of the $\nu_e\bar{\nu_e}$ channel and NFW profile. Right panel: lower limits (solid line) and sensitivity (dotted line) at 90% C.L. on the decaying DM lifetime of the $\nu_e\bar{\nu_e}$ channel and NFW profile. Constraints are plotted as functions of the DM mass, together with the 1σ (green) and 2σ (yellow) containment bands representing the expected sensitivity. Plots from Ref. [119]. 59

2.21 95% CL Upper limits on annihilation into W^+W^- for the Coma and Virgo clusters and for the Andromeda galaxy. Dashed lines assume pure NFW profiles, while solid lines include subhalo contributions (denoted with "sub"); sensitivity curves differ from the limits by multiplicative factors given in Ref. [120] 60

2.22 Positron fraction measured by AMS-02 [122], PAMELA [123] and Fermi-LAT [124]. 62

2.23 Positron spectrum from the combined contribution of all Galactic PWNe with a broken power-law injection ($\gamma = 1.8$ below and $\gamma = 2.8$ above $E_b = 450$ GeV). Secondary positrons are shown separately (dash-dotted blue line). The total spectrum is given by the solid red line. Plot from Ref. [127]. 63

3.1 Artistic renditions of the SAS-2 (left), COS-B (center) and one of the VELA satellites, VELA-5B (right). Images from NASA and ESA 66

3.2 NASA'S CGRO (Credits: NASA), with a schematic view of EGRET instrument (right), taken from [135]. 67

3.3 Top left panel: Fermi being prepared for launch at Cape Canaveral. Top right panel: schematic view of the Fermi satellite components and instruments. Lower Panel: artistic representation of *Fermi* spacecraft, Credit: NASA's Goddard Space Flight Center/Chris Smith (USRA/GESTAR), taken from [137] 69

3.4 Sketch representing the Earth's limb gamma-ray emission where both the zenith angle θ_Z and rocking angle θ_r are shown. Taken from [50]. 70

3.5 Left panel: diagram representing the β angle, i.e. the angle between the solar vector and the orbital plane of the satellite. Right panel: beta angle of the *Fermi* spacecraft during 2019 (taken from [140]). The β angle varies continuously, following both an annual cycle and the $\sim$ 46-day orbital precession period. The angle spans a range of nearly $\pm 50°$. The color scale indicates the observing mode in use: green for the symmetric two-sided rocking profile (used over two orbits), and grey for the asymmetric mode with sinusoidal rocking during orbital day and fixed offset during orbital night. 73

3.6 Exposure maps corresponding to the 3 possible rocking profiles of *Fermi* spacecraft. All maps report an exposure normalized to the average, projected onto an AITOFF coordinate system.**Left panel**: exposure map corresponding to the symmetric $\pm 50°$ rocking profile, which characterized the majority of the *Fermi* mission and enables complete sky coverage within approximately three hours. **Middle panel**: exposure map for the asymmetric $+50°/-60°$ profile, which maintains full-sky coverage within two orbits, though the maximum exposure reaches only about 85% of the uniform coverage. **Right panel**: exposure map obtained using the partial sinusoidal 50° rocking profile, associated with the post-anomaly mode 3 configuration. Maps taken from [141]. 74

3.7 Left: NaI(Tl) crystal scintillator unit. Right: BGO crystal scintillator unit. The photos are taken from ref. [139] 75

3.8 Schematic of the GBM detectors positioning on *Fermi* observatory. From [139]. 76

3.9 **Left panel:** Energy resolution as a function of photon energy for the NaI detector (square markers) and the BGO detector (triangle markers). **Right panel:** Effective area as a function of photon energy at normal incidence for both detector types. The plot in the lower-right part illustrates the simulated impact of the spacecraft structure on the response of a representative detector. Plots from [139]. 77

3.10 Schematic view of the Large Area Telescope (taken from [138]). Gamma-rays pass through the ACD, convert in the TKR, and produce electromagnetic showers in the CAL. 79

3.11 LAT coordinate system. θ is the off-axis angle with respect to the z-axis, and ϕ is the azimuthal angle in the xy-plane relative to the x-axis (oriented toward the Sun). The solar panels lie along the y-axis. (taken from Ref. [144]). 80

3.12 **Left panel**: schematic of a pair conversion inside the TKR . **Right panel**: photo of a TKR tower during its assembly. Taken from [138]. 81

3.13 Exploded view of a CAL tower. Taken from [138]. 82

3.14 **Left panel**: Schematic of *Fermi*-LAT ACD subsystem , taken from ref. [138]. **Right panel**: photo of the ACD, freshly completed, taken from [146]. 83

3.15 Schematic of the *Fermi*-LAT DAQ system architecture. From ref. [138] 85

3.16 Example of a "ghost event" in the LAT (y–z view). In addition to an 8.5 GeV gamma-ray candidate (on the right) there is additional activity in all the three LAT subsystems, with the remnants of a charged-particle track crossing the ACD, TKR and CAL. The small crosses represent the clusters (i.e., groups of adjacent hit strips) in the TKR, while the variable-size squares indicate the reconstructed location of the energy deposition for every hit crystal in the CAL (the side of the square being proportional to the magnitude of the energy release) [144]. 88

3.17 Effective area for the SOURCE event class as a function of energy for normal incidence photons (θ=0). The red curve corresponds to photon converting in the front section of the detector, while the blue one to photons converting in the back section. The black curve corresponds to all the photon events [149]. 94

3.18 LAT effective area for the SOURCE event class as a function of the incidence angle for 10 GeV photons. The curves correspond to photons converting in the front section of the TKR (red), in the back section (blue) and to all photon events (black) [149]. 95

3.19 Comparison of the on-axis effective area as a function of the energy for different event classes [149]. 96

3.20 Top: LAT acceptance as a function of energy. The curves correspond to photons converting in the front section of the TKR (red), in the back section (blue) and to all photon events (black). Bottom: comparison of the acceptance as a function of energy for different event classes (total) [149]. 97

3.21 Top: 68% and 95% containment angles as a function of energy for SOURCE class photons. The curves correspond to photons converting in the front section of the TKR (red), in the back section (blue) and to all photon events (black). Bottom: Comparison of the 68% containment angle as a function of energy for different PSF event types [149]. 98

3.22 Distributions of $\Delta E/E'$ for the different event types of SOURCE class photons with 100 GeV true energy [149]. 99

3.23 Top: Energy resolution ΔE/E, defined as the 68% containment region of the reconstructed photon energy as a function of energy. The curves correspond to photons converting in the front section of the TKR (red), in the back section (blue) and to all photon events (black). Bottom: Comparison of the 68% containment region of the reconstructed photon energy as a function of energy for different energy dispersions [149]. 100

3.24 Schematic of all subsystems onboard AGILE spacecraft. Taken from Ref. [151]. 101

3.25 DAMPE particle detector. Its four subdetectors are visible: the Plastic Scintillator Detector (PSD), the Silicon-Tungsten Tracker (STK), the BGO Calorimeter (CALO) and the NeUtron Detector (NUD). Taken from ref. [90]. 103

3.26 Continuum sensitivity of different X-ray and gamma-ray instruments as evaluated in Ref. [158]. Past missions are shown in dotted lines, currently operating instruments in solid lines and future planned missions in dashed lines. An energy range spanning from $\sim 200\,\mathrm{keV}$ to $\sim 50\,\mathrm{MeV}$ appears as the least explored now. 105

3.27 **Top panel:** e-ASTROGAM spacecraft in deployed configuration. **Bottom panel:** Overview of the e-ASTROGAM payload showing the silicon Tracker, the Calorimeter and the Anticoincidence system. Taken from [160]. 106

3.28 **Left panel:** Exploded view of the Gamma-Ray Telescope aboard AMEGO-X. The Tracker (red) and Calorimeter (purple) work together to characterize incoming gamma rays through multiple detection techniques. **Right panel:** Illustration of the three detection techniques: single-site events enhance sensitivity and response below 100 keV, particularly for transient sources; Compton events (both untracked and tracked) enable imaging below 10 MeV by reconstructing the Compton scattering angle θ from energy (E) and position ($\vec{r}$) measurements; pair-production events enable imaging above 10 MeV, employing techniques similar to those used by *Fermi*-LAT. 107

3.29 **Top panel:** APT instrument configuration shown inside the Falcon 9 payload fairing. **Bottom panel:** Overview of the primary APT detection modes across the relevant energy ranges. 109

3.30 Estimated sensitivity of APT to DM from the measurements on dSph Galaxies. From Ref. [162] 110

4.1 Overview of the Weekly-All-sky files listed on the HEASARC website [165]. The dataset used in this thesis spans the period from August, 4^{th} 2008 to December, 31^{st} 2023, for a total of 185 months of data. 114

4.2 All sky count map with the different ROIs highlighted (top panel) and for the GP (bottom panel). This map was generated from the dataset analyzed in the present thesis. 118

4.3 Photon counts spectra for the different ROIs used in the analysis. The spectra have been built selecting all events, with 64 bin per decade, meaning that each bin is 3.66% $\times E$ wide, where E is the central energy of the bin, for a total of 339 bins. 119

4.4 Integrated livetime vs cosθ for R3, where θ is the off-axis angle (see fig.3.4). The histogram is divided in 40 bins, with ($\Delta\sqrt{1-cos\theta} = 0.025$). 121

4.5 Exposure $\mathcal{E}(E|E')$ in R180 for EDISP3 events. The true energy is on the x-axis, while the observed energy is on the y-axis. 122

4.6 Projection of the exposure matrix corresponding to R180 (shown in Fig. 4.5), along the y-axis (observed energy), at fixed true energies of 1 and 100 GeV. The energy dispersion corresponds to the width of the distribution. Each EDISP type exhibits a broader distribution according to dispersion in energy reconstruction quality, as outlined in Fig. 3.22. 123

4.7 Energy resolution curves corresponding to 68% (full lines) and 95% containment (dashed lines), relative to all different event types in R180. The curves were obtained from the projections along the observed energy axis of the exposure matrix, scanning the true energies. These curves are compatible with the ones declared in *Fermi*-LAT performance (Fig. 3.23). 124

4.8 Profile of the function $-2\Delta ln\mathcal{L}$, evaluated for the different event types as a function line flux at $E_{line} = 16.3\,\text{GeV}$, in R16. The ULs at 95% CL are determined by the intersection of the curves with the horizontal black line at $-2\Delta ln\mathcal{L} = -2.71$. The combined procedure yields stronger constraints (purple line) with respect to the analyses of individual event types. 130

4.9 Photon counts as observed in the data (black points) and as predicted by the best-fit model including the signal component (blue line) for a single window centered at 113 GeV. The lower inset shows the fractional residuals, defined as (data − model)/model, which typically remain within a 25% range across other fit windows as well. 132

4.10 Example of the results from the line feature search using a sliding energy window (width 0.5) fit in $R180$ using all event types combined. Fitted signal features counts superimposed on the photon count spectra. 133

4.11 TS as a function of energy for the combined analysis of the four subsamples corresponding to the different event types EDISP0, EDISP1, EDISP2, EDISP3, calculated for the five different ROIs. The colored lines correspond to different energy window size with w of 0.4, 0.5 and 0.6, respectively. No peculiar excesses are found. . 134

4.12 ULs at 95% CL on the line flux as a function of energy for the combined analysis of the four subsamples corresponding to the different event types `EDISP0`, `EDISP1`, `EDISP2` and `EDISP3`, calculated for the five different ROIs. The colored lines correspond to different energy window sizes, with $w = 0.4$, 0.5 and 0.6, respectively. The grey lines indicate the limits in Ref. [51]. 135

4.13 line flux ULs at 95% CL in R3, R16, R41 and R180 for the combined analysis. The green and yellow bands show the 68% and 95% expected containment bands derived from 1000 background-only Monte Carlo simulations. The limits obtained in Ref. [51] in the same ROIs are also shown (grey line). 136

4.14 **Upper panel**: Upper limit at 95% CL on the velocity-averaged cross section $\langle\sigma_{ann}v\rangle$ as a function of energy from the analysis of R3, R16, R41 and R90 with $w = 0.5$. **Lower panel**: Lower limit at 95% CL on the decay time τ_χ as a function of energy from the analysis of R180 with $w = 0.5$. The green and yellow bands show the 68% and 95% expected central containment bands derived from 1000 background-only Monte Carlo simulations. The limits have been obtained from the combined analysis of the subsamples corresponding to the different event types. The grey lines indicate the limits in Ref. [50]. 138

4.15 TS as a function of energy in R3, R16, R41 and R180 for the combined analysis in the line search case. The green and yellow bands show the 68% and 95% expected containment bands derived from 1000 background-only Monte Carlo simulations. A few outliers can be spotted: in R3, R16 and R41 features with TS of ~ 6, ~ 8 and ~ 13 respectively at $\sim 4\,\mathrm{GeV}$. In any case outliers are quite far from 25. 140

4.16 Global significance s_{global} as a function of the local TS in R3, R16, R41 and R180 in the line search case. The black dots represent the maximum TS values coming from our data set analysis. 141

4.17 Photon counts as observed in the data (black points) and as predicted by the best-fit model including the box-like signal component (blue line) for a single window centered at 113 GeV. The lower inset displays the fractional residuals, defined as (data − model)/model, which typically remain within a 25% range across the scanned energy windows. 143

4.18 Example of the results of the box-shaped feature search using a sliding energy window fit in $R180$, with all event types combined, with fitted box-like features overlaid on the photon count spectra. . 144

4.19 box flux at 95% CL in R3, R16, R41 and R180 for the combined analysis. The green and yellow bands show the 68% and 95% expected containment bands derived from 1000 background-only Monte Carlo simulations. 145

4.20 TS as a function of energy in R3, R16, R41 and R180 for the combined analysis in the box search case. The green and yellow bands show the 68% and 95% expected containment bands derived from 1000 background-only Monte Carlo simulations. A few outliers can be spotted: in R90 and R180 features with TS of ~ 7.5 and ~ 12.5, albeit still not locally significant. 146

4.21 Upper limit extracted from the box search at 95% CL on the $\langle \sigma_{ann} v \rangle$ annihilation cross section as a function of energy for 0.50 energy window only, from the analysis of R3, R16, R41 and R90. 147

4.22 Global significance s_{global} as a function of the local TS in R3, R16, R41 and R180. The black dots represent the maximum TS values coming from our data set analysis. 148

4.23 Normalized off-axis angle θ distributions of the Earth limb photons without the rocking angle cut (red line) and with the rocking angle cut (blue line) compared with the distribution of R180 (purple line). The peak appearing to be centered around 65° is removed selecting events with rocking angles $> 70°$, shaping the final distribution in a similar way to that of R180. 150

4.24 Count map of the Galactic dataset with the first 2 ROIs (R3 and R16, left panel) and the corresponding ones in the limb dataset projected onto galactic coordinates, RL40 and RL105 (right panel). Since the total photon counts of the limb dataset is significantly lower, the corresponding ROIs encompass wider regions of the sky. . 151

4.25 Exposure corresponding to R16 and RL105 for the main analysis dataset (left panel) and the limb sample (right panel) respectively vs observed energy for all event types, at fixed true energy of of 100 GeV. The exposure in the ROI differs of a factor of ~ 250 for any event type. 151

4.26 Upper limits at 95 % CL on the feature signal intensity for both line and box features searches, comparing the ROIs from the main analysis ($R3$ and $R16$) with the corresponding ones from the limb analysis ($RL40$ and $RL105$ respectively). The limits between the 2 datasets differ of a factor ~ 250, which is the same factor between exposures, as reported in Fig. 4.25. 152

4.27 Signal flux fraction as defined in Eq. 4.26 in the line case (left panel) and the box case (right panel) in R3 and R16 (RL40 and RL105 for the limb dataset) as a function of observed energy. The sky-blue line represents the galactic datasets limits, while the dark blue one those from the limb dataset. Limb events are characterized by a significantly lower exposure for the same counts, so a comparison is possible only using flux fraction. Signal flux fractions, on the other hand, are consistent between the two datasets in both searches. . . 153

5.1 Gamma-ray intensity maps of the Galaxy in Mollweide projection, corresponding to the propagation parameters derived from the B/C analysis using the FLUKA cross sections. The upper-left panel shows the bremsstrahlung emission, the upper-right panel displays the gamma-ray emission from π^0 decays, and the lower-left panel presents the inverse Compton (IC) emission. For comparison, the lower-right panel shows the *Fermi*-LAT diffuse emission template, based on the first eight years of data (PASS 8; P8_R3), as provided in `gll_iem_v07.fits` [168]. Plots taken from [169]. 157

5.2 Photon count map in galactic coordinates of the gamma-ray sky template used in this sensitivity study. It is an `HEALPIX` map in Mollweide projection with `nside` = 128, for a total of 196,608 pixels. 158

5.3 Upper limits on line flux at 95% confidence level obtained from the template ROI photon count distributions. Containment bands at 68% (green) and 95% (yellow) CL are extracted from the 300 pseudoexperiments. 161

A.1 Definition of the system of Galactic coordinates (l,b). The galaxy M81 has been rotated and inverted to simulate what our Galaxy might look like as seen by an external observer. (Image of M81 courtesy of NASA and the Space Telescope Science Institute.). From [173] 166

A.2 Distortions of the "Hammer–Aitoff" projection. From [173] 166

List of Tables

4.1 Summary of the cuts applied in the data selection. 116
4.2 J-factors of the different ROIs considered in the analysis. They have been evaluated for the DM profiles for which each ROI is optimized and for both WIMP annihilation and decay. The same values were used in previous researches of *Fermi*-LAT collaboration [50]. 139
4.3 Summary of the cuts applied in the data selection for the Earth Limb photons dataset. 149

Bibliography

[1] Marco Cirelli, Alessandro Strumia, and Jure Zupan. Dark matter, 2024.

[2] S. Navas et al. Review of particle physics. *Phys. Rev. D*, 110(3):030001, 2024.

[3] M. J. Reid and T. M. Dame. On the rotation of the Milky Way determined from HI emission. 832(2):159, nov 2016.

[4] Rubin, V.C. and Thonnard, N. and Ford, W.K., Jr. Rotational properties of 21 SC galaxies with a large range of luminosities and radii, from NGC 4605 (R = 4kpc) to UGC 2885 (R = 122 kpc). *Astrophys. J.*, 238:471, 1980.

[5] T. S. van Aleada, J. N. Bahcall, K. Begeman, and R. Sanscisi. Distribution of dark matter in the spiral galaxy NGC 3198. *Astrophys. J.*, 295:305–313, 1985.

[6] M. Milgrom. MOND Theory. *Can. J. Phys.*, 93:107, 2015.

[7] F. Zwicky. On the masses of nebulae and of clusters of nebulae. *Astrophys. J.*, 86, 1937.

[8] R. Gavazzi et al. A weak lensing study of the Coma cluster. *Astronomy & Astrophysics*, 498(2):L33–L36, apr 2009.

[9] Jennifer M. Gaskins. A review of indirect searches for particle dark matter. *Contemporary Physics*, 00(00):1–32, April 2016.

[10] Douglas Clowe et al. A Direct Empirical Proof of the Existence of Dark Matter. *The Astrophysical Journal*, 648(2):L109–L113, aug 2006.

[11] G. Sigl M. Klasena, M. Pohlb. Indirect and direct search for dark matter. *Progress in Particle and Nuclear Physics*, 2015.

[12] Ruth Durrer. *The Cosmic Microwave Background*. Cambridge University Press, 2008.

[13] Adam et al. Planck 2015 results - i. overview of products and scientific results. *A&A*, 594:A1, 2016.

[14] A. A. Penzias and R. W. Wilson. A Measurement of Excess Antenna Temperature at 4080 Mc/s. *apj*, 142:419–421, July 1965.

[15] M. G. Hauser et al. The COBE Diffuse Infrared Background Experiment Search for the Cosmic Infrared Background. Limits and Detections. *The Astrophysical Journal*, 508(1):25–43, nov 1998.

[16] G. Hinshaw et al. Nine year Wilkinson Microwave Anisotropy Probe (WMAP) observations: cosmological parameter results. *The Astrophysical Journal Supplement Series*, 208(2):19, sep 2013.

[17] J.M. Lamarre et al. The Planck High Frequency Instrument, a 3rd generation CMB experiment, and a full sky submillimeter survey. In *The Cosmic Microwave Background and its Polarization*, volume 47, pages 1017–1024, Minneapolis, United States, March 2003. Elsevier.

[18] N. Aganhim et al. for Planck Collaboration. Planck 2018 results. VI. Cosmological parameters. *The Astrophysical Journal*, 641, September 2020.

[19] W. Hu, N. Sugiyama, and J. Silk. The physics of microwave background anisotropies. *Nature*, 386(6620):37–43, 1997.

[20] Leszek Roszkowski, Enrico Maria Sessolo, and Sebastian Trojanowski. WIMP dark matter candidates and searches—current status and future prospects. *Rept. Prog. Phys.*, 81(6):066201, 2018.

[21] Scott Dodelson and Lawrence M. Widrow. Sterile neutrinos as dark matter. *Physical Review Letters*, 72(1):17–20, January 1994.

[22] Esra Bulbul, Maxim Markevitch, Adam Foster, Randall K. Smith, Michael Loewenstein, and Scott W. Randall. Detection of an unidentified emission line in the stacked x-ray spectrum of galaxy clusters. *The Astrophysical Journal*, 789(1):13, jun 2014.

[23] Hofmann, F. and Wegg, C. 7.1 kev sterile neutrino dark matter constraints from a deep chandra x-ray observation of the galactic bulge limiting window. *A&A*, 625:L7, 2019.

[24] Joseph P. Conlon, Francesca Day, Nicholas Jennings, Sven Krippendorf, and Markus Rummel. Consistency of Hitomi, XMM-Newton, and Chandra 3.5 keV data from Perseus. *prd*, 96(12):123009, December 2017.

[25] Brandon M. Roach, Steven Rossland, Kenny C. Y. Ng, Kerstin Perez, John F. Beacom, Brian W. Grefenstette, Shunsaku Horiuchi, Roman Krivonos, and Daniel R. Wik. Long-exposure nustar constraints on decaying dark matter in the galactic halo. *Phys. Rev. D*, 107:023009, Jan 2023.

[26] Ivana Batković, Alessandro De Angelis, Michele Doro, and Marina Manganaro. Axion-like particle searches with iacts. *Universe*, 7(6), 2021.

[27] H. Quinn R. Peccei. CP Conservation in the Presence of Pseudoparticles. *Physical Review Letters*, 386(6620):37–43, June 1977.

[28] Ciaran O'Hare. cajohare/axionlimits: Axionlimits. `https://cajohare.github.io/AxionLimits/`, July 2020.

[29] Paola Arias, Davide Cadamuro, Mark Goodsell, Joerg Jaeckel, Javier Redondo, and Andreas Ringwald. Wispy cold dark matter. *Journal of Cosmology and Astroparticle Physics*, 2012(06):013, jun 2012.

[30] CAST collaboration: V. Anastassopoulos et al. New cast limit on the axion–photon interaction. *Nature Physics*, 13(6):584–590, May 2017.

[31] F Della Valle, U Gastaldi, G Messineo, E Milotti, R Pengo, L Piemontese, G Ruoso, and G Zavattini. Measurements of vacuum magnetic birefringence using permanent dipole magnets: the pvlas experiment. *New Journal of Physics*, 15(5):053026, may 2013.

[32] Malte Buschmann, Christopher Dessert, Joshua W. Foster, Andrew J. Long, and Benjamin R. Safdi. Upper limit on the qcd axion mass from isolated neutron star cooling. *Physical Review Letters*, 128(9), mar 2022.

[33] Arcadi et al. The waning of the WIMP? A review of models, searches, and constraints. *The European Physical Journal C*, 78(3):1–57, 2018.

[34] Jonathan L. Feng. Dark Matter Candidates from Particle Physics and Methods of Detection. *Ann. Rev. Astron. Astrophys.*, 48:495–545, 2010.

[35] Alessandro De Angelis and Mario Pimenta. *Introduction to Particle and Astroparticle Physics: Multimessenger Astronomy and its Particle Physics Foundations*. Undergraduate Lecture Notes in Physics. Springer Nature, Heidelberg, 2018.

[36] John N. Bahcall and Raymond M. Soneira. The Universe at faint magnitudes, models for the Galaxy and the predicted star counts. *The Astrophysical Journal Supplement Series*, 44:73–110, 1980.

[37] Julio F Navarro. The structure of cold dark matter halos. In *Symposium-international astronomical union*, volume 171, pages 255–258. Cambridge University Press, 1996.

[38] Andrey V. Kravtsov, Anatoly A. Klypin, James S. Bullock, and Joel R. Primack. The cores of dark matter–dominated galaxies: Theory versus observations. *The Astrophysical Journal*, 502(1):48–58, July 1998.

[39] E. Charles, M. Sánchez-Conde, B. Anderson, R. Caputo, A. Cuoco, M. Di Mauro, A. Drlica-Wagner, G.A. Gomez-Vargas, M. Meyer, L. Tibaldo, M. Wood, G. Zaharijas, S. Zimmer, M. Ajello, A. Albert, L. Baldini,

K. Bechtol, E.D. Bloom, F. Ceraudo, J. Cohen-Tanugi, S.W. Digel, J. Gaskins, M. Gustafsson, N. Mirabal, and M. Razzano. Sensitivity projections for dark matter searches with the fermi large area telescope. *Physics Reports*, 636:1–46, June 2016.

[40] V. Springel, J. Wang, M. Vogelsberger, A. Ludlow, A. Jenkins, A. Helmi, J. F. Navarro, C. S. Frenk, and S. D. M. White. The aquarius project: the subhaloes of galactic haloes. *Monthly Notices of the Royal Astronomical Society*, 391(4):1685–1711, 12 2008.

[41] Julio F. Navarro, Aaron Ludlow, Volker Springel, Jie Wang, Mark Vogelsberger, Simon D.M. White, Adrian Jenkins, Carlos S. Frenk, and Amina Helmi. The Diversity and Similarity of Cold Dark Matter Halos. *Mon. Not. Roy. Astron. Soc.*, 402:21, 2010.

[42] A. Burkert. The structure of dark matter halos in dwarf galaxies. *The Astrophysical Journal*, 447(1), July 1995.

[43] Hai-Nan Lin and Xin Li. The dark matter profiles in the milky way. *Monthly Notices of the Royal Astronomical Society*, 487(4):5679–5684, 06 2019.

[44] Michael Gustafsson, Erik Lundström, Lars Bergström, and Joakim Edsjö. Significant gamma lines from inert higgs dark matter. *Physical Review Letters*, 99(4), July 2007.

[45] Lars Bergström and Piero Ullio. Full one-loop calculation of neutralino annihilation into two photons. *Nuclear Physics B*, 504(1–2):27–44, October 1997.

[46] Shigeki Matsumoto, Joe Sato, and Yoshio Sato. Enhancement of line gamma ray signature from bino-like dark matter annihilation due to cp violation, 2005.

[47] Francesc Ferrer, Lawrence M. Krauss, and Stefano Profumo. Indirect detection of light neutralino dark matter in the next-to-minimal supersymmetric standard model. *Physical Review D*, 74(11), December 2006.

[48] Stefano Profumo. Hunting the lightest lightest neutralinos. *Phys. Rev. D*, 78:023507, Jul 2008.

[49] Christoph Weniger. A tentative gamma-ray line from Dark Matter annihilation at the Fermi Large Area Telescope. *Journal of Cosmology and Astroparticle Physics*, 2012(08):007–007, aug 2012.

[50] M. Ackermann et al. Search for gamma-ray spectral lines with the Fermi Large Area Telescope and dark matter implications. *Physical Review D*, 88(8), oct 2013.

[51] M. Ackermann et al. Updated search for spectral lines from Galactic dark matter interactions with pass 8 data from the Fermi Large Area Telescope. *Phys. Rev. D*, 91(12):122002, 2015.

[52] Alejandro Ibarra, Sergio López Gehler, and Miguel Pato. Dark matter constraints from box-shaped gamma-ray features. *Journal of Cosmology and Astroparticle Physics*, 2012(07):043, jul 2012.

[53] Xiaoyong Chu, Suchita Kulkarni, and Pierre Salati. Dark matter indirect signals with long-lived mediators. *Journal of Cosmology and Astroparticle Physics*, 2017(11):023, nov 2017.

[54] M. N. Mazziotta, F. Loparco, D. Serini, A. Cuoco, P. De La Torre Luque, F. Gargano, and M. Gustafsson. Search for dark matter signatures in the gamma-ray emission towards the Sun with the Fermi Large Area Telescope. *Physical Review D*, 102(2), jul 2020.

[55] Zhao-Qiang Shen, Zi-Qing Xia, and Yi-Zhong Fan. Search for line-like and box-shaped spectral features from nearby galaxy clusters with 11.4 years of fermi large area telescope data. *The Astrophysical Journal*, 920(1):1, oct 2021.

[56] David Tucker-Smith and Neal Weiner. Inelastic dark matter. *Phys. Rev.*, D64:043502, 2001.

[57] Douglas P. Finkbeiner, Tongyan Lin, and Neal Weiner. Inelastic Dark Matter and DAMA/LIBRA: An Experimentum Crucis. *Phys. Rev.*, D80:115008, 2009.

[58] Spencer Chang, Graham D. Kribs, David Tucker-Smith, and Neal Weiner. Inelastic Dark Matter in Light of DAMA/LIBRA. *Phys. Rev.*, D79:043513, 2009.

[59] Arjun Menon, Rob Morris, Aaron Pierce, and Neal Weiner. Capture and Indirect Detection of Inelastic Dark Matter. *Phys. Rev.*, D82:015011, 2010.

[60] Shmuel Nussinov, Lian-Tao Wang, and Itay Yavin. Capture of Inelastic Dark Matter in the Sun. *JCAP*, 0908:037, 2009.

[61] Riccardo Catena and Fredrik Hellstrom. New constraints on inelastic dark matter from IceCube. *JCAP*, 1810(10):039, 2018.

[62] Mattias Blennow, Stefan Clementz, and Juan Herrero-Garcia. The distribution of inelastic dark matter in the Sun. *Eur. Phys. J.*, C78(5):386, 2018.

[63] Brian Batell, Maxim Pospelov, and Adam Ritz. Direct detection of multicomponent secluded WIMPs. *Physical Review D*, 79(11), jun 2009.

[64] for Fermi-LAT collaboration A. Abdo et al. Fermi large area telescope observations of two gamma-ray emission components from the quiescent sun. *The Astrophysical Journal*, 734(2):116, jun 2011.

[65] Qing-Wen Tang, Kenny C. Y. Ng, Tim Linden, Bei Zhou, John F. Beacom, and Annika H. G. Peter. Unexpected dip in the solar gamma-ray spectrum. *Phys. Rev. D*, 98:063019, Sep 2018.

[66] D. Seckel, Todor Stanev, and T. K. Gaisser. Signatures of Cosmic-Ray Interactions on the Solar Surface. *apj*, 382:652, December 1991.

[67] Orlando, E. and Strong, A. W. Gamma-ray emission from the solar halo and disk: a study with egret data. *A&A*, 480(3):847–857, 2008.

[68] E. Orlando and A. W. Strong. Gamma rays from halos around stars and the sun. *Astrophysics and Space Science*, 309(1):359–363, 2007.

[69] M. N. Mazziotta, P. De La Torre Luque, L. Di Venere, A. Fassò, A. Ferrari, F. Loparco, P. R. Sala, and D. Serini. Cosmic-ray interactions with the sun using the fluka code. *Phys. Rev. D*, 101:083011, Apr 2020.

[70] C. Amole et al. Dark Matter Search Results from the Complete Exposure of the PICO-60 C_3F_8 Bubble Chamber. *Physical Review D*, 100(2), jul 2019.

[71] E. Aprile et al. Dark Matter Search Results from a One Ton-Year Exposure of XENON1T. *Physical Review Letters*, 121(11), September 2018.

[72] The Fermi-LAT Collaboration. The fermi galactic center gev excess and implications for dark matter. *arXiv e-prints*, 2017.

[73] Michael Kuhlen, Piero Madau, and Joseph Silk. Exploring dark matter with milky way substructure. *Science*, 325(5943):970–973, August 2009.

[74] Lisa Goodenough and Dan Hooper. Possible evidence for dark matter annihilation in the inner milky way from the fermi gamma ray space telescope, 2009.

[75] V. Vitale and A. Morselli. Indirect search for dark matter from the center of the Milky Way with the *Fermi*-Large Area Telescope. In *Fermi Symposium Proceedings*, eConf Proceedings C091122, 2009. arXiv:0912.3828.

[76] D. Hooper and L. Goodenough. Dark matter annihilation in the Galactic Center as seen by the *Fermi* Gamma Ray Space Telescope. *Phys. Lett. B*, 697:412–428, 2011.

[77] K. N. Abazajian and M. Kaplinghat. Detection of a gamma-ray source in the galactic center consistent with extended emission from dark matter annihilation and concentrated astrophysical emission. *Phys. Rev. D*, 86:083511, 2012.

[78] D. Hooper and T. R. Slatyer. Two emission mechanisms in the fermi bubbles: A possible signal of annihilating dark matter. *Phys. Dark Univ.*, 2:118–138, 2013.

[79] Chris Gordon and Oscar Macías. Dark matter and pulsar model constraints from galactic center fermi-lat gamma-ray observations. *Phys. Rev. D*, 88:083521, Oct 2013.

[80] Tansu Daylan, Douglas P. Finkbeiner, Dan Hooper, Tim Linden, Stephen K.N. Portillo, Nicholas L. Rodd, and Tracy R. Slatyer. The characterization of the gamma-ray signal from the central milky way: A case for annihilating dark matter. *Physics of the Dark Universe*, 12:1–23, June 2016.

[81] F. Calore, I. Cholis, and C. Weniger. Background model systematics for the fermi gev excess. *JCAP*, 03:038, 2015.

[82] B. et al. Zhou. Gev excess in the milky way: The role of diffuse galactic gamma-ray emission templates. *Phys. Rev. D*, 91:123010, 2015.

[83] M. et al. Ajello. Fermi-lat observations of high-energy gamma-ray emission toward the galactic center. *Astrophys. J.*, 819(1):44, 2016.

[84] M. Ackermann et al. The spectrum and morphology of the fermi bubbles. *Astrophysical Journal*, 793(1):64, 2014.

[85] Richard Bartels, Emma Storm, Christoph Weniger, and Francesca Calore. The fermi-lat gev excess as a tracer of stellar mass in the galactic bulge. *Nature Astronomy*, 2(10):819–828, 2018.

[86] Dmitry V. Malyshev. Towards resolving the Galactic center GeV excess with millisecond-pulsars-like sources using machine learning. *Phys. Rev. D*, 111(4):043033, 2025.

[87] Andrea Albert, Germán A. Gómez-Vargas, Michael Grefe, Carlos Muñoz, Christoph Weniger, Elliott D. Bloom, Eric Charles, Mario N. Mazziotta,

and Aldo Morselli. Search for 100 MeV to 10 GeV γ-ray lines in the Fermi-LAT data and implications for gravitino dark matter in the $\mu\nu$SSM. *Journal of Cosmology and Astroparticle Physics*, 2014(10):023–023, October 2014.

[88] A. A. Abdo et al. Fermi Large Area Telescope Search for Photon Lines from 30 to 200 GeV and Dark Matter Implications. *Physical Review Letters*, 104(9), mar 2010.

[89] M. Ackermann et al. Fermi LAT search for dark matter in gamma-ray lines and the inclusive photon spectrum. *Physical Review D*, 86(2), jul 2012.

[90] J. Chang et al. The DArk Matter Particle Explorer mission. *Astroparticle Physics*, 95:6–24, oct 2017.

[91] Yun-Feng Liang. Search for gamma-ray spectral lines with the DArk Matter Particle Explorer. *Science Bulletin*, 67(7):679–684, 2022.

[92] M. Ackermann et al. Dark matter constraints from observations of 25 Milky Way satellite galaxies with the Fermi Large Area Telescope. *Physical Review D*, 89(4), feb 2014.

[93] Gary Steigman, Basudeb Dasgupta, and John F. Beacom. Precise relic WIMP abundance and its impact on searches for dark matter annihilation. *Physical Review D*, 86(2), jul 2012.

[94] Ackermann et al. Searching for Dark Matter Annihilation from Milky Way Dwarf Spheroidal Galaxies with Six Years of Fermi Large Area Telescope Data. *Physical Review Letters*, 115(23), nov 2015.

[95] M. Ackermann et al. Constraints on the galactic halo dark matter from fermi-lat diffuse measurements. *The Astrophysical Journal*, 761(2):91, nov 2012.

[96] Abramowski et al. Search for a dark matter annihilation signal from the galactic center halo with h.e.s.s. *Phys. Rev. Lett.*, 106:161301, Apr 2011.

[97] Aleksic et al. Optimized dark matter searches in deep observations of segue 1 with magic. *Journal of Cosmology and Astroparticle Physics*, 2014(02):008, feb 2014.

[98] Kevork N. Abazajian and J. Patrick Harding. Constraints on wimp and sommerfeld-enhanced dark matter annihilation from hess observations of the galactic center. *Journal of Cosmology and Astroparticle Physics*, 2012(01):041, jan 2012.

[99] Kevork N. Abazajian, Nicolas Canac, Shunsaku Horiuchi, and Manoj Kaplinghat. Astrophysical and dark matter interpretations of extended gamma-ray emission from the galactic center. *Phys. Rev. D*, 90:023526, Jul 2014.

[100] A. A. Abdo et al. Observations of Milky Way Dwarf Spheroidal galaxies with the Fermi-LAT detector and constraints on Dark Matter models. *The Astrophysical Journal*, 712(1):147–158, feb 2010.

[101] M. N. Mazziotta, F. Loparco, F. de Palma, and N. Giglietto. A model-independent analysis of the Fermi Large Area Telescope gamma-ray data from the Milky Way dwarf galaxies and halo to constrain dark matter scenarios. *Astropart. Phys.*, 37:26–39, 2012.

[102] Pérez-Romero, Judit. Dark matter gamma-ray searches in galaxy clusters: Status and prospects. *EPJ Web Conf.*, 319:11004, 2025.

[103] R.Abbasi et al. Search for gev-scale dark matter annihilation in the sun with icecube deepcore. *Phys. Rev. D*, 105:062004, Mar 2022.

[104] K. et al. Choi. Search for neutrinos from annihilation of captured low-mass dark matter particles in the sun by super-kamiokande. *Phys. Rev. Lett.*, 114:141301, Apr 2015.

[105] S. Adrián-Martínez et al. Limits on dark matter annihilation in the sun using the ANTARES neutrino telescope. *Physics Letters B*, 759:69–74, 2016.

[106] T. Tanaka et al. An Indirect Search for WIMPs in the Sun using 3109.6 days of upward-going muons in Super-Kamiokande. *Astrophys. J.*, 742:78, 2011.

[107] M.G. Aartsen et al. Search for dark matter annihilations in the Sun with the 79-string IceCube detector. *Phys. Rev. Lett.*, 110(13):131302, 2013.

[108] S. Adrian-Martinez et al. First results on dark matter annihilation in the Sun using the ANTARES neutrino telescope. *JCAP*, 11:032, 2013.

[109] IceCube Collaboration, M. G. Aartsen, and et al. Search for neutrinos from dark matter self-annihilations in the center of the Milky Way with 3 years of IceCube/DeepCore. *The European Physical Journal C*, 77(9):627, 2017.

[110] IceCube Collaboration, R. Abbasi, and et al. Search for Dark Matter from the Galactic Center with IceCube. *Phys. Rev. D*, 85:042002, 2012.

[111] IceCube Collaboration, M. G. Aartsen, and et al. Search for Dark Matter Annihilation in the Galactic Halo with IceCube. *Eur. Phys. J. C*, 73:938, 2013.

[112] IceCube Collaboration, M. G. Aartsen, and et al. Search for dark matter annihilation in the Galactic Center with IceCube-79. *The European Physical Journal C*, 75(10):492, 2015.

[113] IceCube Collaboration, M. G. Aartsen, and et al. Search for neutrinos from dark matter self-annihilation in the galactic halo with the icecube detector. *Eur. Phys. J. C*, 77:146, 2017.

[114] ANTARES Collaboration, S. Adrian-Martinez, and et al. Search of dark matter annihilation in the galactic centre using the antares neutrino telescope. *Phys. Lett. B*, 759:69–74, 2016.

[115] Fermi-LAT Collaboration and MAGIC Collaboration. Limits to dark matter annihilation cross-section from a combined analysis of magic and fermi-lat observations of dwarf satellite galaxies. *JCAP*, 02:039, 2016.

[116] H.E.S.S. Collaboration. Search for dark matter annihilations towards the inner galactic halo from 10 years of observations with h.e.s.s. *Phys. Rev. Lett.*, 117(11):111301, 2016.

[117] M.G. Aartsen et al. The IceCube Neutrino Observatory: instrumentation and online systems. *Journal of Instrumentation*, 12(03):P03012, mar 2017.

[118] IceCube Collaboration, M. Ageron, and et al. ANTARES: The first undersea neutrino telescope. *Nuclear Instruments and Methods in Physics Research Section A: Accelerators, Spectrometers, Detectors and Associated Equipment*, 656(1):11–38, 2011.

[119] R.Abbasi et al. Search for neutrino lines from dark matter annihilation and decay with icecube. *Phys. Rev. D*, 108:102004, Nov 2023.

[120] M.Aartsen et al. Icecube search for dark matter annihilation in nearby galaxies and galaxy clusters. *Phys. Rev. D*, 88:122001, Dec 2013.

[121] Elmo Tempel, Antti Tamm, and Peeter Tenjes. Visible and dark matter in m 31 - ii. a dynamical model and dark matter density distribution, 2008.

[122] M.and others Aguilar. First Result from the Alpha Magnetic Spectrometer on the International Space Station: Precision Measurement of the Positron Fraction in Primary Cosmic Rays of 0.5–350 GeV. *Phys. Rev. Lett.*, 110:141102, Apr 2013.

[123] Bazilevskaya G. Adriani O., Barbarino G. et al. An anomalous positron abundance in cosmic rays with energies 1.5–100 GeV. *Nature*, pages 607–609, Apr 2009.

[124] S. Abdollahi et al. Search for Cosmic-Ray Electron and Positron Anisotropies with Seven Years of Fermi Large Area Telescope Data. *Phys. Rev. Lett.*, 118:091103, Mar 2017.

[125] Stefano Profumo. Dissecting cosmic-ray electron-positron data with Occam's razor: the role of known pulsars. *Open Physics*, 10(1):1–31, jan 2012.

[126] Stefano Profumo. An observable electron-positron anisotropy cannot be generated by dark matter. *Journal of Cosmology and Astroparticle Physics*, 2015(02):043, feb 2015.

[127] Carmelo Evoli, Elena Amato, Pasquale Blasi, and Roberto Aloisio. Galactic factories of cosmic-ray electrons and positrons. *Phys. Rev. D*, 103:083010, Apr 2021.

[128] Fermi Science Support Center. `https://fermi.gsfc.nasa.gov/ssc`.

[129] W. Kraushaar et al. Explorer XI Experiment on Cosmic Gamma Rays. *Astrophysical Journal*, 141:845, 1965.

[130] W. Kraushaar et al. High-Energy Cosmic Gamma-Ray Observations from the OSO-3 Satellite. *Astrophysical Journal*, 341:177, 1972.

[131] C.E. Fichtel et al. High-energy gamma-ray results from the second Small Astronomy Satellite. *Astrophysical Journal*, 198:163, 1975.

[132] G. Bignami et al. The COS-B experiment for gamma-ray astronomy. *Space Science Instrumentation*, 1:245, 1975.

[133] R.W. Klebesadel et al. Observations of Gamma-Ray Bursts of Cosmic Origin. *Astrophysical Journal*, 182:L85, 1973.

[134] N. Gehrels, E. Chipman, and D. A. Kniffen. The Compton Gamma Ray Observatory. *aaps*, 97:5–12, January 1993.

[135] D.J. Thompson et al. Calibration of the Energetic Gamma-Ray Experiment Telescope (EGRET) for the Compton Gamma-Ray Observatory. *Astrophys. J. Suppl.*, 86:629–656, 1993.

[136] B. A. Harmon et al. The Burst and Transient Source Experiment (BATSE) Earth Occultation Catalog of Low-Energy Gamma-Ray Sources. *The Astrophysical Journal Supplement Series*, 154(2):585–622, oct 2004.

[137] Fermi Gamma ray Space Telescope mission page. https://science.nasa.gov/mission/fermi.

[138] W.B. Atwood et al. The Large Area Telescope on the Fermi Gamma-ray Space Telescope Mission. *Astrophys. J.*, 697:1071–1102, 2009.

[139] Charles Meegan et al. The Fermi Gamma-Ray Burst Monitor. *Astrophys. J.*, 702:791–804, 2009.

[140] Fermi Science Support Center - Overview of the Mission. `https://fermi.gsfc.nasa.gov/ssc/data/analysis/documentation/Cicerone/Cicerone_Introduction/mission_overview.html`.

[141] LAT All-Sky Survey Observations following -Y SADA Anomaly. `https://fermi.gsfc.nasa.gov/ssc/observations/types/post_anomaly/`.

[142] GCN: The Gamma-ray Coordinates Network (TAN: Transient Astronomy Network). `https://gcn.gsfc.nasa.gov/`.

[143] E. Bissaldi, A. von Kienlin, G. Lichti, H. Steinle, P. N. Bhat, M. S. Briggs, G. J. Fishman, A. S. Hoover, R. M. Kippen, M. Krumrey, M. Gerlach, V. Connaughton, R. Diehl, J. Greiner, A. J. van der Horst, C. Kouveliotou, S. McBreen, C. A. Meegan, W. S. Paciesas, R. D. Preece, and C. A. Wilson-Hodge. Ground-based calibration and characterization of the fermi gamma-ray burst monitor detectors. *Experimental Astronomy*, 24(1):47–88, 2009.

[144] M. Ackermann et al. The Fermi Large Area Telescope on orbit: Event classification, Instrument Response Functions, ans calibration. *The Astrophysical Journal Supplement Series*, 203(1):4, oct 2012.

[145] W.B. Atwood et al. Design and Initial Tests of the Tracker-Converter of the Gamma-ray Large Area Space Telescope. *Astropart. Phys.*, 28:422–434, 2007.

[146] A.A. Moiseev, R.C. Hartman, J.F. Ormes, D.J. Thompson, M.J. Amato, T.E. Johnson, K.N. Segal, and D.A. Sheppard. The anti-coincidence detector for the glast large area telescope. *Astroparticle Physics*, 27(5):339–358, 2007.

[147] W. Atwood et al. Pass 8: Toward the full realization of the fermi-lat scientific potential, 2013.

[148] A. A. et al. Abdo and Fermi LAT Collaboration. Spectrum of the Isotropic Diffuse Gamma-Ray Emission Derived from First-Year Fermi Large Area Telescope Data. *prl*, 104(10):101101, March 2010.

[149] Fermi LAT Performance. `https://www.slac.stanford.edu/exp/glast/groups/canda/lat_Performance.htm`.

[150] LAT Instrument Response Functions—Overview. `https://fermi.gsfc.nasa.gov/ssc/data/analysis/documentation/Cicerone/Cicerone_LAT_IRFs/IRF_overview.html`.

[151] C. Pittori et al. The agile space mission: an italian success story and its legacy for future space astronomy, 2025.

[152] M. Tavani et al. The agile mission. *A&A*, 502(3):995–1013, 2009.

[153] M. Tavani, A. Bulgarelli, V. Vittorini, and et al. Discovery of powerful gamma-ray flares from the crab nebula. *Science*, 331:736, 2011.

[154] A. Giuliani, M. Cardillo, M. Tavani, and et al. Neutral pion emission from accelerated protons in the supernova remnant w44. *Astrophys. J. Lett.*, 742(2):L30, 2011.

[155] M. Cardillo, M. Tavani, A. Giuliani, and et al. The supernova remnant w44: confirmations and challenges for cosmic-ray acceleration. *Astron. Astrophys.*, 565:A74, 2014.

[156] S. Sabatini, M. Tavani, E. Striani, and et al. Episodic transient gamma-ray emission from the microquasar cygnus x-1. *Astrophys. J. Lett.*, 712(1):L10–L15, 2010.

[157] G. Ambrosi et al. for DAMPE Collaboration. Direct detection of a break in the teraelectronvolt cosmic-ray spectrum of electrons and positrons. *Nature*, 552(7683):63–66, 2017.

[158] G. Lucchetta, M. Ackermann, D. Berge, and R. Bühler. Introducing the MeVCube concept: a CubeSat for MeV observations. *Journal of Cosmology and Astroparticle Physics*, 2022(08):013, aug 2022.

[159] A. Goldstein et al. An Ordinary Short Gamma-Ray Burst with Extraordinary Implications: Fermi-GBM Detection of GRB 170817A. *The Astrophysical Journal Letters*, 848(2):L14, oct 2017.

[160] A. De Angelis et al. for e-ASTROGAM Collaboration. Science with e-ASTROGAM: A space mission for MeV–GeV gamma-ray astrophysics. *Journal of High Energy Astrophysics*, 19:1–106, 2018.

[161] R. Caputo et al. All-sky Medium Energy Gamma-ray Observatory eXplorer mission concept. *Journal of Astronomical Telescopes, Instruments, and Systems*, 8(4):044003, 2022.

[162] James Buckley, Lars Bergstrom, Bob Binns, Jeremy Buhler, Wenlei Chen, Michael Cherry, Stefan Funk, Dan Hooper, John Mitchell, Georgia De Nolfo, Samer Al Nussirat, Stefano Profumo, Brian Rauch, Daniel Stern, Garry Varner, Scott Wakely, and Adrian Zink. The Advanced Particle-astrophysics Telescope (APT). *Bulletin of the AAS*, 51(7), sep 30 2019. https://baas.aas.org/pub/2020n7i078.

[163] A. John et al. The Compton Spectrometer and Imager, 2023.

[164] B. Abbott et al. GW170817: Observation of Gravitational Waves from a Binary Neutron Star Inspiral. *Phys. Rev. Lett.*, 119:161101, Oct 2017.

[165] Index of /FTP/fermi/data/lat/weekly/photon. `https://heasarc.gsfc.nasa.gov/FTP/fermi/data/lat/weekly/photon/`.

[166] Fermitools Reference. https://fermi.gsfc.nasa.gov/ssc/data/analysis/scitools/references.html.

[167] Data Analysis, Simulations and Visualization on the Sphere. http://healpix.sourceforge.net/.

[168] Fermi Science Support Center. https://fermi.gsfc.nasa.gov/ssc/data/access/lat/BackgroundModels.html.

[169] P. De La Torre Luque, M.N. Mazziotta, A. Ferrari, F. Loparco, P.R. Sala, and D. Serini. FLUKA cross sections for cosmic-ray interactions with the DRAGON2 code. *Journal of Cosmology and Astroparticle Physics*, 2022(07):008, jul 2022.

[170] F. Ballarini et al. The FLUKA code: an overview. *Journal of Physics: Conference Series*, 41(1):151, may 2006.

[171] C. Evoli et al. Cosmic-ray propagation with DRAGON2: I. numerical solver and astrophysical ingredients. *Journal of Cosmology and Astroparticle Physics*, 2017(02):015, feb 2017.

[172] M. Ackermann et al. The spectrum of isotropic diffuse gamma-ray emission between 100 MeV and 820 GeV. *The Astrophysical Journal*, 799(1):86, jan 2015.

[173] Malcolm S. Longair. High Energy Astrophysics. In *High Energy Astrophysics*, 1981.

[174] R. C. Jennison. A Phase Sensitive Interferometer Technique for the Measurement of the Fourier Transforms of Spatial Brightness Distributions of Small Angular Extent. *Monthly Notices of the Royal Astronomical Society*, 118(3):276–284, 06 1958.

[175] K. Akiyama et al. First Sagittarius A* Event Horizon Telescope Results. IV. Variability, Morphology, and Black Hole Mass. *Astrophys. J. letters*, 930(2), 2022.